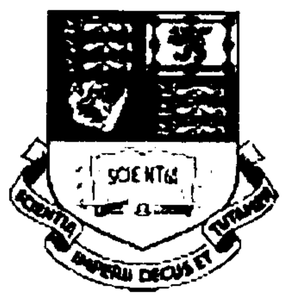
Experimental study of plasma jets produced by conical wire array z-pinches

David John Ampleford



Imperial College London
Department of Physics
Plasma Physics Group

Submitted in partial fulfilment of the requirements for the degree of Doctor of Philosophy in Science of the University of London and the Diploma of Imperial College.
March 2005

BIBL. LONDON. UNIV.

Abstract

Plasma jets are ubiquitous in the universe; active galactic nuclei, protostars and planetary nebulae all produce jets. It is possible to model these jets experimentally in the laboratory provided a number of scaling criteria are met. This thesis describes a new technique allowing the modelling of protostellar jets based on the wire array z-pinch. Experiments were performed on the MAGPIE pulsed power generator ($1MA$, $240ns$) using a modification of the usual cylindrical wire array z-pinch, in which the wires are inclined with respect to the axis (forming a cone).

Convergent flows in a conical wire array z-pinch meet in a conical shock, which ejects a highly supersonic jet (Mach number > 30). This Mach number, and hence the collimation of this jet is dependent on radiative cooling rates and, therefore, wire material; for tungsten the cooling length is comparable to the jet radius, leading to a highly collimated jet. For a given material, the introduction of angular momentum into the jet using a twisted conical wire array has a detrimental effect on this collimation.

The interaction of a jet with an ambient medium is investigated. Experiments where the jet interacts with a static gas cloud demonstrate the formation of a working surface. The observed velocity of the working surface is changed by variation of the density contrast (the ratio of densities in the jet and ambient medium), and this dependence is in agreement with analytic astrophysical models.

Experiments have also been performed with a jet propagating through a side wind. The jet remains well collimated as it is deflected by angles up to 30°. Internal structure is observed in the jet, including the internal oblique shock responsible for the deflection, and the results have been compared to astrophysical models.

The application of conical wire arrays to understanding the physical mechanisms involved in general wire arrays, including wire ablation, has also been explored.

Acknowledgements

The experiments described in this thesis would not have been possible without the collaboration of various member of the MAGPIE team at Imperial, who I would like to thank for their assistance. Firstly I would like to thank my supervisor Dr. Sergey Lebedev, for his continuous help, insight, enthusiasm and encouragement. Also my thanks go to Dr. Jerry Chittenden his help, and many useful discussions and suggestions. I also thank Prof. Malcolm Haines for useful discussions.

Drs. Simon Bland and Simon Bott have both given invaluable advice and assistance in the laboratory experiments and very useful discussions. The assistance of Gareth Hall, James Palmer and Jack Rapley in the lab has also been very much appreciated. The MAGPIE technicians, Alan Finch and John Worley, and Alan Raper in the physics workshop, have done a brilliant job keeping everything running smoothly in the lab and quickly fixing everything that we break. I would also like to acknowledge some previous members of the MAGPIE team, Drs. Farhat Beg and Raul Aliaga-Rossel, who were involved in performing some of the earliest conical wire array results, some of which have been used in this thesis, and also my 4th year MSci project-partner Stephen Hughes, who was involved in the first jet deflection experiments. Off-line characterisation of the gas nozzle for jet-gas interaction experiments was performed in conjunction with undergraduate project students: John Armitage, Laura Rutland, Graeme Blyth and Stuart Christie. I would also like to thank the various visitors to MAGPIE that I've had useful interactions with while doing my PhD.

I have had many useful discussions and suggestions from Dr. Andrea Ciardi who has also, along with Dr. Jerry Chittenden, Dr. Mark Sherlock and Christopher Jennings, performed many useful simulations. I am particularly grateful to Chris and Andrea for putting up with me in the office for the entirety of my time with MAGPIE, and providing useful distractions or (along with the rest of the MAGPIE team) going the to pub when we'd all had enough.

Members of the astrophysics group at the University of Rochester (particularly Prof. Adam Frank) have made a significant contribution to determining the astrophysical relevance of this work.

For funding during my time with MAGPIE I'd like to acknowledge EPSRC (for my Studentship) and AWE (for a CASE top-up).

I'm also very grateful to the non-physics related people who've supported me through my PhD. Thanks to all of the sailing and orchestra (and brass dectet) people, who have always been a useful distraction from physics, and a good excuse to go to get away from London at the weekends. Also to the flatmates I've had over the last few years (Steve, Alastair, Louise and Chris). Finally I am indebted to my family, who have supported me for my entire time at Imperial.

Contents

1 Introduction **13**

1.1 Plasma jets 13

1.2 Laboratory Astrophysics 15

1.3 Conical wire array z-pinches 16

1.4 Aims and outline 18

1.5 Impact of the work & author's contribution 19

2 Experimental background **22**

2.1 The MAGPIE generator and other pulsed power facilities 22

2.2 Diagnostic overview 26

2.3 Optical probing 27

2.3.1 Schlieren imaging 29

2.3.2 Shadowgraphy 30

2.3.3 Interferometry 31

2.3.4 Setup of camera systems 33

2.4 X-ray power 34

2.4.1 PCD cluster 34

2.4.2 XRD cluster 34

2.5 X-ray imaging 35

2.5.1 Time resolved X-ray pinhole cameras 35

2.5.2 X-pinch radiography 37

2.6 MHD Computer simulations 38

3 Conical wire array dynamics **40**

3.1 Overview of conical wire arrays 40

3.2 Wire ablation and precursor streams 42

3.3 The conical shock 51

3.4 Plasma jets from tungsten conical wire arrays 60

3.4.1 Jet tip velocity 60

3.4.2 Tungsten jet temperature 63

3.4.3 Velocity and mass distributions within the jet 65

3.5 Varying the cooling rate in the jet 73

3.6 Producing jets with angular momentum using twisted wire arrays . . 73

3.7 Conclusions 76

4 Comparison of laboratory and astrophysical jets **79**

4.1 Laboratory astrophysics and the scaling of jets 80

4.2 A brief overview of jets from protostars 84

4.3 Laboratory modelling of protostellar jets 86

4.3.1 Laboratory techniques for jet production 86

4.4 The effect of the ISM on protostellar jets 89

4.5 Producing an ambient medium in the laboratory 92

5 Jets propagating in quasi-stationary gas clouds **94**

5.1 Experimental setup 94

5.2 Jet-gas results 96

5.3 Varying density contrast 101

5.4 Interaction of a stainless steel jet with an argon cloud 104

5.5 Conclusions on jet interactions with a gas cloud 106

5.6 Propagation of a W jet in a W cloud 107

6 Jet deflection by a side wind **110**

6.1 Motivation for jet deflection experiments 110

6.2 Experimental setup and wind characteristics 113

6.2.1 Estimates of wind parameters 113

6.2.2 Experiments investigating foil ablation 117
6.3 Comparison of forces on the jet due to ablated material 119
6.4 Results and discussion 120
6.4.1 Experiments using a short interaction region 120
6.4.2 Results using a more uniform wind 128
6.5 Conclusions on jet propagating in a side-wind 137

7 Implosion phase of conical arrays **140**
7.1 Background on the implosion of cylindrical wire arrays 141
7.2 Implosion dynamics of conical wire arrays with small opening angles . 143
7.3 Implosion dynamics of large opening angle conical wire arrays 144
7.4 X-ray pulse shapes 146
7.5 Jets produced by imploding tungsten arrays 147
7.6 Future imploding conical wire array experiments 148

8 Summary **149**

List of Figures

1.1 Emission due to the jet produced by a protostar (HH111). 14

1.2 Conical wire array setup. 17

2.1 Artists impression of the MAGPIE generator. 23

2.2 The diode stack, MITL and load region of MAGPIE. 23

2.3 MAGPIE current pulses for conical wire array load, as well as a $sin^2(t)$ approximation 24

2.4 Diagnostic ports on the vacuum chamber of MAGPIE. 26

2.5 Photographs showing the diagnostic layout of MAGPIE. 28

2.6 Light and dark field schlieren setups 30

2.7 Setup of a Mach-Zehnder interferometer 32

2.8 Transmission of C16H14O3 foils shown by (a) linear and (b) logarithmic plots 35

2.9 Setup for x-ray framing camera. Four pinholes provide four separate images on the MCP. 36

2.10 X-pinch radiography setup. The x-pinch (left) images the wires of the array (centre) onto the film pack (right of the diagram). 38

3.1 Illustration of a conical wire array, including variables used in the discussion 41

3.2 Interferometer image showing the complete conical wire array setup with a W array, opening angle $\theta = 30°$ at $331ns$. 42

3.3 X-pinch radiography of a conical wire array. 43

3.4 Plasma streams shown by end-on XUV and soft x-ray emission of wires and streams. 44

3.5 (a) Interferometer image of an 8 wire Al 38° conical array and (b) a plot of electron density measured on this, along with predictions of electron densities. 46
3.6 Shadowgram of a 16 wire W array at 343ns showing wires and streams. 48
3.7 Curvature of precursor plasma streams in XUV emission from a 16 wire Al array at $249ns$. 49
3.8 (a) Line-outs from an XUV image used for FFT, and (b) FFT results for the full line-out (blue) and the upper (green) and lower (red) halves. The uncertainty in the peak wavelength is approximately the spacing to the nearest data points on the FFT. 51
3.9 Jet formation by conical shock of stellar wind. 52
3.10 Mass incident on the array axis as a function of z for different times using an array with $\theta \sim 30°$. 54
3.11 (a) Schlieren image of a partial conical shock in an 8 wire Al 11° conical wire array and (b) a partial precursor an interferometer image of an 8 wire Al cylindrical wire array taken at $128ns$. 55
3.12 Plot of density incident at a radius of $0.5mm$ for an 11° conical array at $137ns$, along with values of the critical density at $1mm$ derived from when the cylindrical array precursor forms. 57
3.13 Emission from the array in gated imaging: (a) XUV ($h\nu > 40eV$) and (b) soft x-ray ($1.5\mu m$ CHO filter, $h\nu \sim 120 - 290eV$). Both images are at $292ns$. The whole array emits in XUV, however only the conical shock (labelled CS) emits on the filtered image. 58
3.14 Schlieren images of a jet produced by a W conical array at (a) $308ns$, (b) $320ns$ and (c) $331ns$ after start of current (all from the same experiment and on the same scale). (d) is a plot of the tip positions from each of these images. The red lines on the images (a,b,c) correspond to the measured heights of the tip plotted on the graph (d). 61
3.15 Expected position of conical shock collapse and experimental jet tip positions. 63

3.16 A jet leaving the conical shock in both XUV (un-filtered, $h\nu > 40eV$) and soft x-ray ($1.5\mu m$ CHO filter, $h\nu \sim 120 - 290eV$) emission, both on the same experiment at $292ns$. 64
3.17 Radial expansion of a tungsten jet. Jet diameter measured from schlieren images at subsequent times $200\mu m$ behind the jet tip. 65
3.18 Interferometer images, showing that the fringes can not easily be resolved in a jet from an untwisted array (a), however when a twist is introduced the fringes are more easily resolved in jets from arrays with a few degrees of twist (b). 67
3.19 Plot of electrons per unit length within the jet, obtained by integrating the fringe shift in Fig 3.18b across the jet at $313ns$. 68
3.20 Mass flux through the top of the conical shock for a 25° array at $313ns$. 68
3.21 Predictions for the number of electrons per unit length for various values of charge state Z and assuming constant velocity and all material goes into jet. 69
3.22 Predictions for number of electrons per unit length for various values of charge state Z and assuming decreasing velocity and only material incident on a collapsed conical shock is part of the jet. Also shown is the experimental measurements for electrons per unit length within the jet. 71
3.23 Predictions for the mass per unit length in the jet for various times. . 72
3.24 XUV ($h\nu > 30eV$) emission from the jet region at a time similar to when the top of the conical shock collapses ((a) at $280ns$) and later when the jet has fully formed ((b) at $310ns$). 72
3.25 Soft x-ray emission, XUV emission and schlieren/interferometer images of jets from arrays of different materials. 74
3.26 Twisted array setup that leads to both an axial magnetic field and an angular momentum in the precursor streams. 75
3.27 End-on XUV emission from conical arrays without and with twist. . . 76

3.28 Comparison of end-on XUV emission from cylindrical arrays without and with a twist and (on the same scale) the centre of a twisted conical array. The precursor column in both images of cylindrical arrays are not hollow, however the centre of the conical array is hollow. 77
3.29 Jets produced by (a) twisted and (b) untwisted conical W arrays, both taken at $\sim 330ns$. 77

4.1 (a) Experimental layout for laser produced jets in Farley et al. and (b) effect of radiative cooling 1.3ns after laser pulse from Shigemori et al. 87
4.2 The HH 34 bow shock and Mach disk as seen with the Hubble Space Telescope. 90
4.3 Working surface that is formed as a supersonic jet interacts with an ambient medium. 91
4.4 Density plots from simulations by Blondin et al. showing the evolution of the jet and the effects of an ambient medium and radiative cooling. 92

5.1 Setup for gas interaction experiments from both side-on and end-on to the array. The diagnostic layout is shown on the end-on image. . . 95
5.2 (a) XUV emission from a jet interacting with gas at $212ns$ and (b) photo from XUV camera port. 97
5.3 Schlieren images of the jet for experiments with gas present (a) and without gas present (b). Both experiments have an identical array configuration to Fig 5.2. 98
5.4 Interferometer image of jet-gas interaction and phase map derived from it. 99
5.5 Time-series of XUV emission ($h\nu > 30eV$) from a jet-gas interaction with the nozzle $26.5mm$ above the anode plate. The graph shows the working surface trajectory as well as the tip position of the collapsed (later-time) jet from the schlieren image in Fig 5.3a. This confirms that we are seeing an interaction involving the early-time halo jet. . 100

5.6 Time-series of XUV emission ($h\nu > 30eV$) from a jet-gas interaction with the nozzle $22.6mm$ above the anode plate. The bright ring of emission on the centre two images (particularly the image at $223ns$) is re-emission from the gas jet housing. The graph shows the working surface trajectory. 103
5.7 Time-series of XUV emission from a stainless steel jet interacting with argon, with the nozzle $26.5mm$ above the anode plate. 105
5.8 Setup for the interaction of a plasma jet with a cloud of the same material (the precursor column of a cylindrical wire array). Also shown is a setup to interact two counter-propagating jets. 107
5.9 Photograph of the setup for a jet-precursor interaction and a schlieren image of a jet propagating in an un-collapsed precursor column. . . . 108

6.1 Astrophysical observation of HH502 - a deflected jet with 'C-shaped' symmetry 111
6.2 Setup for experiments on the affect of jet propagating in a side-wind . 113
6.3 X-ray intensities measure with PCD detectors which are open and filtered by $1.5\mu m$ and $3\mu m$ CHO filters. 115
6.4 Estimated mass ablation rate and velocity of the flow from the foil based on equations 6.4 and 6.5 and a $sin^4\left(\frac{2\pi(t-60ns}{t_0}\right)$ approximation to the incident intensity (as was plotted on Fig 6.3). 117
6.5 Estimated density profile relative to the foil obtained using the injection rate from equations 6.4 and assuming a constant velocity and accounting for the time of flight between material being ablated and its position at the given times. 118
6.6 Interferogram of two foils ablated by emission from a 16 wire W cylindrical array. 119
6.7 Comparison of expected forces due to a gradient in thermal pressure and momentum transfer from the wind at $340ns$. The density and velocity of the wind have been calculated using equations 6.4 and 6.5. 120

6.8 Interferometer image of jet deflection by a wind impacting a jet at $t = 303ns$. 121
6.9 Fit to the curvature of the jet observed in Fig 6.8 122
6.10 High magnification schlieren image of the deflected jet in Fig 6.8 at $303ns$. 123
6.11 Line integrated electron density profiles at different axial positions measured on the interferometer image in Fig 6.8. 124
6.12 Interferometer image of jet deflection by a wind impacting a jet at $t = 306ns$. The wind is produced by a foil $2.4mm$ from the jet axis (i.e. closer to the jet axis than in Fig 6.8, hence with a higher wind density) 126
6.13 High magnification schlieren image of the same experiment as Fig 6.12. 126
6.14 Setup with a longer, angled target 129
6.15 Schlieren image of a jet deflected by a longer angled target at $343ns$. The initial foil position is marked in blue. For a more detailed labelling of features on this image see Fig 6.18 later. 130
6.16 Fit to the trajectory in Fig 6.15. The z-axis is the position along the jet, and the x-axis is the distance from the original position of the foil. 131
6.17 Interferometer image of the same experiment in Fig 6.15 at $343ns$. . . 132
6.18 Shocks within the jet shown by both high and low magnification schlieren images (both at $343ns$). The labels on the centre image are discussed in the text. 135
6.19 XUV ($h\nu > 30eV$) emission from the same experiment as Fig 6.18 at $380ns$ 136
6.20 Simulations of a jet in propagating in a side-wind. 2D slice from a 3D Gorgon simulation with uniform jet and wind (performed by Dr. A. Ciardi, for a brief description of this code see section 2.6). 137
6.21 Development of the jet-wind interaction with time, shown by XUV emission. 138

6.22 High and low magnification schlieren images showing the interaction of the low density, un-collapsed tip of the jet (from a different experiment to all other images) 139

7.1 Implosion dynamics of a $20\mu m$ Al cylindrical wire array shown on (a) an optical radial streak camera image (radial emission profile vs time), (b) an interferometer image at $231ns$ and (c) a schlieren image at $244ns$. 142

7.2 X-ray pulse from an imploding cylindrical wire array. 142

7.3 Implosion of a $\theta = 16°$ conical array, as shown by (a) interferometry at $253ns$ and (b) schlieren at $265ns$. 143

7.4 Implosion of a $\theta = 38°$ conical array, as shown by (a) interferometry at $180ns$ and (b) schlieren at $192ns$ and (c) soft x-ray emission at 221, 231, 241 and $251ns$. 145

7.5 Sketch of current paths: on the left before wire breakage and on the right after wire breakage. 146

7.6 X-ray pulse shapes for a large opening angle conical array and a cylindrical wire array. 147

7.7 Imploding W jet $333ns$ after the start of the current pulse. The blue arrow indicates the disk-like structure possibly produced as a result of the implosion of the array, as discussed in the text. 148

Chapter 1

Introduction

1.1 Plasma jets

Observations have provided numerous examples of collimated outflows of material from astrophysical bodies. The number of known outflows has greatly increased with the introduction of the Hubble Space telescope (HST). These outflows, often called jets, can be produced by many different forms of astrophysical body. Active galactic nuclei, young stars (protostars) and planetary nebulae all have associated outflows.

The topic of this thesis is the modelling of the jets produced by young stars in the laboratory by scaled experiments. As an example of these jets Fig 1.1 shows an HST image of a jet produced by a protostar.

An important feature of the evolution of these jets is interactions of the jet with an ambient medium and internal shocks within the jets, both of which often aid observations of the jets. For example, when jets from young stars interact with the interstellar medium shocks form (called Herbig-Haro objects after their discoverers) which emit in forbidden lines. These HH objects are bow shocks and knots within the jet and were the first evidence that protostars have associated jets. Figure 1.1 is one of these HH objects - HH111.

A major motivation for investigating all types of astrophysical jets is that the outflow can provide information about the source object. It is thought that jets play a fundamental role in the star formation process, removing angular momentum

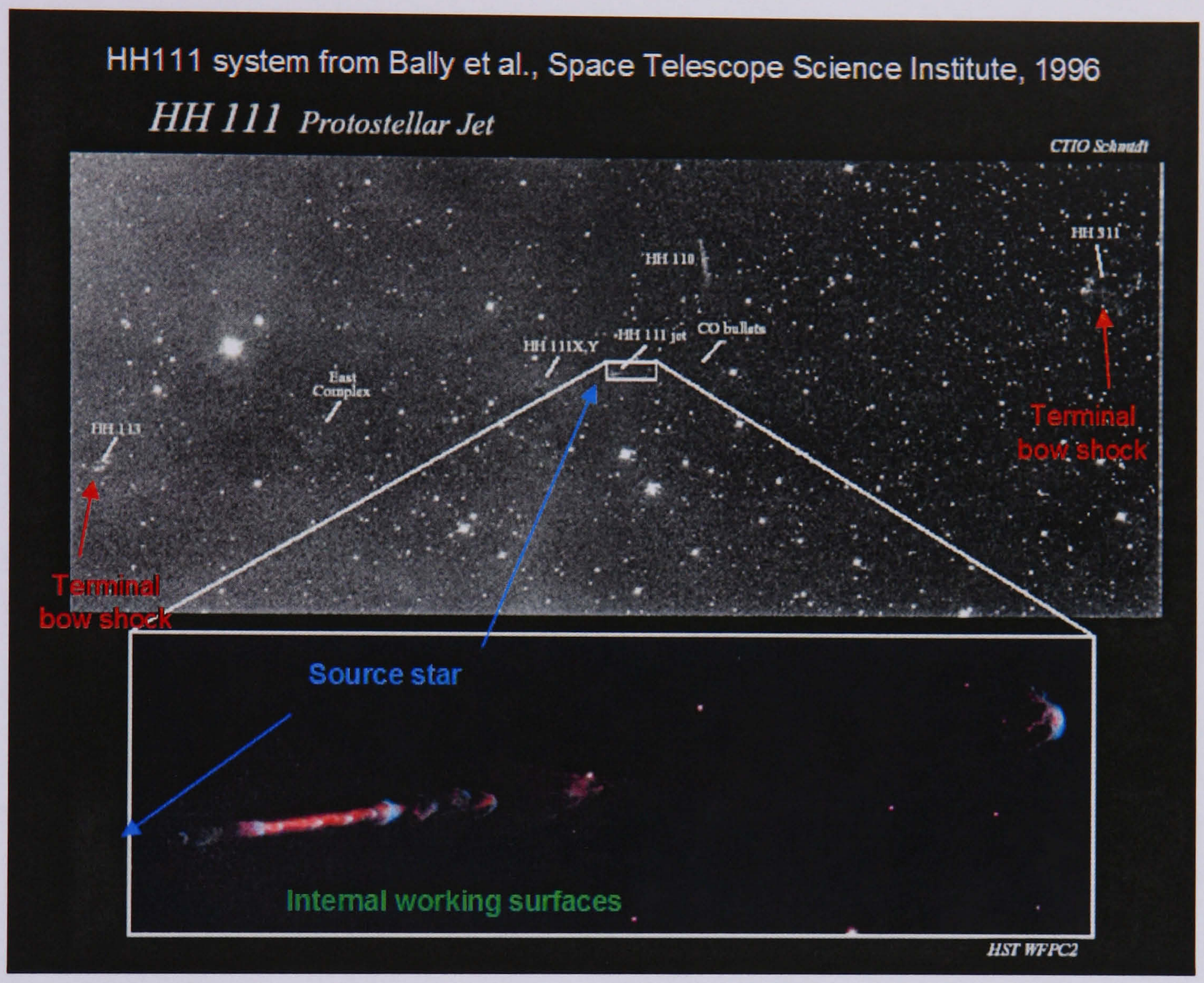


Figure 1.1: Emission due to the jet produced by a protostar (HH111). The image is taken from Bally et al. 1996 [1]. Extra labels have been included to indicate the approximate positions of the source star and terminal bow shocks at the ends of the jet. The upper image is a ground based white light image whilst the lower image shows an HST image with [SII] emission in red and Hα emission in blue. The length of the full outflow seen in the upper image is approximately 7 parsecs ($2 \times 10^{17} m$).

from the accretion disk which allows material to accrete onto the star. In addition it is often much easier to diagnose these jets than the source object.

Various questions remain unresolved concerning protostellar jets. Most notable amongst these are the mechanism for jet production, the effects of angular momentum and magnetic fields on the jet and the effect that the interstellar medium has on the jet (including the formation of shocks and the effect of non-uniformity in the ambient medium).

1.2 Laboratory Astrophysics

Astrophysics provides a wealth of systems that can be investigated to further our understanding of physics. One significant advantage of looking at these systems is the huge contrast of scales from our usual testbed - the laboratory. Unfortunately, in comparison to the laboratory there is a limited range of diagnostics that can be used to study this environment and, more importantly, the observer cannot perturb the system and can normally only study a snapshot much shorter than any characteristic evolution time of the system. Thus assumptions have to be made to piece together a timeline of, say, a star or a galaxy (or, as is the topic of this thesis, a jet from one of these) from the numerous snapshots of different system, each at a slightly different stage of its evolution. However, the combination of astrophysical observations with carefully designed laboratory experiments can provide many useful insights into these processes.

Laboratory experiments have the advantage that the initial conditions can be carefully controlled and diagnosed. The very short experiment durations (less than a second) allows the monitoring of the system for its full evolution. Many more diagnostics are available to understand the laboratory experiments than their astrophysical counterparts and experiments can be controlled and repeatable.

Given certain assumptions about the physical equations governing the development of a system, it is possible [2, 3] to find a number of parameters in the equations that are independent of the scales of the systems. For example if the system can be fully described by hydrodynamics, provided the temporal and spatial scales are

adjusted correctly and the initial conditions are equivalent, the systems will evolve in a similar manner. The main challenge is to decide what the significant physical mechanisms involved in the astrophysical system are, so that then the correct scaling parameters can be exploited.

The development of High Energy Density Plasma (HEDP) laboratory facilities (high power lasers, such as NIF, Vulcan, Omega, NOVA and GEKKO and dense z-pinch drivers such as Z-generator and MAGPIE) for fusion-related research have provided many useful opportunities for laboratory astrophysics (for example those discussed in [4]), providing plasmas in the correct parameter regime for scaled experiments of energetic astrophysical phenomena.

A further advantage of performing laboratory astrophysics experiments is to increase the links between these two highly related fields, allowing for an increased dissemination of knowledge and to provide a testbed to validate and compare simulations from both fields.

1.3 Conical wire array z-pinches

Previous experiments [5, 6] have used lasers as a radiation source to produce a jet, however here we explore a different approach to producing jets in the laboratory. The cylindrical wire array z-pinch has been a major branch of Inertial Confinement Fusion (ICF) research for many years [7]. It has been shown [8] that the early stages of the development of a wire array involves the continuous force-free flow of plasma from a corona around each stationary wire core to the axis. When these flows meet on the array axis a column of plasma is formed (the precursor column). The density and temperature regimes reached by HEDP experiments such as the wire array z-pinch make them suitable for the investigation of energetic astrophysical objects, such as jets. To investigate plasma jets a variation of the usual cylindrical wire array has been used. The wires are inclined with respect to the axis making a conical wire array [9], as shown in Fig 1.2. For this conical array the flows converge onto the array axis, producing a conical shock which acts to thermalise the kinetic energy associated with the radial component of the velocity. At the top of this conical shock

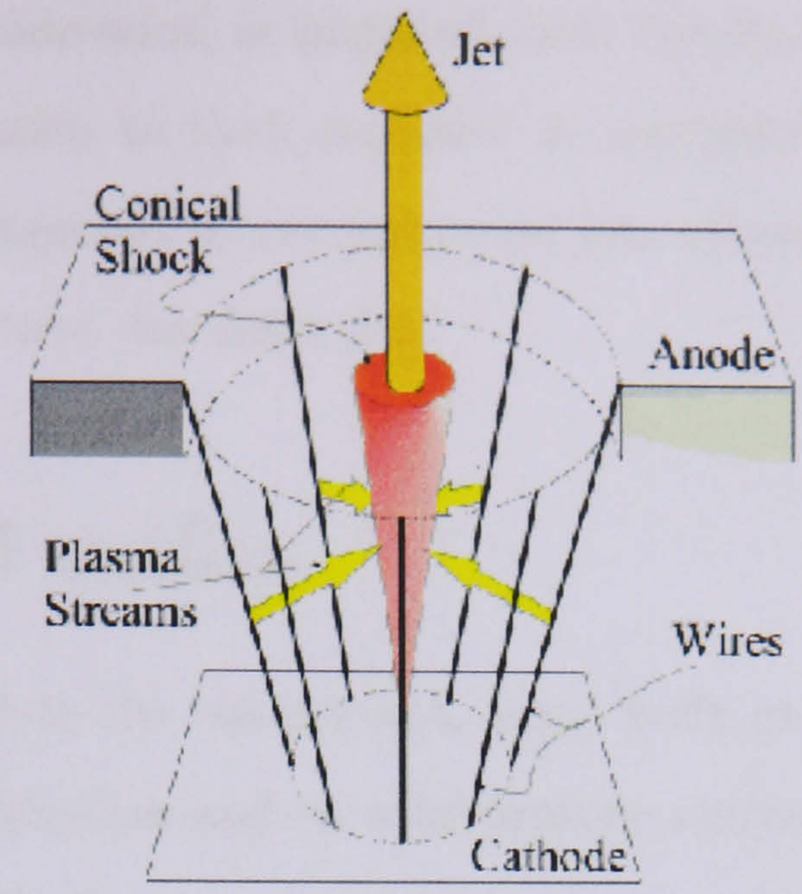


Figure 1.2: Conical wire array setup.

expansion of the flow occurs and a temperature gradient is created by the cooling of the flow. These two effects both form a pressure gradient which acts to accelerate the flow axially. If sufficient array mass is used then the wire cores remain in their initial position feeding mass towards the array axis for the entire current pulse. This is in contrast to the normal wire array z-pinch configuration, where the array mass is chosen such that the array implodes, which causes the array to produce an x-ray pulse.

The outflow of plasma from a conical wire array will thermally expand as it propagates into the vacuum, away from the formation region. If the material used has a high radiative cooling rate it will cool over a short distance (of order the jet radius) as it leaves the conical shock. Thermal expansion is then minimised, thus producing a well-collimated plasma jet that is highly supersonic (Mach number > 30). It is found that such jets have length to width ratios which are large (~ 20), and are produced for a period of a few shock transit times, thus are quasi-steady state.

It has also been possible to use these jets to study the interaction of a jet after formation. Two regimes of interaction have been investigated. The interaction with a quasi-static cloud produces a bow shock which thermalises the kinetic energy of the flow, causing a bright spot in emission similar to working surfaces observed in

astrophysics [10]. If a side-wind is imposed then the flow is found to deflect the jet by a similar mechanism to that expected in astrophysics [11]. The increased diagnostic resolution compared to astrophysical jets allows the imaging of internal oblique shock that produces the deflection.

1.4 Aims and outline

This thesis aims to explore the conical wire array both as a tool to investigate the physics of wire array z-pinches and as a laboratory astrophysics tool to study the jets produced by protostars.

In the next chapter of this thesis we discuss some background required for these experiments. It will give a brief overview of pulsed power machines, and in particular the MAGPIE generator at Imperial College which was used for all of the experiments. The plasma diagnostics used will then be discussed, along with specifics of the diagnostic setup on MAGPIE.

The third chapter discusses the dynamics of conical wire arrays and the jets produced by this technique. This will start with discussions of wire ablation and precursor streams. An astrophysical model for the formation of protostellar jets by a conical shock will then be outlined, and compared with the experimental setup used in the laboratory. Various characteristics of the jets produced by this technique will then be explored. We will also investigate the effects of different cooling rates and angular momentum on the jet.

To make comparisons between any laboratory experiment and astrophysical objects it is necessary to make a number of assumptions and satisfy various criteria. Chapter 4 will discuss in more detail laboratory astrophysics scaling, both generally and with regard to jets. We will give a brief review of protostellar jets and the existing laboratory techniques used to model such jets. It will be shown that the jets produced by conical wire arrays fulfil many of the requirements for scaled modelling of protostellar jets, with the main disparity being the lack of an ambient medium in the laboratory experiments. The expected effects of an ambient medium are discussed.

Chapter 5 describes experiments where a static ambient medium is introduced. Experimental data is compared to astrophysical models for the formation of a working surface at the head of the jet.

The dynamics of a jet propagating in a moving ambient medium is the topic of Chapter 6. The production of a side-wind by photo-ablation of a CHO foil will be discussed. The observed deflection of the laboratory jet will be compared to an astrophysical model for jet deflection.

Chapter 7 will introduce some other experiments that use conical wire arrays before, finally, Chapter 8 concludes this thesis by summarising the results obtained and looking towards potential future experiments.

1.5 Impact of the work & author's contribution

The work presented in this thesis is a new development in the laboratory modelling of protostellar jets. The main results are summarised below and are published in 5 refereed journal articles (4 of which appear in astrophysical literature).

These were the first laboratory experiments to produce radiatively cooled highly supersonic jets in a quasi-steady state manner [9]. We have shown that the cooling rate and Mach number of these flows are similar to those in protostellar jets, and that the laboratory jets are in a regime that can be described by the equations of hydrodynamics (and hence such a connection is valid). These experiments are also the first to introduce angular momentum into a radiatively cooled supersonic jet. This experimental technique and data has been embraced by certain members of the astrophysical community [12].

Most importantly, for the first time it has been possible to propagate a radiatively cooled jet in an ambient medium [13] and to compare these experimental results directly to the astrophysical morphology and analytical models for the interaction. As an extension of this work, the effects of a transverse motion of the ambient medium on the jet have been explored in the laboratory for the first time [14]. These results have been compared to astrophysical analytical and numerical models.

The results of work with conical wire arrays have also had an impact on the

understanding of the physics of wire array implosions [15].

The nature of experiments on the large scale MAGPIE experimental facility requires the involvement of other members of the experimental team in order to obtain the data. The remainder of this section will outline the contribution the author made to this process.

Initial conical wire array experiments were performed on MAGPIE before the author was fully involved in the MAGPIE project. At this time the importance of radiative cooling was established and some approximate values for the jet parameters were determined. Also at this time initial experiments were performed on the interaction of these jets with a target (a CHO foil positioned perpendicular to the direction of jet propagation). Whilst these interaction experiments had limited astrophysical application due to the disproportionately high target density, they demonstrated the potential for using conical wire array jets for interaction experiments. The state of research at this time is outlined by Lebedev et al. [9].

The majority of the experimental data presented in this thesis was obtained since the author became involved in experiments on MAGPIE (with the exception of Figures 3.11b and 3.18b and subsequent plots obtained from this second figure). The author took a leading role in planning the conical wire array experiments, including overall planning of experiments, designing the load hardware and planning the diagnostic setup. He has played a core part of actually obtaining the data, for example building the wire arrays, changing the diagnostic setups, firing MAGPIE, data acquisition and data analysis. Many members of the MAGPIE team assisted in obtaining the data presented in this thesis and, in return, the author has assisted in experiments run by other members of the team related to both wire array physics (for example [15, 16, 17, 18, 19, 20, 21]) and laboratory astrophysics [22, 23]. The author has also contributed to the development of diagnostics during this time.

All of the analysis of experimental data within this thesis has been performed by the author (except where explicitly referenced to another source). Similarly all analytical work presented is performed by the author, including the model for estimating the mass distribution in the jet (again, except where referenced). On both these points, discussions with other members of the MAGPIE team have been

invaluable.

The majority of the simulations discussed in this thesis have been performed by Dr. Andrea Ciardi, and many of these are discussed in [24, 25]. In many cases the author has been involved in discussion on what simulations and parameters would be useful either in understanding the experimental data, or in aiding the design of future experiments. The author has also been involved in comparison of these simulations with experimental data.

Chapter 2

Experimental background

2.1 The MAGPIE generator and other pulsed power facilities

To implode a wire array z-pinch a fast rising current is required; for the work presented in this thesis this is provided by the MAGPIE generator. MAGPIE (Mega-Ampere Generator for Plasma Implosion Experiments [26]) was built in the basement of the Blackett Laboratory, Imperial College London between 1989 and 1993. The generator was designed for single fibre z-pinch experiment, and hence has a high machine impedance (needed to drive a high current through a fast imploding load, which therefore has a high rate of change of inductance). The generator, shown in Fig 2.1, consists of four Marx bank generators, each with $24 \times 0.7\mu F$ capacitors which are charged in parallel via resistors. A small Marx bank triggers the breakdown of 'spark gaps' between capacitors in each of the main Marx modules allowing the capacitors to discharge in series. The current from each Marx module then charges a water-filled 5Ω horizontal, coaxial pulse-forming transmission line (PFL). After four triggered 'line spark gaps' break, the PFLs discharge into the water-filled vertical transfer line (1.25Ω) to the load section.

At the top of the vertical transfer line is a diode stack providing a water-vacuum interface. The inner and outer conductors then converge to the load via a magnetically insulated transmission line (MITL, see Figure 2.2), which prevents breakdown

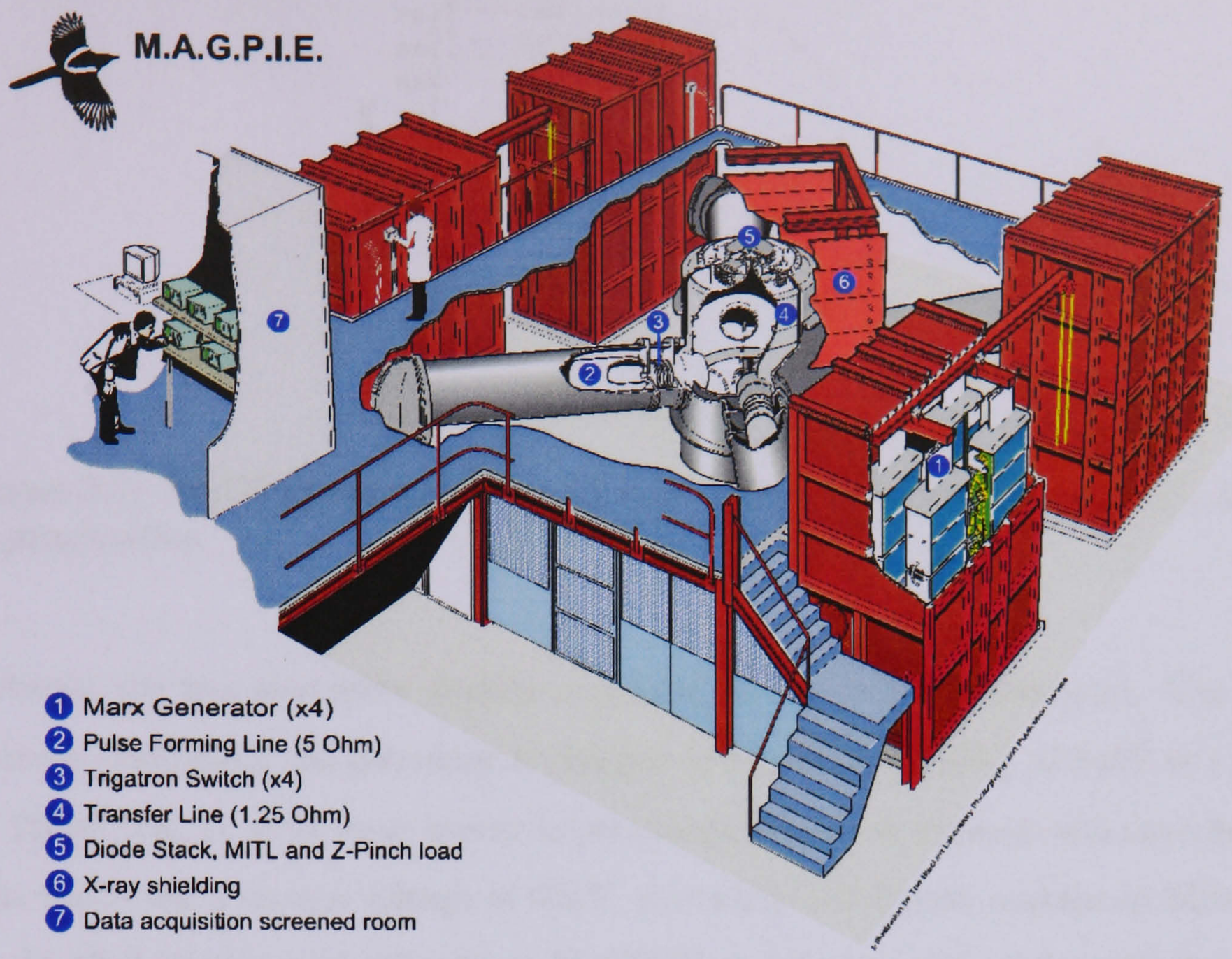


Figure 2.1: Artists impression of the MAGPIE generator [26].

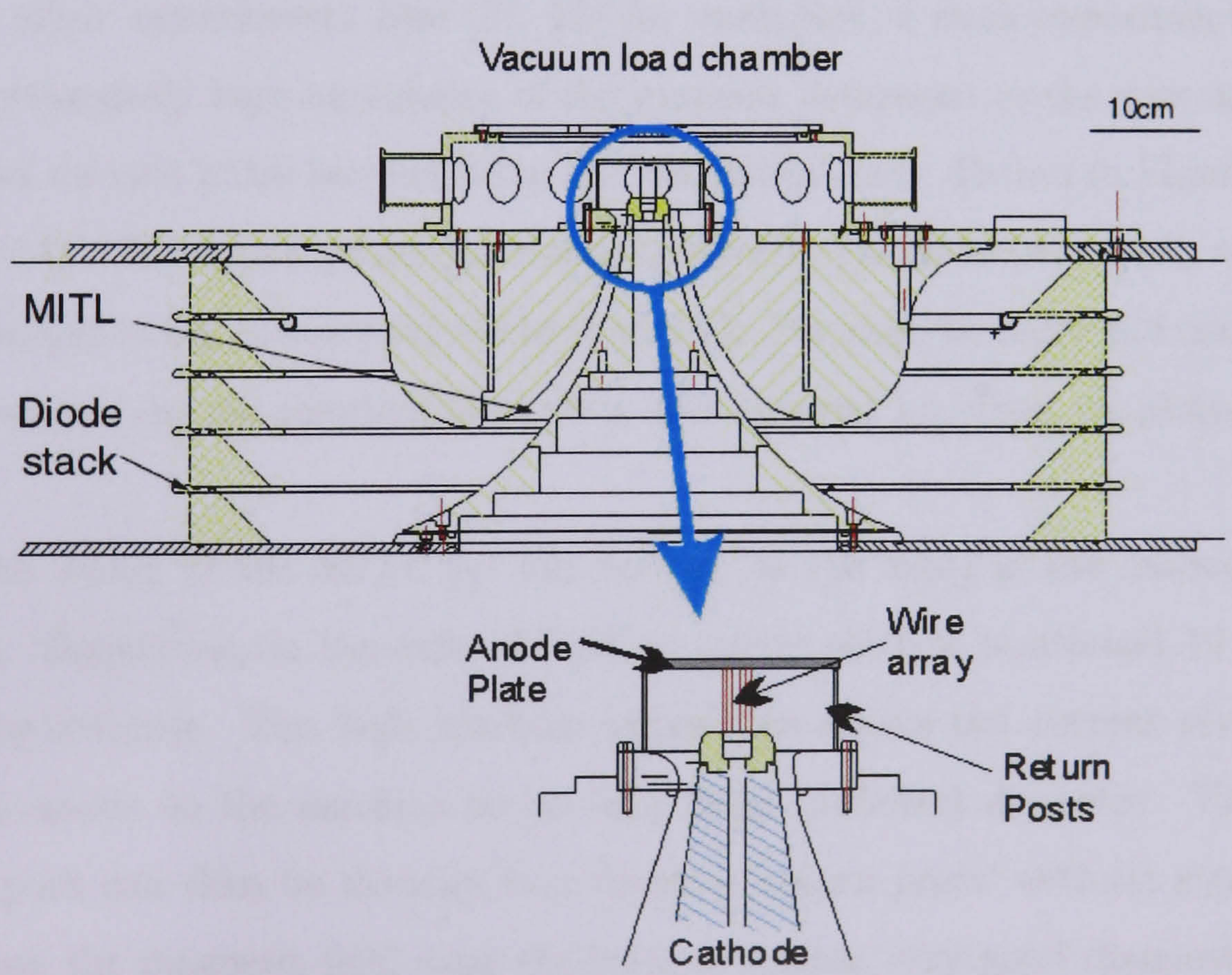


Figure 2.2: The diode stack, MITL and load region of MAGPIE. Broadly based on images in [26].

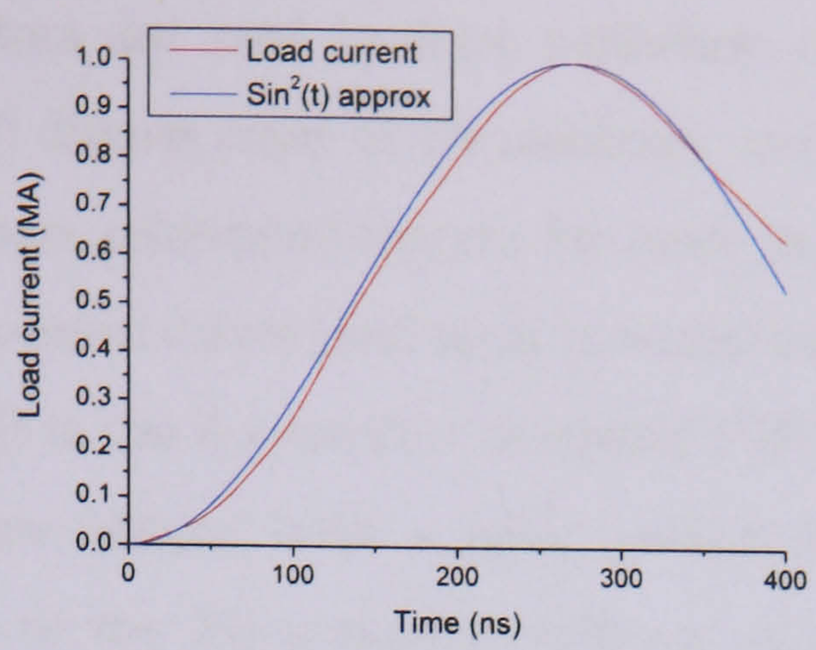


Figure 2.3: MAGPIE current pulses for conical wire array load, as well as a $sin^2(t)$ approximation

between the two electrodes despite a spacing of only a few millimetres. The peak current available if the generator is charged to the full capability of $80kV$ is $1.4MA$ in $250ns$ but, as with most recent experiments, all of the experiments described in this thesis use a charge voltage of $60kV$, providing $1MA$ peak current in $240ns$.

In 1997 the focus of research on MAGPIE switched to wire array z-pinches with the aim of understanding the physics responsible for the high x-ray power produced by wire array experiments (see [27, 28] for examples of such experiments). The disproportionately high impedance of the machine compared to the wire-array load makes the current pulse insensitive to the load inductance. Shown in Figure 2.3 is a typical MAGPIE current pulse (for a standard conical array experiment), which has been obtained using a Rugowski coil in the MITL. For analytic work and simulations, this waveform can be approximated to a sine squared function, as plotted in the figure.

In the centre of the MITL (at the bottom of the load) is the cathode of the machine. Depending on the type of load an anode plate is positioned $12 - 23mm$ above the cathode. The high machine impedance allows the current return path from the anode to the machine to be on a large ($155mm$) diameter. The return current path can then be through four discrete 'return posts' without significantly perturbing the magnetic field near the load, providing very good diagnostic access compared to many other machines where return current 'cans' near the load block a significant fraction of the load from all viewing angles.

Many other generators are used to drive z-pinches; in their review of fast z-pinches Ryutov et al. [7] discuss many of the machines used to drive wire arrays (see individual machine papers referenced therein for more details of other machines). The largest wire array z-pinch driver (and most powerful controlled laboratory x-ray source in the world [29]) is the Z-generator (formerly PBFA-II) at Sandia National Labs, Albuquerque, New Mexico with a peak current of $20MA$. This machine is due to be upgraded to the ZR-generator with an estimated current of $26MA$ machine [30]. Also at Sandia is the slightly smaller Saturn facility [31] with $10MA$ current. There are various intermediate sized machines capable of performing wire array experiments such as Angara-5 in Russia, Double Eagle, Proto II (all with peak current of a few MA), MAGPIE ($1MA, 240ns$) and two $1MA$ $100ns$ rise-time machines - ZEBRA at University of Nevada, Reno and the recently commissioned COBRA generator at Cornell University. There are also numerous smaller scale university based pulsed power devices used for smaller scale plasma focus, single wire and x-pinch loads.

In addition to the standard cylindrical wire array, recently a number of novel multiple-wire z-pinch configurations have been fielded on MAGPIE and other generators. There are various motivations behind such array configurations. The use of a modified cylindrical array configuration can be used to shape the x-ray pulse (e.g. nested wire arrays [32, 29, 33]). Different configurations can be used to aid and verify our understanding of wire array dynamics, such as wire ablation (e.g. mixed wire arrays [8, 16], linear wire arrays [17, 34], radial wire arrays [22], spherical). Also novel designs can take advantage of specific features of array dynamics for applications not directly related to ICF, for example with astrophysical applications (conical, radial) or use the radiation drive for such applications (e.g. radiative shocks and the measurement of equation of state for astrophysically interesting materials). Another type of multi-wire pinch, the x-pinch (two or more wires crossed at a point, producing an 'x' shape [35]) provides a small bright hard x-ray source, which can be used as a radiography source, for example to study wire array experiments (see section 2.5.2).

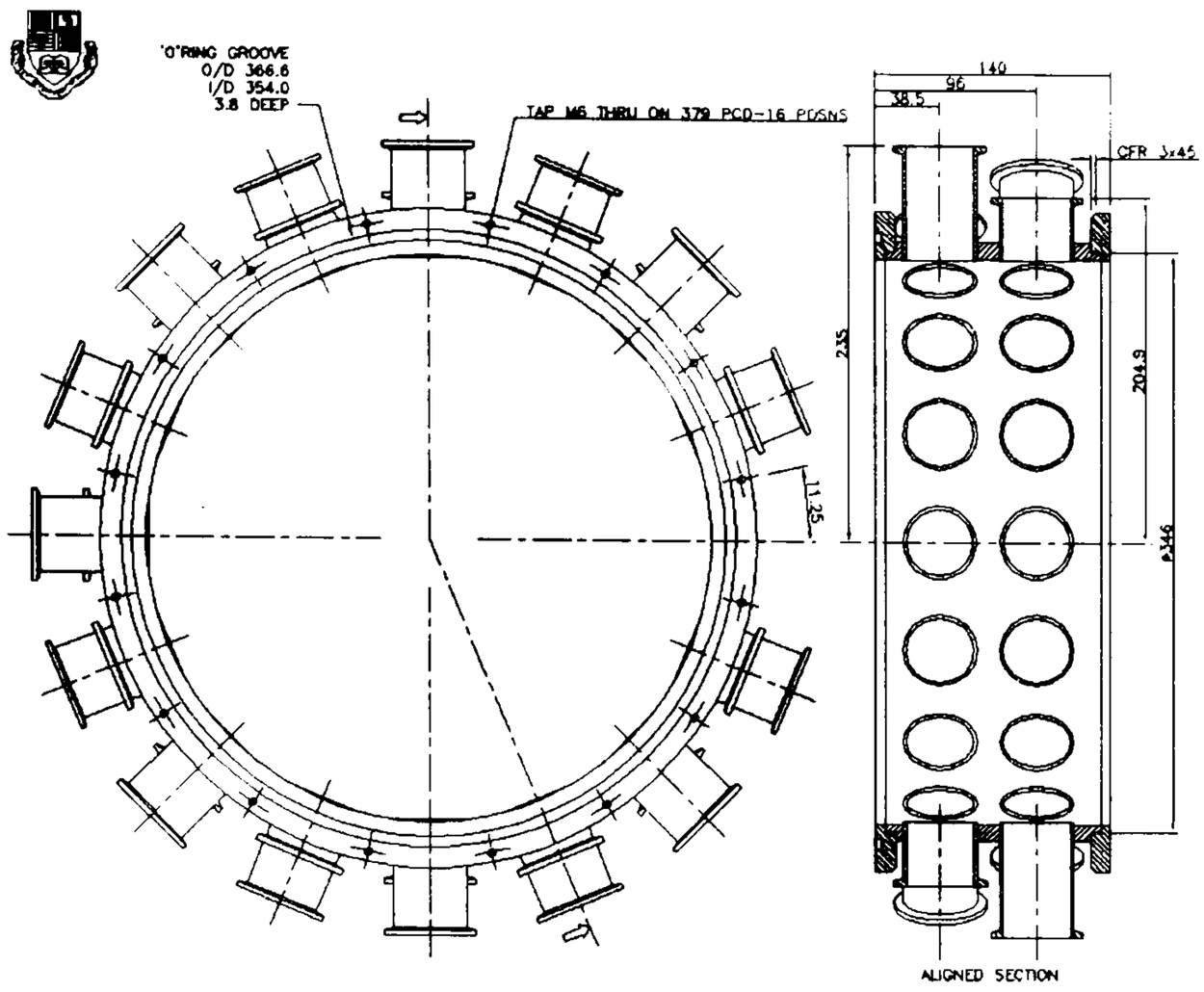


Figure 2.4: Diagnostic ports on the vacuum chamber of MAGPIE.

2.2 Diagnostic overview

A variety of diagnostics are used to examine the evolution of the load during the experiment. Diagnostic access to the load is by 30 radial (or side-on) diagnostic ports through the vacuum chamber, arranged in two layers each with 15 ports (16 fold symmetry with one blank position due to the attachment to the vacuum pumps, as shown in Fig 2.4). Additionally one end-on port allows access looking down the axis of the load.

Two conical array configurations have been used to provide good diagnostic access to different features. The first of these is an arrangement where both the wires and jet can be viewed using the lower diagnostic layer, whilst the second is an arrangement allowing the interaction of the jet with a target to be studied for the entire length of the diagnostic window. In the second arrangement the wire array is positioned between the two layers of diagnostic ports and the interaction is viewed through the upper ports.

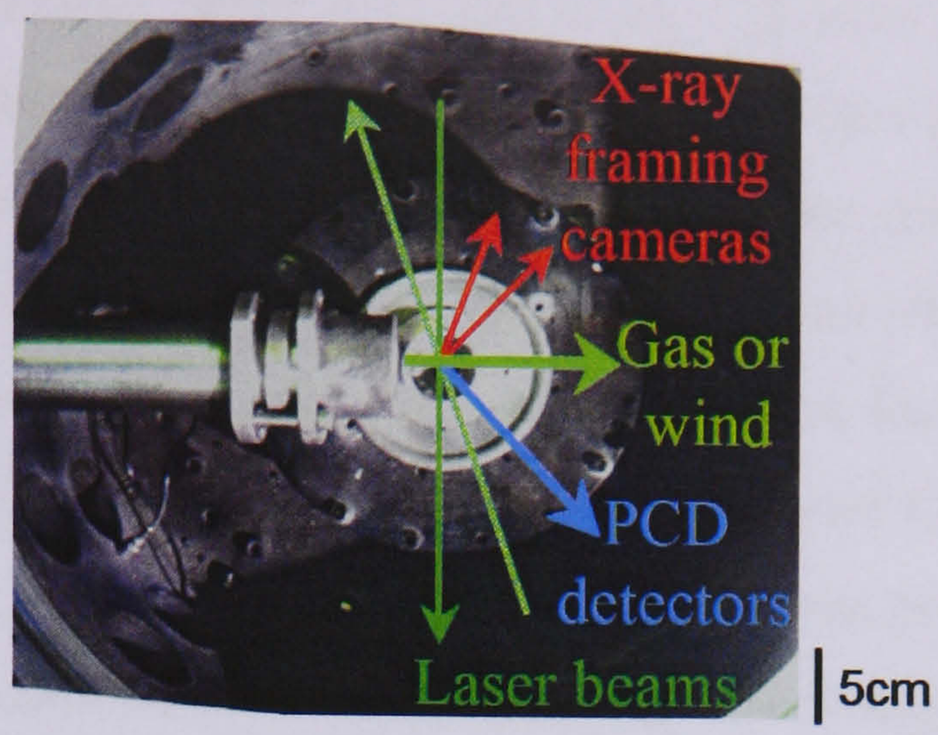
Experiments looking at the interaction of a jet with a target (gas or side-wind as will be described in Chapters 5 and 6 respectively) are one of the few loads fired on MAGPIE that do not have inherent 8 or 16 fold symmetry. For these

asymmetric experiments the layout of the diagnostics is an important part of design and interpretation of the experiments. Figure 2.5a shows a top-down photograph of the load area, with typical viewing angles of the major diagnostics labelled. Shown in Figures 2.5b & c are photographs taken down different diagnostic ports showing how the load region looks for two different target configurations that will be discussed in this thesis. More details of the diagnostic layout for specific experiments are provided in the appropriate chapters.

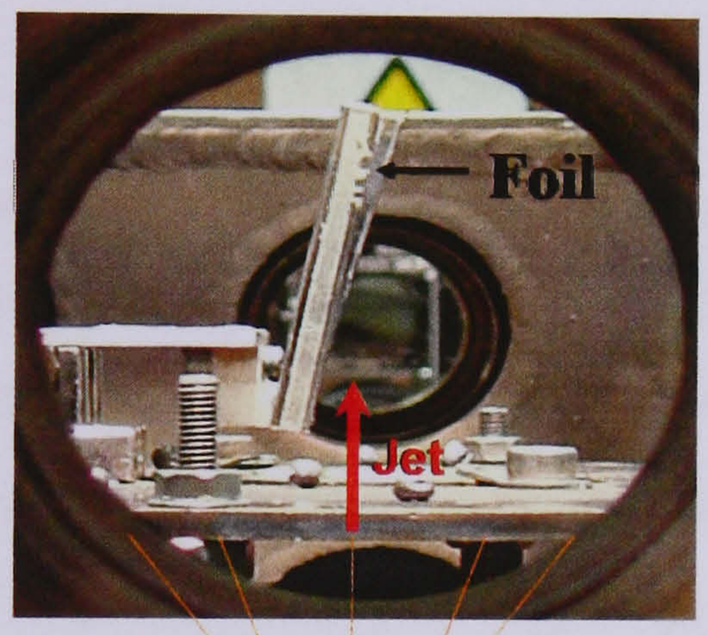
2.3 Optical probing

An Nd-YAG laser system is used to optically probe the experiments, providing information on the plasma refractive index, and hence the electron density of the plasma. The infra-red ($1064nm$) output from the laser rod is frequency doubled to green ($532nm$) using a KDP harmonic generating crystal; this green beam is temporally compressed to $0.4ns$ using SBS pulse compression [36]. The beam is split and expanded to provide various $40mm$ diameter beams through the experimental vacuum chamber. After leaving the chamber the beams are again split into different imaging paths (for different magnifications or functions), each with a 2-lens imaging system focused on the object (wire array or jet) in the chamber. Each imaging path is backed with a 512×512 pixel Cohu 5700 series CCD connected to an image grabbing computer system. All CCDs fielded on the laser imaging system integrate the signal they receive for the whole of the experiment; temporal resolution is provided by the timing and duration of the laser beam. Narrow band ($\delta\lambda \sim$ a few nm) interference filters are used to minimise the intensity of array self-emission on the cameras (although this is not always entirely achieved!). For all imaging paths, a 'background' image is taken prior to the experiment, which is used as a comparison with the 'shot' image.

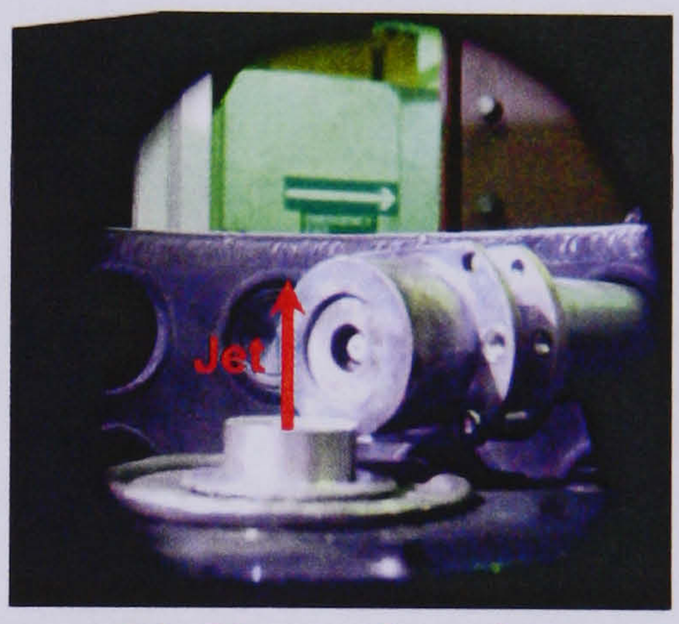
Three laser beams pass through the experimental chamber. Depending on the experiment these beams can either all be on the same path or along two separate paths separated by 22.5° (as was shown on Fig 2.5). When the initial beam has passed through the chamber it is split into 4 imaging paths (labelled Gc1 to Gc4),



(a) Layout



(b) Laser view



(c) X-ray framing camera view

Figure 2.5: (a) Photographs of inside chamber with the main diagnostic viewing angles labelled. The laser paths are drawn in green (with the first beam going vertically top to bottom on the image - the later beams are sometimes re-aligned to also follow this path), the two time resolved x-ray pinhole cameras are in red and the viewing angle of the PCD detectors are shown in blue. Also shown are photos taken from the viewing angle of (b) the main laser path looking at a $3.5cm$ long foil positioned to produce a side wind and (c) one of the x-ray framing cameras towards the nozzle used for gas interaction experiments. The wire and jet positions are drawn on these images.

which are each used for shadowgraphy, schlieren imaging or interferometry cameras with different magnifications. $12ns$ later another beam passes in the opposite direction through the chamber (either on the same path or at an angle of 22.5°), and is then split into 2 imaging paths (Cc1 and Cc2). On some recent experiments, a further $11ns$ later ($23ns$ after the initial beam) a third beam passes through the experimental chamber along the same path as the 2nd. The 2nd and 3rd beams have a slight difference in angle through the chamber ($< 1°$) and after a beam-splitter are isolated near their focal points using apertures. As with the 2nd beam, the third beam is split into two imaging channels (labelled Cc3 and Cc4). When all beams through the chamber are along the same path the cameras provide a 3-frame imaging system to map positions over time, and hence it is possible to derive velocities (and acceleration).

2.3.1 Schlieren imaging

A common laser technique used for plasma physics experiments is schlieren imaging. Schlieren relies on the refraction of light as it passes through the plasma. A ray of laser light passing along, say, the x-axis which passes through plasma with refractive index $\eta(x, y)$ which varies in the y direction, will be refracted by an angle

$$\theta = \int_{path} \frac{d}{dy}\eta(x, y)dl \tag{2.1}$$

A schlieren effect occurs if the beam is refracted out of the imaging system. In practice a two lens imaging system is used to produce an image on a camera. This imaging system provides a focal point of the laser beam; at the focal point between the two lenses a schlieren 'stop' eliminates either rays that have been refracted by less than a given acceptance angle $\theta_{acceptence}$ (dark -field) or greater than a given angle (light-field) (see Fig 2.6).

For dark field schlieren on MAGPIE, a horizontal knife edge or rod stop is normally used to allow only areas with either upwards, or both upwards and downwards density gradients respectively (or horizontal gradients if the stop is positioned vertically). For light field schlieren a variable aperture is used as a stop. On the schlieren setup on MAGPIE a $6mm$ aperture is used at the focal point of a $1m$ lens, leading

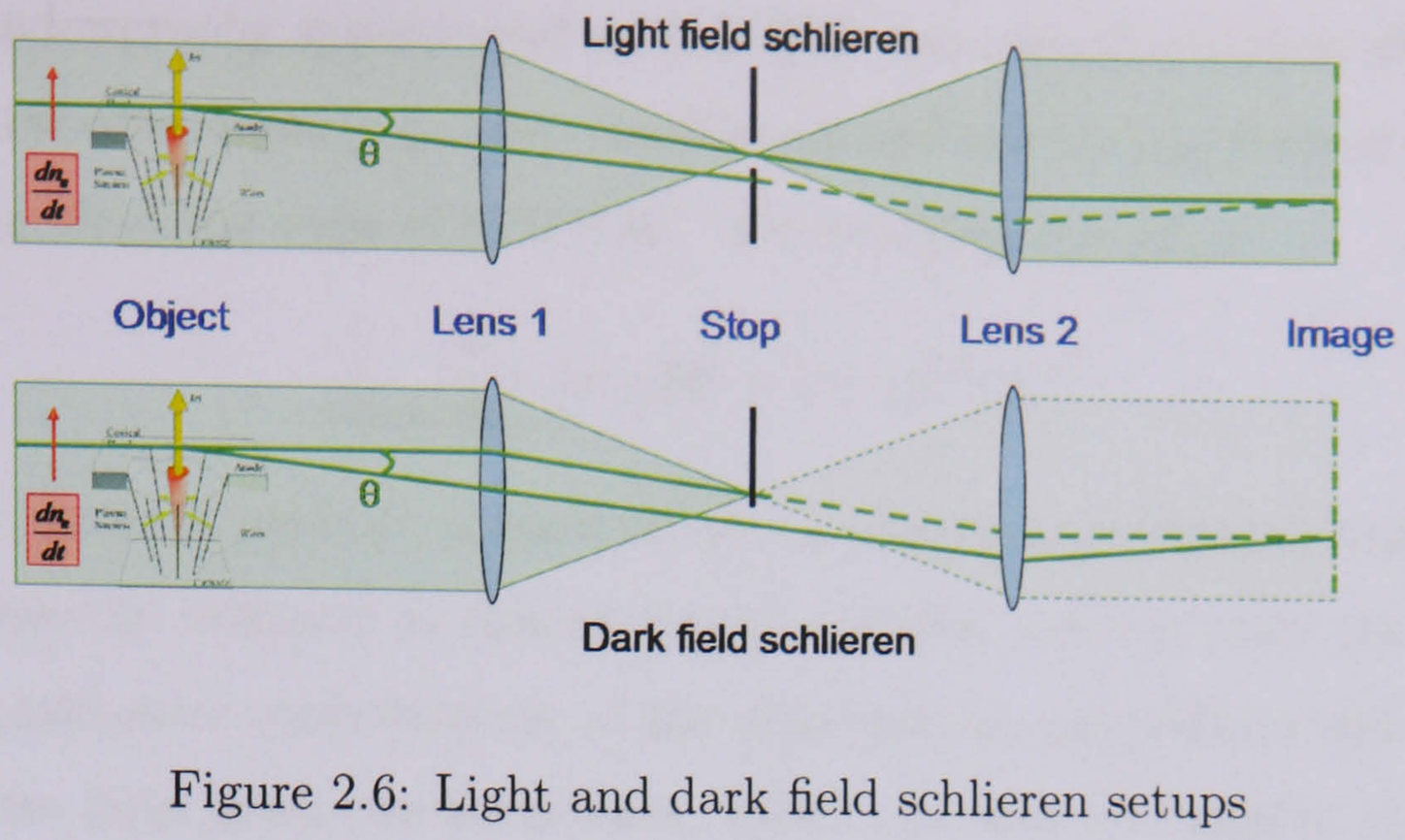


Figure 2.6: Light and dark field schlieren setups

to an acceptance angle of 3.2×10^{-3}rad. This corresponds to a critical line integral of electron density gradient of

$$\int_{path} \frac{d}{dy} n_e(x, y) dl \sim 2.5 \times 10^{19} cm^{-3} \tag{2.2}$$

2.3.2 Shadowgraphy

Another form of laser imaging used in these experiments is shadowgraphy. Parallel light passes through the load area, which has electron density gradients (and hence refractive index gradients). These gradients cause refraction of the beam, producing a lensing effect onto the image plane. There is no stop to eliminate any part of the beam.

The angle of refraction of the beam is sensitive to refractive index, as in equation 2.1.

The intensity incident relative to the un-perturbed beam on the CCD is sensitive to the second derivative of the integral of the refractive index

$$\frac{\delta I}{I} = L \left(\frac{d^2}{dx^2} + \frac{d^2}{dy^2} \right) \int \eta dl \tag{2.3}$$

where x and y are the coordinates in the object plane and L is the distance between the object and image planes [37]. On MAGPIE a twin-lens imaging system is used, so the effective image plane is actually the end of the object to be imaged, i.e. L is the path length through the plasma (or the depth of field if this is shorter).

The shadowgraphy system used on MAGPIE has a small schlieren effect due to experimental constraints (e.g. finite sized lenses and mirrors and limited sized holes through the shielding walls of MAGPIE). The schlieren cut-off is

$$\int_{path} \frac{d}{dy} n_e(x,y) dl \sim 1 \times 10^{20} cm^{-3} \tag{2.4}$$

In this thesis no attempt is made to obtain quantitative data on density distributions from the schlieren or shadowgraphy systems, however they are useful for giving a qualitative understanding of the experiments, particularly indicating the points where large gradients are present, which can then be followed in time (e.g. the jet tip and internal shocks in the jet). The use of three laser beam times in a single experiments reduces the random errors that would be present in following a single point in separate experiments (e.g. due to variations in current pulse shape or imperfections in the wire array). When this three-frame system is used, there is at most a factor of 4 between the acceptance angles of the first and second beams (with the 2nd being the more sensitive), however the second and third frames have an identical acceptance angle. As the schlieren only has an effect if the critical gradient is present, if no camera is subject to a schlieren cutoff then all images are equivalent.

2.3.3 Interferometry

Mach-Zehnder interferometers are used to measure electron densities of the plasma. Figure 2.7 gives a basic schematic of this type of interferometer. A reference beam is split from the probe beam between the laser and the experimental chamber. After a twin-lens imaging system is used to focus the object onto the camera a beam-splitter is used to recombine the two beams. The introduction of a small angle between the probe and reference beams leads to the formation of fringes. In reality both the probe and reference beams have more convoluted paths than the diagram indicates (the length of each arm is ~6m and each has ~4 intermediate mirrors and a beam expander before recombination). Due to these convoluted paths it is sometimes necessary to introduce a linear polariser to ensure the reference and image beams have the same polarisation.

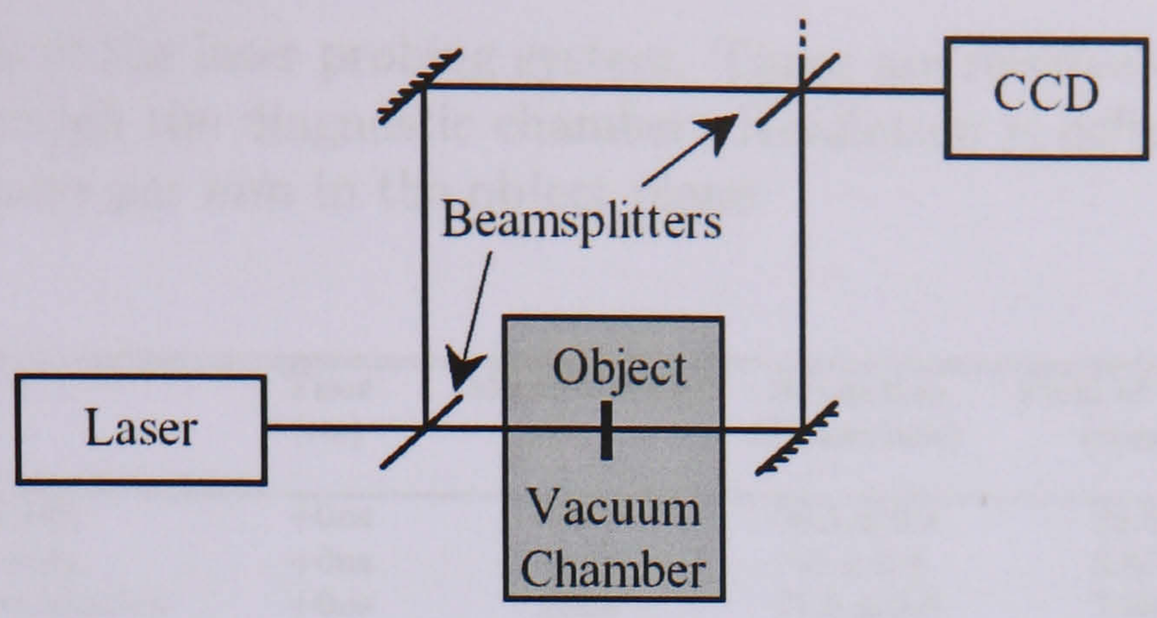


Figure 2.7: Setup of a Mach-Zehnder interferometer

The presence of free electrons in the load leads to a phase shift in the probe beam. When the probe and reference beams are recombined, this phase shift leads to a fringe shift in the interferogram. The number of fringe shifts at a point in the interferometer image represent the line integral of refractive index along that path. For a plasma the electron density is proportional to the refractive index. Hence the number of fringe shifts (f) will be a function of the line-integral of electron density

$$f = 4.48 \times 10^{-12} \lambda(m) \int n_e(cm^{-3}) dl \tag{2.5}$$

Given that the laser used in the experiments has wavelength $\lambda = 532nm$, the integral of electron density can be calculated

$$\int n_e(cm^{-3}) dl = 4.2 \times 10^{17} f \tag{2.6}$$

Various factors govern the limits of density that can be measured. At the low electron density limit, only fringe shifts greater than $\sim \frac{1}{4}$ of a fringe (depending on various factors such as the beam quality) can be measured. Other limits are imposed by density gradients. As with shadowgraphy, although no schlieren stop is intentionally included in the interferometer, the object beam can be refracted out of the imaging system by refractive index gradients in the plasma. This leads to dark areas on the interferogram. In addition, any gradients that lead to either fringe shifts on a scale less than a few camera pixels or fringe spacing less than a few camera pixels will not be resolved.

Two methods have been employed to obtain quantitative data from interferograms. For both of these the shot interferogram is compared to a pre-shot back-

Table 2.1: Details of the laser probing system. Times are relative to the first probe beam passing through the diagnostic chamber. Resolution is defined as number of pixels on the camera per mm in the object plane.

Label	Use	Time (ns)	Magnification	Resolution (Pixels/mm)	Field of view (mm)	Schlieren cutoff (cm^{-3})
Gc1	Shadow/schlieren	+0ns	Low	20.1 ± 0.2	25.5	1.0×10^{20}
Gc2	Shadow/schlieren	+0ns	High	65 ± 0.4	6.60	1.0×10^{20}
Gc3	Interferometer/shadow	+0ns	High	77.5 ± 0.9	7.88	6.2×10^{19}
Gc4	Interferometer	+0ns	Low	20.6 ± 0.2	24.8	6.2×10^{19}
Cc1	Schlieren	+12ns	Low	27.1 ± 0.2	18.9	2.5×10^{19}
Cc2	Schlieren	+12ns	High	54.3 ± 0.9	9.44	2.5×10^{19}
Cc3	Interferometer/schlieren	+12/23ns	Low	20.9 ± 0.2	24.5	2.5×10^{19}
Cc4	Schlieren	+23ns	High	63.8 ± 1.0	8.02	2.5×10^{19}

ground interferogram. Firstly fringe following and counting has been used. In many experiments the fringe shift is slowly varying in the direction perpendicular to the fringes, leading to parallel fringes. Thus, provided the fringe spacing does not change over a given area it has been possible to follow a single fringe across a region and calibrate the measurement with the number of pixels per fringe. Secondly a fringe analysis package FRAN has been used [38]. This program performs an FFT on the data in the interferogram, and then attempts to 'unwrap' complete fringe shift in the image to provide a smooth density plot. This latter technique cannot handle discontinuities in the interferogram (such as those introduced by shocks), however it is sometimes possible to interpret these features by counting fringes on each side of the shock separately.

2.3.4 Setup of camera systems

In all there are up to eight optical probing cameras used on MAGPIE for a single shot. These have been set up to probe the experiment with different magnifications and at different times to provide a time-history of the experiment. The resolution and acceptance angle is different for each camera. Table 2.1 shows the timing, magnification and acceptance angle of each of the cameras.

2.4 X-ray power

The conical arrays that are the topic of this thesis emit in reasonably low energies - XUV and soft x-rays ($<200eV$, $>62\mathring{A}$). Hence, although harder x-ray diagnostics are available on MAGPIE, only diagnostics that cover these softer energies are used in this thesis, so the discussion here is limited to such diagnostics. As very little data from these PCD and XRD detectors is discussed in this thesis (only in Sections 6 and 7), only relevant details of these detectors is presented here (for a more detailed discussion of these devices see [39, 40, 41]).

2.4.1 PCD cluster

A pack of 5 diamond photo-conducting diodes (PCDs) is used to measure the intensity of emission produced by the array or jet. A 350V bias voltage is imposed across each PCD, and any current through the PCD measured by a resistor and an oscilloscope. Incoming photons produce electron-hole pairs in the diamond, causing a drop in resistance of the diamond and producing a voltage on the scope. Various calibrations (including [40]) have shown that the PCD response is reasonably flat between $10eV$ and $5keV$, and for the $350V$ bias voltage used on MAGPIE the sensitivity is $2.1 \times 10^{-3} A/W$. Given that the element of the PCD is $1mm \times 3mm$ and the signal is monitored on a 50Ω scope, we can find the intensity I at a distance d from a point source using the voltage V on a PCD a distance d_{PCD} from the source

$$I\left(\frac{W}{cm^2}\right) = 3.15 \times 10^{-7} \times V_{PCD} \times \left(\frac{d_{PCD}}{d}\right)^2 \tag{2.7}$$

Various band-pass filters are used to select the wavelength range to which each PCD is sensitive. For non-imploding conical arrays PCDs are typically fielded open (i.e. uniform transmission) or with $1.5\mu m$ or $3.0\mu m$ polycarbonate (C16H14O3) filters. These filters transmit radiation $\sim 120 - 290eV$, as is shown in Fig 2.8.

2.4.2 XRD cluster

On some earlier conical array experiments X-ray Diodes (XRDs) were fielded. These consist of a grounded mesh anode in front of a solid cathode with a bias voltage of

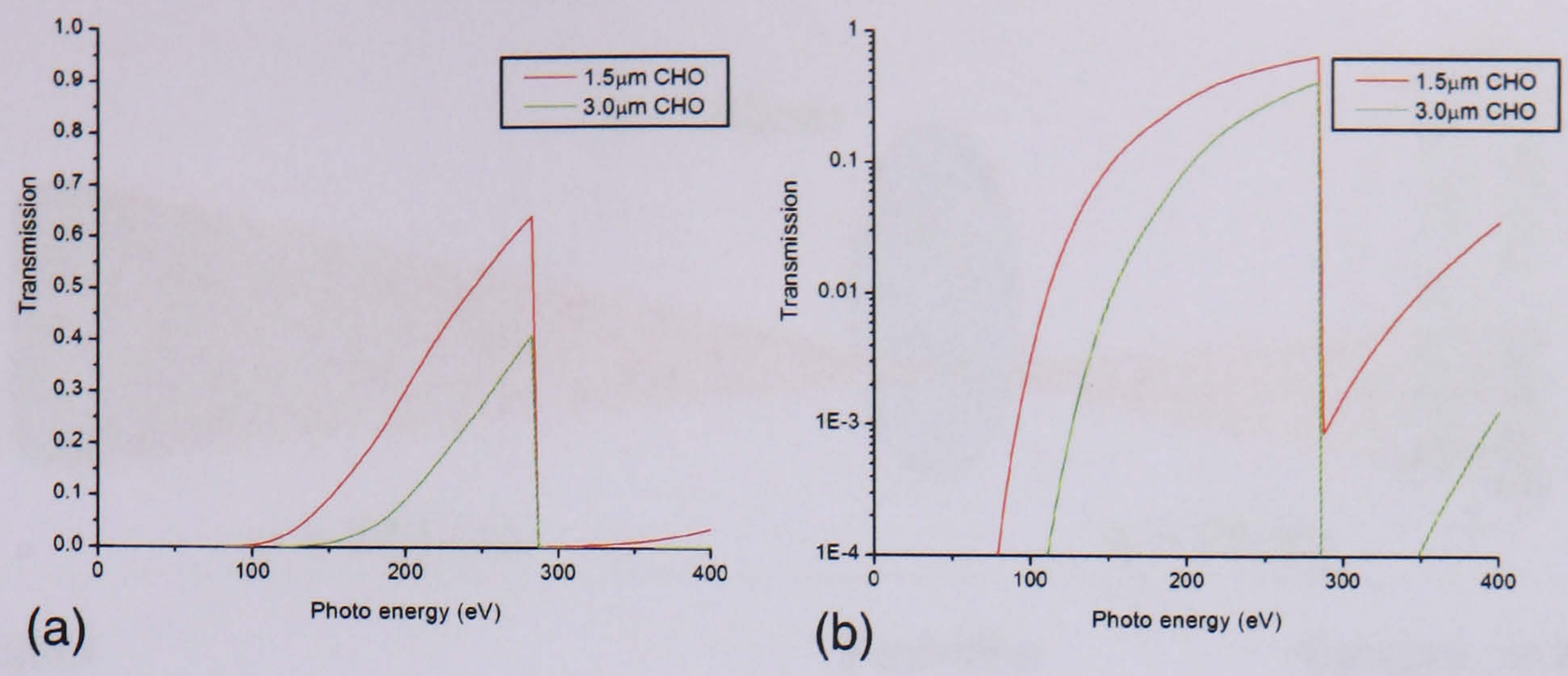


Figure 2.8: Transmission of C16H14O3 foils shown by (a) linear and (b) logarithmic plots

$350V$. Incident photons liberate electrons from the cathode, which are collected by the anode. As with the PCDs a 50Ω scope provides a load resistance with which to monitor the current. Again CHO filters can be used to define the frequency range used (Fig 2.8). The XRDs have a response which is highly frequency dependent, so PCDs signals are used in preference where available, however on some very early imploding conical experiments (as will be discussed in section 7) the PCDs were not fielded.

2.5 X-ray imaging

2.5.1 Time resolved X-ray pinhole cameras

Cameras are fielded on MAGPIE that provide spatially and temporally resolved soft X-ray or XUV (extreme ultra-violet) emission profiles. A simple pinhole camera system (Fig 2.9) is used to produce an image on a micro-channel plates (MCP). Two MCPs (by Schulz Scientific) consisting of 4 active elements in a quadrant configuration are used (Fig 2.9). Each MCP element is individually energised by a $4.7 - 5.8kV$ supply providing four temporally resolved frames.

The MCP's have a flat response over the range $150\mathring{A}$ to $1200\mathring{A}$ ($10 - 80eV$ [42]). The response of the camera is strongly dependent on the supply voltage V, typically

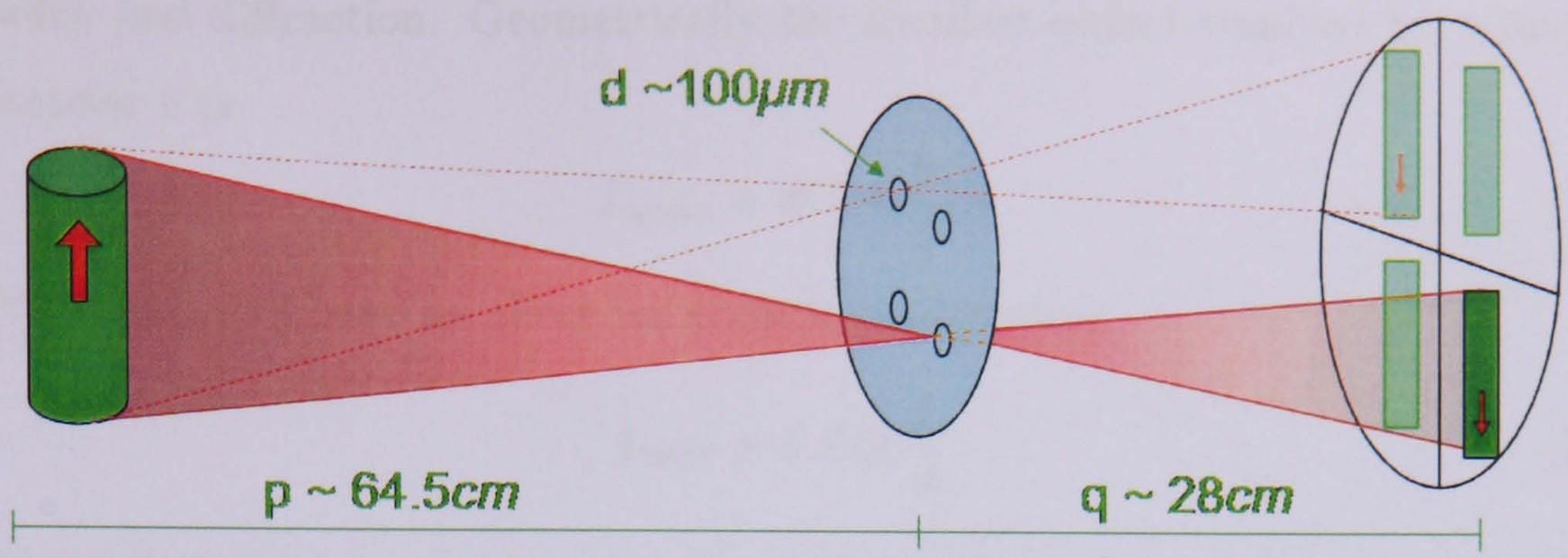


Figure 2.9: Setup for x-ray framing camera. Four pinholes provide four separate images on the MCP.

with a V^5 dependence on voltage. The cameras are usually operated in a mode where the integration time (the full width, half maximum of V^5) is $3ns$. The two MCPs used are $44mm$ and $56mm$ in diameter, with $2mm$ dead zone between the different elements on the MCP. Different cables lengths are used to individually define the timing of each frame of the camera. The $44mm$ camera is usually setup for $9ns$ inter-frame time whilst the $56mm$ camera can be used in two modes, with $10ns$ and $30ns$ inter-frame times respectively. The $30ns$ inter-frame mode provides a total monitoring period of $90ns$, which is sufficient time to follow the evolution of a jet interaction from start to finish, whilst the $10ns$ inter-frame allows the detailed study of a single period of the interaction.

The magnification of the system is the ratio of the distance from the pinhole to the camera q to the object to pinhole distance p. As will be evident in some of the results presented in later chapters (and to some extent the image used in Fig 2.9), it is possible for the images from these four pinholes to be not exactly aligned with the camera. This results in part of the image falling in the dead-zone between the quadrants and occasionally a slight overlap between images. This has been minimised where possible by careful positioning of the camera and reducing the magnification (and hence size of the image on the camera).

There are two factors defining the resolution of this type of imaging system,

geometry and diffraction. Geometrically the smallest object resolved by a pinhole of diameter d is

$$L_{geom} = d(1 + \frac{p}{q}) \tag{2.8}$$

Diffraction will have an effect for objects smaller than

$$L_{diff} = 1.22p.\frac{\lambda}{d} \tag{2.9}$$

Two techniques are used to define the wavelength range incident upon the MCP. Firstly the pinhole size can be chosen such that diffraction effects set a lower energy limit on the objects resolved. For a typical setup used in the experiments ($p = 64.5cm$, $q = 28cm$, $d = 100\mu m$), if no filter is used then diffraction will become important when $L_{diff} > L_{geom}$, implying $\lambda > 42nm$ or $h\nu < 30eV$. The size of object that can be resolved at this energy is $L \sim 300\mu m$. Alternatively a thin CHO foil (1.5 to $5\mu m$) can be used as band pass filters (the transmission of which were shown earlier in Fig 2.8).

2.5.2 X-pinch radiography

Point projection backlighting has been used to image high ion densities such as in the wire cores, as shown in Fig 2.10. An x-pinch (two or four wires crossed to produce an 'X' [35]) acts as an x-ray source. This is mounted in one of the four current return posts of MAGPIE and thus receives a current of $250kA$ in $240ns$. An Al x-pinch with four wires, each $20 - 50\mu m$ diameter provides a $1ns$ hard x-ray pulse from a spot size of $10 - 15\mu m$ [43]. A $12.5\mu m$ Ti filter is used to select x-ray energies of $2 - 5keV$, thus limiting wire array emission reaching the Kodak DEF or M100 film which is used to record the projected image. Varying the diameter of the wires in the x-pinch is used to control the approximate timing of the x-pinch firing, and the exact timing is monitored by a PCD which also has a $12.5\mu m$ Ti filter.

The magnification of the x-pinch radiograph is determined by geometry as the ratio of the distance between the x-pinch and the film and the distance between the x-pinch and the object. On MAGPIE the standard setup has a magnification of

$$m = \frac{42.75cm}{7.75cm} = 5.52 \tag{2.10}$$

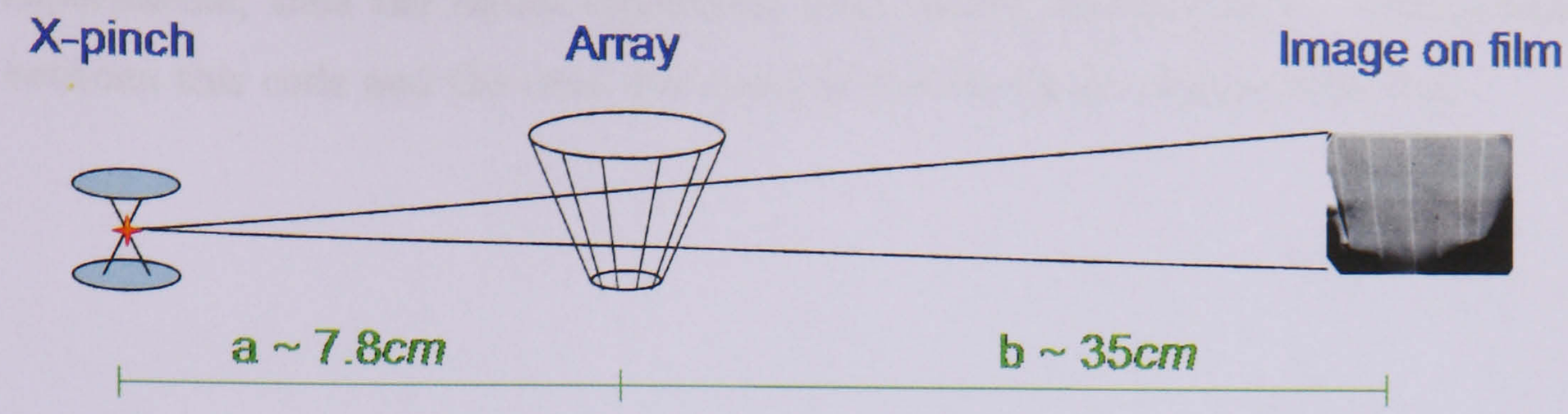


Figure 2.10: X-pinch radiography setup. The x-pinch (left) images the wires of the array (centre) onto the film pack (right of the diagram).

2.6 MHD Computer simulations

Computer simulations have provided a useful input into design of experiments and the interpretation of experimental results. Three computer codes have been used to model conical wire array experiments, two with roots in z-pinch physics, the other from an astrophysics background.

Gorgon [44, 25] is a resistive MHD code that can be run in 1, 2 or 3 dimensions. Most of the application of this code to conical wire arrays and jets [25] use the 2D version. This is a two temperature code, modelling electron and ion temperatures, with electron-ion coupling. Radiation loss is modelled using optically thin recombination, however this is scaled to account for line emission. Low density material ($< 10^{-4} kg/m^3$) is treated as vacuum.

A 2D hybrid model developed by [45, 46] has been used to model wire arrays, including jets from conical wire arrays. Ions are treated as particles, whilst electrons are treated as a fluid. The advantage of using a code that treats ions as particles is that ion-ion collisions can then be appropriately modelled. This is particularly importantly for modelling the early stages of precursor column or conical shock formation and the effect of a side wind on a jet (Chapter 6).

The astrophysics code, AstroBEAR [47], has also modelled jet deflection. This is an MHD code with adaptive mesh refinement, which has been used to model astrophysical jet-wind interactions. The materials available in this code are those abundant in astrophysics, not the high atomic number materials used in the laboratory

experiments, thus the initial conditions need careful consideration. Comparisons between this code and the data discussed in this thesis are discussed in [14].

Chapter 3

Conical wire array dynamics

3.1 Overview of conical wire arrays

A conical wire array consists of a set of fine (tens of μm diameter) metallic wires, that are each inclined with respect to the axis, creating a conical arrangement as illustrated in Fig 3.1. As current passes through the wires the wire cores remain relatively cold whilst a hotter coronal plasma forms a continuous stream to the axis. In contrast to cylindrical arrays, for the conical array a radial component to the current ($\mathbf{J_r}$) is present, hence the Lorentz $\mathbf{J} \times \mathbf{B}$ force on the corona has an axial component ($\mathbf{F}_z = \mathbf{J}_r \times \mathbf{B}_\theta$). As the flows meet on the axis the radial component of the momentum from all of the streams cancels and the kinetic energy associated with this momentum is thermalised in a conical shock. Radiative cooling limits the thermal expansion of the streams and plasma column. The axial component of momentum from the streams is conserved, producing an axial outflow or jet. This flow is additionally accelerated by a steep pressure gradient at the top of the conical shock, producing a jet of plasma.

In the conical array the magnetic field and inter-wire spacing vary along the length of the array. Conical wire arrays are thus useful for understanding wire ablation. Additionally the density incident upon the conical shock, unlike for the precursor column in a cylindrical array, depends on axial position (due to the change in ablation rate and the difference in the time of flight from the wires to the axis). These differences from cylindrical wire arrays make conical wire arrays a useful plat-

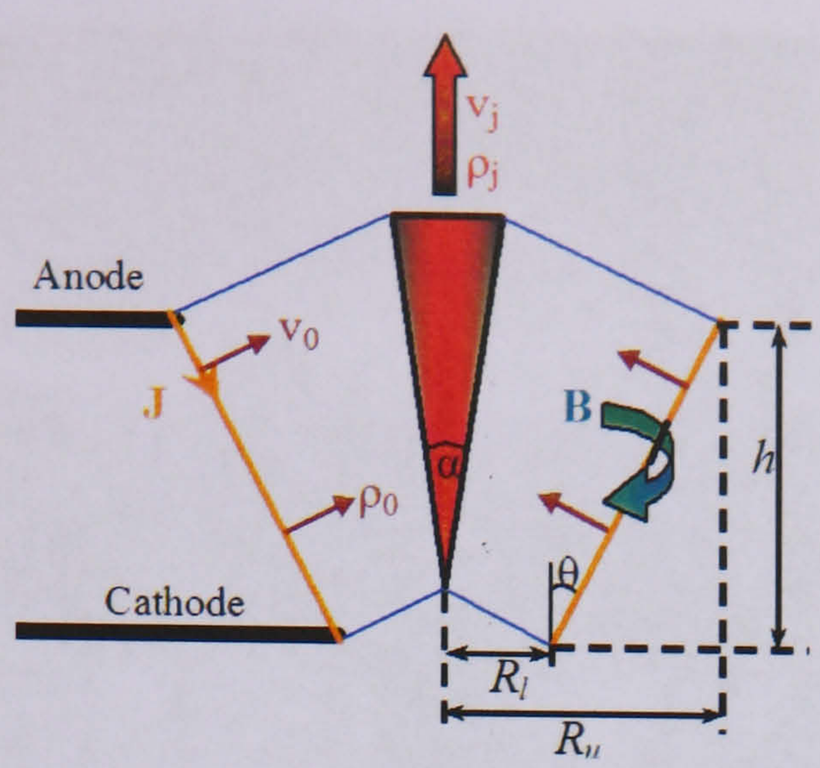


Figure 3.1: Illustration of a conical wire array, including variables used in the discussion: R_l and R_u are the upper and lower radii of the conical array, h is the array height, θ and α are the array and conical shock opening angles, v_0 and ρ_0 are the velocity and density of the ablated plasma streams and v_j and ρ_j are the velocity and density of the jet. The direction of current **J** and magnetic field **B** are also shown.

form for exploring physics of a wire array z-pinch, independent of any astrophysical motivations.

As an overview of the jet production process, Fig 3.2 shows an interferogram of the complete system $331ns$ after the start of current. In the lower half of the image is the conical wire array, and in the upper half is the jet of plasma that has left the formation region. The wire array configuration in this figure consists of sixteen tungsten wires, each $18\mu m$ in diameter (shortened to $16 \times 18\mu m$). As with most wire arrays that will be discussed in this chapter (except where stated otherwise), the base diameter of the array is $\phi_{base} = 16mm$, which is identical to the diameter of standard cylindrical wire arrays fielded on MAGPIE and the wires are inclined at $\theta = 30°$ with respect to the axis. The mass per unit length of the array is sufficiently large that wire cores remain at their initial positions for significantly longer than the duration of the MAGPIE current pulse, so no implosion occurs (except the experiments described in section 7, which explores imploding conical wire arrays).

The cooling rate of the precursor streams from the wires, the conical shock and the jet can be varied by changing the wire material. In addition to W arrays (that have a high cooling rate), conical arrays have used a variety of other wire materials, including Al and Fe (which have a lower cooling rate). The most significant effect

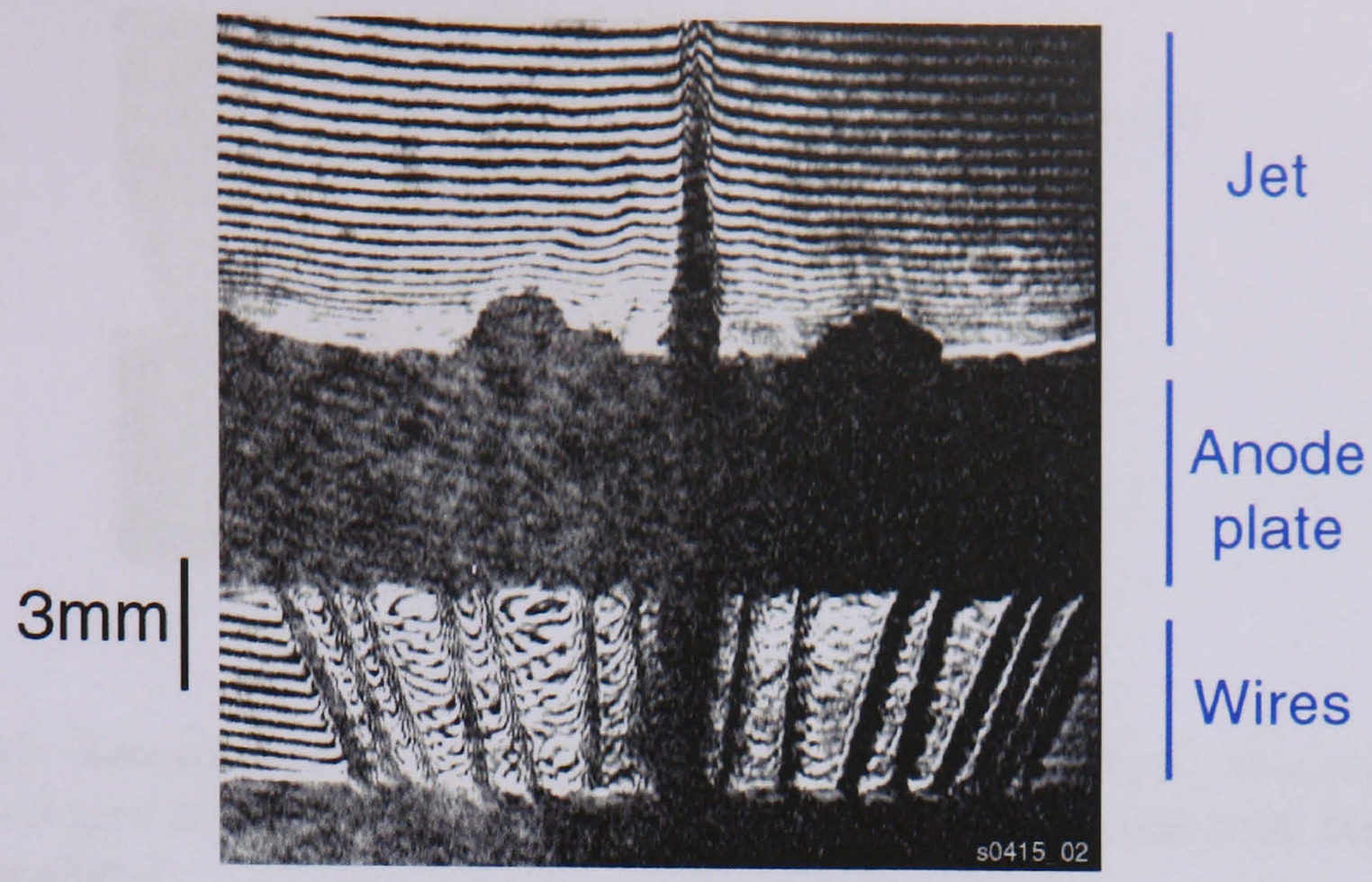


Figure 3.2: Interferometer image showing the complete conical wire array setup with a W array, opening angle $\theta = 30°$ at $331ns$.

of decreasing the cooling rate is that thermal expansion leads to poor collimation of the jet.

Normally the conical arrays fielded are shorter than the standard MAGPIE cylindrical arrays ($h_{con} \sim 12-15mm$ compared to $23mm$ for cylindrical arrays), allowing diagnostics to view both the array and the jet that is formed within a $40mm$ diagnostic port and reducing axial variations in the precursor flows that reach the conical shock (as will be discussed in section 3.3).

3.2 Wire ablation and precursor streams

The ability to form a conical shock and produce jets from conical wire arrays exploits an important feature of wire array z-pinches on mega-ampere generators - the presence of precursor plasma flows from the wires which produce a precursor plasma column [8]. In this section evidence and details of these streams in conical wire arrays will be examined both with application to the jet production and array physics.

X-pinch radiography in Fig 3.3 shows that, for a $16 \times 18\mu m$ conical W array, wire cores are still intact $217ns$ after the start of current (the latest time achieved

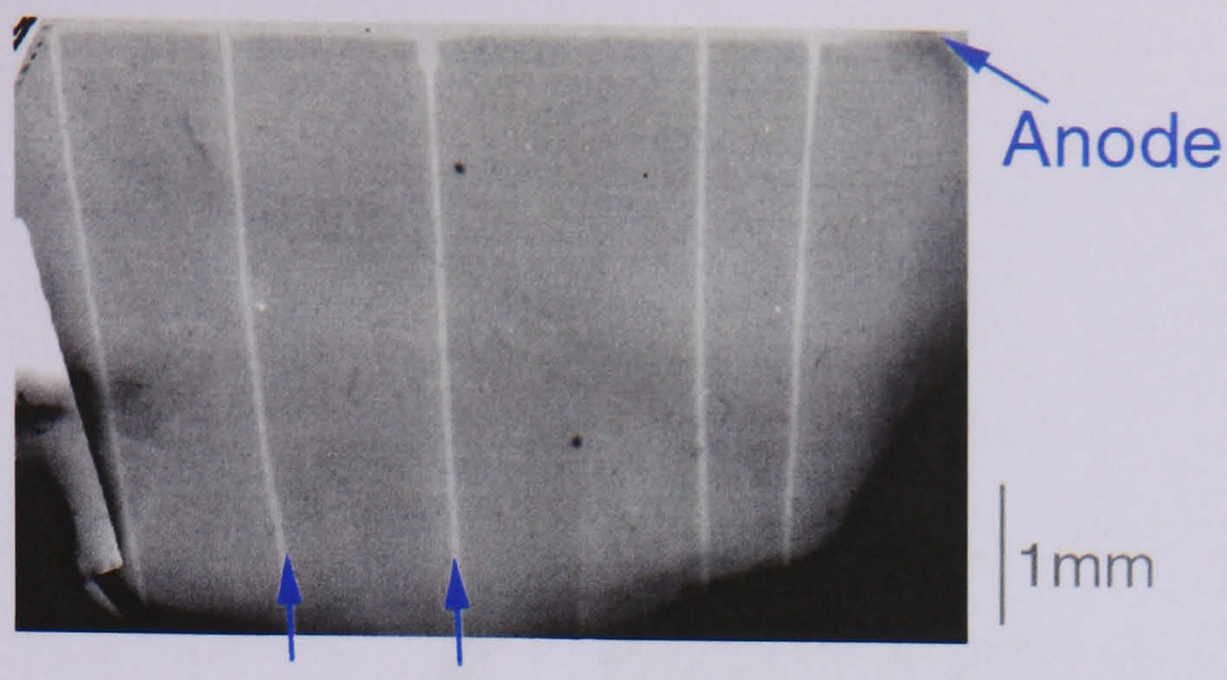


Figure 3.3: X-pinch radiography (photon energies $h\nu \sim 2 - 5keV$) of a conical wire array (mid-grey is no absorption, white is 100% absorption - additional black is due to light leakage).

with x-pinch radiography of conical arrays) and retain a significant fraction of their original mass. The wire cores have expanded from the original wire diameter of $18\mu m$ to $44\mu m$. This is consistent with experiments using single wires [48, 49] and cylindrical wire arrays [8, 43], where cold dense wire cores are surrounded by a hot, low density coronal plasma. Due to the high resistivity of the cold wire cores and the low resistivity of the coronal plasma, the coronal plasma carries the majority of the current.

The field structure in a wire array is the combination of the fields from individual wires, creating a 'global' magnetic field. The Lorentz $\mathbf{J} \times \mathbf{B}$ force due to the global field is toward the array axis, however for a conical wire array there is an added axial component to the Lorentz force due to the radial component of the current.

Comparison of Fig 3.2 with an image taken before the shot shows that, in addition to the wire cores remaining dense, they are also stationary. The wires do not move as a whole under the $\mathbf{J} \times \mathbf{B}$ force. Instead the $\mathbf{J} \times \mathbf{B}$ force acts on the current carrying coronal plasma, whilst the wire cores remain at their original position (until, depending on the mass per unit length in the array, the wire core mass runs out and an implosion occurs). There are many indications (for example using a convolute current return path from the axis [50, 21]) that most of the current (>99%) is not advected toward the axis by the coronal plasma but instead remains in the vicinity

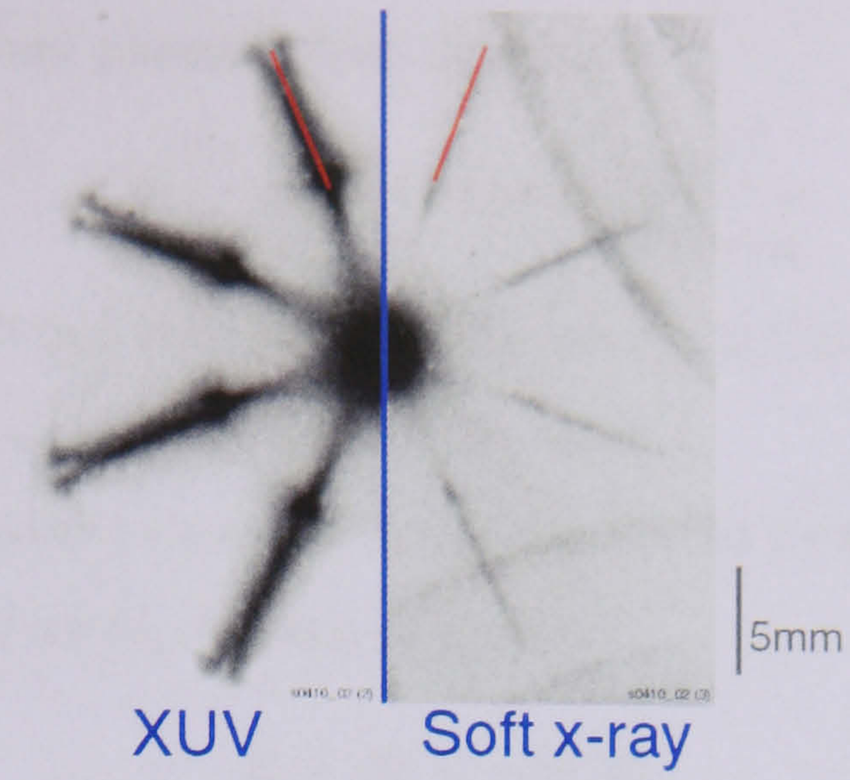


Figure 3.4: Plasma streams shown by end-on emission of wires and streams. (a) is unfiltered (XUV, $h\nu > 40eV$) at $135ns$ and (b) is filtered by $1.5\mu m$ CHO (soft x-ray, $h\nu \sim 120 - 290eV$) at $144ns$. The approximate initial positions of two wires are marked in red. Non-radial structure seen on the right-hand image is damage to the film.

of the original wire position. There are two explanations for the majority of the current remaining at this radius. Firstly the coronal plasma cools relatively quickly after leaving the vicinity of the wire, and thus has a higher resistivity. Secondly the inductance of the coronal plasma is lowest near the wire cores, so this is a preferable current path while the current is rising.

Looking at the end-on XUV emission from the array shown in Fig 3.4 we see that the precursor flows are discrete streams. On the outside of the image the wires are emitting (i.e. shown in black) on both the XUV and soft x-ray cameras. From each of these wires is a tight collimated line of emission to the array axis, which are the precursor plasma streams. On the softer emission these streams continue all the way to the axis, but are lost on the harder emission as they cool. There is little divergence of the streams indicating that they are highly supersonic. Where the streams meet on the array axis is a bright area of emission as the kinetic energy of the streams is thermalised in the conical shock. This conical shock will be discussed in section 3.3.

Given that the current remains in the vicinity of the wire cores, which are known to be stationary, it is possible to apply a rocket model [8]. If the wire cores in an array are static, then there must be force balance between the $\mathbf{J} \times \mathbf{B}$ force and the

momentum of the coronal plasma which is ablated.

$$V_{abl}\frac{dm}{dt} = \mid \mathbf{J} \times \mathbf{B} \mid = -\frac{\mu_0 I^2}{4\pi R_{array}} \tag{3.1}$$

where V_{abl} is the velocity of the ablated material, $\frac{dm}{dt}$ is the rate of mass ablation, I is the current and R_{array} is the radius of the array.

For a conical wire array this equation is complicated by the dependence of radius on axial position z and array opening angle θ

$$R = R_0 + z\cos(\theta) \tag{3.2}$$

Thus in a conical array the magnetic field strength, B, varies along the length of a wire due to the dependence of array radius on axial position

$$B \sim \frac{1}{R} \sim \frac{1}{R_0 + z\cos(\theta)} \tag{3.3}$$

As current is constant along the wire, the magnitude of the $\mathbf{J} \times \mathbf{B}$ force decreases from the cathode to the anode (bottom to top of the array) and is given by

$$V_{abl}\frac{dm}{dt} = -\frac{\mu_0 I^2}{4\pi(R_0 + z\cos(\theta))} \tag{3.4}$$

Experiments using cylindrical wire arrays [51] have measured the velocity of the coronal streams by tracking different density contours. End-on (axial) interferometry has been used to track an electron density contour of $10^{17}cm^{-3}$, giving a velocity of $\sim 150km/s$. Given a sufficiently large inter-wire gap $d_{gap} > \pi\phi_{core}$, experiments on various facilities suggest that the wire velocity remains invariant [15]. The inter-wire gap in our experiments is $3mm$ near the cathode and larger elsewhere. From Fig 3.3 the core size $\phi_{core} \sim 44\mu m$. Thus the setup for conical wire arrays is well within the invariant ablation velocity regime.

Taking the ablation velocity to be invariant, the mass ablation rate must vary with both axial position and time. The current of MAGPIE increases (roughly as $sin^2(\pi t/t_0)$) until maximum current at $t_0 = 240ns$, thus the mass ablation rate is proportional to $I(t)^2$, or

$$\frac{dm}{dt} \propto \sin^4(\pi t/2t_0) \tag{3.5}$$

For jet production experiments the mass per unit length (M_L) of the array is chosen such that not all mass is ablated during the current pulse, i.e. $M_L > \int(\frac{dm}{dt})dt$.

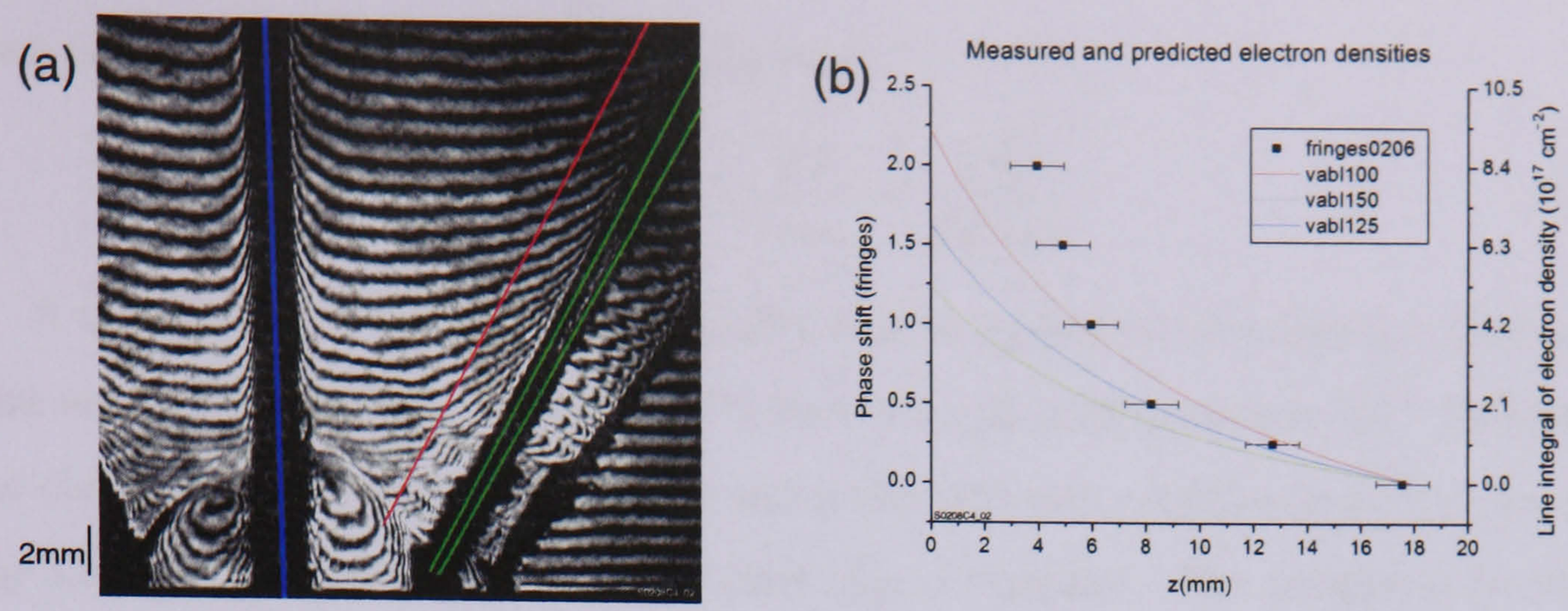


Figure 3.5: (a) Interferometer image of an 8 wire Al 38° conical array, with the axis marked in blue and wire positions in green. (b) Plot of line integral of electron density along the red line on (a), along with predictions of electron densities for $v_{abl} = 1, 1.25, 1.5 \times 10^5 m/s$, assuming $Z = 4$, and two overlapped wires.

The geometry of a conical wire array makes it difficult to measure either the ablation velocity or the mass ablation rate (especially with any axial dependence). However if we assume that the velocity will remain invariant, even with the conical configuration, then we can test the implications of the hypothesis experimentally, as well as verifying the velocity of ablation. Laser interferometry (Fig 3.5) can be used to measure the electron density distribution at an arbitrary distance in front of the wires. Unfortunately this image shows an array that has just started to implode near the cathode, however this will not affect the mass distribution that was ejected from the wires before wire breakage occurred. It is not possible to measure the electron density absolutely at any point as there is no known point of zero phase difference, however relative electron densities can be determined. It should also be noted that the rocket model determines the mass ablation rate, however the interferometer image gives information about electron density, so the charge state must be considered in switching between the model and the interferometer data. Electron densities have been determined for a line (shown in red on the interferogram) $d = 3.7mm$ radially inwards from two wires on opposite sides of the array that are overlapped (each shown in green).

The electron density as a function of axial position is shown in Fig 3.5(b). Also shown on this graph are predicted electron densities. These electron densities have

been calculated using the mass ablation rate

$$n_e = Zn_i = \frac{Z\rho}{m_{ion}} = \frac{Z\frac{dm}{dt}}{v_{abl}m_{ion}} \tag{3.6}$$

A charge state $Z = 4$ has been determined for the precursor streams in cylindrical wire arrays from radially resolved XUV spectroscopy measurements [52]. Although the charge state is density dependent and hence will vary slightly along the wire in Fig 3.5, for simplicity we will assume that this is constant. The predicted electron densities have been determined by taking into account the time of flight between material leaving the wires ($\frac{d}{v_{abl}}$) and normalised using the density at $17.5mm$. Predictions have been made for three different values of the ablation velocity, $v_{abl} = 1$, 1.25 & $1.5 \times 10^5 m/s$. The best fit to the data is found using an ablation velocity of $v_{abl} = 1.25 \times 10^5 m/s$. The three data points at the left of the graph (at $z = 5.0$, 6.3 & $7.5mm$) do not fit the predictions as at these axial positions the contributions to the density from the other wires in the array become significant.

The mass ablation rate discussed above was the average rate of mass ablation from the wires. We will now look in more detail at the smaller scale structure present in wire ablation. Figure 3.6 is a laser shadowgram of the array at $343ns$, showing the coronal plasma surrounding the wire cores. It is evident in the figure that the corona around the wire and the flow of plasma toward the axis are not uniform along the wire, and instead show evidence of modulations. Similar modulations have been observed in cylindrical wire arrays [8]. The wavelengths of the perturbations appear to be highly dependent on wire material ($0.5mm$ for Al, $0.25mm$ for W), however appear to be constant in time and independent of current per wire. This fixed wavelength modulation occurs in any wire array configuration where a global magnetic field is present (including linear arrays [17, 34], radial arrays and single wires with an imposed magnetic field [53]), however not in single wire experiments where no global field is present [49, 48].

The modulation in the coronal flow produces fingers of plasma which illustrate the direction of the coronal flow (assuming that the 'source point' of the flow is static). As expected the streams near the edge of the array are perpendicular to the wires on the image (i.e. in the direction of the expected $\mathbf{J} \times \mathbf{B}$ force), and hence have

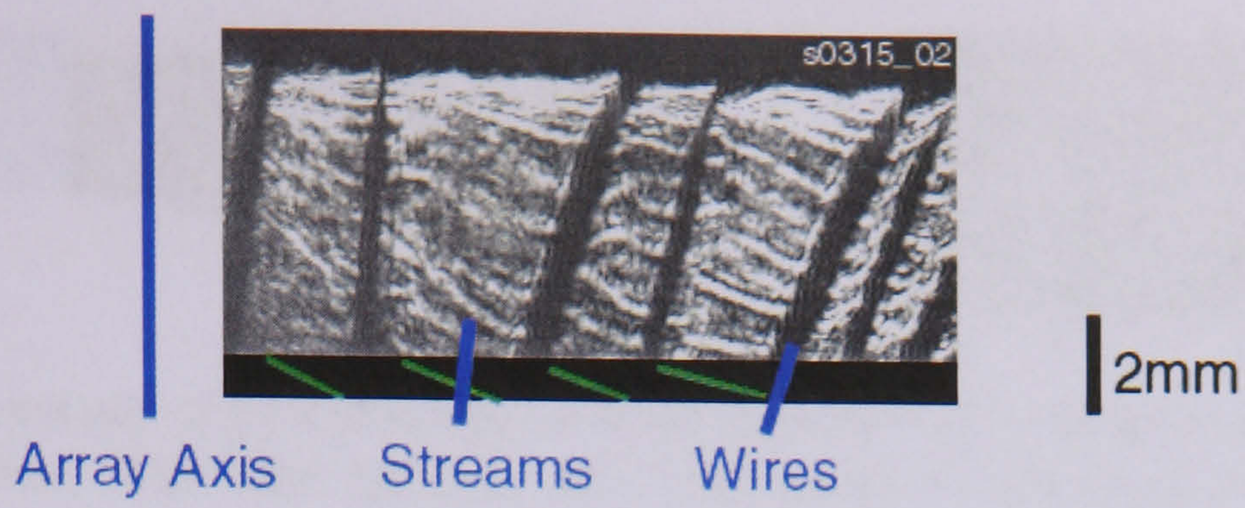


Figure 3.6: Shadowgram of a 16 wire W array at 343ns showing wires and streams. In green below the main image are the expected angles of the streams.

an axial component. The streams from the wires in the centre of the image appear to be 'steeper' than 90° to the wires, however this is merely due to perspective (as illustrated at the base of Fig 3.6).

It is not known what causes the axial modulations seen (e.g. [54]). Possible explanations include the $m = 0$ MHD instability, or some instability seeded by imperfections in the wire introduced in the manufacturing process, however the latter is unlikely as the structure only appears in the presence of a global magnetic field (i.e. not in experiments with a single wire).

There is an indication in experiments using Al conical arrays that the precursor flow is more complicated than for W conical wire arrays or Al cylindrical wire arrays. Figure 3.7 shows XUV emission from an Al array at $240ns$. The image shows that after the streams leave the wires they first travel downwards (towards the cathode) and then curl back upwards (towards the anode), but never appear to reach an angle perpendicular to the wires. In the experiment shown the wires are inclined at $\theta = 35°$ to the axis, although a similar, but slightly less pronounced effect has been seen at the usual 30° opening angle. At present the explanation for this effect is unclear. One potential explanation is that rather than a real force, the effect could be due to the mass ejection point moving with time, so the curved streams are tracing the time-history of the system, rather than a real deflection of the flow. As the streams are at $\sim 45°$ to the wire the ejection point would need to travel at approximately the ablation velocity. If it were moving at such a velocity the change in position of the ejection point would be seen on the different frames of

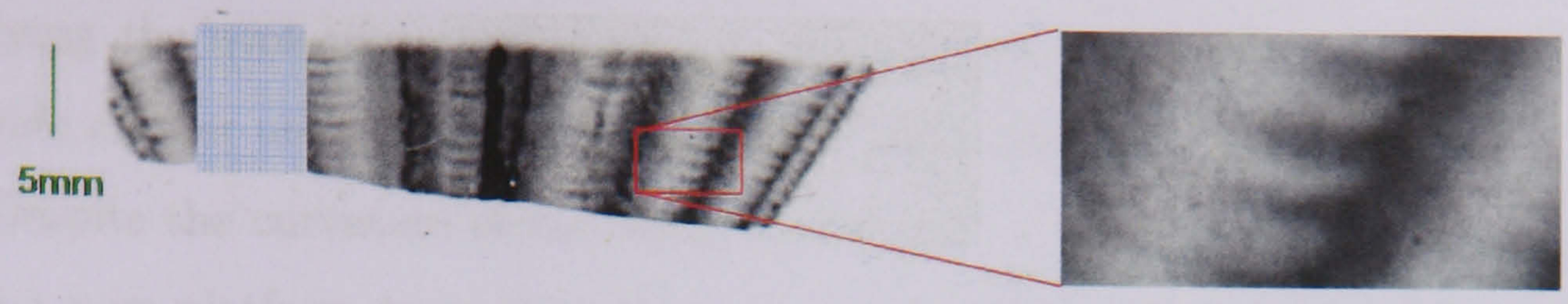


Figure 3.7: Curvature of precursor plasma streams in XUV emission from a 16 wire Al array at $249ns$. The blue hatched area represents a dead-zone between frames on the camera.

the XUV four frame cameras (the ejection point will move 1.25 to $1.75mm$ in the $10ns$ between successive frames on the camera). Comparison of the different frames implies that the ejection point is static.

Whilst the mechanism for this curvature of the streams is unknown, the fact that no curvature is seen in cylindrical arrays can be used to suggest some possible explanations. The curvature could be linked on the fact that the wire spacing near the anode is large ($5.9mm$) for the shots where this effect has been observed. In cylindrical wire arrays the spacing is typically a factor of ≥ 2 smaller than this. The exact mechanism by which this larger wire spacing could cause the curvature is unclear. Also the variation in this spacing along the wire could have some effect.

A further explanation for this effect, which could potentially be very interesting for array physics, is that the observations are near peak current. One of the mechanism holding the current in the vicinity of the wire cores is that this path has a large radius, hence has a lower inductance than other paths which are closer to the array axis. Hence the reverse voltage $L\frac{dI}{dt}$ is smaller near the wire cores. At peak current, the rate of change of current is zero, and thus the product $L\frac{dI}{dt}$ is zero for all paths, so a resistively preferable path may then be taken.

Early in the evolution of cylindrical wire arrays ($\sim 120 - 150ns$) the plasma streams are slightly angled (by $\sim 5°$), however by peak current the streams are straight and radial. At present it is unclear whether there is any link between the angled streams in cylindrical arrays and the curvature in conical wire arrays.

Various experiments have been performed in an attempt to understand the cause of these modulations in ablation rate, including experiments where wires have wire diameter perturbations of different wavelengths artificially seeded [18, 19]. Further

BIBL. LONDIN. UNIV.

studying the evolution of natural and imposed modes in such experiments may provide a fuller understanding of the natural modulations.

Despite the curvature of the streams observed in conical arrays, they may provide a new platform to explore the cause of the perturbation. For conical array experiments both the magnetic field strength and inter-wire spacing vary between the two electrodes by a factor of ~ 2 (depending on the actual load design). By comparing different ends of the array in a single conical array experiment it is possible to investigate any effect of the magnetic field or wire spacing on the modulation wavelength, whilst keeping all other parameters equivalent (e.g. the current pulse shape). In the figures shown so far in this chapter there is no obvious change in the perturbation wavelength along the wires. Direct measurements indicate that the wavelengths match those found in cylindrical arrays ($\sim 500\mu m$ for Al and $\sim 250\mu m$ for W).

Fourier transforms will now be used to provide a better measure of the wavelength of the modulations. Line-outs have been taken from an XUV emission image of an Al conical array, similar to Fig 3.7 however with an opening angle $\theta = 30°$. This line-out is split into two halves, one for the top half of the array and one for the bottom half (shown in Fig 3.8a). The full line-out, and the two 'half' line-outs are then fourier transformed (using an FFT algorithm within the data analysis package Origin 7.0) to provide a plot of amplitude against spatial frequency (Fig 3.8b). The bin size on the FFT are large ($\pm 10\%$ of the natural modulation frequency for the FFT of each half) due to the relatively small number of wavelengths investigated. This leads to a large error ($\pm 10\%$) in the fundamental wavelength determined.

Each of the FFT's peaks at a wavelength of $520 \pm 100\mu m$ along the wire (i.e. $520\mu m \cos(\theta) = 450\mu m$ along the axial direction). This value of $520\mu m$ is similar to the value for cylindrical Al arrays. There is no measurable difference in the wavelength between the top and bottom halves of the array indicating that, although a global field is required to produce these perturbations, a change in field strength by a factor of 2 does not substantially alter the wavelength of the modulation. Although using smaller line-out lengths would make any difference that exists more distinct, unfortunately this would also lead to an increase in the bin sizes and thus the errors.

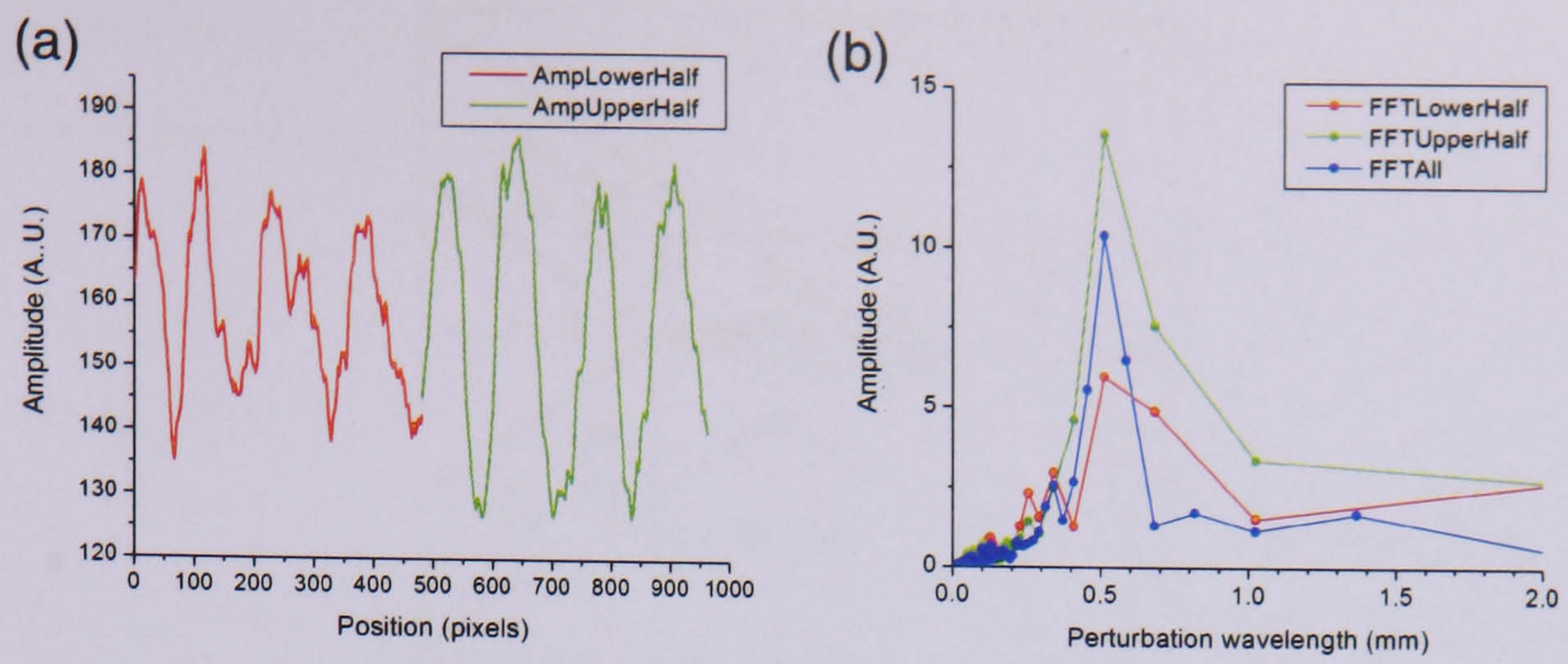


Figure 3.8: (a) Line-outs from an XUV image used for FFT, and (b) FFT results for the full line-out (blue) and the upper (green) and lower (red) halves. The uncertainty in the peak wavelength is approximately the spacing to the nearest data points on the FFT.

The extreme case of conical wire array, the radial wire array may be able to provide more information on any change in wavelength as the magnetic field varies by an order of magnitude along the wire. Experiments are now underway on MAGPIE to investigate this.

3.3 The conical shock

The precursor plasma flow in a conical wire array produces a region near the array axis where there are conically convergent flows. Canto et al. 1988 [55] describe such a system with convergent conical flows as a mechanism for the production of interstellar jets.

In the model by Canto the interaction of an isotropic stellar wind with an homogeneous environment produces a spherical shock. Pressure variations around the star alter this shock from a sphere into an oval, causing refraction of the stellar wind. The shape of this shock is determined by balance of the ram pressure of the wind, the centrifugal pressure and the gas pressure in the surrounding medium. As matter flows toward the tip the centrifugal force dominates and this shape of the shock becomes more accentuated. Eventually a steady system with matter flowing toward an acute tip is formed (Fig 3.9 - from [55]). At this tip a conical shock is formed, redirecting the stellar wind away from the star. This produces a cylindrical

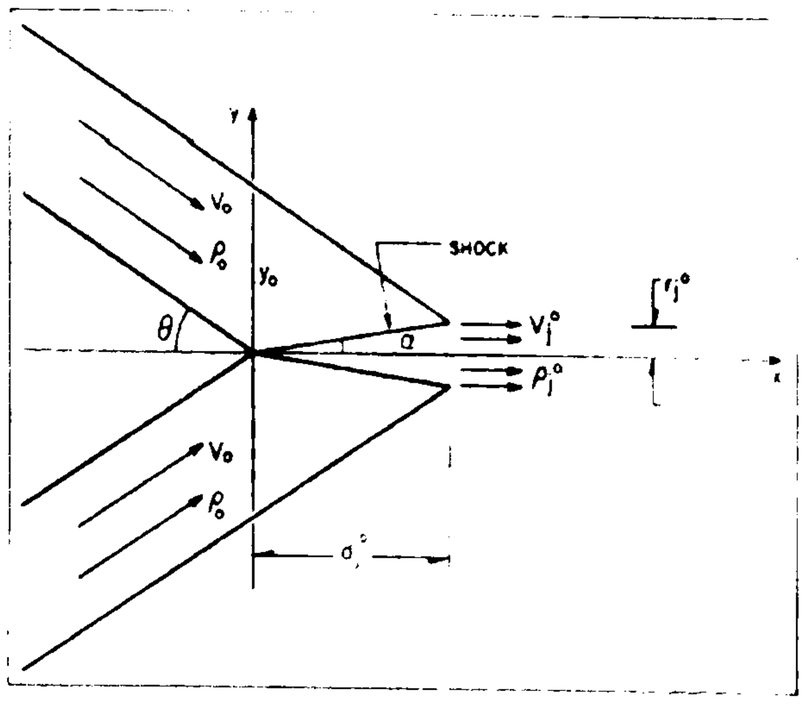


Figure 3.9: Jet formation by conical shock of stellar wind (reproduced from Canto et al. [55]).

stream or jet flowing away from the star.

Assuming the case where there is a strong adiabatic shock the compression factor across the shock will be $\xi = \frac{\gamma-1}{\gamma+1}$, where γ is the ratio of specific heats. The opening angle of the conical shock, α can be calculated to be $\tan\alpha = \xi^{1/2}$. From this, derivations in Canto give the jet radius r_j, mass density ρ_j and jet velocity v_j as:

$$r_j = \frac{y_0 \tan\alpha}{(\tan\theta + \tan\alpha)} \tag{3.7}$$

$$\rho_j = \rho_0 \frac{(1 + \tan\theta/\tan\alpha)}{\xi} \tag{3.8}$$

$$v_j = \frac{v_0 \cos(\theta + \alpha)}{\cos(\alpha)} \tag{3.9}$$

For the astrophysical (low atomic number) jets the system can be assumed to be radiatively cooled if

$$v_0 \sin\theta \leq 200 \frac{km}{s} \tag{3.10}$$

The solution for the radiatively cooled case requires a more in-depth analysis, however it can be concluded that a narrow conical shock with a small opening angle is formed leading to a highly supersonic jet with a radius much smaller than the width of the initial flows. The same parameters of the jet can also be found (see [55]). but the solution becomes material dependent. The material dependence of these jet parameters limits any direct quantitative comparison between the laboratory jets and the astrophysical model. Similarly, due to the material dependence and other

dependencies of the radiative cooling rate there is no direct analogue to equation 3.10 for our laboratory system.

The main results found by [55] for the radiatively cooled case is that the shock opening angle α is small, leading to a small jet radius and an axial velocity of the flow that is similar to the initial axial component of the flow ($v_j \sim v_0 \cos(\theta)$). We will later be able to investigate the change in jet diameter for different materials and hence cooling rates [56].

The astrophysical community now believes that the production of stellar jets is likely to be magnetically driven [57, 58], however it is likely that the collision of convergent flows still plays an important role. Experiments are currently underway to produce magnetically launched jets using radial wire array z-pinches [22], however that work is outside the scope of this thesis.

The convergent conical plasma flows of a conical wire array are broadly similar to the configuration outlined by Canto [55]. For tungsten with typical parameters of our streams ($v_0 \sim 150 km/s$, $\theta \sim 30°$) and conical shock radius r_{cs} we find that we are within the radiating case (cooling distance $d_{cool} \sim 1mm \sim 2r_{cs}$ - see section 3.4.2 and equation 3.25 later for details of similar calculations). A major difference between the Canto model and the flows in a conical wire array is that in the wire array the density incident on the conical shock varies with both time and axial position. As has previously been discussed the rate with which mass leaves the wire (as was shown experimentally in Fig 3.5) and hence also reaches the array axis will clearly be subject to these two dependencies:

$$\left(\frac{dm}{dt}\right)_{ablated} \propto \frac{I(t)}{R} \tag{3.11}$$

An additional dependence on axial position is introduced by the time of flight from the wires to the axis; due to the geometry of the system there is a variation in the lag between flow elements leaving the top and bottom of the wire and arriving at the top and bottom of the conical shock $\left(\Delta t_{fl} \sim \frac{R_{top} - R_{base}}{V_{abl} \cos(\theta)}\right)$. The current and hence also the mass ablation rate increases with time (until peak current at 240ns). Thus at a given time the plasma which reaches the axis near the cathode will have been ablated later and hence by a higher current than the plasma incident near the

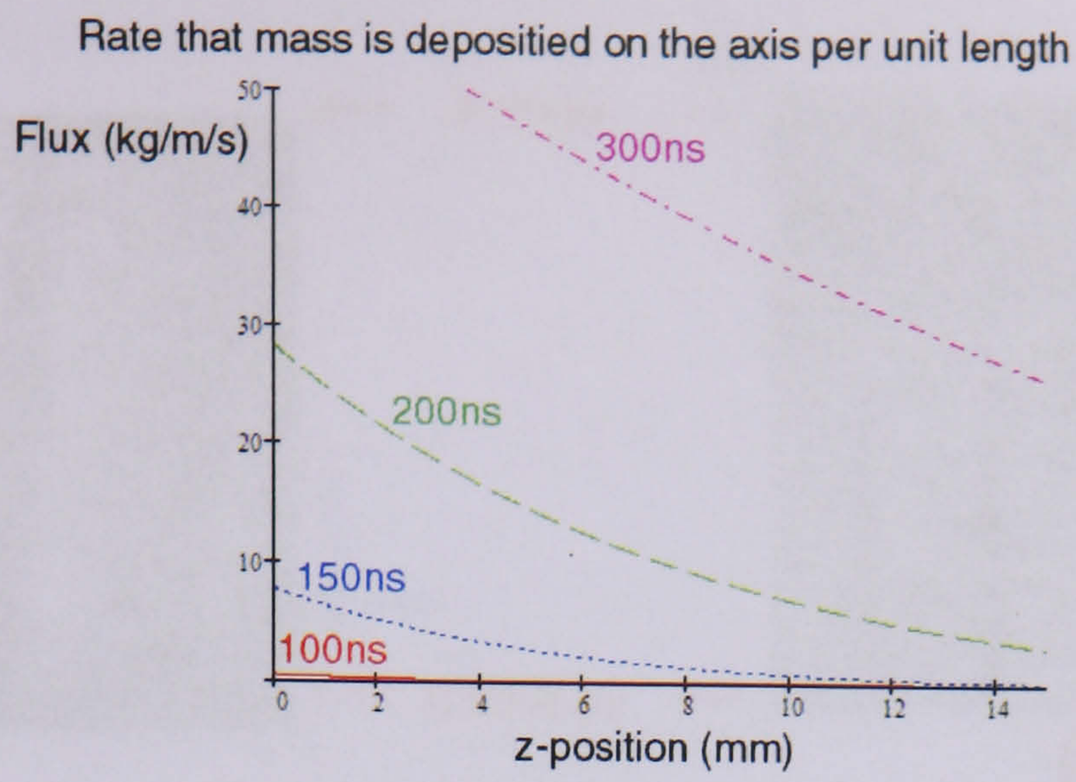


Figure 3.10: Mass incident on the array axis as a function of z for different times using an array with $\theta \sim 30°$.

anode. Even near the cathode, where the array diameter is similar to a cylindrical wire array, as the stream velocity is not wholly radial the time of flight to the array axis is greater than the cylindrical case. These axial dependencies all cause a higher density incident on the axis near the cathode than near the anode. Figure 3.10 shows predictions for the masses incident on the axis at different positions at different times for a $16mm$ base diameter, 30° opening angle array taking into account these dependencies.

To investigate the early stage of conical shock formation it is useful to first look at the process of precursor formation in aluminium cylindrical wire arrays. The formation of the precursor column has been explored analytically and numerically (using a kinetic model) [45] and experimentally on MAGPIE [8, 52, 20]. When precursor flows of an aluminium wire array initially meet on the array axis they have a low density and hence the ions are collisionless (mean-free-path $\lambda > R_{array}$). As the density of the flows increases the mean free path decreases and a conical shock begins to form. As calculated in [45], the flows become collisional for a $16mm$ cylindrical wire array by $\sim 130ns$ and a broad precursor column begins to form with a diameter $\sim 2mm$, which is similar to the mean-free-path of the flows. This precursor column thermally expands for $\sim 30ns$ to a diameter of $\sim 3-4mm$, until the collision time τ_c is sufficiently small to allow efficient ion-electron equilibration and the thermal energy is radiated out of the precursor column. At this time ($\sim 160ns$ for an

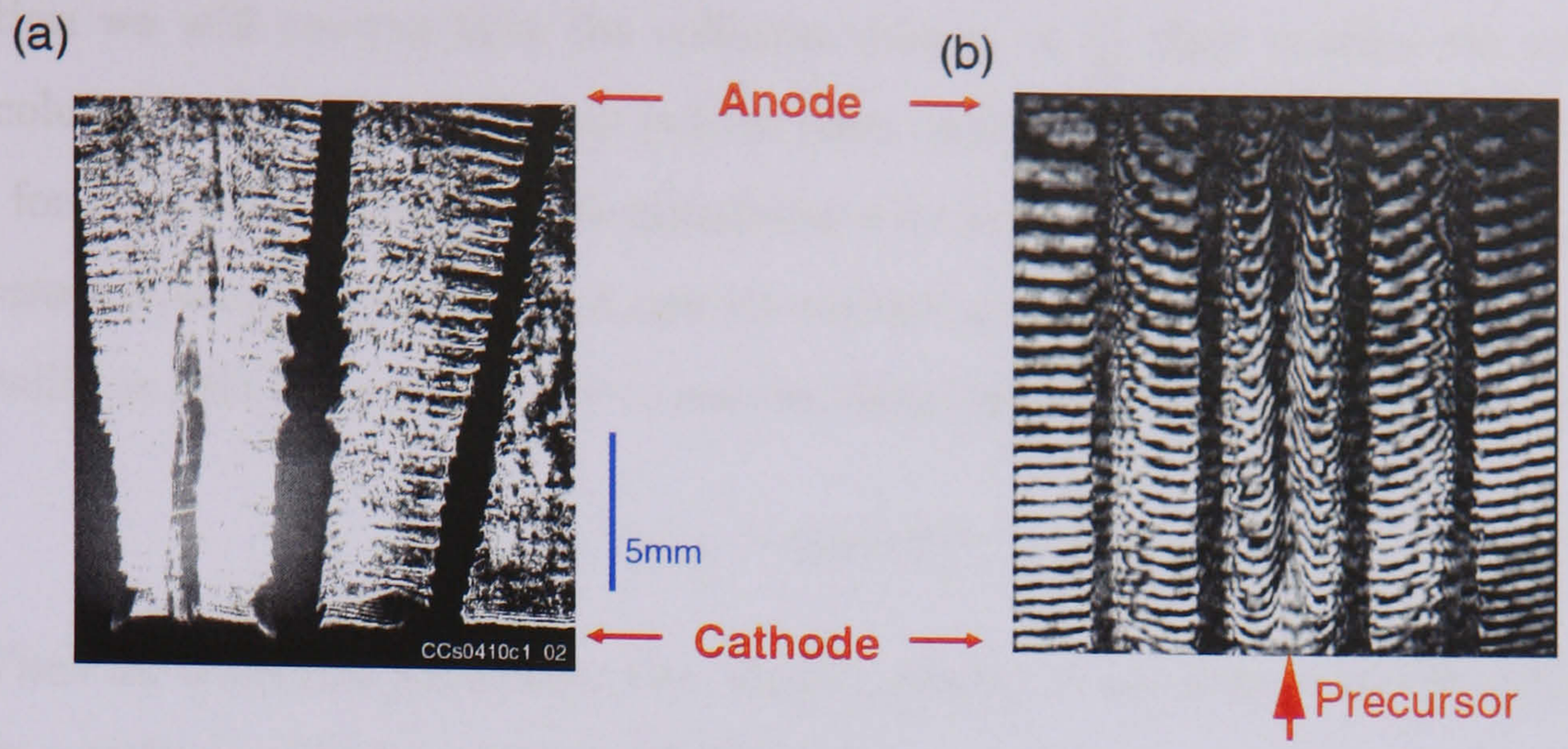


Figure 3.11: (a) Schlieren image of a partial conical shock in an 8 wire Al 11° conical wire array and (b) a partial precursor an interferometer image of an 8 wire Al cylindrical wire array taken at $128ns$.

array of 32 Al wires on $16mm$ diameter) the column collapses to a tighter, $1mm$ diameter column before slowly starting to expand again. Experiments indicate that this collapse occurs earlier for lower wire number arrays.

In a conical wire array it is expected that a similar process of column formation, expansion and then collapse will occur. At a given time the density of the streams near the base of the array is higher, therefore the mean free path will be shorter, and thus a well defined shock will form here first. Experimentally this can be seen in Fig 3.11a. This figure shows an Al wire array, $137ns$ after start of current. The conical shock has collapsed at the base of the axis, where the mean free path of the streams is small. Further from the cathode the shock is not visible on the schlieren image as the collision rate of the streams remains low so collapse has not occurred, thus no sharp density gradient is present. It is interesting to note that there is also some variation in the time that precursor column formation occurs at different axial positions in cylindrical wire arrays. However the precursor column forms first at the anode of the array, as illustrated in Fig 3.11b and the time for the precursor column to form over the full length of a cylindrical array is just a few nanoseconds, compared with tens to hundreds of nanoseconds in conical wire arrays (depending on the array configuration). The asymmetry in cylindrical arrays has yet to be explained.

To predict when the column will collapse in a conical array for a given axial

position we will assume that the collision time $\tau_c \propto \frac{v^3}{n_i}$ that enables the ions on the column to heat the electrons (which then radiate efficiently) will be similar to that for the column collapse in a cylindrical wire array. For a conical wire array the precursor plasma streams are not exactly counter-propagating. Instead, to calculate the collision rate it is appropriate to use the radial component of the ablation velocity

$$v_{con,r} \sim v_{abl}\cos(\theta) \tag{3.12}$$

Thus for a conical wire array the critical density of the flows that we expect to cause a collapse of the conical shock will be

$$N_{con,crit} \approx \frac{N_{cyl,crit} \times v_{con,r}^3}{v_{cyl}^3} \tag{3.13}$$

$$\sim N_{cyl,crit} \times \cos^3(\theta) \tag{3.14}$$

where it has been assumed that the ablation velocity (perpendicular to the wire) for conical and cylindrical arrays is the same. Given that the same material is used in each array then this can be converted to a relationship between mass densities

$$\rho_{con,crit} \approx \rho_{cyl,crit} \times \cos^3(\theta) \tag{3.15}$$

For an 8 wire cylindrical wire array the precursor column collapses at $120ns - 128ns$ (as is shown by the partially collapsed column in Fig 3.11b). The flows that are on the axis of the cylindrical array at this time were ablated from the wire $t_{flight} = \frac{r_{array}}{v_{abl}}$ earlier. Assuming $v_{abl} \sim 1.25 \times 10^5 m/s$ these streams were ablated at $59 \pm 4ns$. Applying the rocket model to the current at this time implies that the ablation rate was $27 \pm 3kg/m/s$. When these flows reach a radius of $0.5mm$ (the approximate size of the precursor at when it forms) from the axis convergence of the flows implies that the average density in the flows will be $7.1 \pm 1.6 \times 10^{-4} kg/m^3$.

Using the equation for the critical density in a conical array (equation 3.15) for an 11° opening angle conical array the critical density will be $6.7 \pm 1.5 \times 10^{-4} kg/m^3$.

Figure 3.12 is a plot of the density incident at a radius $r = 0.5mm$ of an 11° with a lower diameter of $16mm$ at $137ns$ after the start of current (the time that the laser image in Fig 3.11a was taken). Also drawn on the plot are the expected upper and lower limits to the critical density ($\rho_{crit} \sim 6.7 \pm 1.5 \times 10^{-4} kg/m^3$). From

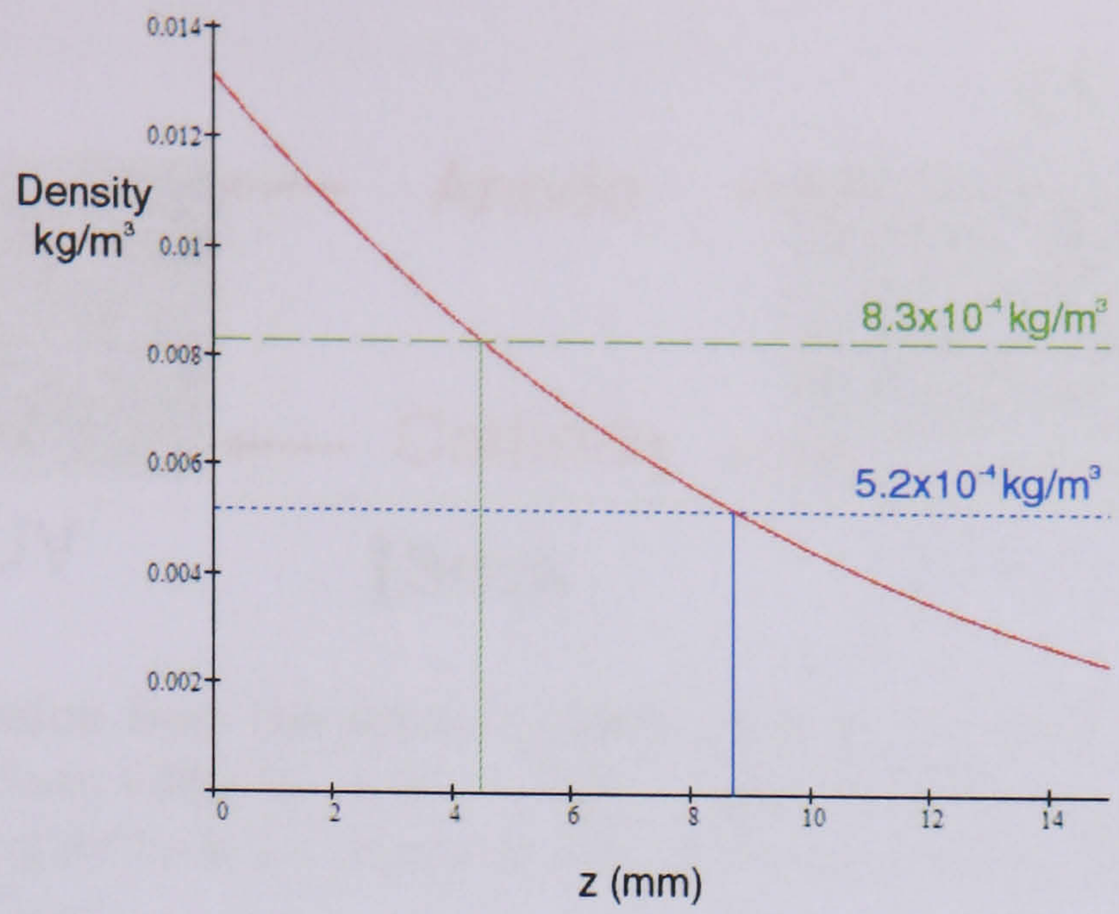


Figure 3.12: Plot of density incident at a radius of $0.5mm$ for an 11° conical array at $137ns$, along with values of the critical density at $1mm$ derived from when the cylindrical array precursor forms.

the plot we find that for this setup the flow density is equal to the critical density for z between $4.4mm$ and $8.6mm$ at $137ns$. Hence we expect the top of the conical shock at this time will be at $z = 4.4mm - 8.6mm$. Measurements on Fig 3.11a indicate that the length of the conical shock is $7.4mm$. Hence this analytic method for determining the collapse of the conical shock appears to be consistent with the experimental data.

The conical shock formation process is similar in a W array, however due to radiative cooling the final column diameter is less ($\sim 0.5-1mm$). For both materials, once the precursor flows become fully collisional along the full length of the array a steady conical shock similar to that described by Canto [55] is formed.

Figure 3.13 shows gated XUV ($h\nu > 40eV$) and soft x-ray ($1.5\mu m$ CHO filter giving $h\nu \sim 120 - 290eV$) images of a tungsten conical wire array. We see that, whilst the XUV image shows similar intensities of emission from the wires, streams and conical shock, the soft x-ray image shows only emission from the conical shock. This could be due to a higher radiation temperature on the axis as the kinetic energy associated with the radial velocity of the precursor plasma streams is thermalised. Spectroscopic measurements of the precursor streams and column in Al cylindrical wire arrays on MAGPIE [52] suggest a higher ion charge state Z in the precursor

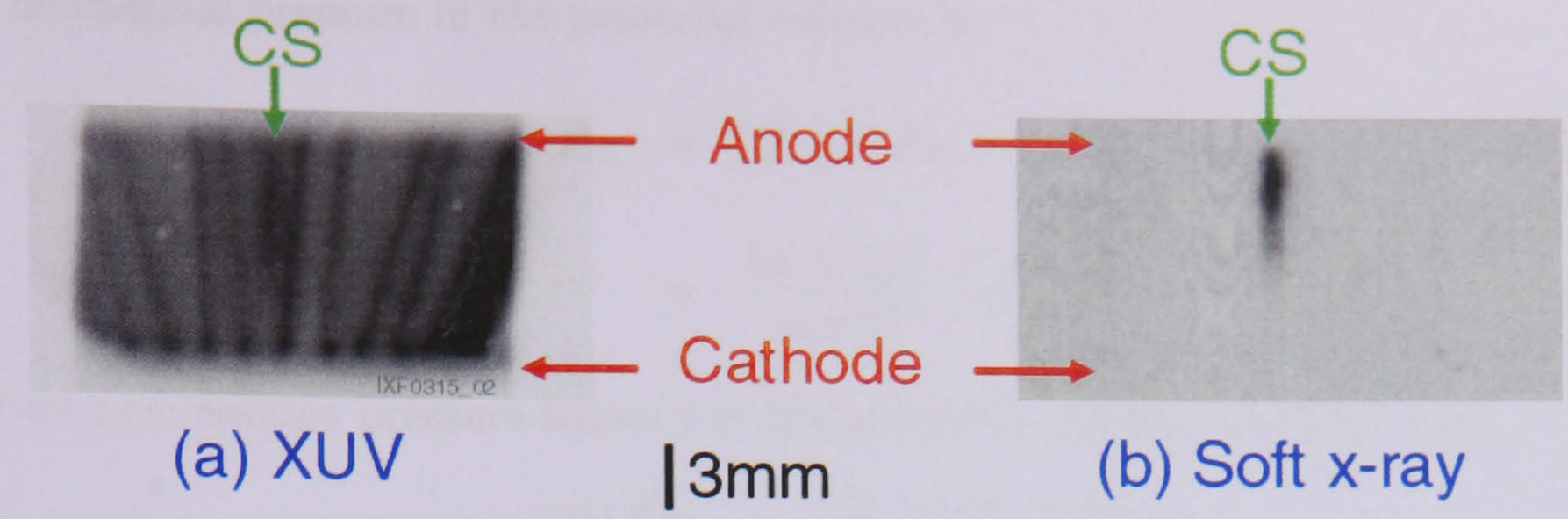


Figure 3.13: Emission from the array in gated imaging: (a) XUV ($h\nu > 40eV$) and (b) soft x-ray ($1.5\mu m$ CHO filter, $h\nu \sim 120 - 290eV$). Both images are at $292ns$. The whole array emits in XUV, however only the conical shock (labelled CS) emits on the filtered image.

column than in the streams ($Z_{streams} \sim 5-6$, $Z_{column} \sim 7$). The combination of the increase in average charge state and higher density in the precursor column suggest that the precursor column (and hence also the conical shock in a conical wire array) is hotter than the precursor plasma streams. A temperature $T \sim 50eV$ has been deduced for the precursor column [52]. PCD measurements and time resolved XUV emission images of conical arrays both show that there is transmission of radiation through a $1.5\mu m$ CHO filter, and the transmitted intensities are similar to cylindrical wire arrays (but with a lag due to the different time of flight), indicating that the conical shock of a conical array is also likely to have a temperature of $\sim 50eV$ and a charge state $Z \sim 7$. For a conical wire array the component of velocity parallel to the edge of the conical shock remains unaffected.

Similar deductions from spectroscopy are not possible in W arrays due to the very large number of possible energy transitions, which merge to form a continuum-like spectrum. Based on pressure balance we can find an estimate for the temperature and ionisation state in a W precursor column (based on calculation by [52]) The kinetic pressure P_{kin} incident on a precursor column of unit length and radius R is

$$P_{kin} = \rho v^2 \tag{3.16}$$

$$= \frac{v_{abl}}{2\pi R}.\frac{dm}{dt} \tag{3.17}$$

The thermal pressure in the precursor column is

$$P_{th} = (Z+1)Tn_i \tag{3.18}$$

$$= \frac{(Z+1)T}{m_i \pi R^2} \int \frac{dm}{dt} dt \tag{3.19}$$

If we now assume pressure balance in the precursor column, then we have

$$\frac{v_{abl}}{2\pi R} \frac{dm}{dt} = \frac{(Z+1)T}{m_i \pi R^2} \int \frac{dm}{dt} dt \tag{3.20}$$

$$\frac{2(Z+1)T}{m_i R} = \frac{1}{v_{abl}} \cdot \frac{\int \frac{dm}{dt} dt}{\frac{dm}{dt}} \tag{3.21}$$

Assuming that wire ablation can be described by a rocket model with a constant ablation velocity, then the right hand side of equation 3.21 is merely a function of the current pulse shape and time. Hence for two different materials (Al and W), the left hand side of equation 3.21 can be rearranged

$$(Z+1)_W T_W \sim (Z+1)T_{Al} \frac{R_W m_W}{R_{Al} m_{Al}} \tag{3.22}$$

Given the atomic masses and precursor radii of these two materials we find that

$$(Z+1)T \sim 570eV \tag{3.23}$$

Whilst the electron density in the conical shock is approximately an order of magnitude lower than that required for local thermal equilibrium (LTE) [59], we will assume LTE in an attempt to give an estimate of charge state and temperature within the conical shock. Ryutov et al. [60] have determined that, for a high Z z-pinch plasma, based on [61, 62], an approximation to the LTE effective ionisation state Z can be found if the temperature T satisfies

$$I_Z \approx 5T \tag{3.24}$$

where I_Z is the ionisation potential of a charge state Z. Using this model for $(Z+1)T = 570eV$ we determine a charge state $Z \approx 12$ and a temperature $T \approx 47eV$. As the LTE assumption is not fully valid in the conical shock, the real ionisation state will be slightly lower that 12, and the temperature will be slightly higher than $47eV$ [63].

From these values of $(Z+1)T$ for Al and W conical shocks we can determine the sound speed. For Al the sound speed is $36km/s$ and for W it is $17km/s$. The sound transit time for the shock is $\sim 55ns$ for Al, and about half of this in W (due to the smaller conical shock diameter). As material continues to be fed into the conical shock for a few transit times (240ns), the action of the shock can be considered to be steady-state.

3.4 Plasma jets from tungsten conical wire arrays

Within the conical shock there will be an axial velocity similar to the axial component of the initial flows ($v_{abl}sin(\theta) = 6.25 \times 10^4 m/s$ for $\theta = 30$). At the tip of the conical shock a strong pressure gradient is present, which will accelerate the flow along the axis.

To study the propagation of this accelerated flow experiments with conical wire arrays used a hollow anode plate. The large diameter of the hole in the anode plate (the upper diameter of the array, $\sim 30mm$) prevents any photo-ablated material from the anode disturbing the flow of material out of the conical shock.

3.4.1 Jet tip velocity

Figure 3.14 shows schlieren images from a single experiment with a W jet at three different times. In the first image (at 308ns) a long narrow column of plasma is seen. The diameter decreases towards the jet tip. The tip of the jet, which is $9.4mm$ from the anode, has a diameter of $\sim 175\mu m$ whilst the diameter nearer to the anode plate is $560\mu m$. The tight collimation of this jet is the result of low thermal expansion due to the high rate of radiative cooling of tungsten.

The 3-frame laser shadowgraphy system shows that the plasma is propagating upwards, away from the conical shock. As these images are a known time apart and the scales are known it is possible to determine the velocity of the tip. The positions, with associated error margins are plotted on Fig 3.14d. The gradient of the graph indicates that for this experiment the axial velocity of the jet tip is $\sim 275 \pm 13 km/s$. It is assumed the different acceptance angle of the first camera does not affect the

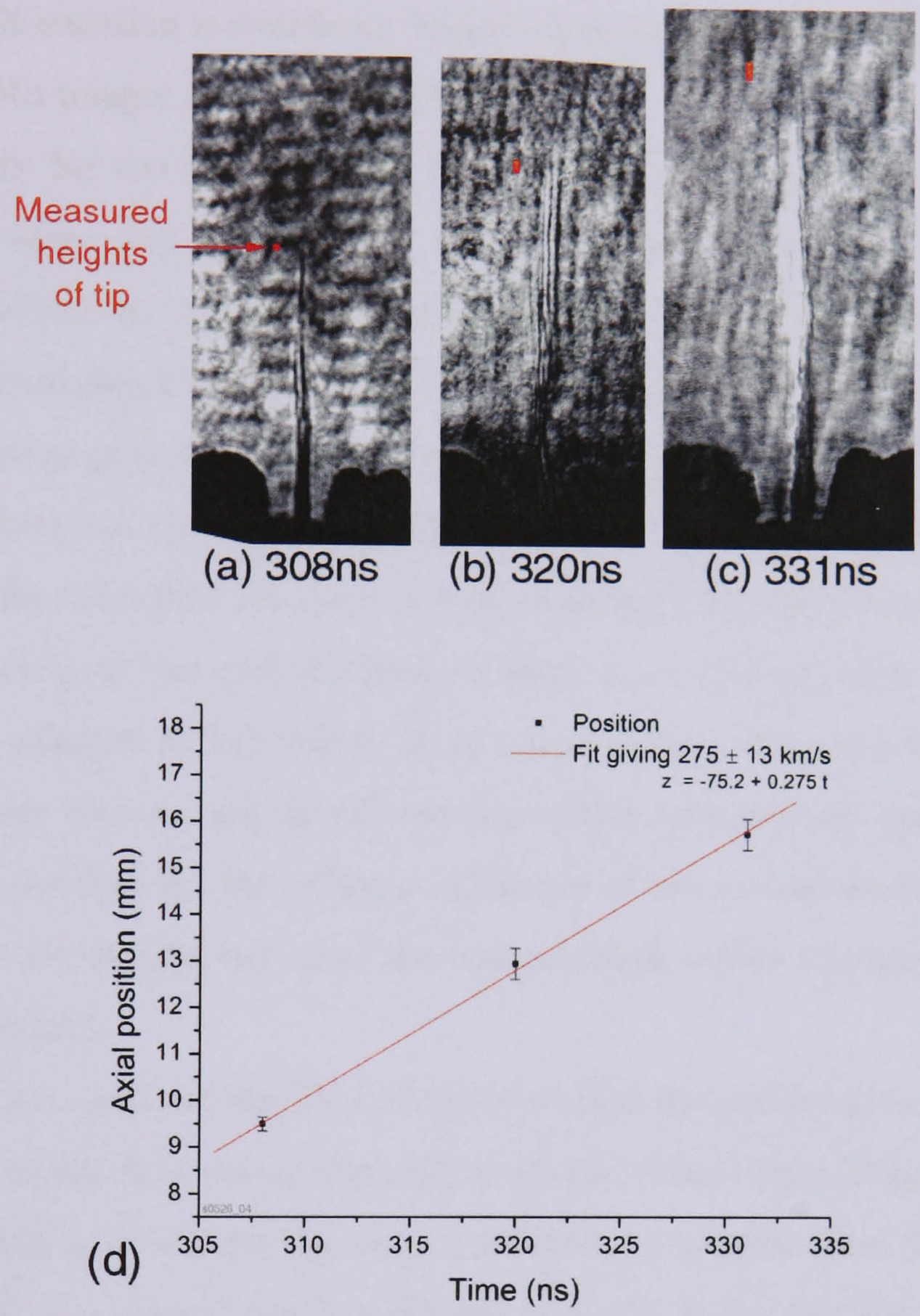


Figure 3.14: Schlieren images of a jet produced by a W conical array at (a) $308ns$, (b) $320ns$ and (c) $331ns$ after start of current (all from the same experiment and on the same scale). (d) is a plot of the tip positions from each of these images. The red lines on the images (a,b,c) correspond to the measured heights of the tip plotted on the graph (d).

length of jet imaged, particularly as the trajectory here is in agreement with the other two cameras, which have matched acceptance angles.

On the 2nd image in the series a sharp density gradient in the body of the jet has led to interference between different areas of the probe beam. Also on the 3rd image some self-emission is seen from the jet which is brighter than the probe beam, however on both images the jet tip is visible.

The velocity for the tip is a factor of 3.5 greater than the axial component of the precursor flows, indicating that the flow has been accelerated by the conical shock. It is possible to compare the trajectory of the jet tip to the estimated phase velocity of conical shock formation. If we use the same approach as in Section 3.3, using as a starting point the collapse time of a W precursor column in a cylindrical array (157-173ns) but now applying this to a 16 wire, $\theta = 30°$ tungsten array, we can establish the time that the conical shock will form for different axial positions. The phase velocity of the conical shock collapse is $\sim 155 km/s$ and the top of the conical shock collapses at $291 \pm 9 ns$. If we compare this with the jet tip trajectory (Fig 3.15) we see that the jet tip left the top of the conical shock between 295 and 300ns - within the error for the collapse at the top of the conical shock. Thus we can determine that the jet did not leave the conical shock before the top of the conical shock had collapsed.

This result and simulations [25] both suggest that the acceleration of jet material mostly occurs as the flow leaves the conical shock, rather than along the length of the shock. That is, if the jet tip was accelerated to greater than $176 km/s$ when another part of the conical shock collapsed it would leave the top of the conical shock earlier than $295 ns$ (at $240 ns$ if it was accelerated to 270km/s when the base of the conical shock collapsed).

The acceleration at the top of the conical shock is due to a pressure gradient which is set up by both the drop in the temperature of the jet as it leaves the conical shock and thermal expansion. Both of these process will occur over the cooling length of the jet, d_{cool}, which is the length it takes for the jet to radiate its internal energy.

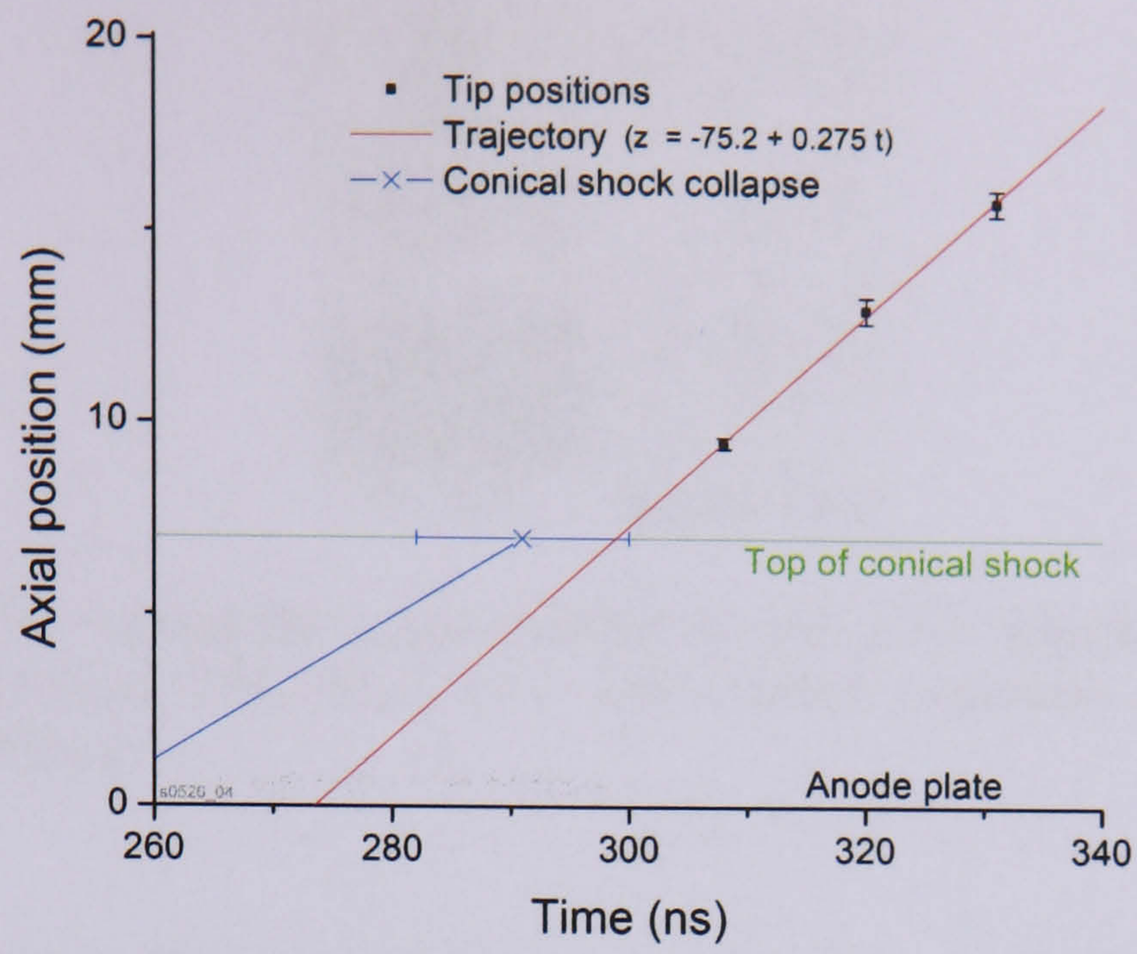


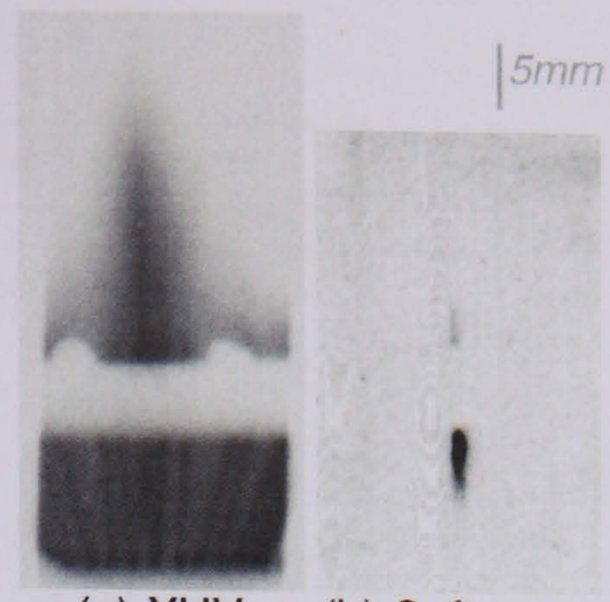
Figure 3.15: Expected position of conical shock collapse and experimental jet tip positions.

3.4.2 Tungsten jet temperature

Tungsten has a high rate of radiative cooling [56]. This high cooling rate has been made evident so far by the observation that the precursor flows are well collimated streams rather than expanding fan-like structures. Also radiative cooling led to the relatively small size of the tungsten conical shock in comparison to an Aluminium conical shock. In the jet this high rate of radiative cooling manifests itself as a highly supersonic (therefore near-parallel) jet in contrast to a fast expanding sub- or trans-sonic flow. Due to radiative cooling in the conical shock, the velocity of the flow within the conical shock already has an internal Mach number $\mathcal{M} \sim 4$.

We can see how rapidly a tungsten jet cools using x-ray imaging. Figure 3.16 indicates that, whilst an XUV image shows a long jet (of similar length to that seen in laser probing) soft x-ray imaging shows that the jet cools such that the emission drops below the threshold of the camera within $\sim 1mm$ of the conical shock.

An estimate of the cooling length can be calculated using the emitted power due to free-bound recombination P_{fb}. Although free bound emission is only one of the emission mechanisms present (others include line emission and Bremsstrahlung) a



(a) XUV (b) Soft x-ray

Figure 3.16: A jet leaving the conical shock in both XUV (un-filtered, $h\nu > 40eV$) and soft x-ray ($1.5\mu m$ CHO filter, $h\nu \sim 120 - 290eV$) emission, both on the same experiment at $292ns$.

good estimate of the total emitted power can be given as the free bound emission rate multiplied by a factor between 10 and 100 [44]. For the density of plasma in the jet tip as it leaves the conical shock ($\sim 5\times10^{18}cm^{-3}$, if the flow is moving at $75km/s$, the density dropping as it accelerates) the power emitted is 10^{11} to $10^{12}Wcm^{-3}$ [64]. The thermal energy in the jet is $\frac{3}{2}(Z+1)n_i k_b T = 240Jcm^{-3}$. Hence the time to radiate this energy is $\tau_{rad} = 4$ to $40ns$ (still depending which factor was used to account for other types of emission). Given the jet tip velocity of $270km/s$ the cooling rate indicates a cooling length for the flow to radiate the internal thermal energy

$$d_{cool} = \tau_{rad} v_{jet} \sim 0.5mm \tag{3.25}$$

Hence the jet will cool over a distance of order the jet radius (in agreement with Fig 3.16), however the actual cooling length will vary in time due to the dependence of the cooling rate on the flux of material leaving the conical shock.

Although the jet is relatively cold after a few cooling lengths a small thermal expansion occurs, which can be used to predict the temperature of the jet. Simulations and experimental data both suggest that in the body of the jet the axial velocity is less than the tip velocity of 270km/s. For simplicity we will use the expansion near the jet tip to calculate the temperature. The width of the jet has been measured on three subsequent schlieren images $200\mu m$ behind the jet tip. Figure 3.17 shows a plot of the expansion of the jet. From the graph the rate of expansion is found to be

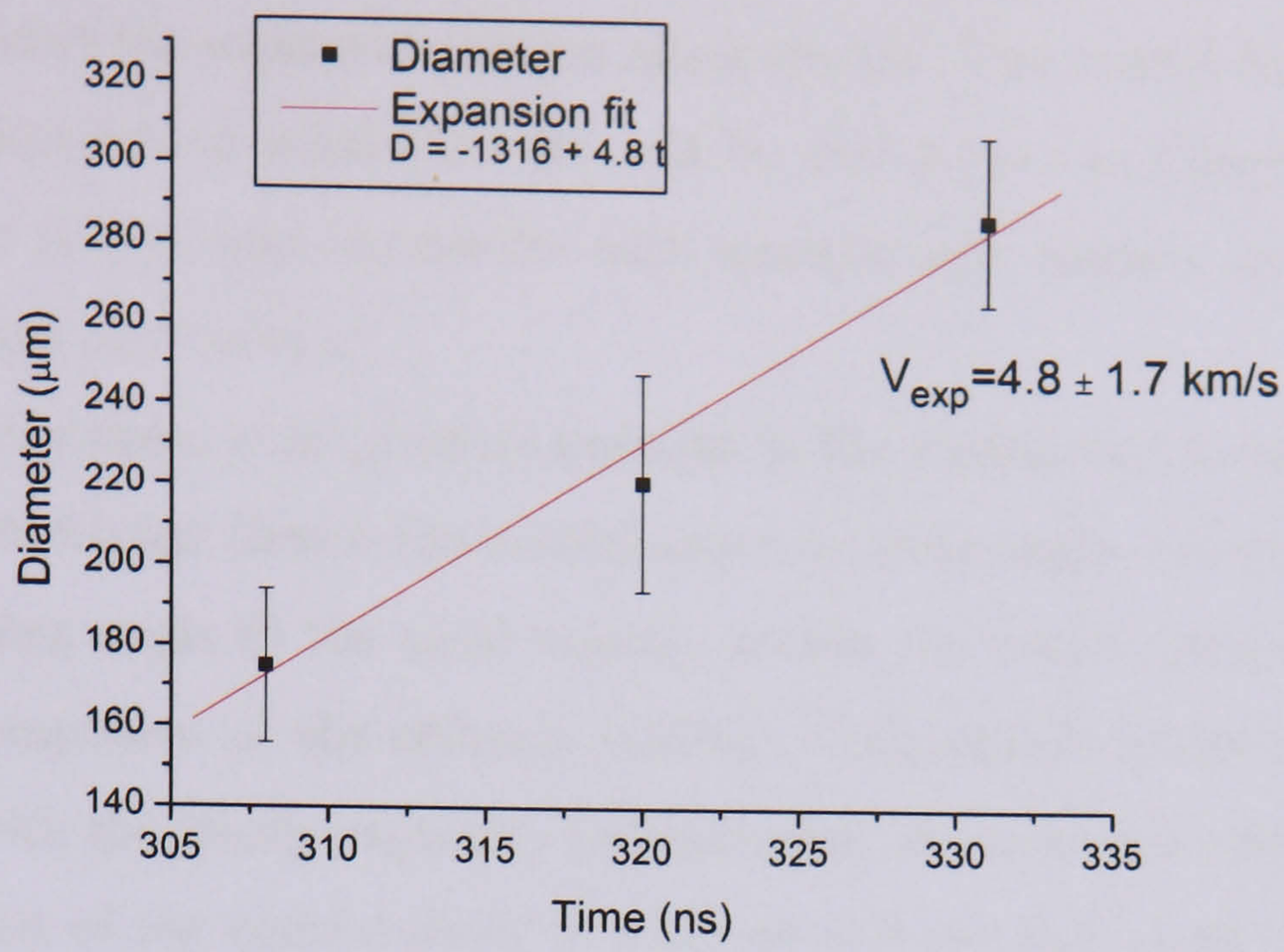


Figure 3.17: Radial expansion of a tungsten jet. Jet diameter measured from schlieren images at subsequent times $200\mu m$ behind the jet tip.

$4.8 \pm 1.7 km/s$ ($4.8 \times 10^5 cm/s$). Assuming that this expansion is at the sound speed and given that the jet velocity is $\sim 270 km/s$, this corresponds to a Mach number $\mathcal{M} = \frac{V_{jet}}{c_s} \sim 60$.

From the sound speed, given the atomic mass ($M_{At} = 184$ for tungsten) it is possible to determine the product of jet temperature and charge state

$$(Z+1)T(eV) = \left(\frac{c_s(m/s)}{10^4}\right)^2 M_{At} \sim 32eV \tag{3.26}$$

where we have used the isothermal sound speed as we do not have a good measure of the adiabatic index γ of the flow. We note that for a high rate radiative cooling γ is expected to be of order unity.

Assuming a charge state of $Z \sim 2$ (calculated using equation 3.24) this implies a jet temperature $T_e \sim 11eV$.

3.4.3 Velocity and mass distributions within the jet

In the previous sections we have determined various parameters of the precursor plasma flows ($\rho(z,r,t)$, v_{abl}), the conical shock (collapse time and size) and the jet (the launch time and velocity of the tip, however we have been unable to measure

the velocity in the body of the jet). We can now combine all of these observations together to predict the mass distribution along the jet. This model for the density and velocity distribution within the jet will be useful later in Chapters 5 and 6 where, in order to compare our results with astrophysical models, we will require estimates of these parameters.

Assuming that there is no pressure gradient in the conical shock and that radiative cooling is dominant (hence the conical shock opening angle α is much less than the array opening angle θ) the axial velocity within the conical shock will simply be the axial component of the ablation velocity. Comparison of the conical shock collapse time with the jet tip trajectory indicates that all acceleration of jet material occurs at the top of the conical shock in what we will call the 'acceleration region' (the first few cooling lengths of the jet as it leaves the conical shock, which we will assume to have negligible thickness). Once the material has left this acceleration region it is relatively cold (a few eV), so no significant pressure gradients are present to further accelerate the flow. Thus from the end of the acceleration region the jet material will travel ballistically. We can now test all of these interpretations using experimental data for the density distribution within the jet.

To measure the density distribution within the jet interferometry (Fig 3.18) has been used. As can be seen in Fig 3.18a (which is from the same experiment as was used to characterise the jet in Fig 3.14 and Fig 3.17) the large density and large density gradient at the centre of the jet cannot be properly resolved. In an attempt to gain better resolution a higher magnification interferometer has been used, however the field of view is then limited to only a small portion of the jet. Instead, for the remainder of this discussion a jet produced by a wire array that has a slight twist (a few degrees) around the array axis will be used (Fig 3.18b). This twist introduces a small azimuthal component to the flows that leave the wires which results in an increase in jet radius, enabling better measurements to be obtained with the interferometer. The effect of twist will be discussed more fully in Section 3.6. Whilst the twist may slightly affect some of the parameters discussed up to this point (e.g. tip velocity), many of these cannot be measured in a jet from a twisted array (e.g. jet expansion is then dominated by angular momentum rather than thermal

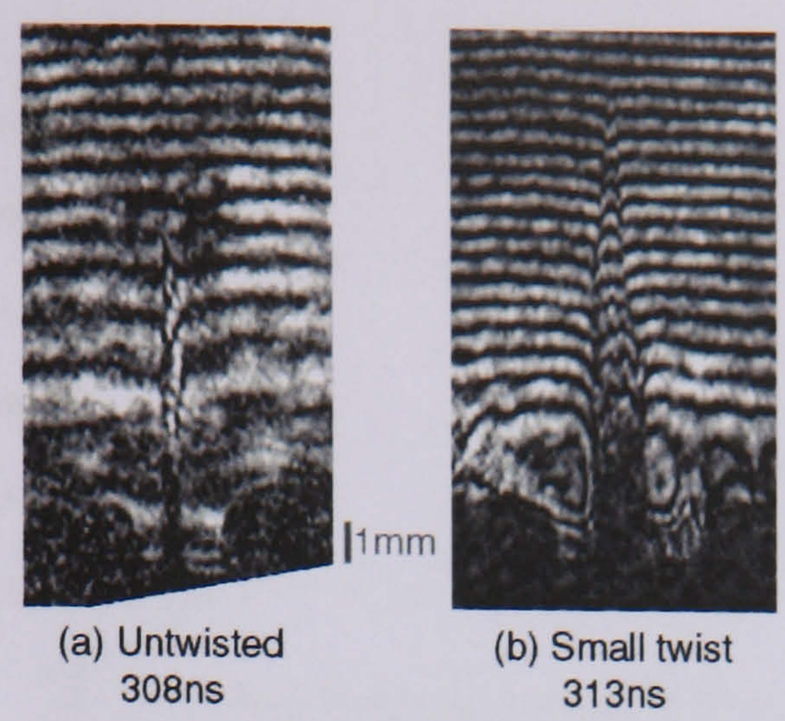


Figure 3.18: Interferometer images, showing that the fringes can not easily be resolved in a jet from an untwisted array (a), however when a twist is introduced the fringes are more easily resolved in jets from arrays with a few degrees of twist (b).

expansion, so it is not possible to determine an accurate tip temperature).

Figure 3.19 shows a plot of the electron density per unit length along the jet at $313ns$. This plot is obtained by integrating the line-integral of electron density ($\int n_e dl$) across the jet in the image. For this experiment the jet tip velocity is measured to be $220km/s$ (less than the earlier case, probably due to the twist in the array). The electron density decreases significantly from the top of the conical shock to the jet tip. This presumably results from the combination of the increase in the rate of mass ablation from the wires with time, a change in velocity of the outflow and a drop in ionisation state as the flow cools. From previous measurements we know that the ionisation state will drop along the jet from the conical shock ionisation state ($Z_{cs} \sim 12$) to the jet tip ionisation state ($Z_{tip} \sim 2$).

In an attempt to recreate the mass distribution analytically, initially we will over simplify the problem by making two assumptions. These assumptions are used partly to simplify the initial discussion but also to demonstrate that these are in fact important considerations. Later we will consider the result if we relax these assumptions.

Firstly we will assume that all of the material ablated from the wires contributes to the jet mass (ignoring whether the conical shock has collapsed). Each section of the wire will contribute to this flux, however the time for material from each section of the wire to reach the top of the conical shock will depend on the axial position.

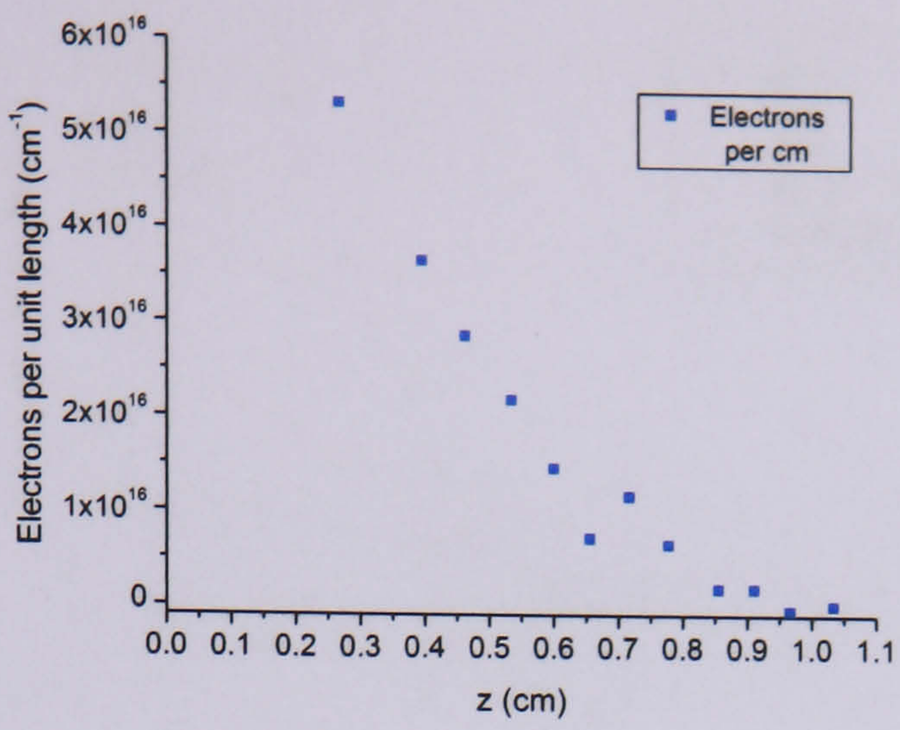


Figure 3.19: Plot of electrons per unit length within the jet, obtained by integrating the fringe shift in Fig 3.18b across the jet at $313ns$.

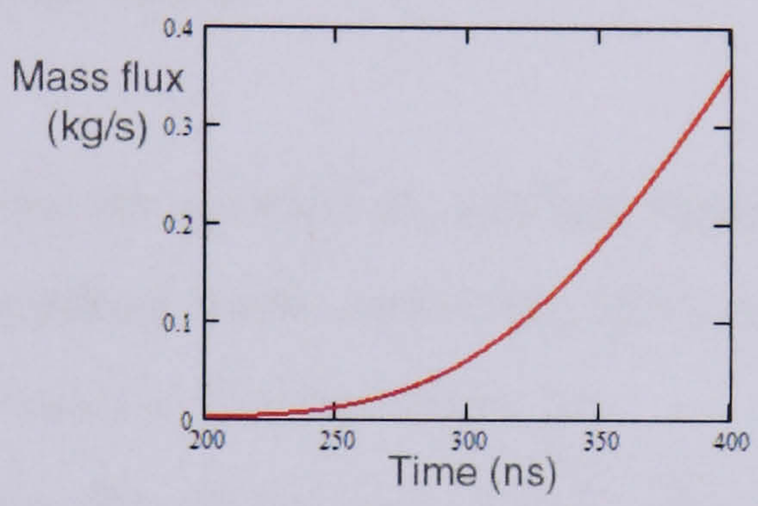


Figure 3.20: Mass flux through the top of the conical shock for a 25° array at $313ns$.

Taking into account this time of flight we can integrate the contributions from each section of the wire giving the flux reaching the top of the conical shock as a function of time. This flux out of the top of the conical shock is shown in Fig 3.20.

Our second assumption is that velocity of the material being injected into the jet (after the acceleration region) is constant in time. The obvious choice for the velocity of the material is the velocity of the jet tip ($V_j = 220km/s$) as any other choice of velocity would not be able to reproduce the correct tip velocity. Figure 3.21 shows plots of the electrons per unit length of the jet for this velocity. Plots have been included for various different charge states in the range $Z = 1-13$. There are two notable differences between the densities produced by this method and the experimental data; the predictions do not provide the correct gradients in mass per unit length and predict that jet material will be ahead of the jet tip.

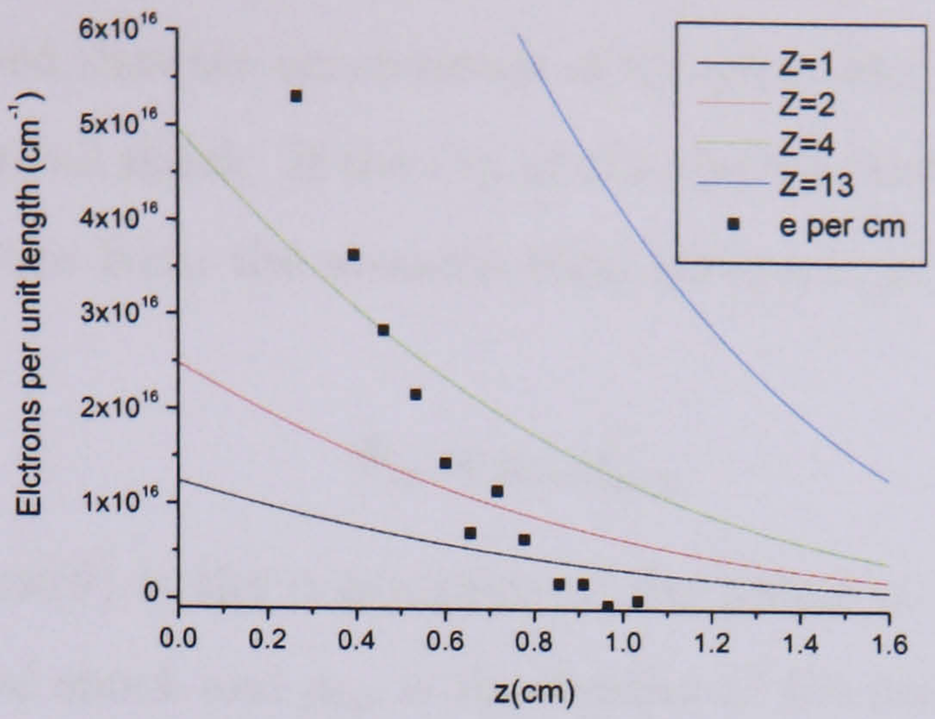


Figure 3.21: Predictions for the number of electrons per unit length for various values of charge state Z and assuming constant velocity and all material goes into jet. Also shown is the experimental measurements for the number of electrons per unit length within the jet at $313ns$.

The differences between the predictions and the experimental data are a direct consequence of the assumptions made concerning the use of all mass ablated from the wires and a constant velocity for the whole jet.

We have already made the connection between the collapse of the top of the conical shock and the trajectory of the jet tip (which were compared in Fig 3.15). If we are to correctly predict the jet tip velocity then we must exclude flows that are incident on an area of the conical shock that has not collapsed. As was seen in both Fig 3.12 and Fig 3.15, using the collapse time of the precursor in a cylindrical array to determine the critical density leads to a large range of possible times for the collapse of the conical shock.

To minimise the error in the critical density we can trace back on the earlier trajectory (Fig 3.15) to determine when the tip left the conical shock and then use the density incident at the top of the conical shock at this time (at a given radius). Thus only streams that have a density

$$\rho_{inc}(t)_z > \rho_{inc}(270ns)_{top of shock} \tag{3.27}$$

when they arrive at the conical shock will be used in the calculation. All others will not contribute to the narrow jet and will be ignored.

The other assumption made earlier was that the jet velocity is constant along the flow. It is believed that the acceleration of the jet is due to the pressure gradient at the top of the conical shock. If the top of the conical shock is in pressure balance with the ram pressure from the streams then the pressure P_{cs} within the conical shock will be

$$P_{cs} \propto \rho_{inc} v_{perp}^2 \tag{3.28}$$

where $v_{perp} = v_{abl}\cos(\theta)$ is the component of the ablation velocity that is perpendicular to the conical shock and ρ_{inc} is the density of the precursor streams incident on the edge of the conical shock. In terms of the mass per unit length incident on the array axis $\left(\frac{dm}{dt} = 2\pi r_{cs}\rho v\right)$ this becomes

$$P_{cs} \propto \frac{\frac{dm}{dt}}{2\pi r_{cs}} v_{perp} \tag{3.29}$$

where r_{cs} is the radius of the conical shock. Thus for a constant sized conical shock the pressure will be proportional to $\frac{dm}{dt}$.

There is only limited data on the size variation of the conical shock for conical arrays, however much more data is available for the precursor column in cylindrical wire arrays [20]. These measurements indicate that after formation the precursor expands at a rate of $\frac{d}{dt}r_{cs} \sim 1.25\mu m/ns$. Using this expansion rate and the measured size of the conical shock as well as the rocket model to find $\frac{dm}{dt}$ we find that the pressure in the conical shock is approximately constant in time, and possibly dropping almost linearly by 10% over $60ns$ after formation.

Assuming that the pressure in the jet is negligible due to the low temperature in the jet then the force that accelerates the material at the top of the conical shock is almost constant in time, and possibly decreasing slightly. The flux of material that this force is accelerating is however increasing approximately linearly with time. Thus the change in velocity, which we can take to be proportional to the pressure in the shock, will linearly decrease in time at a rate $\frac{d}{dt}v_j = -1.8 \times 10^{12} m/s^2$. This change in ejection velocity with time agrees with MHD simulations [25].

The earlier assumption that the jet had a constant velocity was equivalent to saying that the pressure at the top of the conical shock was proportional to the flux

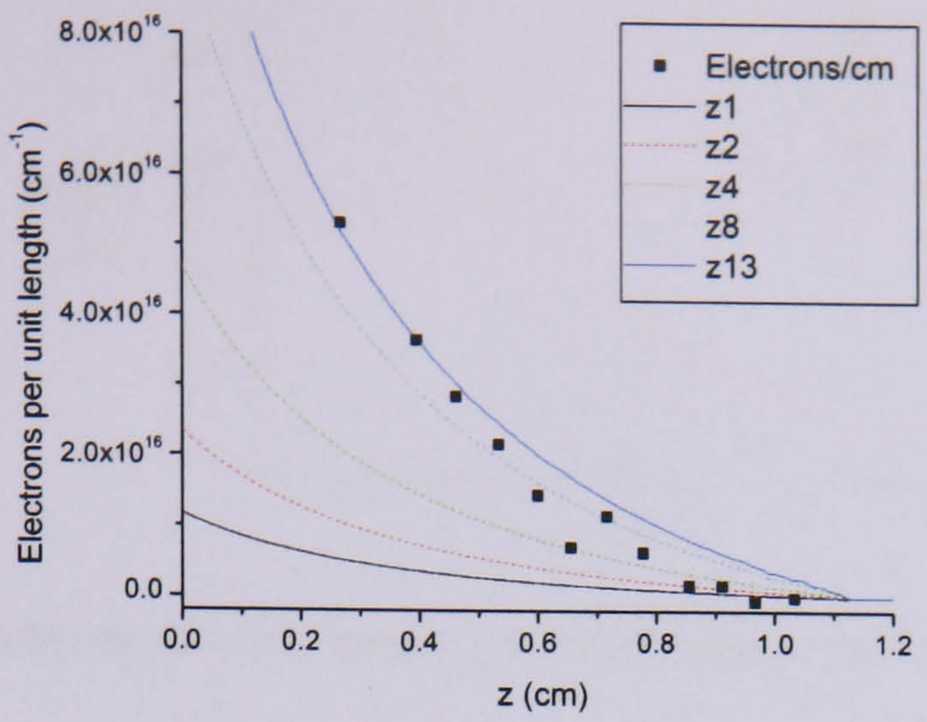


Figure 3.22: Predictions for number of electrons per unit length for various values of charge state Z and assuming decreasing velocity and only material incident on a collapsed conical shock is part of the jet. Also shown is the experimental measurements for electrons per unit length within the jet.

being accelerated, which would have been the case if the size of the conical shock had been constant.

If we now incorporate the collapse of the conical shock and the variation in jet velocity with time into our calculation we find the distribution of electrons shown in Fig 3.22. As would be expected near the conical shock a charge state $Z_{cs} \approx 12$ fits the data whilst closer to the tip a charge state $Z_{tip} \approx 2$ provides a better fit.

We can now look at how the density distribution will evolve over time. Figure 3.23 shows the mass distribution at various times using this method. It can be seen that, due to the stretching effect produced by the differential velocity the density profile becomes slightly flatter as it propagates.

We have seen that excluding the precursor plasma flows that do not collide with a collapsed conical shock provides a good fit to the number of electrons per unit length in the collimated jet. Clearly this material is still somewhere in the system, and is in fact forming a low density halo surrounding the jet.

Low density plasma halo around the jet

In addition to the tightly formed jet that has been discussed up to this point, which is produced by the collapsed conical shock, there is also material flowing above the

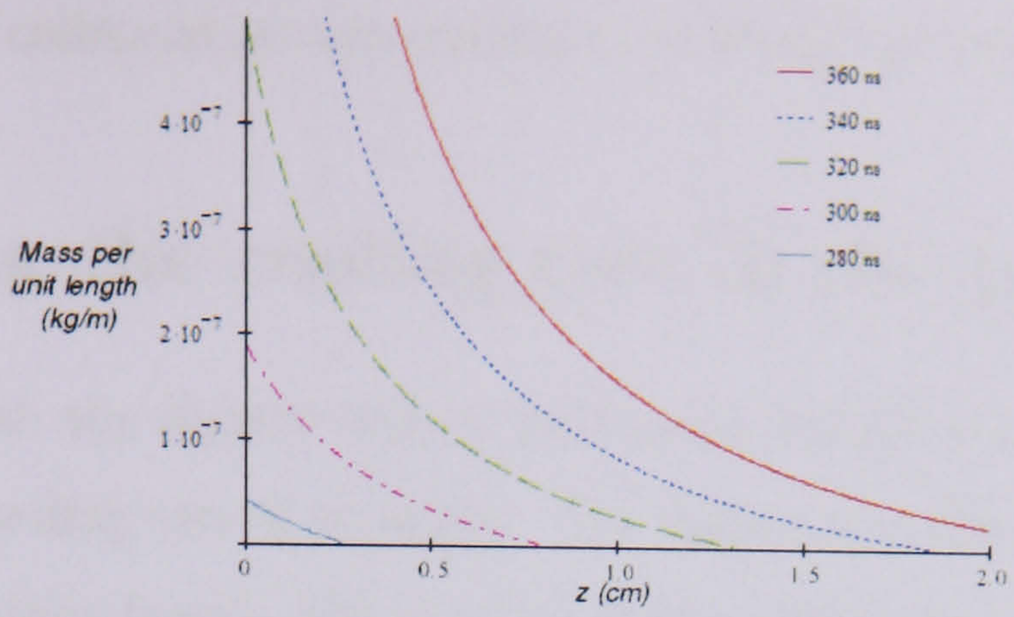


Figure 3.23: Predictions for the mass per unit length in the jet for various times.

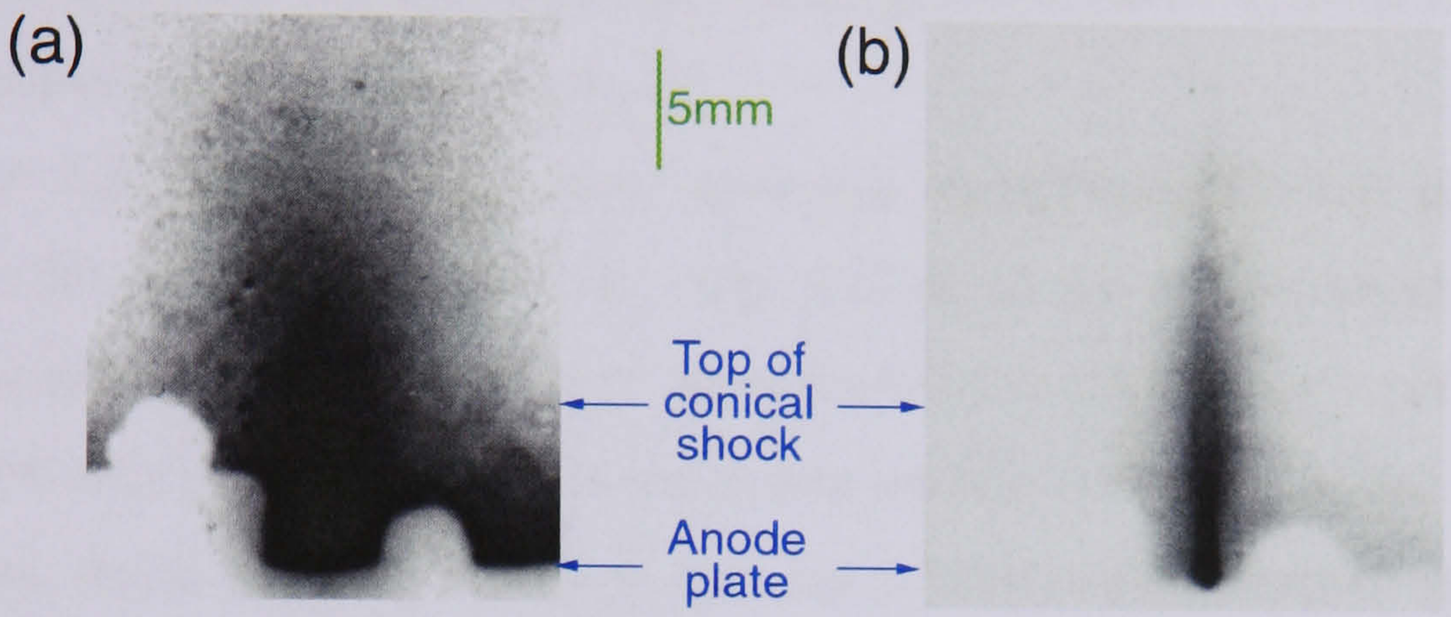


Figure 3.24: XUV ($h\nu > 30eV$) emission from the jet region at a time similar to when the top of the conical shock collapses ((a) at $280ns$) and later when the jet has fully formed ((b) at $310ns$).

anode plate which comes from the broad low density conical shock that is formed prior to collapse of the conical shock. The broad conical shock is formed by flows that are collisional ($\lambda < R_{array}$), however it has not collapsed as the collisions are not sufficiently frequent to cause fast electron-ion equilibration (analogous to the broad precursor that forms in cylindrical wire arrays prior to collapse). Due to the low density of this 'halo' plasma it is more easily imaged in XUV emission than by interferometry. Figure 3.24a shows XUV emission from the jet at $280ns$ after start of current. This is before the top of the conical shock in this shot has even collapsed.

The large diameter ($\sim 10r_j$) of the plasma halo results in a very low density ($\leq \frac{\rho_j}{100}$). The halo plasma is expected to have a high ion temperature as the density is too low to allow rapid electron-ion equilibration. The velocity of this flow is likely to be comparable to the tip velocity of the collapsed jet, as no bow-shock is seen

from the later time collapsed jet attempting to overtake the early-time broader jet.

3.5 Varying the cooling rate in the jet

As already discussed, the tightly formed jet from a tungsten array is the result of the high radiative cooling rate of tungsten. The radiative cooling rate of a jet is best described by the cooling length (the product of the cooling time and the velocity of the jet). To vary the cooling length of the jet the array material can be changed; for the typical temperatures and densities of the jet the radiative cooling rate increases with increasing atomic number [56, 64].

Figure 3.25 shows jets from three materials - aluminium (Z=13), stainless steel (iron, Z=26) and tungsten (Z=74). The process in the conical shock for each of these materials will be similar, with the exceptions of the size and opening angle of the conical shock, which are both dependent on the cooling rate [24]. Thus, once the conical shock has fully collapsed the rate at which mass reaches the top of the conical shock will be similar.

The different cooling lengths of each jet can be seen in the soft x-ray emission images (top row) - Al emits in this energy range ($h\nu > 120eV$) for most of the jet length, however tungsten cools below the threshold of the filter within approximately a jet radius of leaving the conical shock. A significant difference is also seen in the morphology of each jet - the W jet is a well defined column of plasma, whereas the Al jet is more disrupted. The most significant effects of cooling can be seen on the diameter of the conical shock and jet and the collimation of the jet - thermal expansion is greater for Al, so the opening angle of the jet is larger ($\sim 12°$) compared to the W jet ($\leq 2°$).

3.6 Producing jets with angular momentum using twisted wire arrays

In a conical wire array it is possible to introduce an angular momentum and an axial magnetic field (B_z) into the system by imposing a twist on the wire array (Fig 3.26).

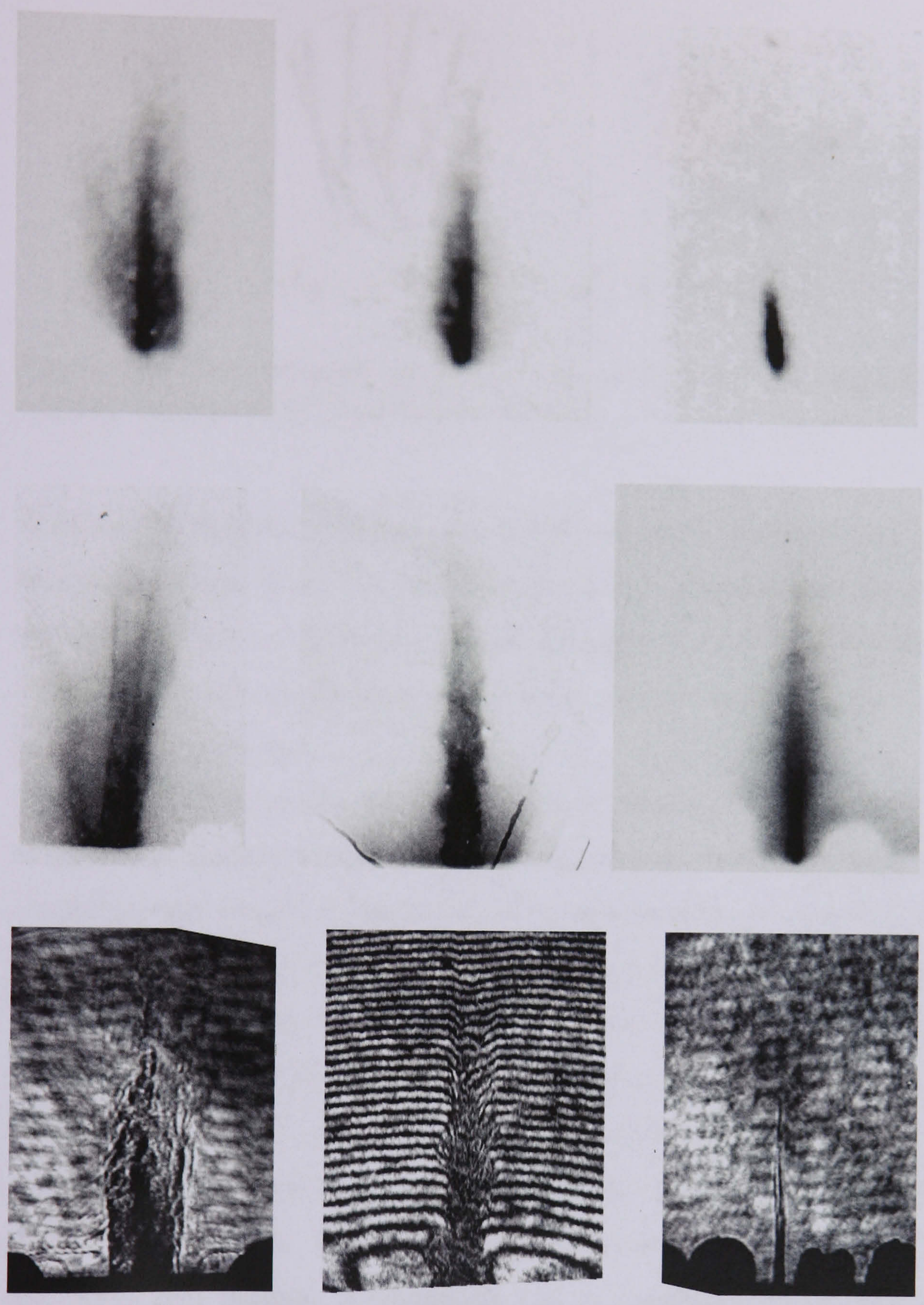


Figure 3.25: Soft x-ray emission (top), XUV emission (middle) and schlieren/interferometer images (bottom) of jets from arrays of different materials: Aluminium (left), Stainless steel (centre) and Tungsten (right). All images are taken at times $t \sim 300 - 320ns$ after the start of current.

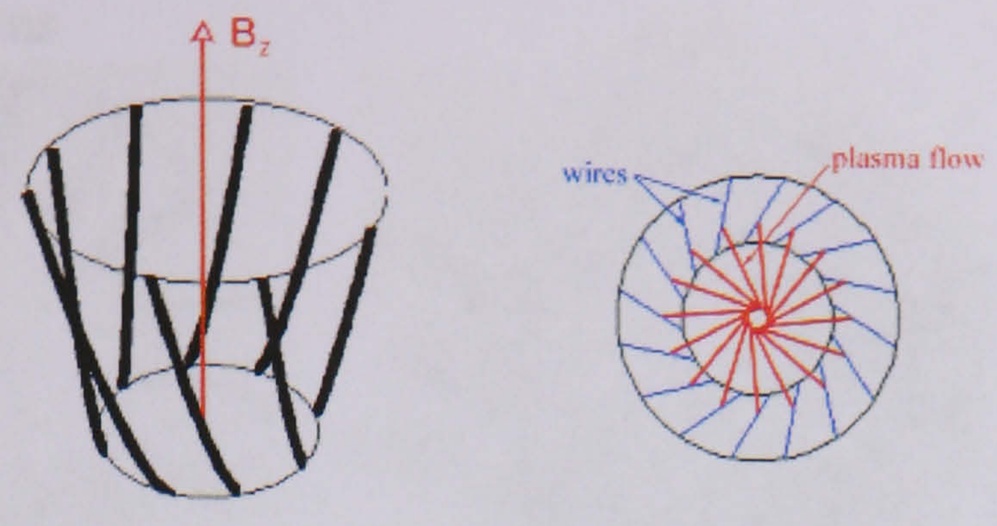


Figure 3.26: Twisted array setup that leads to both an axial magnetic field and an angular momentum in the precursor streams.

With such a 'twisted array' the azimuthal component of the current (J_θ) generates an axial magnetic field. This axial component of magnetic field combines with the radial component of the current (which is present in all conical wire arrays), to give an azimuthal force on the corona as it leaves each wire ($F_\theta = J_r \times B_z$) leading to an azimuthal velocity v_θ.

Figure 3.27 shows end-on XUV images of two conical wire arrays - one without a twist and the other where the anode (upper electrode) has been rotated by $\frac{\pi}{8}$ clockwise with respect to the cathode (lower electrode). It should be noted that in the end-on image of the twisted array the streams for all positions along the wire are integrated, however they are not above each other, hence there is a false impression that the streams are less collimated than in the un-twisted case. The end-on image of the twisted array shows that the conical shock is hollow, whereas in the untwisted case the conical shock is not hollow. There are two possible explanations for this hollow conical shock. Firstly the axial magnetic field may resist compression by the convergent plasma. Alternatively the v_θ component of the precursor streams will cause the flows to 'miss' the axis and impart angular momentum on the conical shock.

Cylindrical wire arrays can help to determine which of these scenarios is occurring. Figure 3.28 shows normal and twisted cylindrical arrays. Here a well defined precursor of similar sizes that is not hollow is present on both images, even with the twisted cylindrical array having twice the twist angle of the previous conical array.

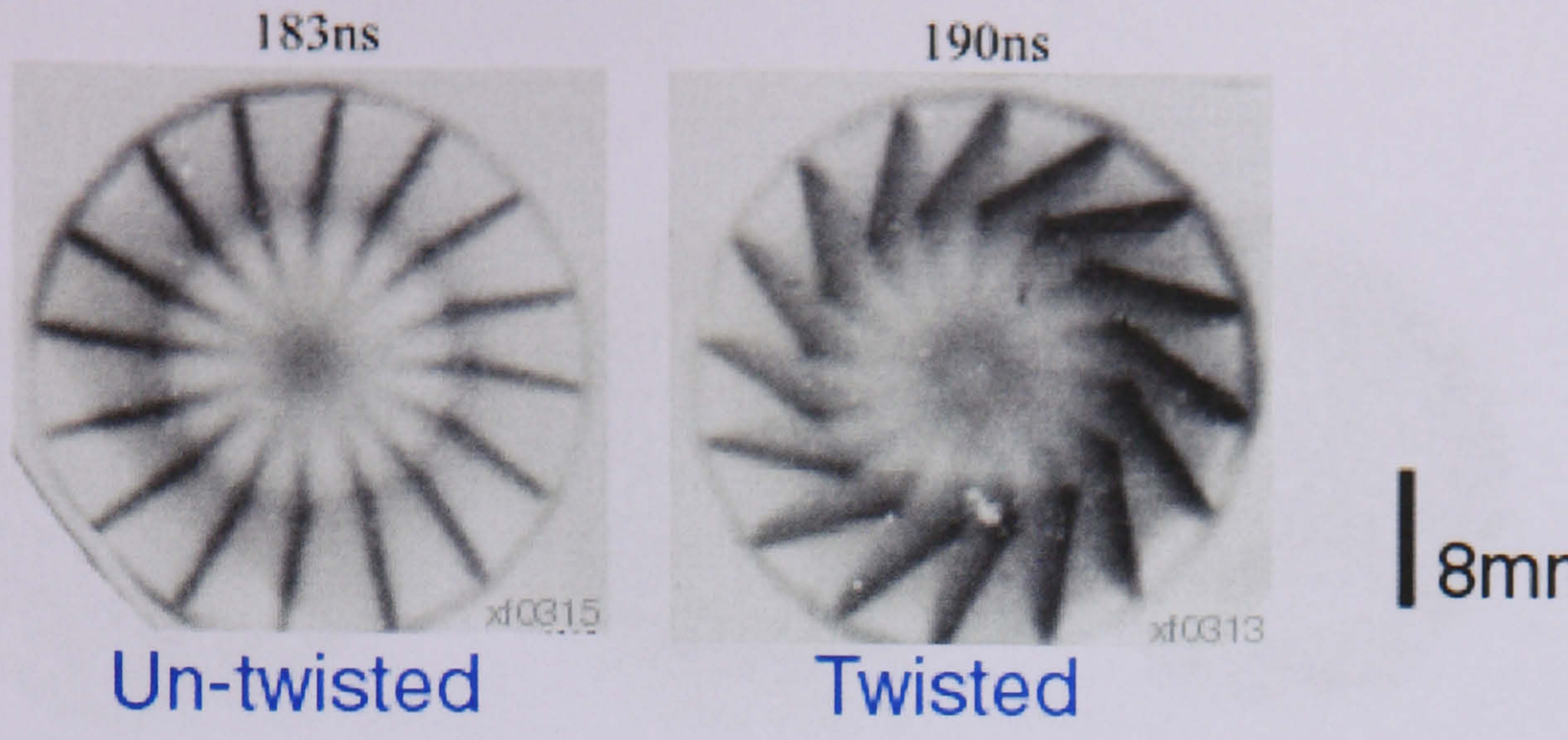


Figure 3.27: End-on XUV emission from conical arrays without and with twist.

For the twisted cylindrical setup there is an azimuthal component to the current, however no radial component. Hence for a given twist angle the cylindrical array will have axial magnetic field of comparable or larger magnitude than the conical array, however there will be no angular momentum in the twisted cylindrical array ($F_\theta \propto J_r$, but $J_r = 0$). As the precursor column in this setup is not hollow, it can be concluded that the hollow conical shock in Fig 3.27 is due to the angular momentum in the streams rather than the attempted compression of a magnetic field.

The angular momentum in the conical shock is transferred into the jet that is produced. In shadowgraphy images of a jet from a twisted conical array (Fig 3.29) it is clear that the jet is diverging. The image also displays significantly more internal structure in the jet than was seen in untwisted tungsten jets. Laser interferometry indicates that the jet is relatively hollow, which is consistent with an expansion due to rotation. Thus angular momentum is seen to have a significant detrimental affect on jet collimation.

3.7 Conclusions

We have explored conical wire arrays as a means to produce jets in the laboratory and investigate the physics of wire array z-pinches. Concerning wire arrays, we have seen that modulations are seen in conical arrays similar to those already discovered in other array configurations where a global magnetic field is present. It appears

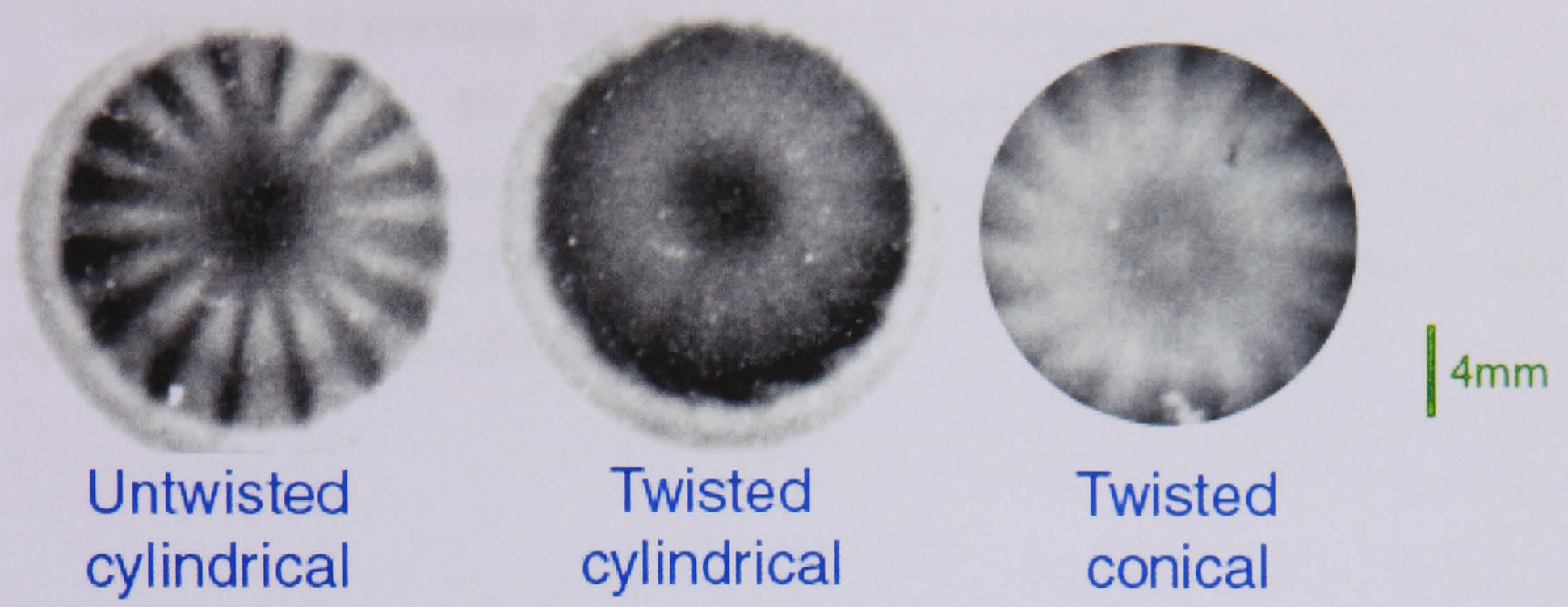


Figure 3.28: Comparison of end-on XUV emission from cylindrical arrays without and with a twist and (on the same scale) the centre of a twisted conical array. The precursor column in both images of cylindrical arrays are not hollow, however the centre of the conical array is hollow.

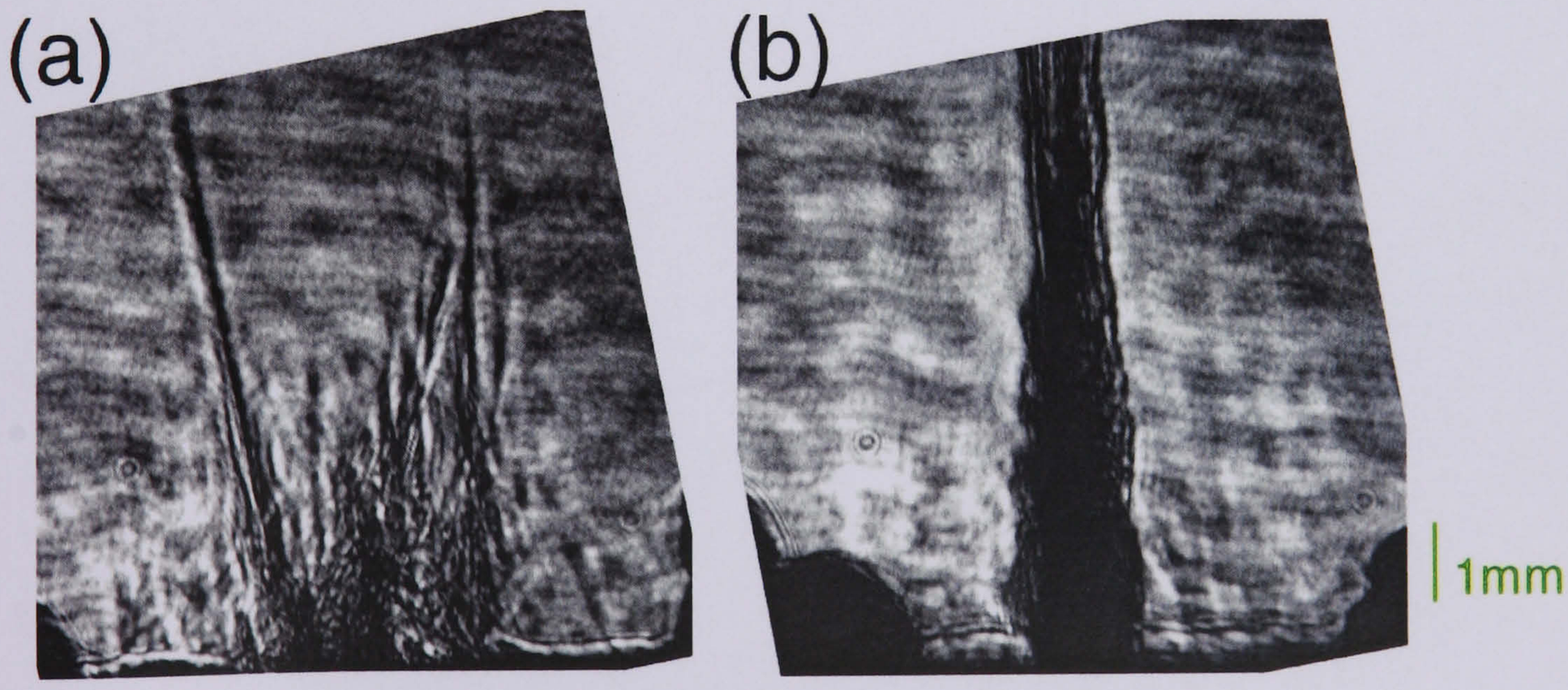


Figure 3.29: Jets produced by (a) twisted and (b) untwisted conical W arrays, both taken at $\sim 330ns$.

that the modulations are unaffected by the change in field strength and wire spacing along the wires of a conical array.

Redirection of precursor plasma streams in a conical shock has been used to produce a plasma jet. We have found that these jets are radiatively cooled, and seen that varying the rate of radiative cooling has an affect on the collimation and morphology of the jet. The introduction of angular momentum into the jet also significantly effects the collimation.

Chapter 4

Comparison of laboratory and astrophysical jets

In the previous chapter a technique for producing radiatively cooled high Mach number jets in the laboratory was demonstrated and a number of parameters of these jets were determined. With the exception of using a jet formation mechanism that is similar to one proposed for astrophysical jets no real link has yet been made to astrophysics. We will now explore what potential connections can be made between astrophysical jets and these laboratory experiments, either using the previously discussed setup or by modifying this setup.

Collimated jets are produced by astrophysical bodies on many different scales; there is evidence for outflows associated with Planetary nebulae (PN, see [65, 66]), young stellar objects (YSOs or protostars, which will be discussed in more detail later in this chapter) and active galactic nuclei (AGN, see [67]).

As well as the large variation in the spatial scales between these different types of astrophysical jet, the physical parameters and characteristics of these jets are also very different, for example AGN jets are highly relativistic, well collimated flows, whilst PN jets are non-relativistic very poorly collimated flows. The level of understanding of these different types of jet also varies significantly - very little is known about AGN jets (for example whether they consist of a positron-electron or atomic plasma [67]), whereas most parameters of stellar jets are reasonably well known, although they do vary significantly between individual jets. There remain

many unresolved questions concerning formation and propagation of all these types of jet.

4.1 Laboratory astrophysics and the scaling of jets

Given the variety of astrophysical phenomena currently known, it is very useful to be able to both perform simulations and experiments that are relevant to the astrophysical systems. Clearly to perform controlled experiments it is necessary to reduce both the temporal and spatial scales by many orders of magnitude without affecting the important underlying physics (and hence not altering the evolution of the scaled systems). This is possible provided that certain scaling criteria regarding the fundamental physics of the systems are met. The choice of scaling criteria will depend on both the physical mechanisms that determine the evolution of the system and the structure of the system. It is equally important that the initial conditions of the two systems are also equivalent.

Ryutov et al. [2, 3] discuss the similarity conditions required to consistently model the astrophysical object for the case of an arbitrary astrophysical situation that follows the equations of hydrodynamics and ideal MHD.

Hydrodynamic scaling

There are a number of requirements before a system can be considered as purely hydrodynamic. If the system is evolving then these condition should be fulfilled for the entire period of the evolution and region of interest.

Firstly a fluid description of the plasma should be valid, hence the mean free path for the collision of ions should be less than the characteristic scale of the system.

Dissipative processes should be negligible, that is, the Peclet number (Pe, ratio of heat convection to conduction) must be large. Similarly, viscous effects should be negligible, hence the Reynolds number (Re, ratio of inertial force to viscous force) should be large.

The characteristic size of hydrodynamic instabilities also places a restriction on the spatial scale of the system [2]. Small scale structure will be dissipated if the

spatial scale of the problem (h), the characteristic length scale of hydrodynamic instabilities λ, Reynolds and Peclet numbers do not satisfy

$$\frac{\lambda}{2\pi h} < Re^{-1/2} \tag{4.1}$$

$$\frac{\lambda}{2\pi h} < Pe^{-1/2} \tag{4.2}$$

For every system a sufficiently small length scale exist where the hydrodynamic description will breakdown (e.g. on length scales smaller than the mean free path). It is not necessary that this length can be scaled between the two systems, however it will set a lower limit on the scale that the similarity can be applied.

Assuming that the system can be properly described by the equations of hydrodynamics it is possible to perform a transformation such that the Euler equations [61, 62] are invariant. This 'Euler Similarity' [2] requires the scaling of position $\mathbf{r}$, density ρ, pressure p, time t, and velocity $\mathbf{v}$ between a system labelled 0 and another labelled 1 to be described by

$$\mathbf{r_0} = a\mathbf{r_1};\ \rho_0 = b\rho_1;\ p_0 = cp_1;\ t_0 = a\sqrt{\frac{b}{c}}t_1;\ \mathbf{v_0} = \sqrt{\frac{c}{b}}\mathbf{v_1} \tag{4.3}$$

where a, b and c are dimensionless scaling factors.

For a system of characteristic length scale h the scaled initial conditions are found by considering the variable as the product of a dimensionless function $\mathbf{F}$ of the scaled position ($\frac{\mathbf{r}}{h}$) and the scaling factor of the variable (say $\tilde{\mathbf{v}}$). For example the initial velocity is given by

$$\mathbf{v_{t=0}} = \tilde{\mathbf{v}}\mathbf{F}\left(\frac{\mathbf{r}}{h}\right) \tag{4.4}$$

and similarly for pressure and density. Provided the dimensionless functions that scale the velocity, pressure and density are equivalent, two systems will evolve similarly if they have the same Euler number, where the Euler number is determined by substituting for b and c into the velocity in equation 4.3, or

$$Eu = \tilde{v}\sqrt{\frac{\tilde{\rho}}{\tilde{p}}} \tag{4.5}$$

Ryutov et al. [2] note that this Euler number is of the form of a Mach number, and show that if a system is strongly driven (i.e. supersonic) and the characteristic

velocity is chosen as the velocity of a flow then the Mach number ($\mathcal{M} = \frac{v}{c_s}$) and Euler number are equivalent.

The characteristic timescales (τ) of two systems can be linked by

$$\tau_1 = \tau_0 \frac{h_1}{h_0} \sqrt{\frac{\tilde{p_0}/\tilde{\rho_0}}{\tilde{p_1}/\tilde{\rho_1}}} \tag{4.6}$$

or for a strongly driven system, a simpler expressions is to define a characteristic time

$$\tau \sim \frac{h}{c_s} \tag{4.7}$$

The above discussion assumes both systems can be described by pure hydrodynamic. If radiation transport has an effect in the astrophysical system, it is then necessary to scale the equations of radiation-hydrodynamics [68]. For a system that is optically thin, the effects of radiation can be handled by a radiation loss term, which can be characterised by a parameter such as the ratio of the cooling time (a characteristic time for energy less) to the timescale for hydrodynamic evolution [69]. Such a treatment is only valid if the exact nature of the cooling function does not effect the dynamics of the system (e.g. it is not valid for the modelling of cooling instabilities in shocks).

Whilst ideally a system is only considered hydrodynamic if no magnetic field is present, in reality the hydrodynamic equations are still valid if a small magnetic field is present provided that it does not have a dynamic affect. If this is not the case then the equations of MHD are required to fully describe the system.

MHD scaling

The jets produced in the experiments described in this thesis do not have a magnetic field, however for completeness the requirements for scaling for MHD systems are included here. If a dynamically significant magnetic field is present (i.e. $\beta = \frac{(Z+1)nkT}{B^2/2\mu_0}$ is small) [3], there is an additional condition to the Euler Similarities given in equation 4.3 above, namely on the magnetic field $\mathbf{B}$, which transforms with the square root of the scaling factor c. The initial conditions can be handled in a similar way to those in the hydrodynamic case.

In addition to the previously described limits due to hydrodynamic dissipation and viscosity, for the MHD case the scaling is only valid for systems with negligible ohmic dissipation and therefore a large magnetic Reynolds number (ratio of velocity to magnetic diffusion)

$$Re_M = \frac{vL}{D_M} \tag{4.8}$$

where v is a characteristic velocity, L is a characteristic spatial scale and D_M is the magnetic diffusivity.

The areas of the system where magnetic effects are important (measured by the value of the plasma β) must be similar between the two systems.

Jet characterisation

To perform laboratory experiments that are useful in understanding dynamic astrophysical systems that can be described by hydrodynamics or MHD it is necessary to meet the above scaling criteria. It is equally important that all dimensionless parameters that describe the behaviour of the specific type of object are similar between the two systems. For an adiabatic supersonic flow two such parameters are the Mach number $\mathcal{M}$ and the ratio between the jet density and the ambient density, the density contrast η. That is, independent of the scale, two adiabatic supersonic hydrodynamic flows will behave in the same manner if they have the same Mach number and density contrast.

Observations have indicated that radiative cooling has an important effect on the behaviour of certain astrophysical jets. Blondin et al. [69] simulate radiatively cooled jets and determine a third dimensionless parameter to describe the behaviour of radiative cooled jets. The cooling of the jet can be characterised by a cooling parameter χ, which is defined as the ratio of cooling distance d_{cool} to the jet radius r_j. This cooling distance is defined as the distance behind a radiative shock to a point with an arbitrarily defined lower temperature. An equally valid definition of the cooling length is the product of the characteristic speed and cooling time (the time for the jet to radiate a certain fraction of its internal energy).

Thus (as described by [69] and [24]) the behaviour of radiatively cooled jets is

governed by three dimensionless parameters, that is the

$$\text{Mach number } \mathcal{M} = \frac{v_j}{c_s} \tag{4.9}$$

$$\text{Density contrast } \eta = \frac{\rho_j}{\rho_a} \tag{4.10}$$

$$\text{Cooling parameter } \chi = \frac{d_{cool}}{r_j} \tag{4.11}$$

along with the earlier stipulations on the mean free path and Peclet and Reynolds numbers.

The characteristic spatial scale of a jet is conveniently defined as the radius of the jet (r_j). Hence an arbitrary length within each system can be defined as the number of jet radii (for example the cooling length may be a few jet radii). Similarly a temporal scale of the system can usefully be defined as the time for a shock to cross the jet ($\tau \sim \frac{2r_j}{c_s}$).

If magnetically driven jets (assuming they follow an MHD behaviour) are to be scaled then the requirements described above for MHD scaling must be employed. In particular, a key characteristic of some models of jet production is the variation in β between different regions of the plasma, which must then be properly reproduced in the scaled experiments.

4.2 A brief overview of jets from protostars

Next we will look at some observational evidence for protostellar jets. This is not intended as a complete review of protostellar jets, but more as an overview of the important parameters and characteristics that are of interest to modelling these jets in the laboratory.

In 1950s George Herbig and Guillermo Haro observed 'compact nebulae with peculiar spectra near dark clouds' [57]. Subsequent authors have realised that these so-called Herbig-Haro (HH) objects are in fact strong shocks within a highly collimated jet. Often two such flows propagate in opposite directions from a single star, which has led to the conclusion that these are in fact bipolar jets produced by a star situated between the two jets.

As well as discrete HH emission regions along the flow, occasionally these jets can be photo-ionised by local stars, leading to optical emission along the complete beam [57]. To date over 300 HH objects have been observed [70].

Estimates of the parameters of these stellar jets based on observations and simulations vary by orders of magnitude between different jets. Generally lengths are of the order of $0.01 - 1pc \sim 3 \times 10^{14-16}m$, velocities of hundreds of km/s and densities of $10^{2-3}cm^{-3}$. Collimation of these jets is normally very good with length to width ratios of order 100:1 or sometimes higher. Simulations indicate that jet collimation is significantly enhanced by radiative cooling. The cooling length of the jets are typically $5 \times 10^{12}m$, which results in a dimensionless cooling parameter $\chi \sim 1$. Typically jets have temperatures $T \sim 10^4 K (\sim 1eV)$, which implies they have a Mach number $\mathcal{M} \sim 10 - 100$.

There are various observations that suggest that there is likely to be some magnetic field within these jets [58]. Zeeman splitting of emission from the jet has indicated that this field may reach a few kG near the source. Far from the source star it is thought that this magnetic field does not have an effect on the global dynamics, although in some regions (notably shocks) the magnetic field can affect the observational properties [10].

Observations of the formation region of protostellar jets are difficult due to the luminosity of the source star, because the star is embedded in a molecular cloud, or because the formation region is too small to resolve. Various models have been developed in an attempt to explain the formation of these jets. Some proposed mechanisms (such as the model by Canto et al. [55], described in section 3.3) are purely hydrodynamic, however it is now commonly accepted that magnetic fields play an important role. A notable example is a model where a 'magnetic tower' structure is formed [71]. In such a model differential rotation in the accretion disk twists poloidal magnetic field lines producing a toroidal component of the field, which then accelerates and collimates the plasma [71].

Whatever the actual mechanism for jet production, it is known that this is a vital part of star formation. Accretion disks around stars have considerable angular momentum which must be dissipated in order for the star to accrete mass. Jets

are an obvious recipient of this angular momentum. Observational techniques are now reaching the stage where different doppler shifts can be resolved on different sides of the star axis. Some interpretations of this data indicate rotation of the jet [58]. If these interpretations are correct then the observations indicate that both constituent jets of a bipolar system have the same rotation, which is consistent with the angular momentum being introduced at the ejection stage.

This link between jets and the star formation process shows the importance of studying the jets in order to fully understand the process by which stars are formed.

4.3 Laboratory modelling of protostellar jets

4.3.1 Laboratory techniques for jet production

Various techniques have been developed to produce supersonic jets in the laboratory. Early experiments produced adiabatic jets, as described by Norman et al. [72] and references therein. Recently, however, advances in high energy density physics (HEDP) facilities have expanded the regimes that can be reached in the laboratory, and hence the astrophysical phenomena that can be modelled in the laboratory. This includes the possibility to produce radiatively cooled jets in the laboratory.

The first laboratory experiments to study radiatively cooled jets were those on the Nova laser by Farley et al. [6] and on GEKKO-XII by Shigemori et al. [5]. The experimental setup for both these experiments is similar, and is shown in Fig 4.1a (reproduced from [6]). These experiments use the mechanism proposed by Canto et al. [55] of convergent conical flows (as was described in section 3.3), to form a supersonic jet. Conical targets are irradiated for 100ps by five beams of the Nova laser (351nm) or six beams of the GEKKO-XII laser (530nm) respectively. After ablation from the target surface, plasma stagnates collisionally on axis.

As these laser driven jets radiate they cool and the density of the jet increases, thus the collimation is improved. Radiative cooling rates are a direct consequence of the ionisation state and therefore material. Various target materials are used in the Shigemori experiments, including CH, Al, Fe and Au. Figure 4.1b is taken from [5] and shows that radiative cooling has a significant effect on the collimation of different

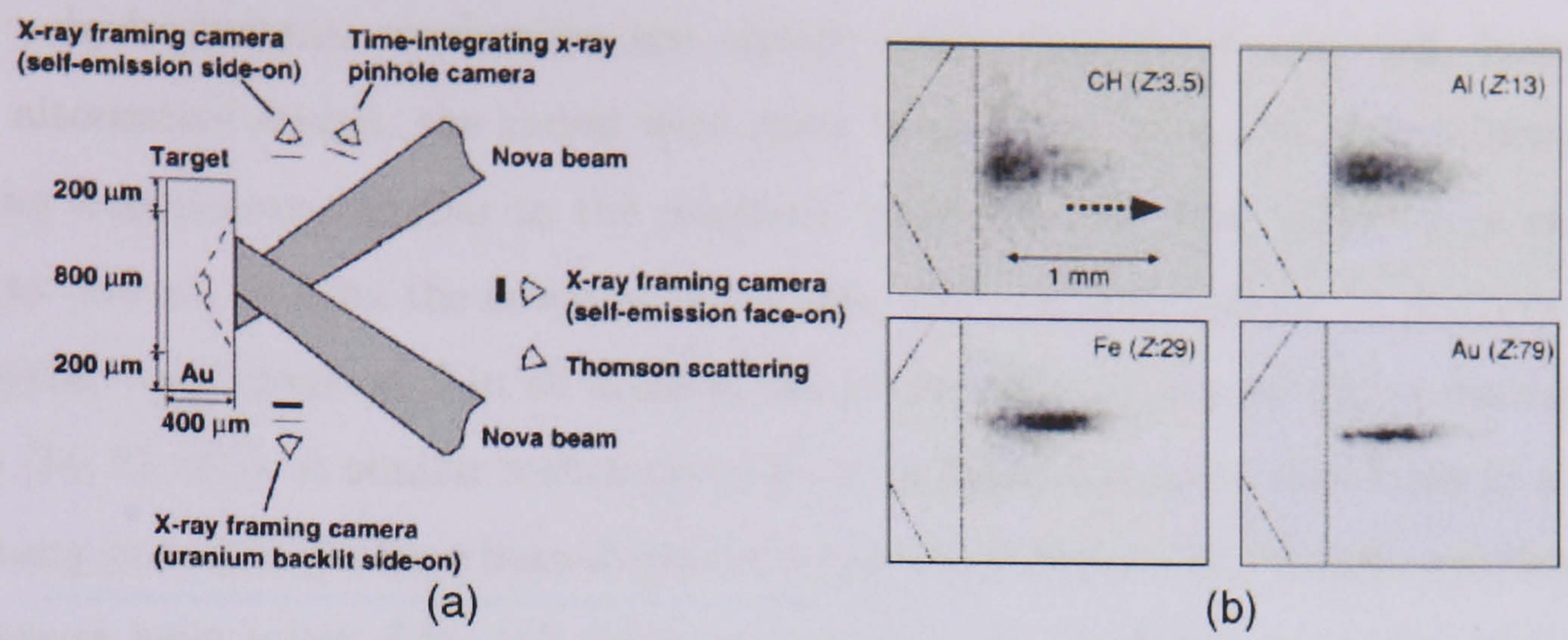


Figure 4.1: (a) Experimental layout for laser produced jets in Farley et al. [6] and (b) x-ray framing images (unknown energy range) of different materials 1.3ns after laser pulse, showing the effect of radiative cooling on jet collimation. from Shigemori et al. [5].

jets. The jets produced by conical gold targets have a velocity $6-8\times10^{7}cms^{-1}$ and density peaking at about $0.2g/cm^{3}$.

The main limitation to this kind of experiment is that it cannot produce a steady state jet. The relatively short pulse from the laser leads to the production of a single radiatively collapsing bullet, rather than either a continuous outflow or rapidly repeated bursts as are found in astrophysics (as discussed briefly by [5]). We can see this numerically by considering the sound transit time across the jet. For these experiments the sound speed is $c_s \sim 10^4 m/s$, so a shock will cross the jet radius ($r_j \sim 100\mu m$) in a time $t_{cross} \sim 10ns$. The total mass injection time into the jet will be of the same order as the laser pulse length, which is orders of magnitude less than this transit time ($t_{laser} \sim 100ps$).

Recently Foster et al. [73] have developed a new technique for producing jets that uses either direct laser drive or radiation drive from a wire array z-pinch to drive a shock in a Ti foil attached to a the end of a cylindrical hole in a CH holder. As the shock interacts with the walls of the holder a jet is produced. This jet production technique is highly suited to exploring the effects of small scale turbulence on the jet, particularly with the aim of benchmarking laboratory and astrophysical codes.

Wire array z-pinches can also produce jets using the array as a plasma source instead of a radiation source. The use of the conical wire array to produce a jet

by a hydrodynamic mechanism has already been extensively discussed, however an alternative design, the radial wire array is emerging as a tool to produce jets using a mechanism similar to the magnetic towers discussed by [71]. These radial array jets are outside the scope of this thesis, however they appear to produce the required conditions on β in all areas of the jet production process (for a discussion see [74, 23, 22]). A similar technique to these radial arrays using flux loops in a low density pre-filled gas have been discussed by Hsu and Bellan [75]. These experiments however have a low β for the entire experiment area implying any connections to YSO jets are limited.

Table 4.3.1 shows a range of parameters of the jets produced by protostars, by the laser driven experiments of Shigemori et al. [5] and by our conical wire array experiments. The first section of this table gives a number of general parameters of these flows, illustrating the vast difference in scales between the astrophysical and laboratory jets. The second section of this table demonstrates that a fluid description of both the YSO and z-pinch jets is valid [24]. We note that it is not a requirement that the localisation, Reynolds and Peclet numbers are matched between the two systems, only that they are at the correct limits to allow a fluid description ($\frac{\lambda_{mfp}}{r_j} \ll 1$, $Re \gg 1$, $Pe \gg 1$), however any discrepancies between these parameters will limit the smallest spatial scale on which the similarity is valid. It has been assumed that we are interested in a point far from the source star, such there are no dynamically significant magnetic fields and hence hydrodynamic scaling can be applied. The final section of the table compares the dimensionless parameters (scaling criteria) specific to radiatively cooled jets that must be equal for the similarity to hold.

As can be seen in the table the similarity criteria for jets from conical wire arrays are similar to those from YSOs. Unlike many of other techniques for jet production, conical wire arrays continue to produce jets in a quasi-steady manner (for many characteristic times). In addition they have the potential to impart axial magnetic fields and angular momentum on the flow.

The notable discrepancy in the similarity between conical array jets and those from protostars is the density contrast between the jet density and the ambient

Table 4.1: Parameters for astrophysical and laboratory jets. The first group shows some characteristic parameters of the different jets. The second group of parameters are those illustrating the applicability of a fluid description (reproduced from [24]) and the final group are parameters that characterise radiatively cooled jets (as defined in equations 4.9 - 4.11). The two values of the density contrast for conical wire arrays (marked *) correspond the the prevously discussed experiments ($\eta \gg 100$) and the experiments that will be discussed in the next two chapters ($\eta \sim 1$).

Parameter	YSO	Laser (Shigemori [5] Gold)	Conical wire array (W on MAGPIE)
General flow variables			
Length (cm)	3×10^{17}	0.1	2
Width (cm)	2×10^{16}	10^{-3}	0.1
Dynamical time Scale	10^3 years	100ps	100ns
Electron temperature (eV)	1	500	10
Jet tip velocity (km/s)	~ 100	~ 100	~ 200
Jet density, ρ (g/cm^3)	$\sim 10^{-22}$	$\sim 10^{-2}$	10^{-4}
Validity of fluid description			
Localisation parameter $\frac{\lambda_{mfp}}{r_j}$	$\ll 10^{-6}$		$\leq 10^{-4}$
Reynolds Number (Re)	$> 10^8$		$10^5 - 10^8$
Peclet number (Pe)	10^7		$2 - 2 \times 10^3$
Jet scaling			
Mach number, $\mathcal{M}$	> 10	10-50	> 20
Density Contrast, η	1-2	$\gg 100$	$\gg 100/\sim 1^*$
Cooling Parameter, χ	0.1-10	40/0.7	1

density. Although a halo is present around the jet in the experiments, this is of a negligible density ($\rho_{halo} < \frac{\rho_j}{100}$). Before exploring methods of introducing an ambient medium into the experiments we will first look at what effects occur when a jet propagates in an ambient medium, which would not have been observed in our jet experiments outlined in Chapter 3.

4.4 The effect of the ISM on protostellar jets

Since HH objects were first associated with shocks in collimated flows, the interaction of these jets with the surrounding interstellar medium has been of interest to the astrophysical community.

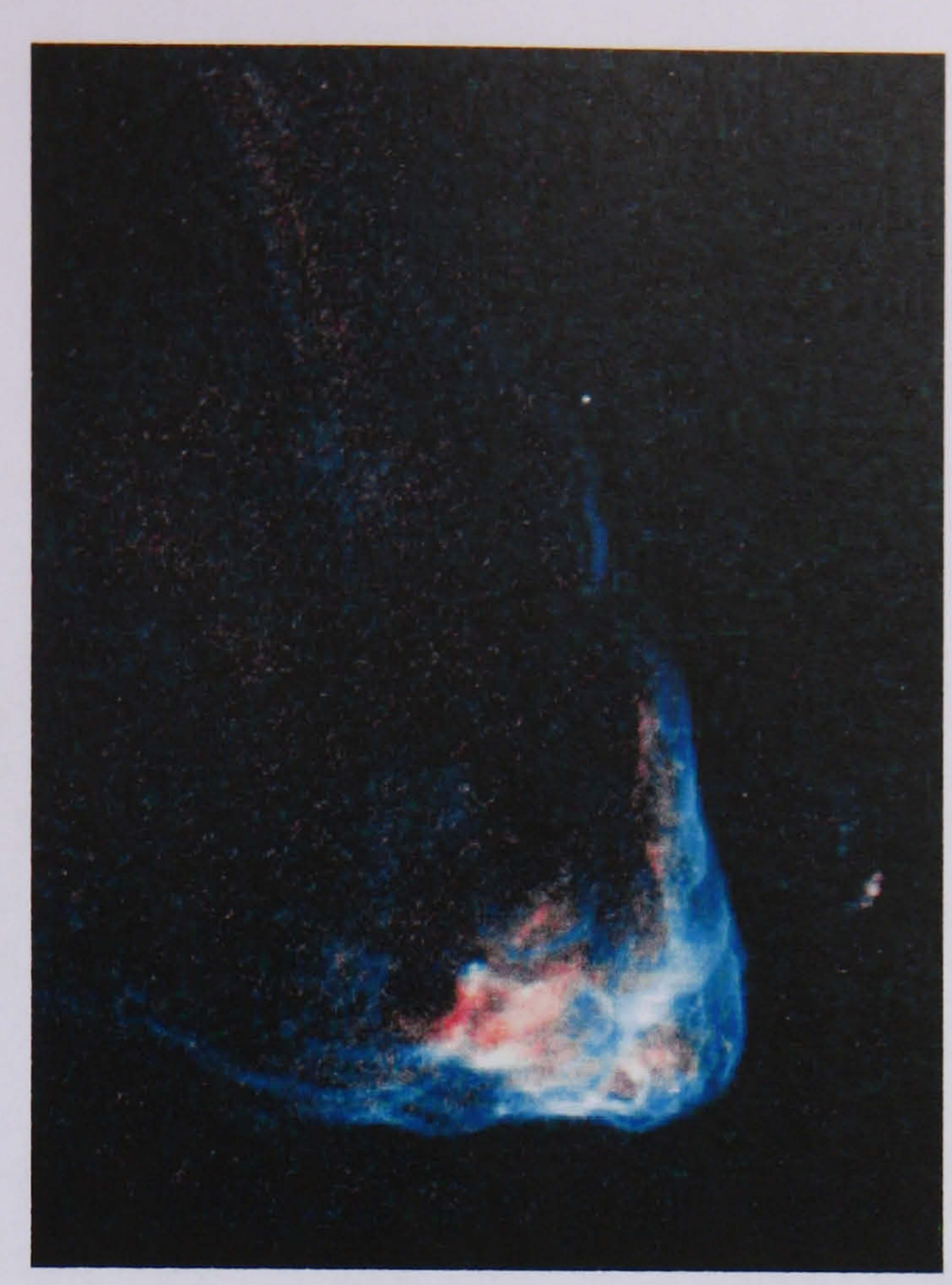


Figure 4.2: The HH 34 bow shock and Mach disk as seen with the Hubble Space Telescope. The jet has propagated from the top left of the image towards the centre. The high-excitation bow shock dominates in $H\alpha$ (green) and the low-excitation Mach disk is prominent in [SII] (red). Reproduced from [57].

Numerous authors have simulated the interaction of a supersonic radiatively cooled jet in an ambient medium in an attempt to understand the structures observed at the 'working surface' which forms as a protostellar jet tip meets the interstellar medium. Such a structure is shown in Fig 4.2, which is a composite of emission from different emission lines, imaged by HST. An accepted model of this type of interaction has now emerged, as is illustrated in Figure 4.3. As jet material flows from the left of this sketch it is shocked by the static ambient medium producing a Mach disk, which is moving supersonically. Ahead of this Mach disk a bow shock forms in the ambient medium (in the frame of the Mach disk, the ISM is flowing from the right of the image and forming a stand-off shock). This whole structure (Mach disk and bow-shock) is usually referred to as the working surface of the jet.

These interactions between the jet and ambient medium, as well as internal

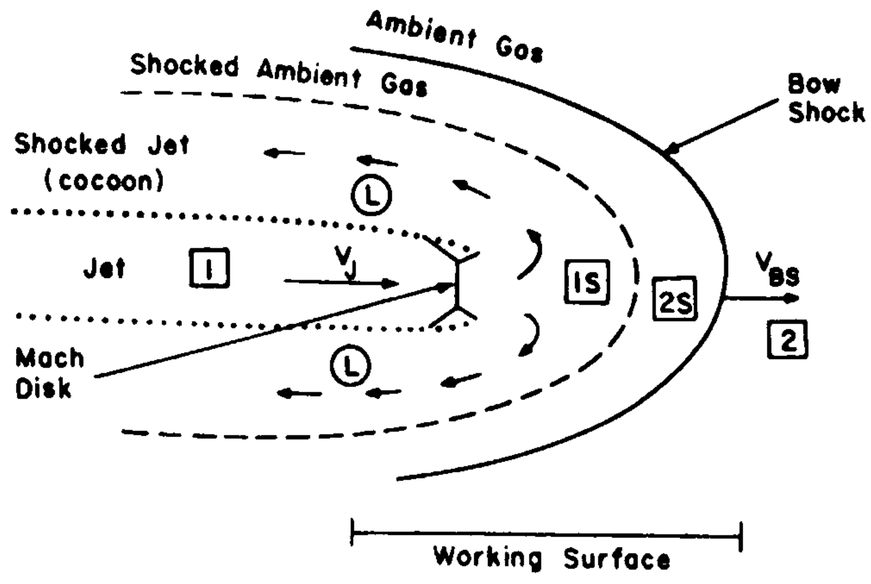


Figure 4.3: Working surface that is formed as a supersonic jet (labelled 1) interacts with an ambient medium (labelled 2). In the frame of the working surface jet material is entering into the image from the left and ambient material is entering from the right. Areas labelled 1S and 2S identify regions of shocked jet and ambient medium respectively. Reproduced from Hartigan [10].

working surfaces (a similar structure that is formed by velocity variations within the flow), are important for observing the jets. The shocks provide brighter emission than an unshocked portion of the beam itself as can be seen in Fig 4.2 (and also earlier in Fig 1.1). Often these jets would not be sufficiently luminous to be discovered if they did not propagate in the ISM (e.g. see [57]).

From conservation of momentum it is possible to determine the velocity of the working surface where the jet flow meets the ambient gas [69, 72]. For a density contrast η the velocity of the bow shock v_{bs} is given as a function of jet velocity v_j.

$$v_{bs} \approx v_j \frac{1}{1+\eta^{-1/2}} \tag{4.12}$$

Typically, protostellar jets propagate through an ambient medium with a mass density of a few tenths that of the jet. This ambient density is large enough for the mean free path of the jet to be less than the characteristic scale of the system (the jet radius) and hence produces a bow shock at the jet tip. The ambient medium is likely to also have an effect on jet collimation.

Numerous authors (including [10, 69]) have simulated the evolution of radiatively cooled jets in an ambient medium. Of particular interest are the effects of varying the density ratio and the cooling length. The results of some of these simulations are shown in Fig 4.4. It can be seen from the figure that smaller cooling parameters lead to a narrower jet. Increasing the density ratio stabilises the jet and greatly

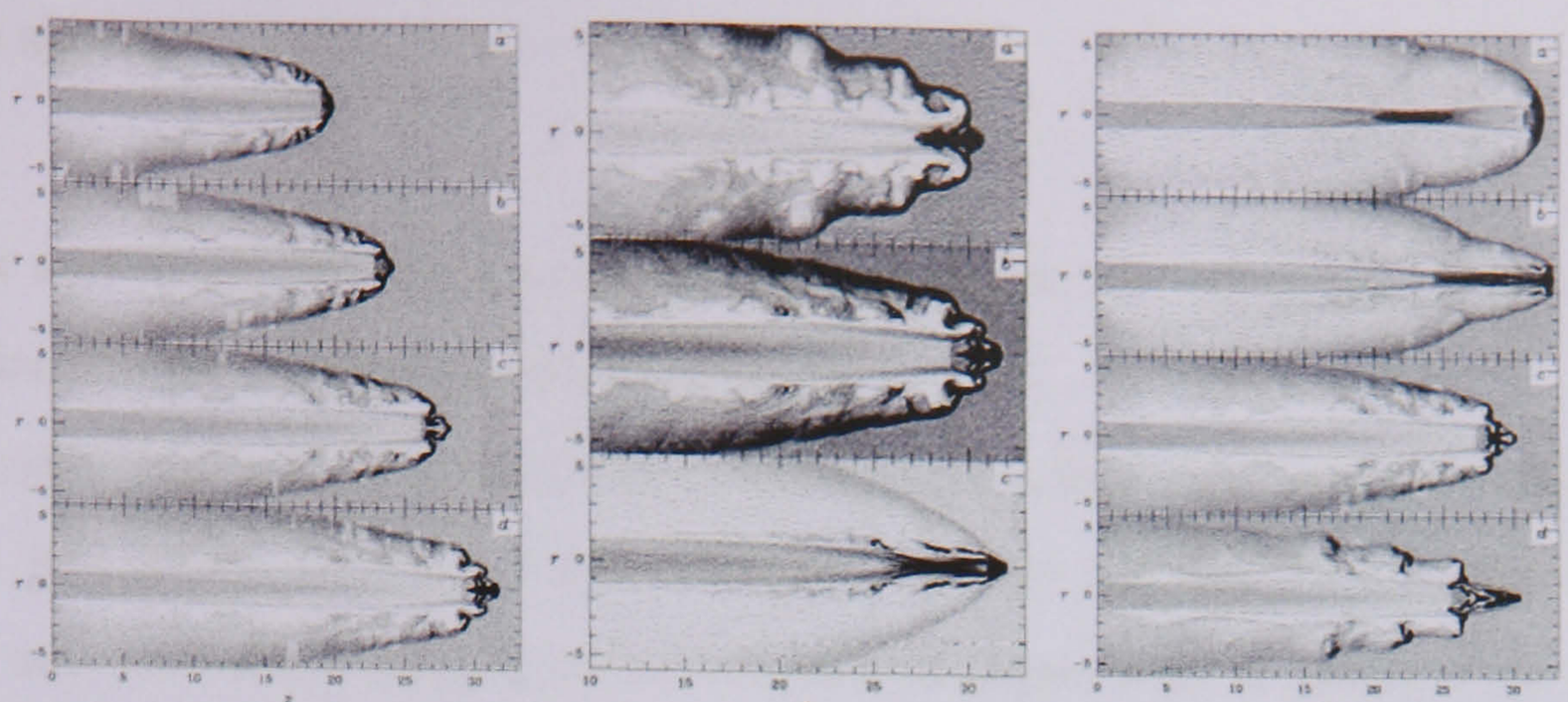


Figure 4.4: Density plots from simulations by Blondin et al. [69] showing the evolution of the jet and the effects of an ambient medium and radiative cooling. Density plots (white= $0cm^{-3}$, black= $200cm^{-3}$) are shown for (a) the time evolution (1000, 1200 & 1400 years) and effects of varying (b) density ratio ($\eta = 0.33, 1.0$ & 3.0) and (c) cooling parameter ($\chi_b = \chi_j = \infty, 2.2, 0.55$ & 0.22) of a radiating jet.

improves the collimation.

4.5 Producing an ambient medium in the laboratory

In the experiments discussed in Chapter 3 (along with all of the other jet production techniques outlined in section 4.3.1) no ambient medium was present, hence there was no working surface produced at the head of the jet. In order to investigate this feature it is clearly necessary to introduce an ambient medium into the experiments.

Earlier we defined the density contrast as the ratio of jet density to ambient density. Astrophysical jets are normally the same material as the ISM (hydrogen), so for simplicity the density contrast is normally taken to be the ratio of ion number densities. For our experiments it is convenient to use an ambient material such as argon, with an atomic mass significantly less than the jet material (which is usually tungsten).

Thus the density contrast is better described by the mass density ratio between

the two species:

$$\eta = \frac{\rho_j}{\rho_a} = \frac{n_j m_j}{n_a m_a} \tag{4.13}$$

where n and m are the ion density and mass respectively; subscript j and a denote values for the jet and the ambient medium.

To experimentally investigate the effect of a background medium on jet propagation two techniques have been developed to vary the density contrast between the jet and its surrounding medium. Both techniques aim to provide an ambient medium of similar mass density to the jet ($\eta \sim 0.1 - 1$). In chapter 5 a technique for producing a quasi-stationary ambient medium using a gas nozzle is described. In Chapter 6 we will discuss experiments where an off-axis CHO foil is photo-ablated to produce an ambient medium. The ablated target produces a side-wind which imparts transverse momentum onto the jet in addition to providing the correct density contrast.

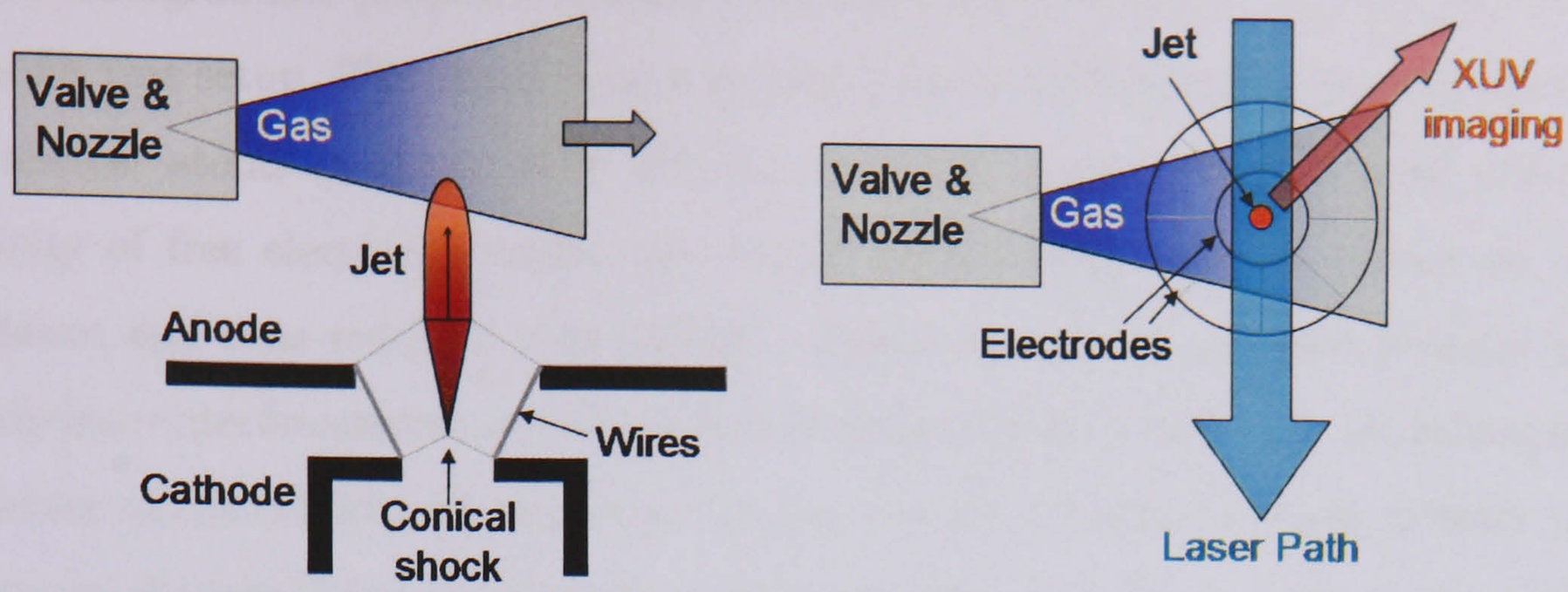
Chapter 5

Jets propagating in quasi-stationary gas clouds

5.1 Experimental setup

To model the interaction of protostellar jets with the ISM in the laboratory an ambient medium must be introduced into the experiments. Earlier in Section 3.4.3 we discussed the low density jet that is ejected by the array prior to the formation of the fully collapsed jet. Clearly, in addition to the main jet interacting with a target-plasma introduced above the array, this low density jet will also interact with the target-plasma. In this chapter we will first describe the interaction of this low density, early-time jet with a gas cloud, before exploring the interaction of the collapsed jet with the gas.

Ideally for such experiments a uniform, static gas would fill the entire vacuum chamber, however this is not possible due to the technique used to produce the jet; if gas was present in the MITL or wire array regions during the experiment then the load voltage would short circuit, preventing jet production. Instead a system has been developed to introduce a gas cloud into the region where the jet propagates using a supersonic nozzle and fast valve, as illustrated in the side and end-on diagrams in Fig 5.1. The diagnostic layout for these experiments is also shown on the end-on diagram (Fig 5.1b). Argon was used as the ambient gas for these experiments as it is an atomic gas, is safe to work with and was readily available.



(a) Side view (b) Top view

Figure 5.1: Setup for gas interaction experiments from both side-on and end-on to the array. The diagnostic layout is shown on the end-on image.

An experimental configuration with the nozzle $18mm$ from the axis was decided on as this provided a sufficiently high gas density on the array axis with only minor adjustments of the array configuration from that was used in Chapter 3. It was however necessary to make slight modifications to the wire array design from the earlier configuration; by reducing the lower (cathode) diameter from $16mm$ to $8mm$ and increasing the length of the array it was possible to keep the same array opening angle and top (anode) diameter. Two-frame schlieren imaging of a tungsten jet produced with this modified configuration indicates that the jet tip velocity $v_j \approx 270km/s$, which is similar to the tip velocity for the earlier configuration.

A nozzle with Mach number $\mathcal{M} = 4$ was used to produce a cloud of gas a few cm wide along the array axis without gas entering the load region. The valve was backed with a pressure of 50 Bar. Given that the sound speed of argon at room temperature is $c_s = 320m/s$, the gas velocity from a $\mathcal{M} = 4$ nozzle will be of the order of $v_{cold} \approx 1.2km/s$. If the gas is heated by emission from the wire array it will expand with a slightly higher velocity, but this should remain negligible compared to the jet velocity.

Trial experiments with the gas in the configuration shown in Fig 5.1 determined that the gas could not be triggered more than $1.4ms$ before the start of current without the load voltage dropping. Experiments were performed (in conjunction

with undergraduate project students) to determine the density of the gas on the jet axis for this setup. The small change in refractive index for a given number density of neutral atoms (a factor of $\sim$ 100 less than the change due the same number density of free electrons) meant that direct measurements of the density for the distance and time required were difficult. Measurements using Mach-Zehnder and Michelson interferometers as well as Moire Deflectrometry [76] were all attempted, however the sensitivity of each was too low. A good measure of the density was obtained by introducing obstructions into the flow at a point closer to the nozzle and with a longer delay after opening the valve. The thickness of the shocks from the obstructions were used to find the mean free path of the gas, and hence the density. Using this technique a number density $n_{gas} = 4 \pm 1 \times 10^{17} cm^{-3}$ was determined. For the actual interaction experiments the gas nozzle is positioned twice this distance from the jet axis. The interferometry data near to the nozzle indicated that the gas is divergent, forming a cone-shaped distribution, with the apex at the nozzle; the cross-section of this cone will be proportional to the square of the distance to the nozzle. Hence, assuming a constant flux, an inverse square divergence occurs and number density will be approximately $n_{gas} \approx 1 \times 10^{17} cm^{-3}$, or equivalently a mass density $\rho_{gas} \sim 6.7 \times 10^{-3} kg/m^3$.

5.2 Jet-gas results

Figure 5.2 shows an XUV emission image of the interaction of a tungsten jet with a gas cloud taken $212ns$ after the start of current, along with a photo of the setup taken through the same diagnostic port on the vacuum chamber (the XUV camera is not perpendicular to the direction of gas flow, as was shown on Fig 5.1b). The XUV image shows a jet that has propagated along the z-axis from the wire array (at the base of the image) towards the gas. The faint oval ring of emission on the left of the image is re-emission from sharp edges on the gas nozzle housing (as seen on the photograph in Fig 5.2). The gas is approximately cone shaped, with the apex at the nozzle. This cone of gas has been perturbed from its original profile by the presence of the wire array; it is assumed that this is the result of low density array

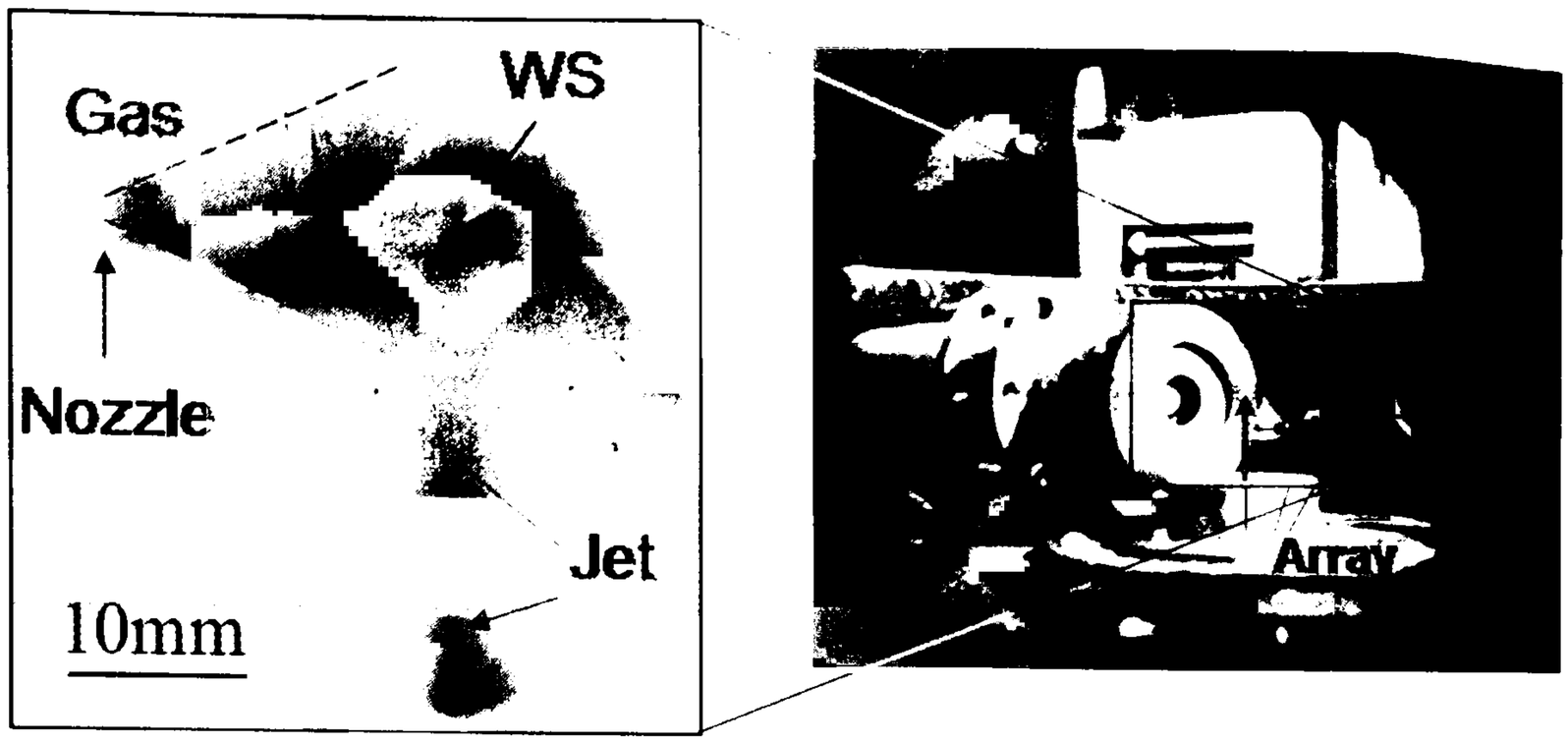


Figure 5.2: (a) XUV emission ($h\nu > 30eV$) from a jet interacting with gas at $212ns$ and (b) photo from XUV camera port. On the XUV image the jet is labelled and the hashed band indicates a dead-zone between the different elements of the MCP. A ring of emission from the gas valve housing can just be seen on this XUV image (this will be more obvious on later images). The working surface is believed to be the small area of strongest emission (labelled WS) in the centre of the broader emitting bow-shock.

material impacting the gas. Within the gas, above the axis of the array is a bright spot of emission (labelled WS on the image). The width of this emission ($\sim 3.5mm$) is similar to the diameter of the emission from jet material below the gas. Thus this bright spot in emission is likely to be the result of jet material colliding with the gas. The height of the emission is $300\mu m$. This object can only be resolved if it is emitting photons of energy $h\nu > 30eV$ (as discussed in sections 2.5.1), hence the object is hotter than the jet. This indicates that some of the kinetic energy of the jet has been thermalised as it meets the gas, producing a working surface.

It is interesting to compare the position of the collapsed jet (as was investigated for most of chapter 3) with the XUV image. Figure 5.3 shows two schlieren images of the jet at slightly later times than the XUV image; one of these is from the same experiment as Fig 5.2, and the other is from an experiment with an identical array configuration however with no gas present. In both images we see that the well formed jet has not actually reached the gas at this time. Instead all of the effects seen in Fig 5.2 are the result of an interaction of the gas with the low density jet that was ejected at early time by the un-collapsed conical shock.

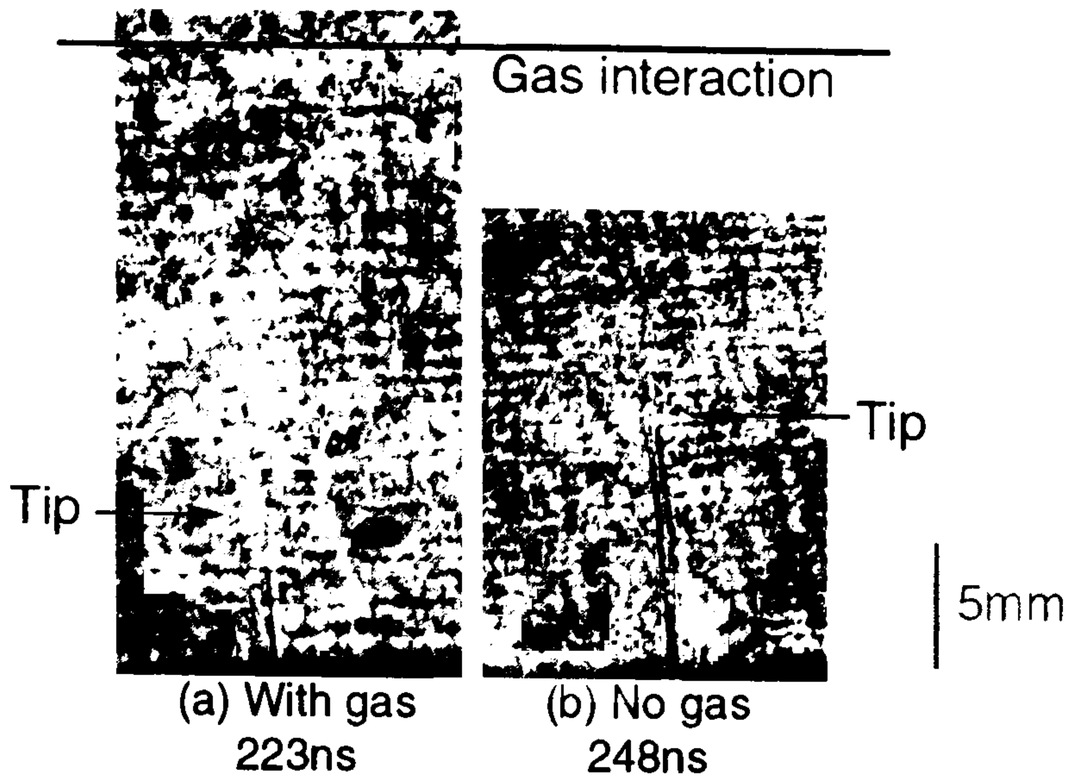


Figure 5.3: Schlieren images of the jet for experiments with gas present (a) and without gas present (b). Both experiments have an identical array configuration to Fig 5.2. The position of the jet tips and the interaction seen in Fig 5.2 are marked. These schlieren images confirm that the interaction in Fig 5.2a is the early-time halo jet rather than the later-time collapsed jet (seen on the schlieren image).

Figure 5.4 shows a laser interferometer image (for a slightly different gas position, but at equivalent stage of the evolution) and a phase map obtained from the interferometer image using a fringe analysis package, FRAN [38]. The general structure in the phase map is similar to the XUV image in Fig 5.2, however there is only a slight increase in density where the jet meets the gas, hence the bright spot in XUV emission is likely to be due to an increase in temperature rather than an increase in density.

We have imaged a region of stronger emission in the centre of the gas which is thought to be a working surface forming from the interaction of the denser core of the jet with the gas cloud. Astrophysical models [10] suggest that the working surface should consist of both a Mach disk and a bow shock. The experimental images do show another, broader bow-shock-like feature however MHD simulations indicate that this is too wide to be the bow shock produced by the central denser portion of the jet, and is more likely to be caused by the less dense edges of the jet. A possible explanation for not distinguishing the central mach disk and bow shock could be that the two shocks are closer than the diagnostics used can resolve. Alternatively we know that the diagnostics used are integrating along one axis of a 3D system and hence the central bow shock in the gas (caused by the central denser

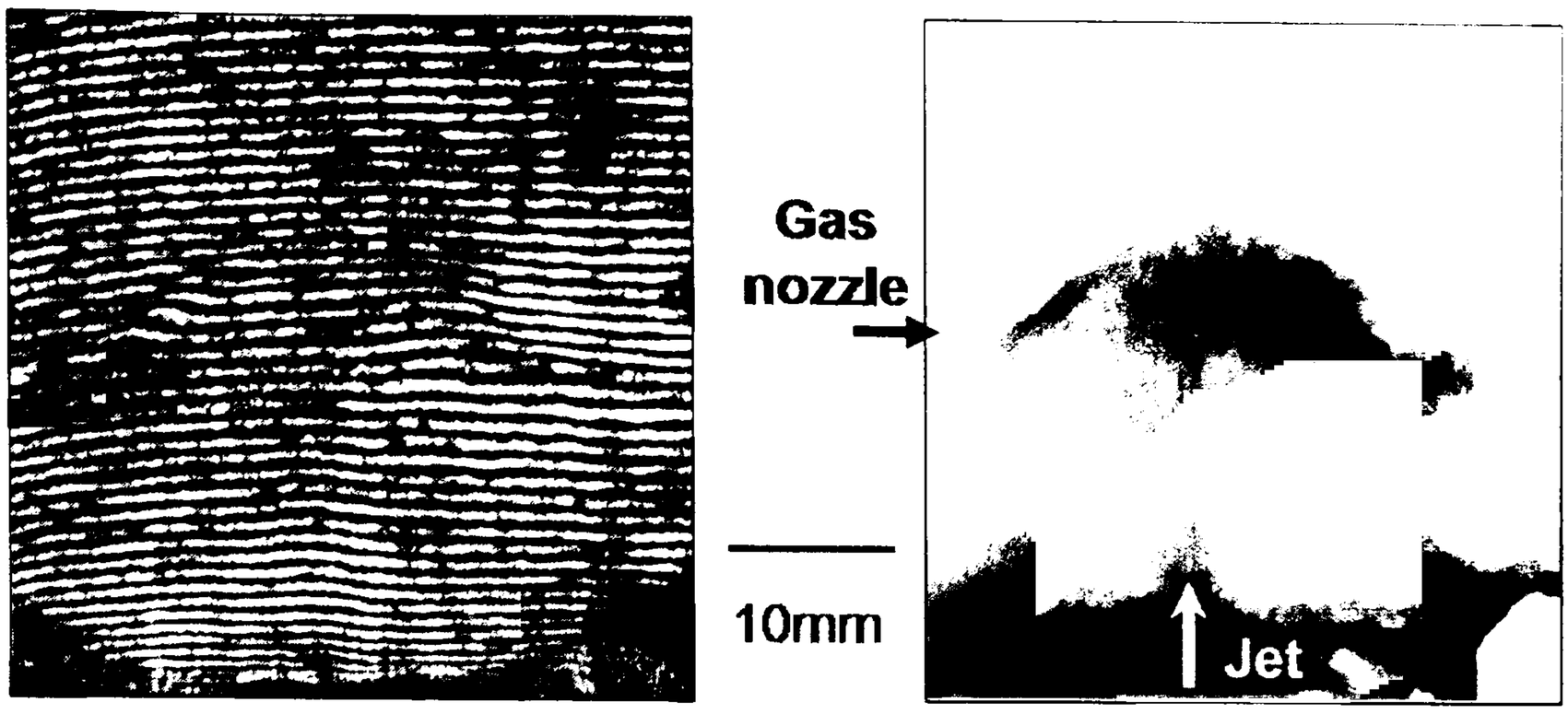


Figure 5.4: Interferometer image of jet-gas interaction and phase map derived from it. On the phase map white indicates sparse regions and black represents a phase shift of 2π, or a density of $\int n_e dl = 4.2 \times 10^{17} cm^{-2}$.

portion of the jet) might not be observed because it is overlapped with either the Mach disk or the broad halo bow shock.

Figure 5.5 shows the evolution of this jet-cloud interaction. Both the bow shock in the ambient medium (from the outer part of the jet flow) and the jet working surface (from the centre of the flow) move axially. The axial position of the working surface is plotted against time on Fig 5.5e, showing that the working surface velocity is constant and $v_{ws} \sim 127 \pm 10 km/s$. This velocity is significantly slower than the jet tip velocity in vacuum ($v_j \sim 270 km/s$). It is assumed that the halo velocity is similar to the jet tip velocity (as discussed in Section 3.4.3). Equation 4.12 earlier gave the working surface velocity as a function of the density contrast η. This can be rearranged to give the density contrast as a function of velocity

$$\eta = \left(\frac{v_j}{v_{ws}} - 1 \right)^{-2} \tag{5.1}$$

From $v_j = 270 km/s$ and $v_{ws} = 120 km/s$, the density contrast for the arrangement in Fig 5.5 is found to be $\eta = 0.8 \pm 0.2$ (that is, the jet density is 80% of the gas density).

Although the jet material that is involved in the interaction is not from the collapsed (later time) jet we can still use the analytic method described in section 3.4.3 to estimate the density of the jet. Unlike the earlier discussions we are now interested in the flows that reach the un-collapsed conical shock so we will not

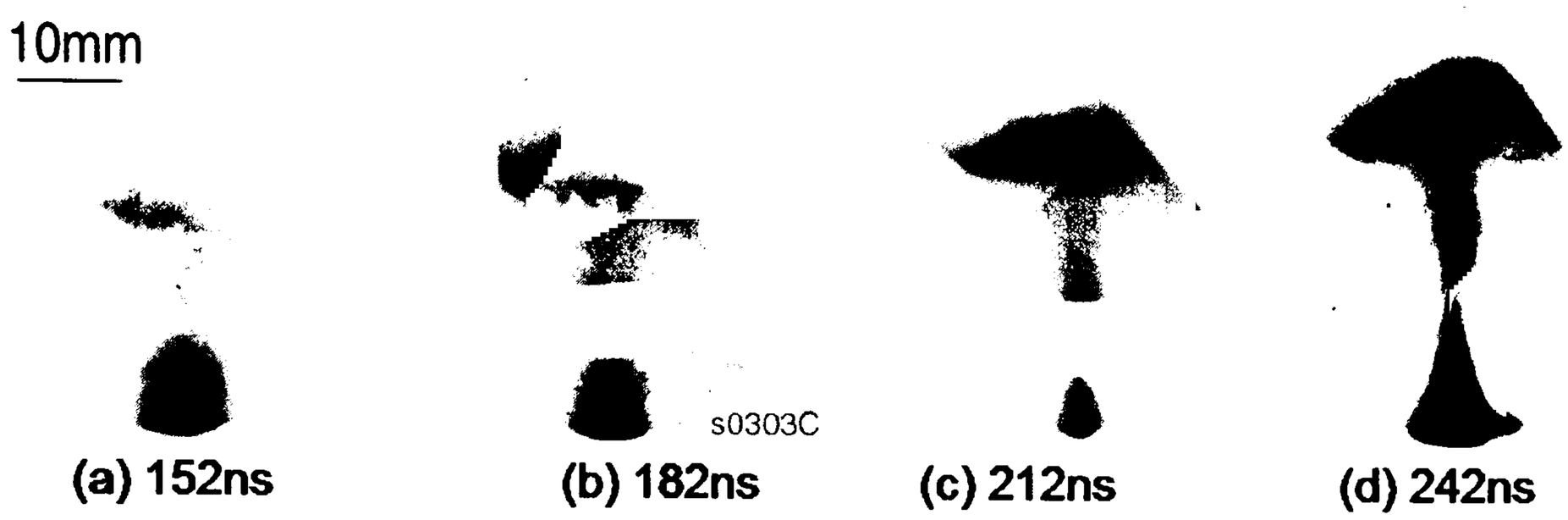


Figure 5.5: Time-series of XUV emission ($h\nu > 30eV$) from a jet-gas interaction with the nozzle $26.5mm$ above the anode plate. The graph shows the working surface trajectory as well as the tip position of the collapsed (later-time) jet from the schlieren image in Fig 5.3a. This confirms that we are seeing an interaction involving the early-time halo jet.

exclude these from the calculation of the jet density. Using this method with the array configuration used for these gas-interaction experiments gives the density of the flow as $\rho_j \sim 1 \times 10^{-4} kg/m^3$ for a point $19.5mm$ above the end of the conical shock (at the centre of the gas nozzle, $26.5mm$ above the anode) at $230ns$ (the time that the working surface passes the centre of the gas nozzle in Fig 5.5), where we have assumed that most of the jet mass is concentrated in a central beam of diameter equal to the width of the working surface ($\sim 3.5mm$).

Using the density contrast and the predicted jet density the density of the argon can be determined

$$\rho_{Ar} = \frac{\rho_j}{\eta} = \frac{1 \times 10^{-3} kg/m^3}{0.8} \sim 1.2 \times 10^{-3} kg/m^3 \tag{5.2}$$

This density is of the same order as the density predicted from cold characterisation of the gas, ($\rho_{Ar,pred} \approx 6.7 \times 10^{-3} kg/m^3$).

The working surfaces shown on Fig 5.5 are not perpendicular to the direction of jet propagation as might be expected; instead they are diagonal from bottom left to top right and the angle changes with time. This is likely to be due to a change in ambient gas density between the two sides of the shock (from the divergence of the gas), which would lead to a variation in the density contrast and hence the working surface velocity.

5.3 Varying density contrast

Before the collapse of the conical shock occurs there is no efficient mechanism for the ions to lose their thermal energy, hence we expect that the ions of the early-time jet to be hot and therefore expanding. In the experimental setup discussed above the jet has expanded to a diameter of $\sim 3.5mm$ before it interacts with the gas. A similar expansion will also occur in the axial direction. If the separation between the wire array and the gas is reduced, then the dynamic age of the jet will be reduced and the expansion (in both directions) will be less, thus the jet density will be greater. Thus the relative axial positions of the array and gas can be used as a tool to alter the density of jet involved in the interaction and hence vary the density contrast between the jet and the gas.

In the previous case the centre of the gas nozzle was $26.5mm$ above the anode plate. In the XUV images shown in Fig 5.6 the centre of the gas nozzle is $22.6mm$ above the anode plate ($15.6mm$ from the top of the conical shock). Again we see that the working surface propagates upwards. The width of the working surface is smaller than the previous case (previously $3.5mm$, now $1.7mm$), illustrating the reduced diameter of the jet. The jet material that is causing the interactions seen in Figures 5.5 and 5.6 was ejected from the array at similar times, implying that the flux of plasma out of the array in the two cases is similar. If we ignore any axial expansion, then we expect the density to scale as the inverse of the area of the working surface, so in this new case will be greater by a factor of $\left(\frac{3.5mm}{1.7mm}\right)^2 = 4.2$. Thus the density of the jet in Fig 5.6 will be $\rho_j \sim 4.2 \times 10^{-3} kg/m^3$.

Assuming that the gas density is identical in this setup as it was for Fig 5.5 we can use this value of the jet density to determine the density contrast as

$$\eta = \frac{\rho_j}{\rho_a} = \frac{4.2 \times 10^{-3} kg/m^3}{1.2 \times 10^{-3}} = 3.5 \tag{5.3}$$

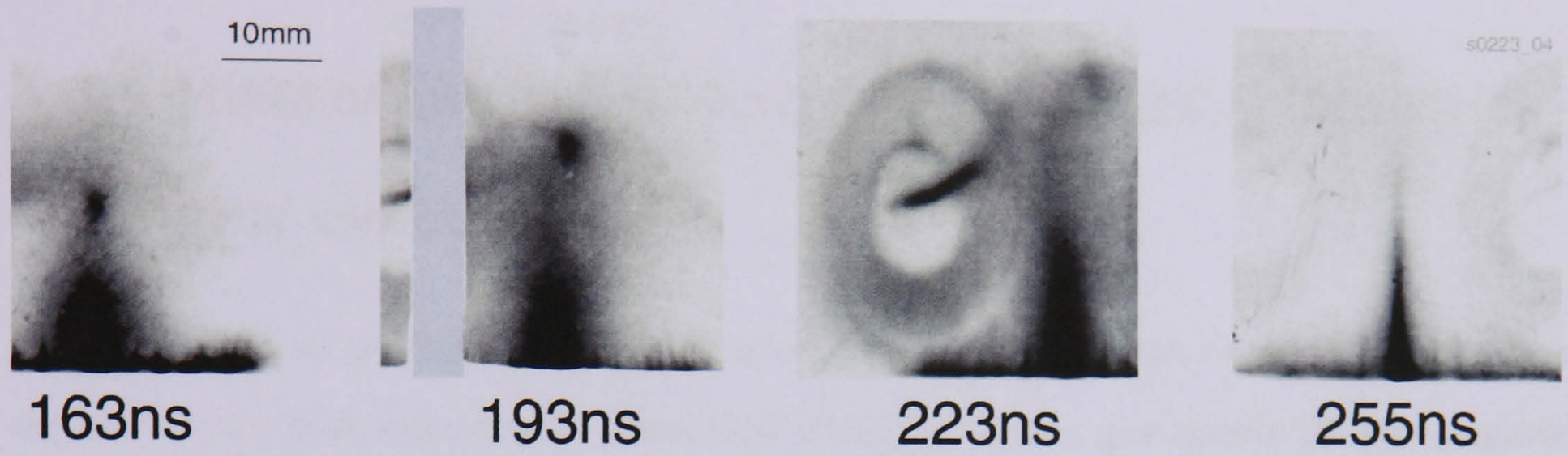
From this density contrast we can predict the velocity of the working surface in Fig 5.6.

$$v_{ws} = v_j \frac{1}{1+\eta^{-1/2}} \tag{5.4}$$

$$= \frac{270 km/s}{1+3.5^{-1/2}} = 176 km/s \tag{5.5}$$

Following the working surface with time in Fig 5.6 gives a velocity of for the working surface of $190 \pm 20 km/s$. The estimated and measured velocities are not in exact agreement, but are within the error in the experimental velocity. Estimating the axial expansion of the jet is more complicated, however is likely to be a much smaller effect as this expansion is not into vacuum.

On the last image of Fig 5.6 we can see that, as the collapsed jet reaches the gas it propagates freely through the gas without any observable affect from the gas. For tungsten, due to the high atomic mass, there is a large delay between the first collisions on the array axis and the collapse of the conical shock. Hence for tungsten the working surface produced by the pre-collapsed jet fully propagates through the gas before the more dense collapsed jet reaches the gas. This means that, by the time



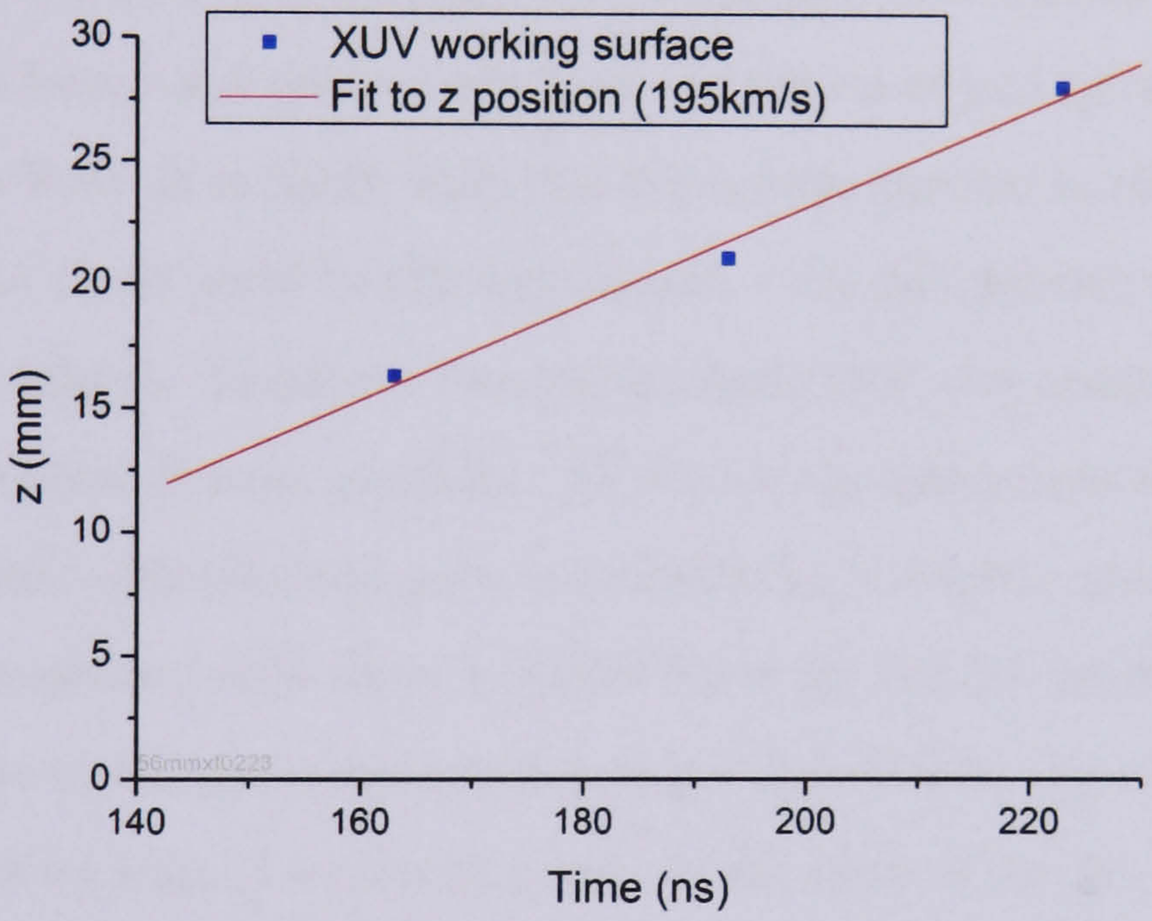


Figure 5.6: Time-series of XUV emission ($h\nu > 30eV$) from a jet-gas interaction with the nozzle $22.6mm$ above the anode plate. The bright ring of emission on the centre two images (particularly the image at $223ns$) is re-emission from the gas jet housing. The graph shows the working surface trajectory.

the collapsed jet reaches the gas, the gas has been dissipated by the first working surface. In addition, as the collapsed jet forms relatively late in time it has a high density, hence the density contrast η between the collapsed jet and the gas is large. By using a different material we can vary the delay between the first collision of flows on the axis and the collapse of the conical shock.

5.4 Interaction of a stainless steel jet with an argon cloud

Figure 5.7 shows a stainless steel jet interacting with the gas cloud. The setup is similar to the first experiment described above with the gas nozzle 26.5mm above the anode plate (as was used in Fig 5.5). In the first two frames of this figure a jet working surface forms and moves both in the direction of jet injection and also in the direction of gas flow. It is likely that this transverse motion is related to the asymmetry in the gas cloud prior to the experiment - the gas density decreases from left to right on the images. There are two mechanisms that can cause a transverse force on the jet due to this density gradient. Firstly as the gas is heated the pressure will increase, and hence the thermal pressure caused by a density gradient will increase. This thermal pressure could cause a direct force on the jet material. Secondly the thermal pressure in the gas could accelerate gas material in the transverse direction; this flow could then impart a ram pressure on the head of the jet. MHD simulations indicate that the thermal pressure gradient required to directly accelerate the jet is far greater than that likely to be produced by this setup. Hence the transverse motion is probably due to a transverse motion of the gas. Such a system will be discussed in more detail in Chapter 6

In the second frame of Fig 5.7 a second working surface has begun to form as the head of the main jet body collides with cloud material that has not been shocked by the first working surface system. By the third frame this secondary working surface has also propagated upwards. Figure 5.7d shows a graph of the positions of each of these working surfaces in time. The second working surface is travelling at 200km/s compared to 120km/s for the first working surface. Using equation 4.12 this change

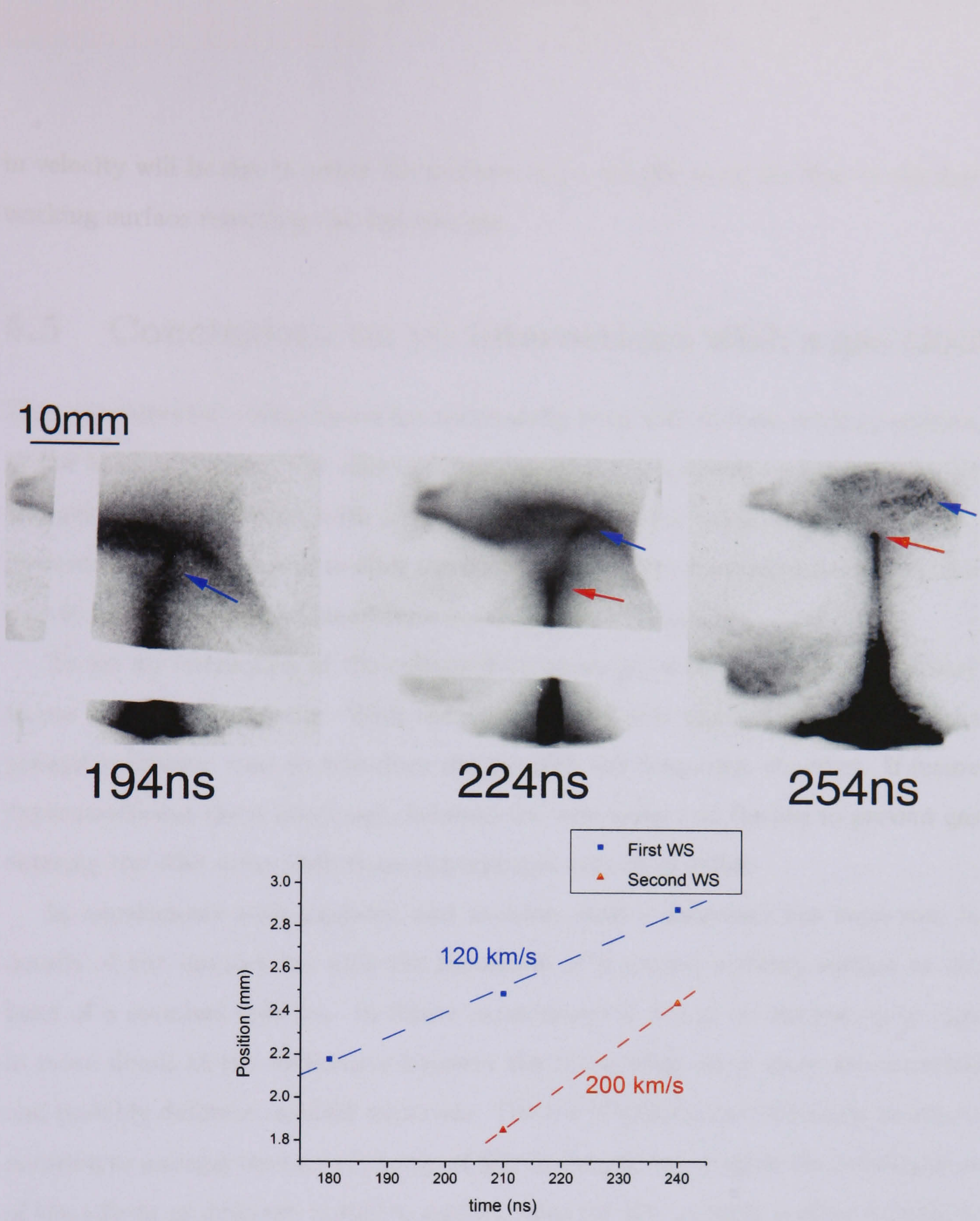


Figure 5.7: Time-series of XUV emission from a stainless steel jet interacting with argon, with the nozzle $26.5mm$ above the anode plate. The blue and red arrows show the positions of the first and second working surfaces respectively (at $254ns$ the first working surface is less defined, and may have expanded horizontally). The graph shows the trajectories of the two working surfaces.

in velocity will be due to either the increase in jet density along the flow or the first working surface removing the ambient gas.

5.5 Conclusions on jet interactions with a gas cloud

This experimental configuration has successfully been able to form working surfaces at the head of the jet. The affect of changing the density contrast between the jet and gas has been evident, with a significant change in the working surface velocity, however it would be useful to alter the density contrast to more extreme values, and also to have more precise measurements of the density contrast.

To see an interaction of the collapsed tungsten jet with the gas it is necessary to use a higher gas density. With the current setup this was not possible with the present technique used to introduce the gas into the diagnostic chamber. If future experiments can use a diaphragm between the wire array and the gas to prevent gas entering the wire array then these experiments may be possible.

In experiments with tungsten and stainless steel a difference has been seen in details of the interaction, with the formation of a second working surface at the head of a stainless steel jet. In future experiments it would be interesting to look in more detail at the differences between the interaction using more jet materials and possibly different ambient materials. The use of different jet materials would, in addition to altering the rate of change of flux in the jet, would allow the investigation of the effects of different radiative cooling rates for the working surface (currently there are insufficient results to draw any conclusions on such effects). If the actual jet has a lower rate of radiative cooling it may also be possible to see any effects on collimation of the jet, such as the ambient pressure and the potential to form instabilities, for example the Kelvin-Helmholtz instability.

One feature that was seen on the stainless steel-argon interaction (shown in Fig 5.7) is the motion of the first working surface away from the gas nozzle. It is thought that this may be due to the ram pressure from a slight flow of the gas away from the nozzle (occurring as a results of the gas being heated by emission from the array). This concept of a side-wind acting on the jet has some astrophysical relevance, so we

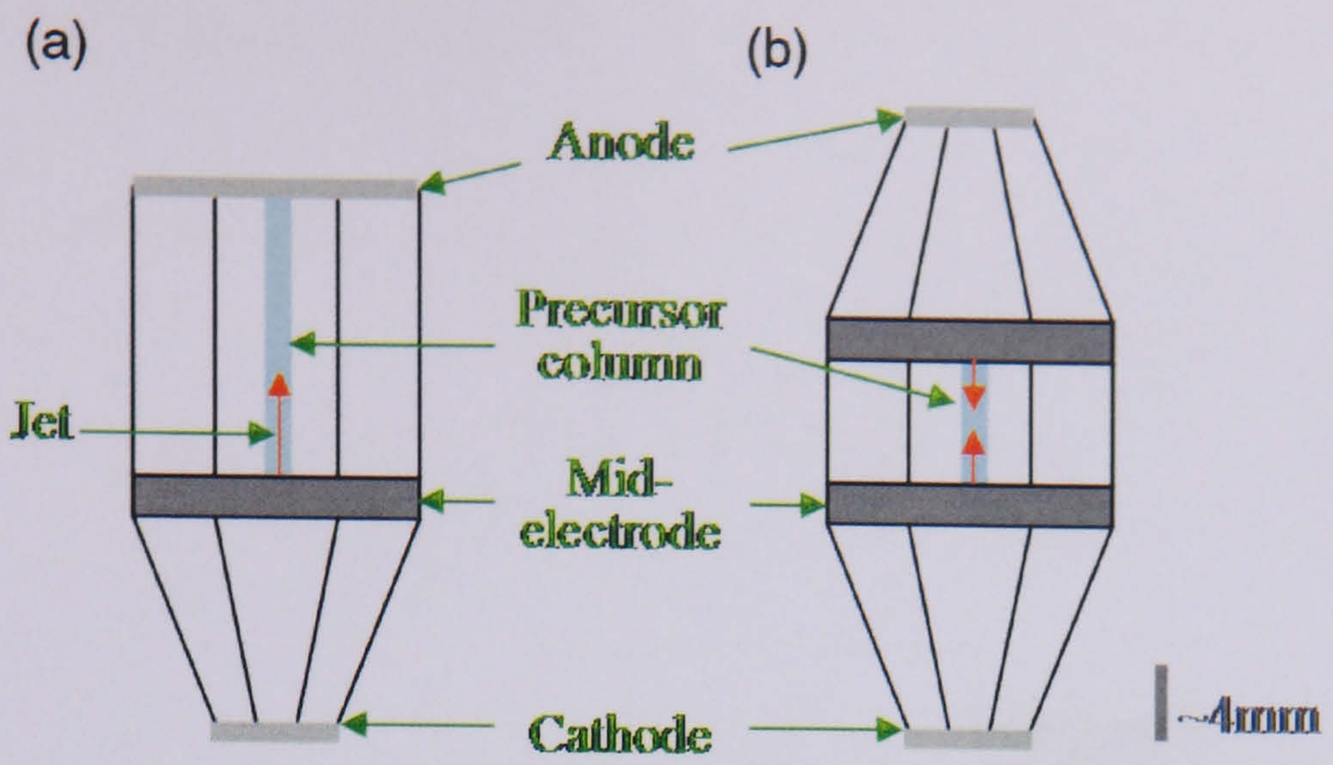


Figure 5.8: Setup for the interaction of a plasma jet with a cloud of the same material (the precursor column of a cylindrical wire array). Also shown is a setup to interact two counter-propagating jets.

will attempt to model this in a more controlled manner in the next chapter. Before discussing such experiments we will first outline preliminary results from another technique for interacting a jet with a plasma cloud. This next technique has the advantages that the jet and cloud are both the same material (as is the case for astrophysical jet-cloud interactions), and the cloud should be more symmetric.

5.6 Propagation of a W jet in a W cloud

Experiments have been attempted with the aim of interacting a jet produced by a conical wire array with the precursor plasma column produced by a cylindrical wire array, in the configuration shown in Fig 5.8a. These experiments are presently only in the preliminary stages. A similar setup (Fig 5.8b) has been used in an attempt to interact two counter-propagating jets.

Figure 5.9 shows a schlieren image of the base of the area where the jet enters the precursor column. A fine jet-like column (diameter $100\mu m$) is seen in the centre of a precursor plasma column that has not yet collapsed (of diameter $1mm$). The data is inconclusive as to whether this is actually a jet or the early stage of precursor column collapse (as was shown in Fig 3.11b).

In experiments that have attempted to interact two jets with opposite ends of

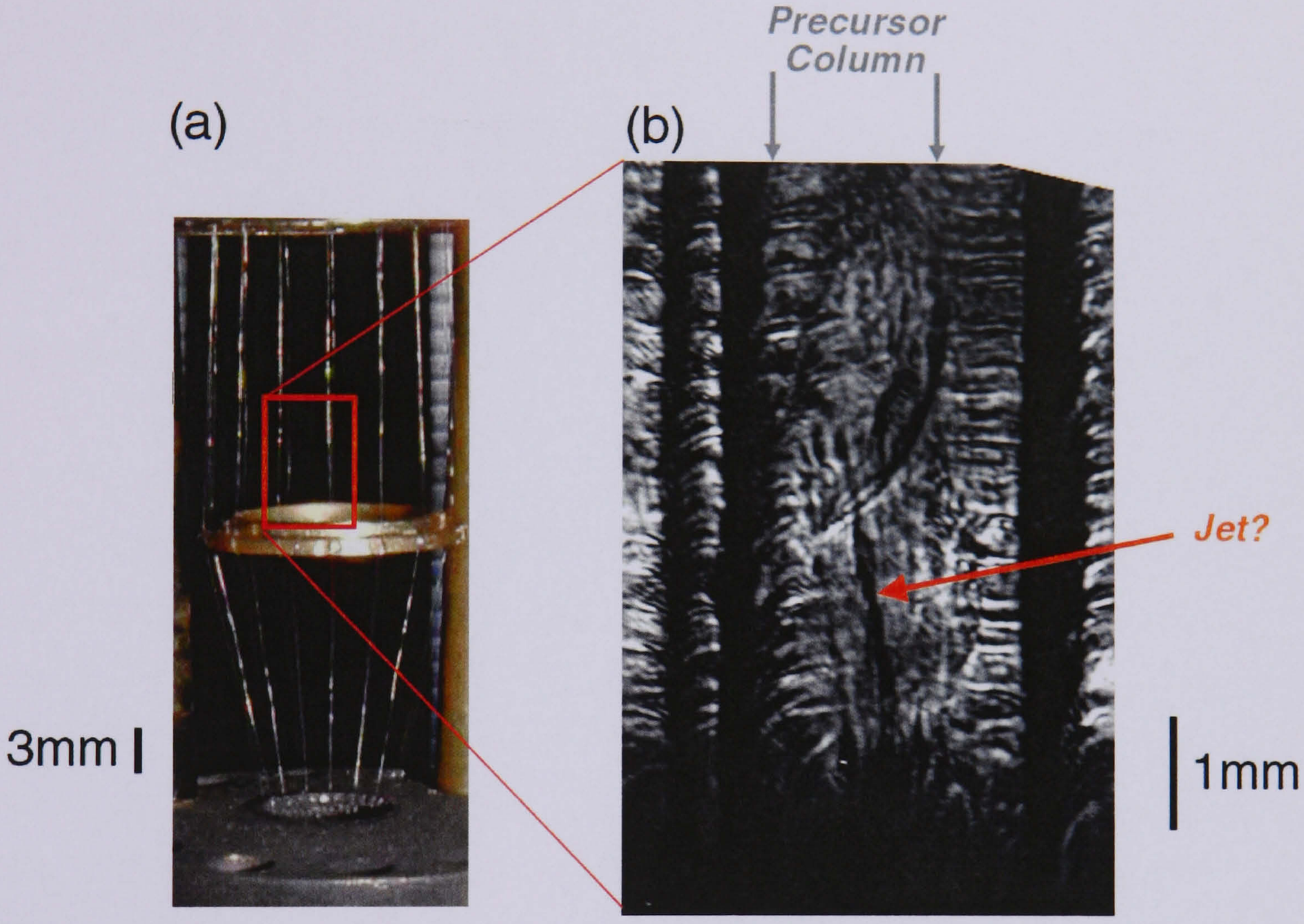


Figure 5.9: Photograph of the setup for a jet-precursor interaction and a schlieren image of a jet propagating in an un-collapsed precursor column.

a short precursor column the jets appear to alter the alignment of the precursor column.

Future experiments on jet-precursor interactions would benefit from varying the relative diameters of the conical and cylindrical portions of the array to control the time of collapse of the conical shock and precursor column.

Chapter 6

Jet deflection by a side wind

6.1 Motivation for jet deflection experiments

Astrophysical observations show that some stellar jets are not straight, and instead exhibit a steady curvature over a significant fraction of their length (many jet radii). Bally & Reipurth 2001 [77] discuss many observations of such deflected jets. As with un-deflected jets these deflected jets normally occur as a pair of counter-propagating jets. These deflected bipolar jets fall into two categories - those with S-shaped [78] and those with C-shaped symmetries [77]. Jets with S-shaped symmetry correspond to a rotating source star, so the jets merely trace out a history for the orientation of the stellar ejection axis; there is no real deflecting force on the jet material. In contrast, pairs of jets with C-shaped symmetries (Fig 6.1) are of more interest as they are deflected by an interaction of the jets with the local environment.

The mechanisms behind the deflection in the C-shaped jets has been the subject of various studies. Hurka et al. [79] investigate the potential effects of an ambient magnetic field on the jet and conclude that to produce a significant, steady deflection would require an ambient magnetic field $B_a \sim 1000\mu G$, which is an unrealistically large field for the interstellar medium (by a factor of ≥ 5 [79]).

Bally and Reipurth [77] discuss whether photo-ablation of the surface of a jet can, by a rocket effect, deflect a portion of the jet. It is shown that, whilst this mechanism can explain some of the observed instances of C-shaped jet symmetry, it is not responsible for the deflection of other jets. Canto and Raga 1996 [80] look at

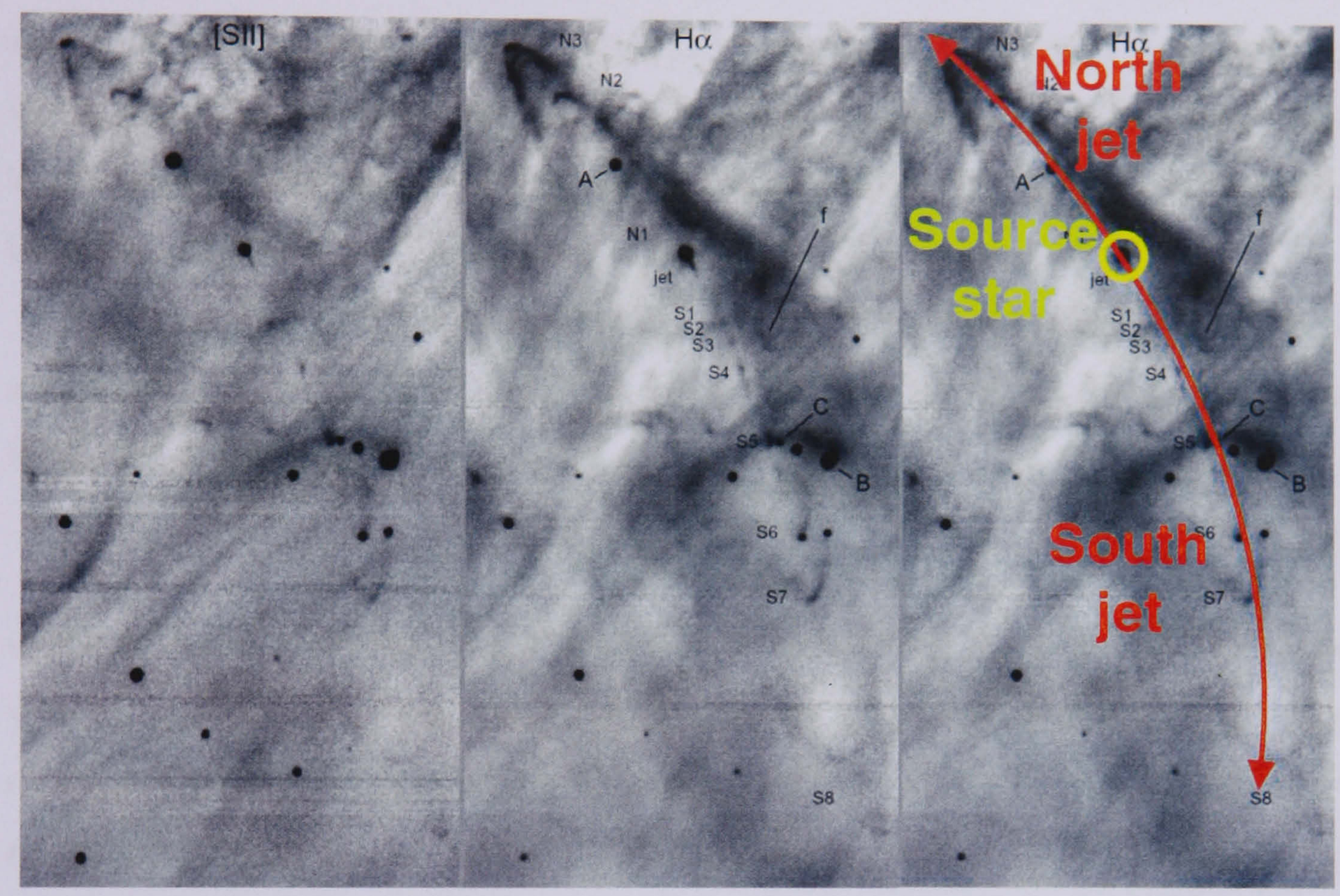


Figure 6.1: Astrophysical observation in Hα (a) and [S II] (b) of HH502 - a deflected jet with 'C-shaped' symmetry, reproduced from [77]. Also shown (c) is a copy of the [SII] emission image with the source star and North and South jets illustrated and labelled. Labels on the original [SII] image denote internal shocks in the North (N1-3) and South (S1-8) jets.

the effect of a pressure gradient on a highly supersonic flow and conclude that the final trajectory for a radiatively cooled jet will be almost straight as the jet bores through the ambient medium.

Balsara & Norman [81] and Canto & Raga [82] discuss the dynamics of jet deflection by the ram pressure produced by a supersonic side-wind. For protostellar jets such a wind can be produced by differential motion of the source star and the surrounding interstellar medium. This is given more weight by observations which show that within a nebula many C-shaped jet structures are present, each with the jets deflected back towards the central star forming region, hence the effective wind is produced by the motion of the star through the ISM [77]. Similar mechanisms have been proposed to explain both AGN jets [81] and YSO jets [82].

Canto and Raga [82] derive a radius of curvature λ for the deflection of an isothermal jet near the stagnation point (the point where the jet velocity is perpendicular to the wind velocity)

$$\lambda = \left(\frac{\dot{M} v_j^3}{\pi c_s^2 \rho_a v_a^2} \right) \tag{6.1}$$

where $\dot{M}$ is the mass flux in the jet, v_j is the jet velocity, v_a is the ambient wind velocity, ρ_a is the ambient density, and c_s is the sound speed in the jet. If any attempt is made to apply this model to non-isothermal flows then c_s should be the sound speed in the jet as it is deflected, hence if any heating of the jet occurs during the interaction then the sound speed will be higher than the sound speed of the un-deflected jet.

The derivation of this radius of curvature by Canto & Raga is for the case of an isothermal jet, however both YSO jets and our laboratory jets have a finite cooling length. Therefore it is more appropriate to perform 3D radiative hydrodynamic simulations of jets in a side-wind, as done by Lim & Raga 1998 [83]. These simulations show that a similar trajectory can be fitted to radiatively cooled jets if an average sound speed in the deflection region is used.

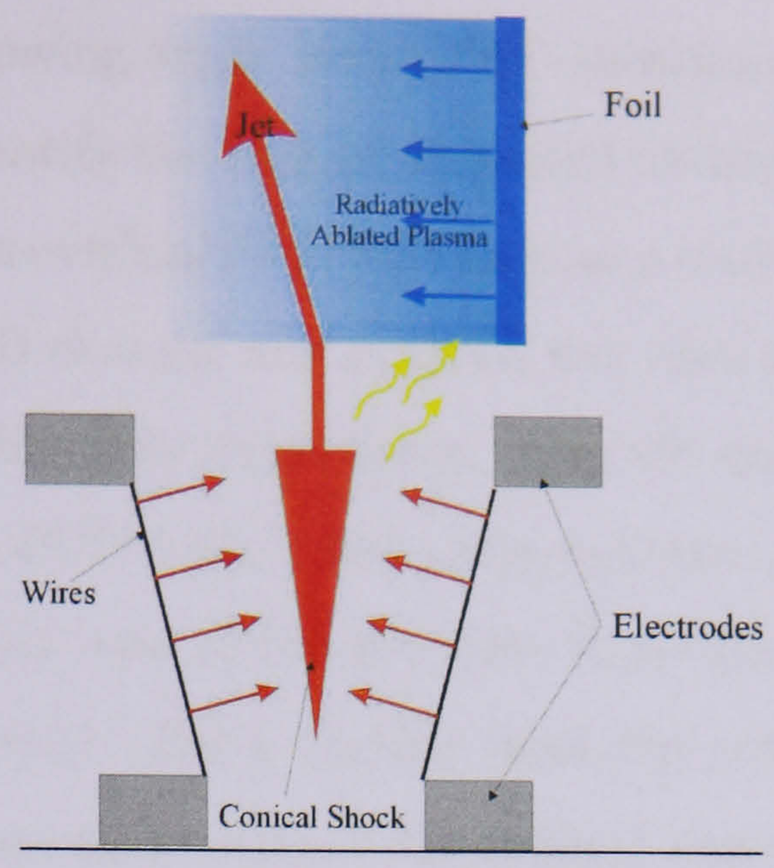


Figure 6.2: Setup for experiments on the affect of jet propagating in a side-wind

6.2 Experimental setup and wind characteristics

In order to study the interaction of a jet with a side-wind in the laboratory it is necessary to produce a flow which is approximately planar and exerts a known ram pressure ($\rho_a v_a^2$) on the jet. To produce such a wind in the laboratory we can take advantage of the soft x-ray emission from both the conical shock and the corona surrounding each wire during the formation of the jet. If this radiation is incident on a CHO foil then the foil will ablate and expand, producing a wind. For these experiments the CHO foil is positioned a few millimetres from the array axis in the region where the jet will propagate, as shown in Fig 6.2.

6.2.1 Estimates of wind parameters

To fully understand any results obtained with this setup and to make any connections to astrophysical models it is necessary to know the characteristics of the wind, specifically both the density and velocity. An analytical method that provides an order of magnitude estimate of the wind parameters will now be outlined, and then compared with some experimental results for the ablation of the foil before the jet deflection results are discussed.

If it is assumed that the coronal plasma and precursor are optically thin then the conical shock will act as a volume emitter; the intensity of radiation emitted will

be independent of the viewing angle, hence PCD measurements from side-on to the array can be used to quantify the energy deposited on the foil.

Figure 6.3 shows three overlaid PCD signals from a conical wire array experiment. In purple is an open PCD channel and in green and blue are PCD channels filtered with $1.5\mu m$ and $3\mu m$ CHO foils respectively. The left axis of the graph shows the intensity incident on the PCD (calculated using equation 2.7).

In the experiments the base of foil is $0.5cm$ from the top of the conical shock however the remainder of the foil is further from the conical shock, and the base of the foil is further from other areas of the conical shock. If we assume that the target is positioned $\sim 1cm$ from the radiation source (which for simplicity we will take as a point source) and the PCD is $21cm$ from the source then we can estimate the intensity of radiation in at the position of the target. This intensity is shown right hand axis of Fig 6.3.

At $130ns$ after the start of current, the open PCD saturates at an intensity of $4.4 \times 10^4 W/cm^2$, equivalent to an intensity of $2.0 \times 10^7 W/cm^2$ at the target. For the remainder of the experiment the incident intensity is larger than this value.

As an approximation it is assumed that the x-ray pulse shape is proportional to the rate that mass is incident on the axis, assuming an average time of flight from the wires to the axis along the array and using the intensity on the PCD at $130ns$ to calibrate, that is

$$I_{incident} \propto \sin^4\left(\frac{\pi(t - t_{fl})}{t_0}\right) \tag{6.2}$$

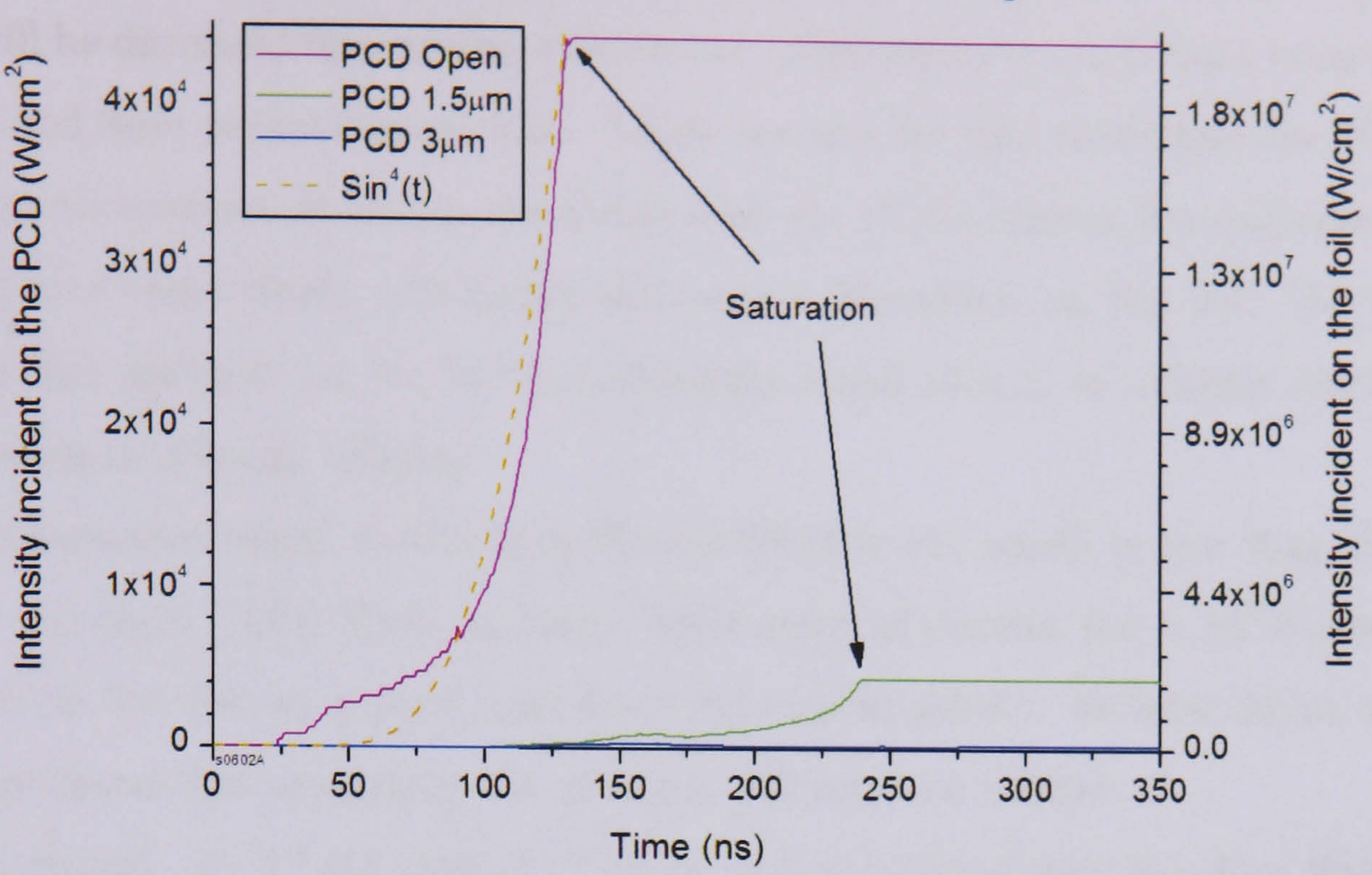
This was plotted on Fig 6.3, and reasonably approximates the sharply rising section of the PCD signal.

In jet-wind interaction experiments the targets are not positioned perpendicular to the source so the intensity incident upon the target at an angled by θ when the PCD saturates is

$$I_{incident} = 2 \times 10^7 \cos(\theta) \frac{W}{cm^2} \tag{6.3}$$

Typically in the experiments the angle between the normal to the foil and the centre of the conical shock is 70°, so the foil has an incident intensity of $I_{inc} \sim 6.8 \times 10^6 W/cm^2$.

(a)



(b)

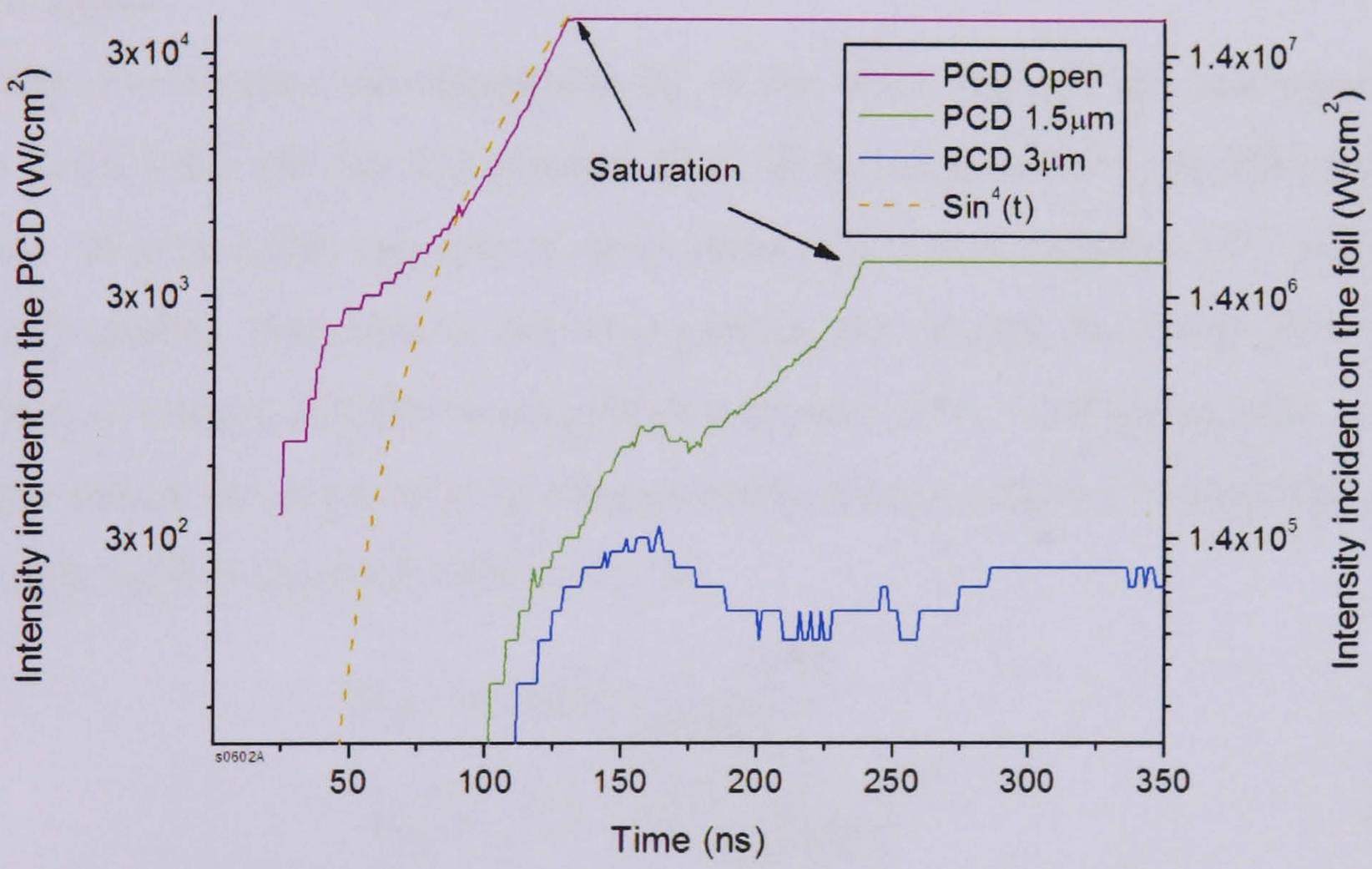


Figure 6.3: X-ray intensities measure with PCD detectors which are open and filtered by $1.5\mu m$ and $3\mu m$ CHO filters. This is shown by (a) a linear plot and (b) a log plot. All signals have been scaled to compensate for attenuators used on the scope, and hence saturate at different voltages (hence the different saturation levels). Also shown in a $sin^4\left(\frac{2\pi(t-60ns}{t_0}\right)$ approximation.

The fraction of this intensity that is absorbed by the foil can be calculated by comparison of the open and filtered PCDs on the plot. In the different experiments which will be discussed later in this chapter two different target foils have been used - $1.5\mu m$ and $3\mu m$ polycarbonate foils. These are also the foils that filter the PCDs. Assuming all emission is within the range that the PCDs have a flat response the absorption of these filters will match the energy deposition on the foil. We note that the flux incident on the foil is sufficiently small that it is unlikely that it's transmission is strongly affected.

The maximum signal on the $3\mu m$ filtered PCD is 1V, which is less than 1% of that on the open PCD. Thus at $130ns$ after start of current $6.8 \times 10^6 W/cm^2$ is absorbed on the foil (at a point 1cm from the conical shock). At later times, after the signal shown has saturated, the intensity will increase further.

As expected, the $1.5\mu m$ filtered PCD has a larger signal than the $3\mu m$ filtered, however when it saturates at $240ns$ this signal is only 10% of the saturated 140V unfiltered signal.

In order to estimate the characteristics of the wind we will use the equations given by Lindl 1995 [84] for the exhaust blow-off for an indirect-drive ICF capsule implosion. Whilst Lindl assumes a drive energy of a few hundred eV, which is significantly greater than that in our experiments, we will use the predictions from this method to obtain an order of magnitude estimate of the wind parameters. Lindl determines values the exhaust wind characteristics from a capsule, namely the mass ablation rate $\dot{m}$ and the wind velocity V_a as

$$\dot{m}_a = 10^7 \left(\frac{I}{10^{15}W}\right)^{3/4} \tag{6.4}$$

$$V_a = 1.7 \times 10^7 \left(\frac{I}{10^{15}W}\right)^{1/8} \tag{6.5}$$

Hence we can estimate how the mass ablation rate and velocity will behave, which are shown in Fig 6.4. It is seen in the figures that after $130ns$ (while the mass ablation rate is less than 30% of its maximum value) the velocity varies by less than 30% - for simplicity we will assume the velocity to be constant at a value $V_a = 2 \times 10^6 cm/s$.

The mass ablation rate and the time of flight to a given position x relative to

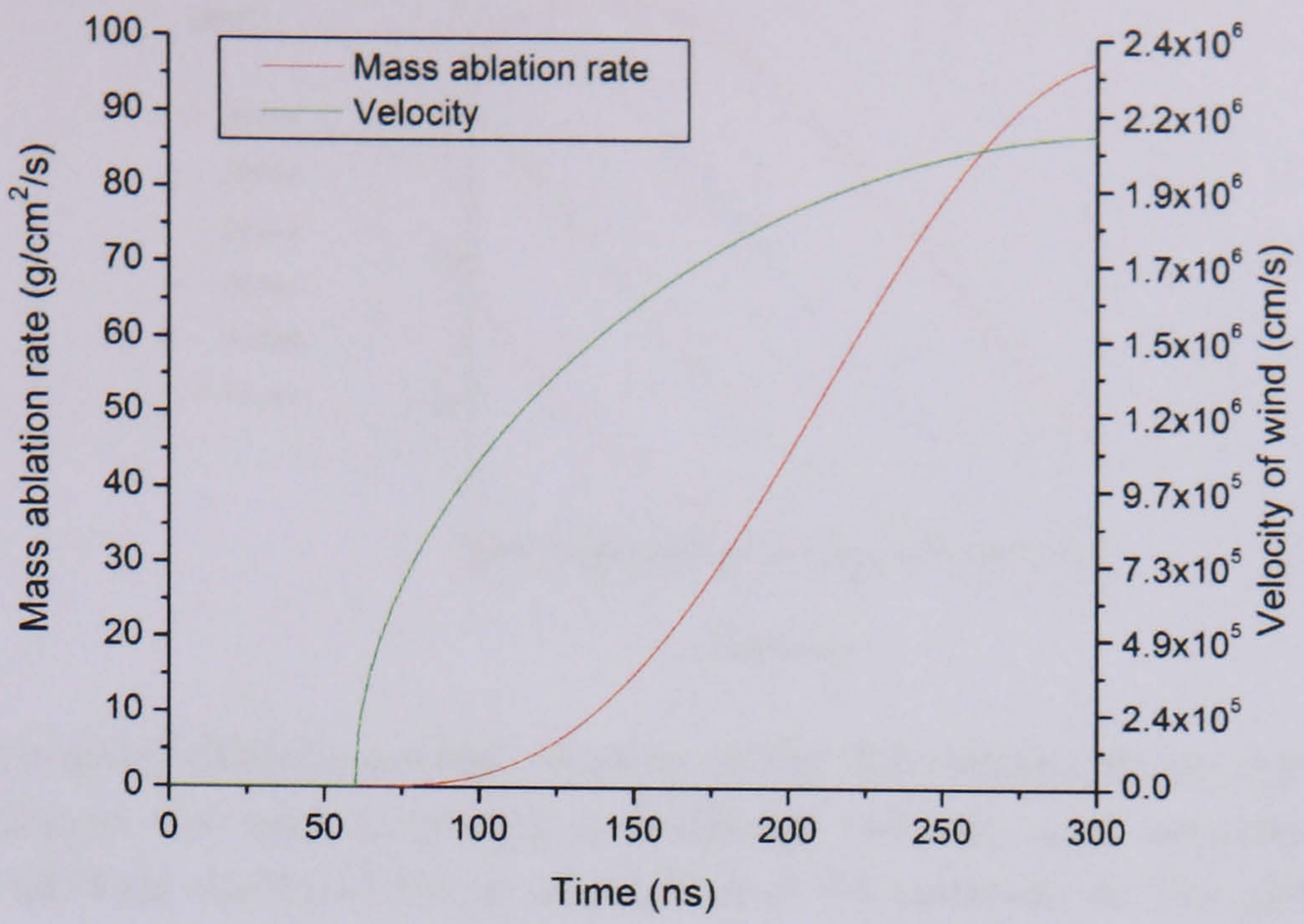


Figure 6.4: Estimated mass ablation rate and velocity of the flow from the foil based on equations 6.4 and 6.5 and a $sin^4\left(\frac{2\pi(t-60ns}{t_0}\right)$ approximation to the incident intensity (as was plotted on Fig 6.3).

the foil ($t_{fl} \sim \frac{x}{v}$) can be used to determine the density distribution relative to the foil, as is plotted in Fig 6.5. For these predictions it has been assumed that the foil is $1cm$ from the source, which is acting as a point source. Clearly areas of the foil further from the source will have a lower incident radiation, leading to a lower density in front of the foil.

6.2.2 Experiments investigating foil ablation

Experiments have been performed to compare the above model to the electron distribution from a foil ablated using a non-imploding cylindrical wire array (which has a similar x-ray pulse to conical wire arrays, but which does not produce a jet). The array had similar dimensions to the conical array used for jet deflection experiments ($16 \times 18\mu m$ W, $16mm$ diameter), and the intensity incident on PCDs are similar, except the cylindrical array emits $\sim 20ns$ earlier (corresponding to a smaller time of flight between the wires and the axis).

Two target foils are positioned vertically in a position similar to that for jet deflection experiments. The wind from each foil will be in approximately the horizontal

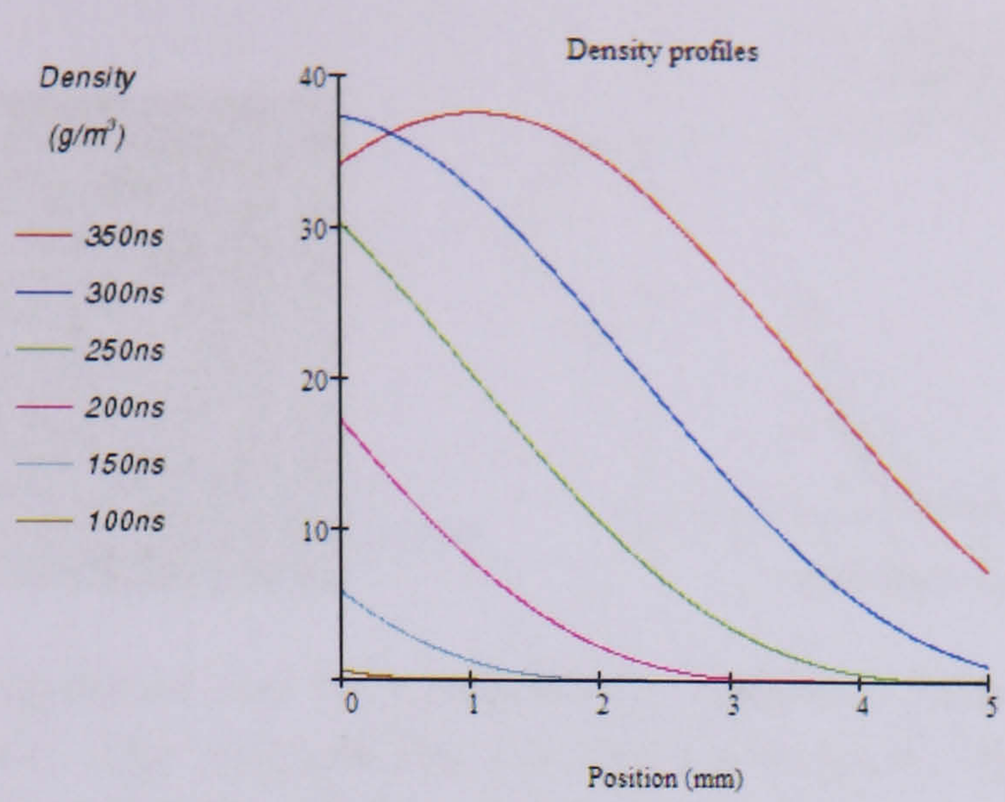


Figure 6.5: Estimated density profile relative to the foil obtained using the injection rate from equations 6.4 and assuming a constant velocity and accounting for the time of flight between material being ablated and its position at the given times.

direction towards the array axis. Figure 6.6a shows an interferogram of the two foils above the array. The separation between the two foils is sufficiently large that the winds do not interact. An area $\sim 2mm$ around the original foil positions is shown as black on the schlieren images due to deflection of the beam out of the optical system. Further from the target fringes are visible. From these fringes electron density profiles relative to each foil have been found (Fig 6.6b). As can be seen in the plot the prediction is in reasonable agreement with the data a few mm from the initial foil position. Further from the foil however the gradient in the density is lower than that predicted. This is likely to be a result of the lower velocity of material ablated at early-times, which we have disregarded in our predictions. Hence this method appears to provide an order of magnitude estimate of the wind density at $277ns$ for the region $2 - 2.5mm$ from the foil. As will be seen in the results discussed later, the experiments are generally performed at later times with the target foil nearer to $4mm$ from the jet.

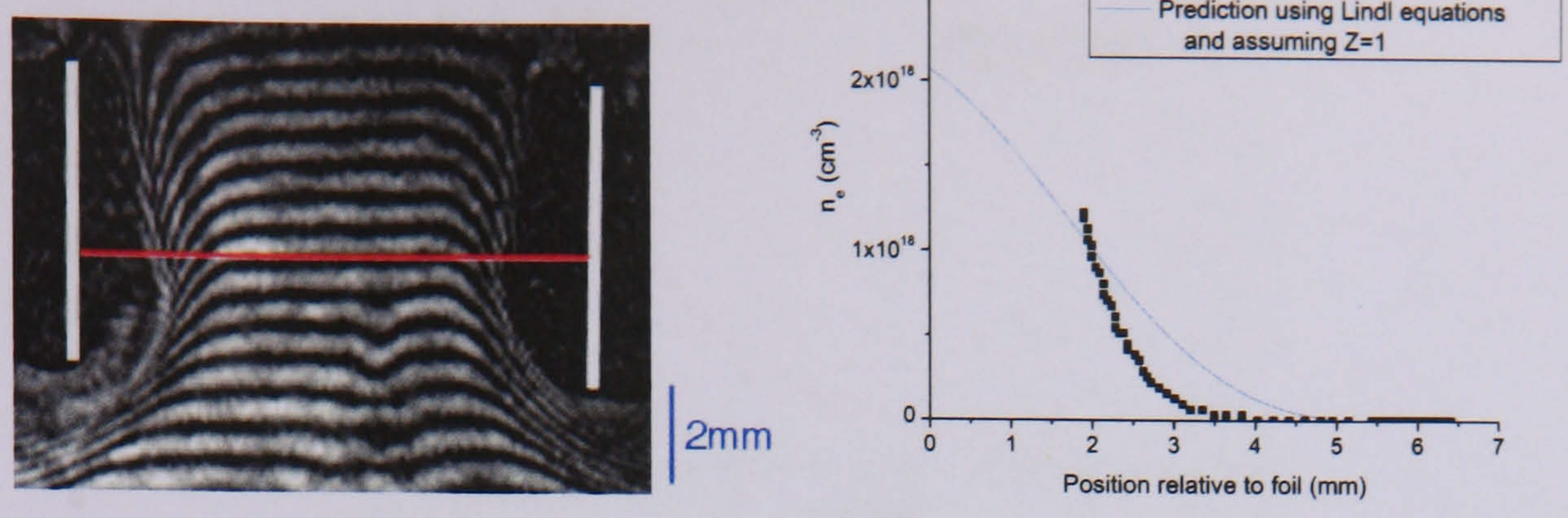


Figure 6.6: Interferogram of two foils ablated by emission from a 16 wire W cylindrical array at $277ns$. The original foil positions are shown in white. The graph shows measured and predicted electron density distributions along the red line on the interferogram. The predictions assume a charge state $Z = 1$.

6.3 Comparison of forces on the jet due to ablated material

As seen in Figures 6.5 and 6.6, the target proposed for these experiments has a significant density gradient, and hence also pressure gradient in addition to the transverse motion required to model jets propagating in a side-wind. Before beginning to discuss experimental data for jet deflection it is useful to compare the magnitudes of the forces expected due to the kinetic pressure from the wind and the gradient in thermal pressure.

First we consider the force $F_{\nabla P}$ due to the gradient in the thermal pressure. The force per unit volume can be calculated from the density gradient in the wind (assuming constant temperature and charge state).

$$F_{\nabla P} = -\nabla(P_w) \tag{6.6}$$

$$= -\frac{dN_w}{dx}(Z+1)k_bT \tag{6.7}$$

The force per unit volume due to the ram pressure F_{ram} from the wind will be

$$F_{ram} = \frac{\rho_w v_w^2 A}{V} \tag{6.8}$$

$$= \frac{\rho_w v_w^2}{r_j} \tag{6.9}$$

Figure 6.7 shows a plot of the ratio of these two forces per unit volume of the jet $300ns$ after the start of current, using the predicted density distribution found

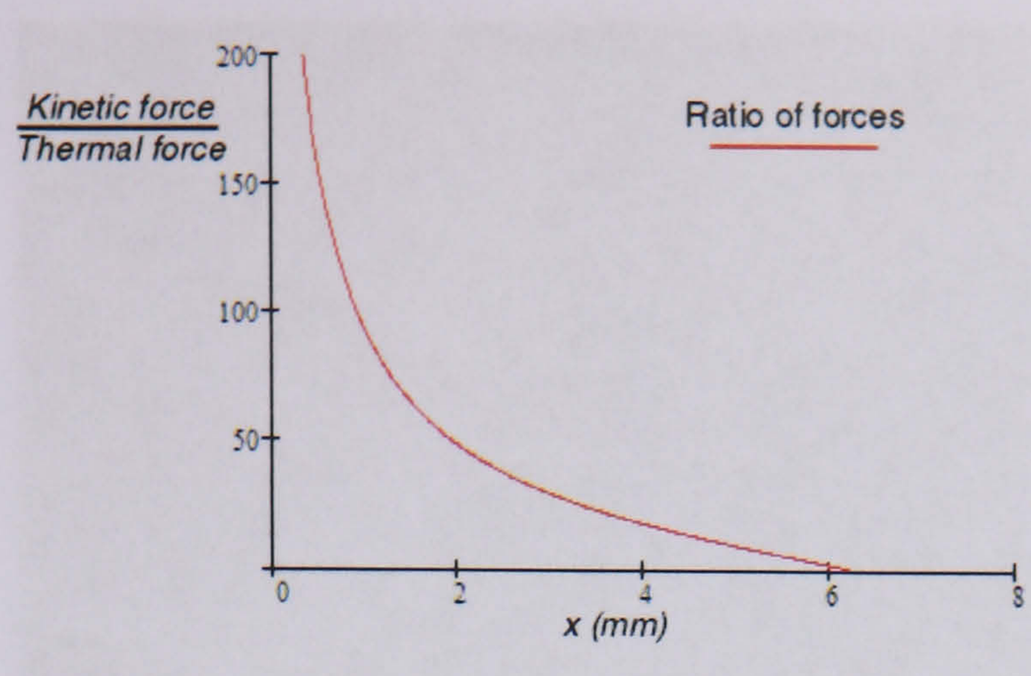


Figure 6.7: Comparison of expected forces due to a gradient in thermal pressure and momentum transfer from the wind at $340ns$. The density and velocity of the wind have been calculated using equations 6.4 and 6.5.

using equations 6.4 and 6.5 and assuming a jet radius $r_j = 0.25mm$ and charge state $Z = 1$. It is clear from the graph that, provided the distance from the foil x is less than $5mm$ (when the magnitude of both forces actually becomes negligible) the momentum transfer from the wind will lead to a force on the jet which is at least an order of magnitude greater than the force on the jet due to the gradient in the thermal pressure.

6.4 Results and discussion

6.4.1 Experiments using a short interaction region

We start our investigation of the effect of a side wind on the jet by using a wind which extends only a few jet radii along the direction of jet propagation. This setup with a short interaction length allows good diagnostic access to the system; in addition to viewing the interaction region, with a short wind it is possible to view the wire array and portions of the jet both before and after the actual interaction. This allows, for example, any change in the collimation to be seen. It will later be shown that, whilst this short interaction regime provides good diagnostic access to the deflection, the use of a longer interaction length is more relevant to the deflection of astrophysical jets (where the deflection occurs over a length of many jet radii). We will then explore the dynamics of deflection using a longer interaction region.

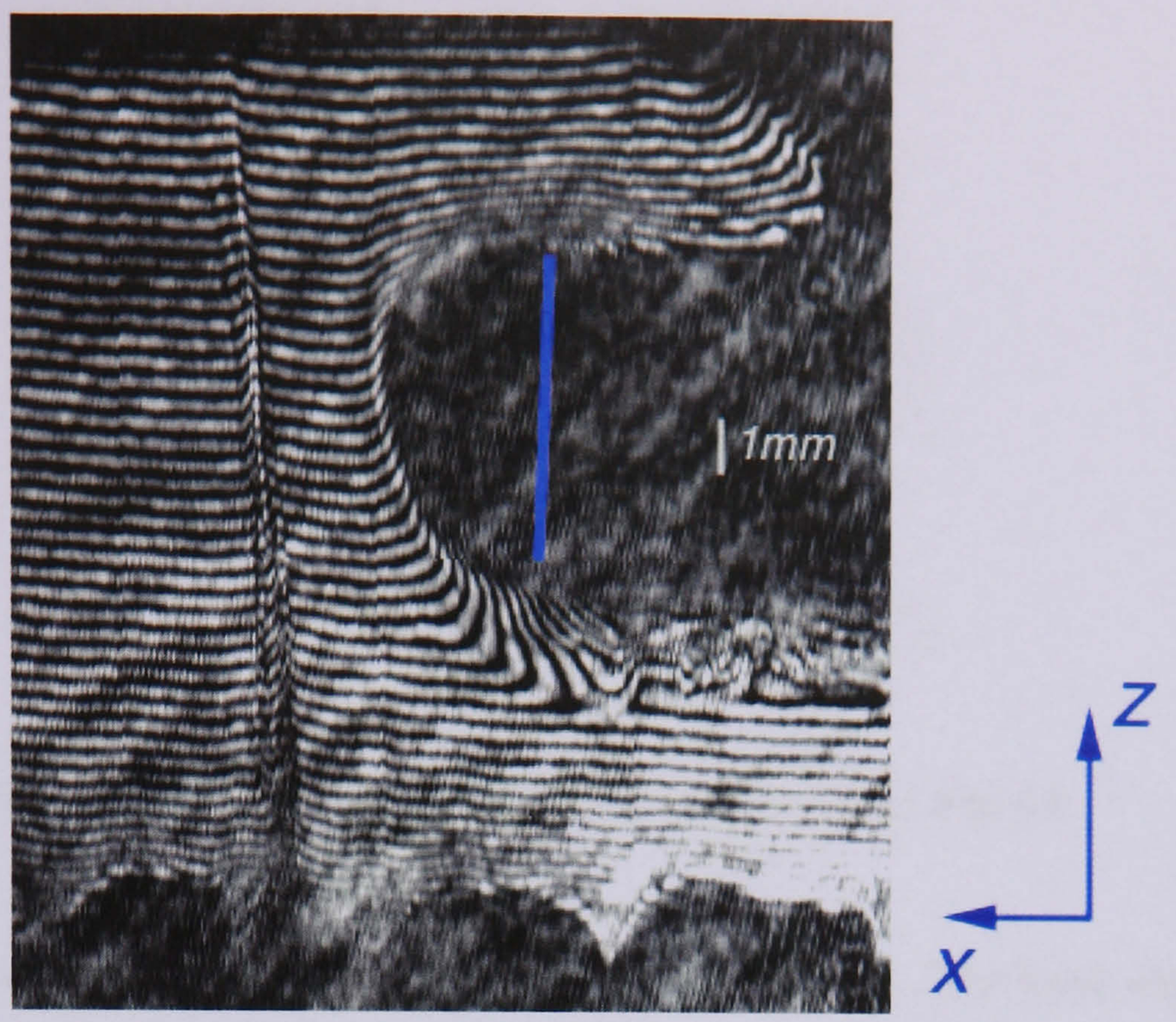


Figure 6.8: Interferometer image of jet deflection by a wind impacting a jet at $t = 303ns$. The wind is produced by a foil $4.6mm$ from the jet axis (shown by a blue line). The axes used in the discussion are labelled. The laser probe beam is perpendicular to direction of propagation of both the wind and the jet.

Figure 6.8 shows a jet passing through this short region of side-wind. The foil is positioned on the right of the image (drawn in blue on the image, $4.6mm$ from the jet axis), producing a wind which flows from right to left, and as with all previous images the jet is propagating from the base of the image. As the jet passes the foil it is deflected by the wind. The total deflection of the jet once it has left the region where the wind is present is 4°. The jet is still intact after the interaction, however it does begin to expand. Comparison of this image to schlieren images without a wind present indicates that all of the jet we are viewing in Fig 6.8 is the collapsed jet (i.e. it was ejected by a collapsed conical shock).

To measure the radius of curvature of the deflected jet we fit a quadratic function to the experimental trajectory. If the foil surface is defined as the z axis and the distance from the foil as x then the form of this fit will be

$$x = \frac{1}{2\lambda} z^2 + ... \tag{6.10}$$

where λ is the radius of curvature near the minimum value of x.

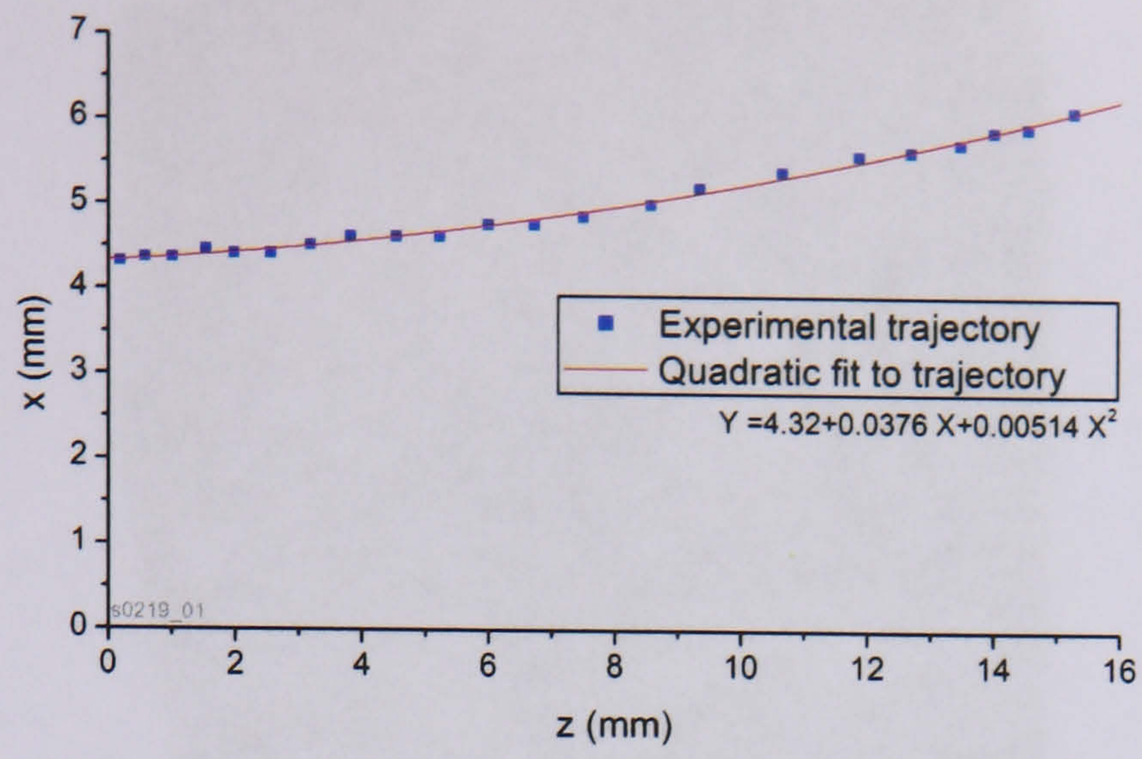


Figure 6.9: Fit to the curvature of the jet observed in Fig 6.8

Figure 6.9 shows a fit to the trajectory of the jet in Fig 6.8. The peak electron density across the jet width has been used to generate this trajectory. From the trajectory we find that the radius of curvature of the jet is

$$\lambda = \frac{1}{2 \times 0.0051} = 97mm \tag{6.11}$$

On the interferometer image (Fig 6.8) we see that the jet is expanding as it leaves the wind. This indicates that the jet has been heated in the interaction and hence has a lower Mach number. The flow is divergent with a half-opening angle $\phi = 4°$, giving a Mach number $\mathcal{M} = \frac{1}{\tan\phi} = 14$. If there is any low density wind material in the region where the opening angle has been measured then this will lead to a pressure on the outside of the jet and hence a smaller opening angle than $\tan^{-1}(\frac{1}{\mathcal{M}})$. Thus the measurement of the divergence sets an upper limit on the Mach number. Making the assumptions that the axial velocity of the jet remains constant during the interaction and any ambient pressure is small compared to the internal pressure in the jet, this Mach number implies that the sound speed of the jet has increased, and hence the temperature in the jet has increased. Figure 6.10 shows a high magnification schlieren image of the point where the jet is deflected. On this image a sharp density gradient is present (shown as a sharp white feature in the centre of the jet), which is likely to be a shock within the jet. This connects with astrophysical models that suggest that an oblique internal shock setup within the jet by the side wind is responsible for deflection of the jet [83]. As material crosses

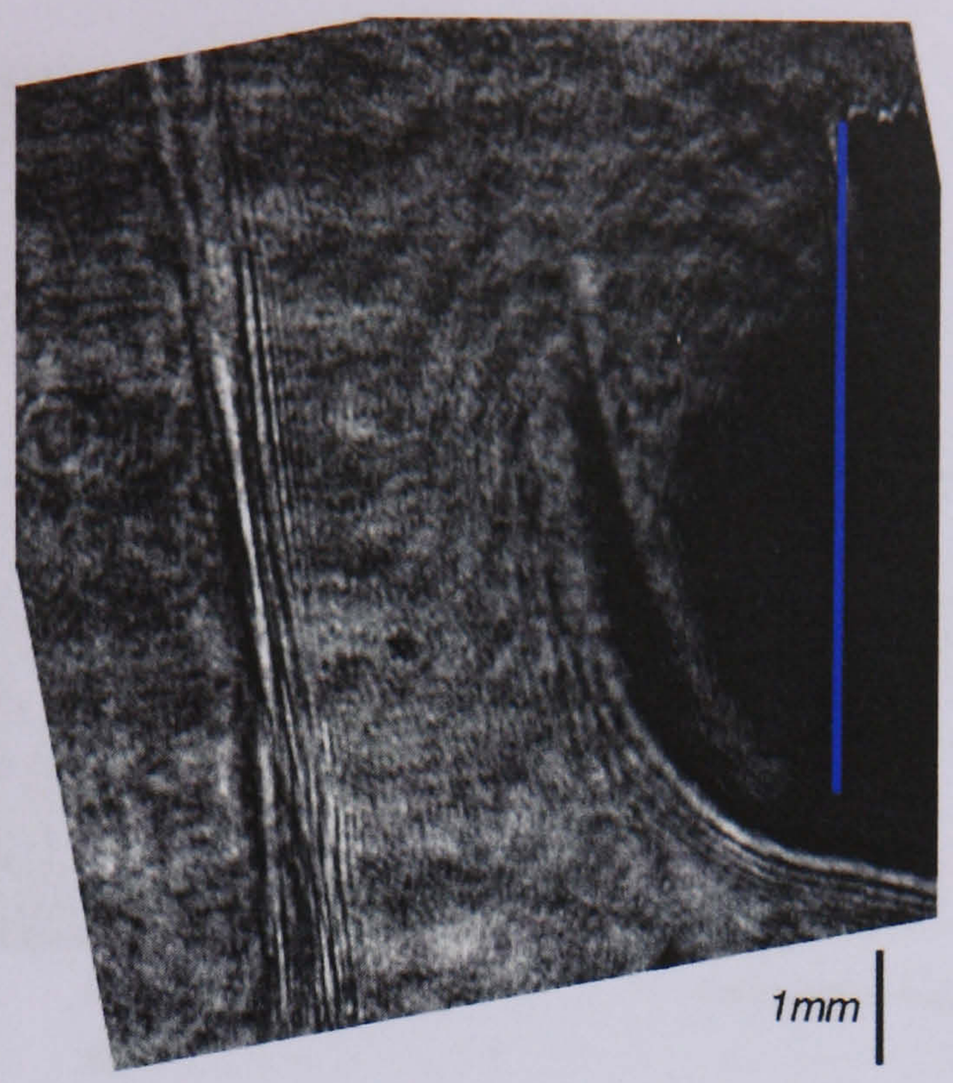


Figure 6.10: High magnification schlieren image of the deflected jet in Fig 6.8 at $303ns$.

this oblique shock it will be heated, causing an increase in the sound speed. The shock can also be seen on the interferometer image, however is made more clear by examining the electron density distribution across the jet at various axial positions (Fig 6.11). The expansion of the jet as it leaves the wind is also clear on these line-outs.

Although we have seen that the interaction in our experiments results in the heating of jet material from its pre-deflection temperature we will now see how the result compares to the astrophysical model for the isothermal deflection of jets by Canto & Raga 1995 [82].

The equation from Canto & Raga for the calculation of the radius of curvature (Equation 6.1) uses the sound speed in the jet. Whilst we can determine an approximate sound speed from the jet divergence after the deflection this will be significantly affected by radiative cooling after the deflection. Instead we will rearrange equation 6.1 to calculate the sound speed of the deflected jet using the experimental radius of curvature, and then compare the sound speed with the divergence of the jet.

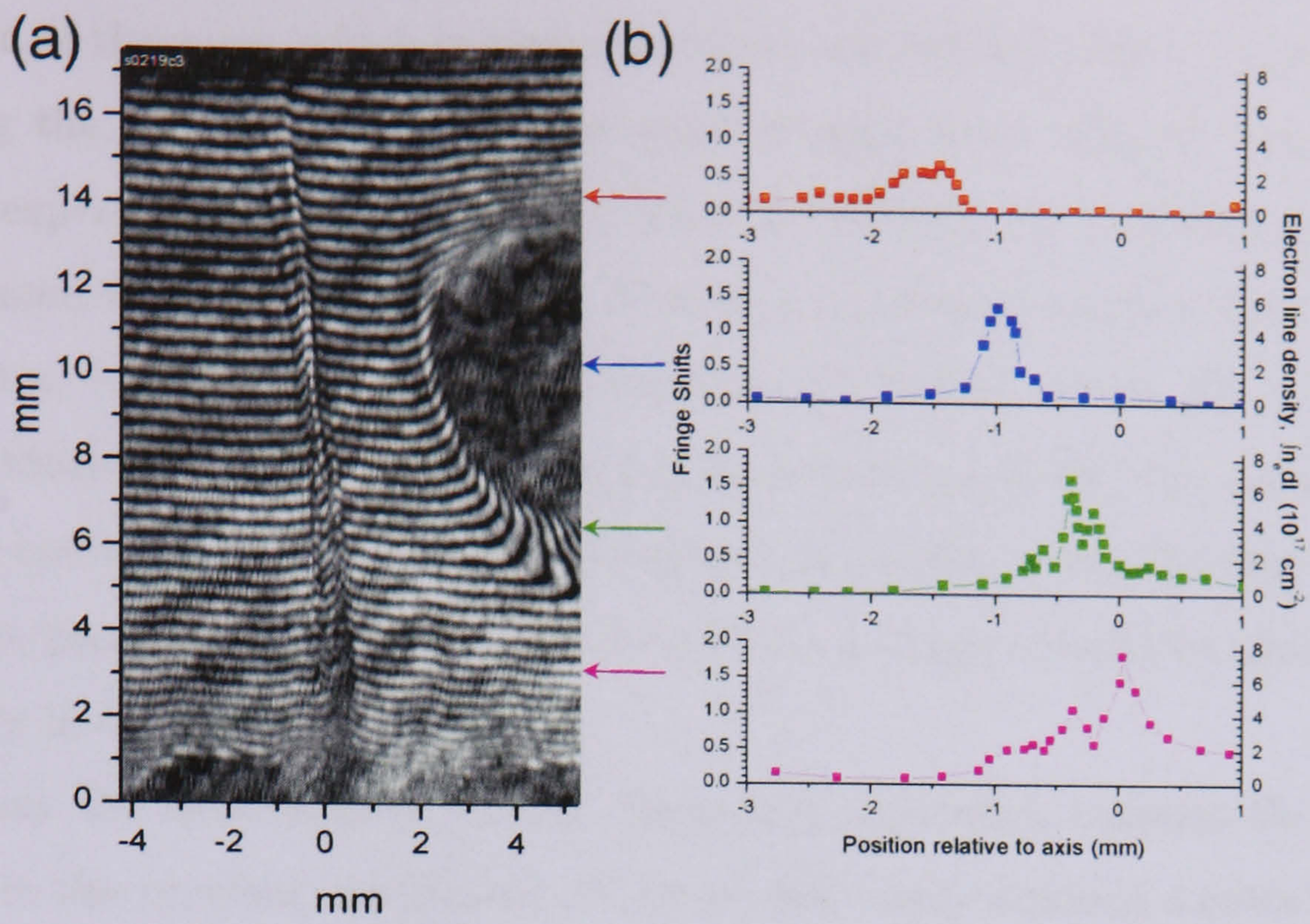


Figure 6.11: Line integrated electron density profiles (b) at the marked axial positions on the interferometer image (a) (which is identical to Fig 6.8). Note that the path length through the wind is ~ 20 times the path length through the jet.

Rearranging equation 6.1 for the sound speed gives

$$c_s = \sqrt{\frac{\dot{M}_j v_j^3}{\pi \lambda^2 \rho_w v_w^2}} \tag{6.12}$$

In order to use this equation we require values for the density and velocity in both the jet and wind. The model developed earlier (in chapter 3) predicts the mass flux in the jet as $\dot{M}_j \approx 8 \times 10^{-3} kg/s$. This is equivalent to a mass per unit length of $\frac{M}{L} \approx 7 \times 10^{-8} kg/m$, which is in agreement with the electron density in the jet if a charge state of $Z \sim 2$ is used. Using the equations from Lindl [84], and assuming the wind velocity is a constant $v_w = 2 \times 10^4 m/s$, we find that the mass density of the wind $4.6mm$ from the target at $300ns$ will be $\rho_w \sim 2.5 \times 10^{-3} kg/m^3$. Fringe measurements on the image (given that the target is $1cm$ along the direction of the probing laser beam) gives an electron density of $4 \times 10^{17} cm^{-3}$. The charge state of the wind is hard to determine as it is likely that, as well as the wind heating the jet, the jet will also heat the wind, thus altering the charge state. The ratio of the predicted ion density and measured electron density indicates an ion charge state $Z \sim 2$, which is consistent with the shocks causing a slight heating and increase in

ionisation of the wind (which is assumed to have an initial charge state $Z \sim 1$).

Using the predicted values for the wind density, wind velocity and jet mass flux, an experimentally based estimate of the jet velocity ($v_j \approx 220km/s$) and the experimental radius of curvature ($\lambda = 97mm$) in equation 6.12 gives a sound speed in the jet $c_s \sim 30km/s$. Thus the Mach number of the flow will be $\mathcal{M} \sim \frac{220}{30} = 7.7$.

This Mach number calculated using the isothermal model by Canto & Raga is of a similar order to that determined by expansion of the flow, hence for this case with a low ram pressure on the jet the model by Canto & Raga reasonably describes the trajectory of the jet.

To vary the wind density we can change the separation between the foil and the jet. In the previous experiment the target foil was positioned $4.6mm$ from the jet axis; we will now look at the effect of moving the foil closer to the jet, which will provide a more dense wind. Figure 6.12 shows an interferometer image of the deflection of a jet by a target that is positioned $2.4mm$ from the array axis. This image is taken at a similar time to the previous images ($t = 306ns$), but the deflection is much more distinct, with a total deflection angle of 30°. From the interferometer image a radius of curvature $\lambda = 16mm$ has been calculated to fit the complete trajectory. The earlier method for calculating the wind density predicts that the wind density will be $\rho_w \sim 2 \times 10^{-2} kg/m^3$. As we are looking at a similar time and axial position as in Fig 6.8 the mass flux in the jet will be $\dot{M} \sim 8 \times 10^{-3} kg/s$.

We can now compare this second experiment with the model by Canto & Raga. Equation 6.12 estimates a sound speed in the jet $c_s \approx 100km/s$. Assuming the jet velocity is still $v_j \sim 220km/s$ this corresponds to a Mach number $\mathcal{M} \approx 2.1$.

Due to the high deflection angle in this experiment the jet does not remain in a constant wind density; as the jet moves away from the foil the density of the wind will drop. Figure 6.13 shows a high magnification schlieren image of this deflection in this second configuration. This higher magnification image allows us to fit the jet trajectory in specifically the region where the sharpest deflection is occurring. We find a radius of curvature $\lambda = 4 \pm 1cm$, from which the Canto & Raga model implies limits on the Mach number

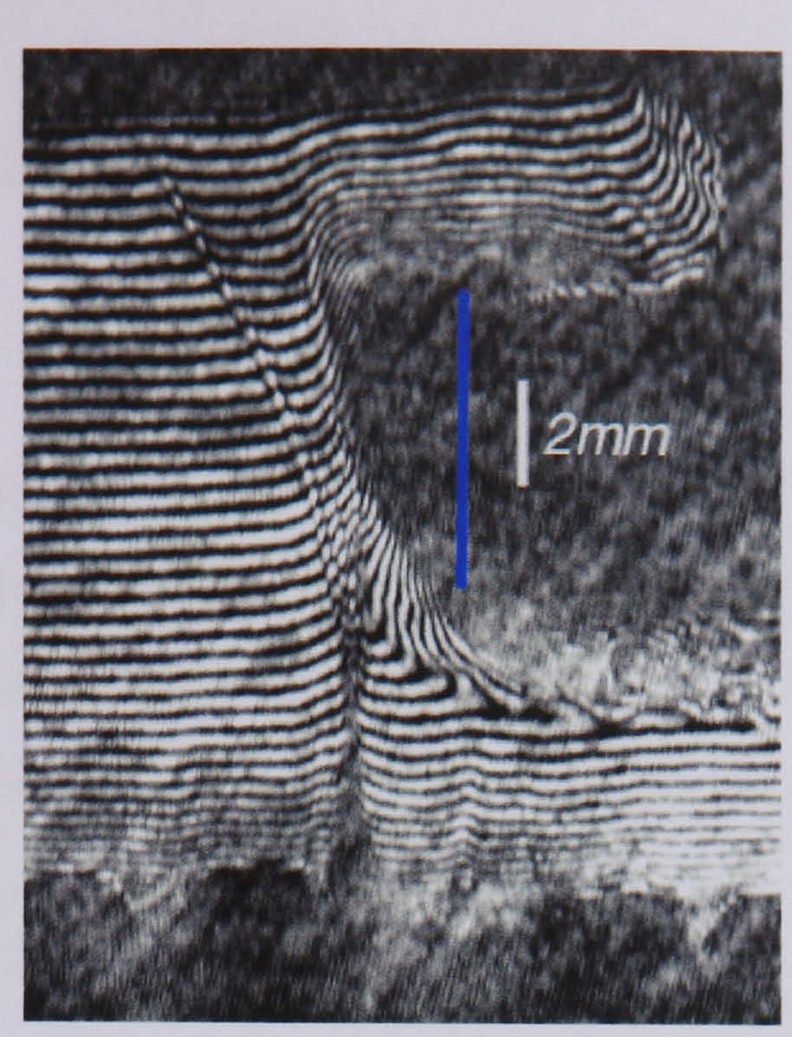


Figure 6.12: Interferometer image of jet deflection by a wind impacting a jet at $t = 306ns$. The wind is produced by a foil $2.4mm$ from the jet axis (i.e. closer to the jet axis than in Fig 6.8, hence with a higher wind density)

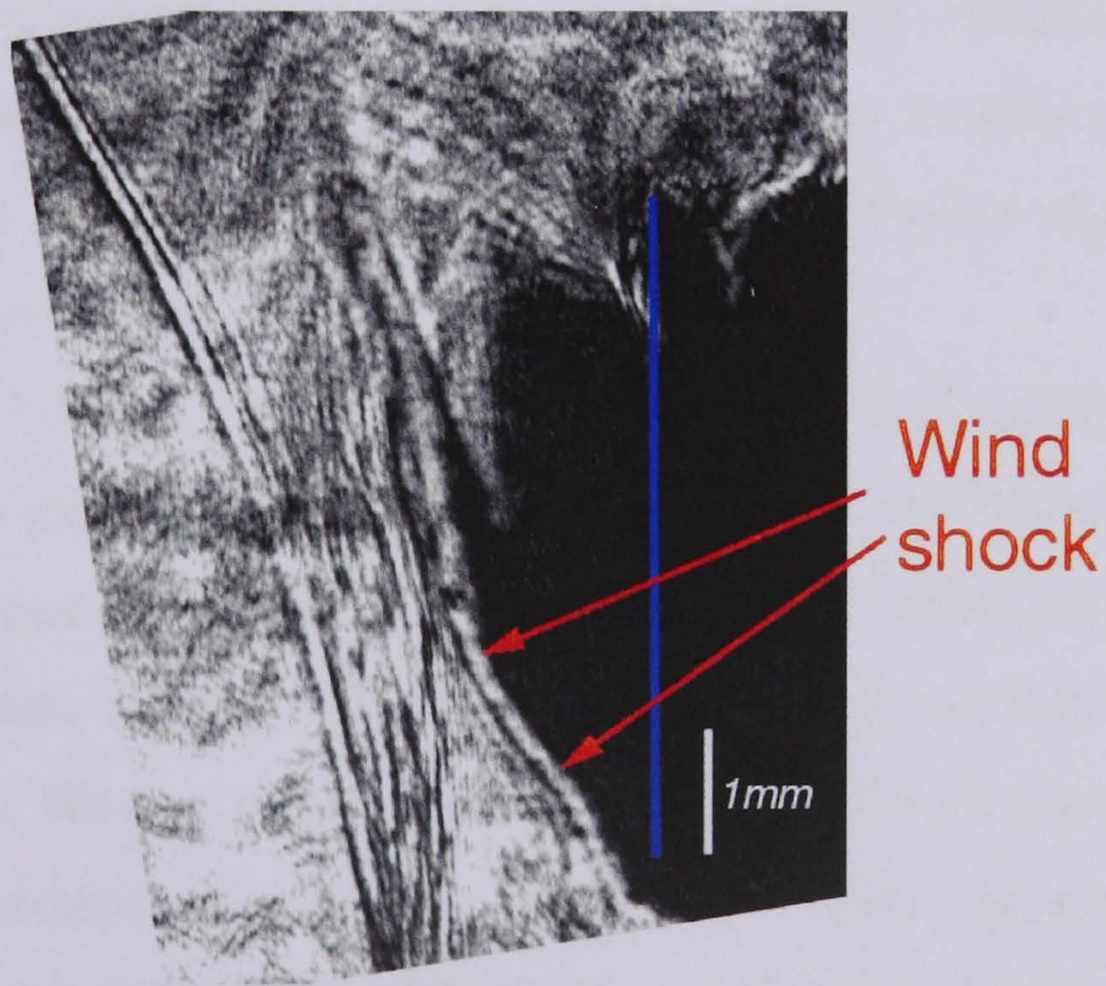


Figure 6.13: High magnification schlieren image of the same experiment as Fig 6.12.

$$2.5 \leq \mathcal{M} \leq 9.8 \tag{6.13}$$

The larger limit on the Mach number ($\mathcal{M} = 9.8$) gives an opening angle of the flow

$$\phi = tan^{-1}\left(\frac{1}{9.8}\right) = 6° \tag{6.14}$$

From the interferometer image (Fig 6.12) we see that the opening angle of the well defined flow after it has left the wind is small ($\phi \leq 1°$). One possible explanation for the disagreement between the model by Canto & Raga and our results is seen by studying the details of the deflection in the high magnification schlieren image (Fig 6.13). At the base of the image the jet is seen expanding with a full opening angle 10° (hence $\phi = 5°$). As this right extent of the jet meets a shock in the wind the sharp density gradient ceases. This shock in the wind is probably produced by the interaction of the halo around the jet with the wind. A similar shock in the wind was seen earlier in Fig 6.8, however it was far from the jet, thus did not affect the jet propagation. It is unclear in the interferometer image of this second experiment (Fig 6.12) whether the right boundary of the jet is completely disrupted (and continues to propagate as a less collimated flow), or this portion of the jet is deflected by the shock into the left extent of the jet, producing a highly collimated flow. We note that whilst the most obvious feature of the jet on the interferometer has a radius $r_j \sim 100\mu m$, this is surrounded by a lower density, broader plasma flow, which is approximately $1mm$ wide.

For the second experiment just described (Figures 6.12 and 6.13) the jet is bent out of the higher density wind near the target, hence the density of wind incident on the jet is a strong function of the axial position. Thus any conclusions using the model by Canto & Raga (which assumes constant ambient density) with this setup are limited. We now consider for what distance the jet should be subjected to a constant ram pressure to produce a quasi-steady state interaction (as is the case for astrophysical jet deflections). We have seen that shocks (both internal oblique shocks and shocks in the wind) play an important role in the deflection of the jet. To study the behaviour and effect of these shocks fully they should be allowed to develop in approximately constant ambient conditions.

A shock will cross the jet in a time less than the ratio of the jet radius and the sound speed ($t_{cross} < \frac{r_j}{c_s}$). The maximum time that the jet is influenced by the side-wind (of length d_{target}) is $\frac{d_{target}}{v_j}$. Hence for a shock to be allowed to cross the jet (and potentially be reflected) the transit of the shock should be less than the time that the jet is influenced by the wind:

$$\frac{d_{target}}{v_j} > t_{cross} \sim \frac{r_j}{c_s} \tag{6.15}$$

This can be rearranged to incorporate the definition of a Mach number $\mathcal{M} = \frac{v_j}{c_s}$:

$$\frac{d_{target}}{r_j} > \mathcal{M} \tag{6.16}$$

For the case discussed above, if we assume the best case of the jet remaining in the a constant wind density for the full length of the foil, then the length of the interaction was $\sim$ 10 jet radii, however the jet Mach number was $\sim$ 20 (the actual Mach number depending on the heating of the jet during the interaction). This clearly does not satisfy equation 6.16, so a longer interaction length is required. Using a longer interaction also minimises the consequences of any end-effects of the target, such as the shock between the wind and the jet halo. Thus the full trajectory of the jet and internal structure is better studied using a longer target and hence interaction region.

Clearly just extending the length of the target will not eliminate the problem of the jet being deflected out of the denser portion of the wind. If we angle the target with respect to the jet axis we can minimise the dependence of the distance between the foil and jet on axial position. If the distance between the jet and foil is approximately constant then the wind density incident on the jet will also be approximately constant.

6.4.2 Results using a more uniform wind

To provide a more uniform ram pressure on the jet we can use a longer, angled foil as shown in Fig 6.14. The angled foil will produce an ambient flow that is no longer perpendicular to the jet, but instead has a downward component. A ram pressure that is not perpendicular to the initial direction of jet propagation is in fact highly

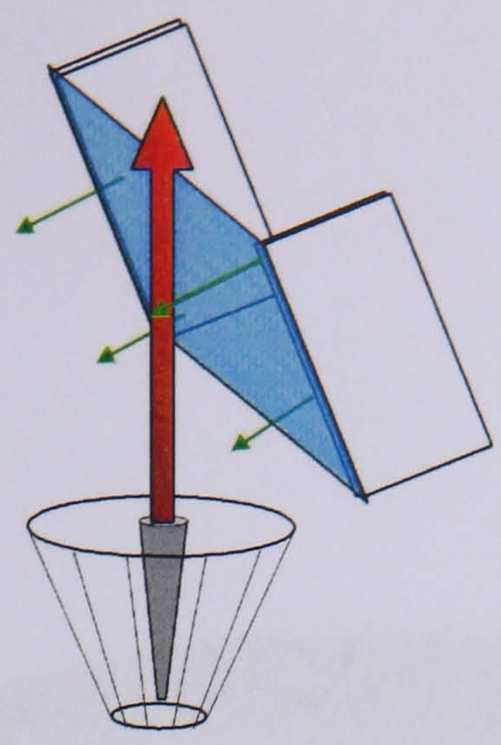


Figure 6.14: Setup with a longer, angled target

relevant to the deflection of astrophysical jets as it is rare for a star's ejection axis to be perpendicular to the direction of motion of the star through the ISM [82]. By using an angled target it is possible to study the 'stagnation point' of the side wind (the point where the wind is perpendicular to the jet, which is where the model by Canto & Raga [82] can be applied independent of whether the interaction is isothermal or adiabatic). In experiments with a straight target (such as in the previous two experiments described) the stagnation point is near the base of the interaction. At the base of the target there are likely to be end effects present, for instance a cylindrical divergence of the wind, a fairly rapid change in jet to ambient density ratio, imperfections in the lower edge of the target foil before the experiment and the shocks between the low density halo and the target foil. Thus if the target is vertical then the region near the stagnation point is perturbed by end effects.

Figure 6.15 shows a schlieren image of the deflection of a jet in this modified configuration. As with the previous images the jet is propagating from the base of the image and the wind is flowing from right to left.

The interaction of the jet is much more complex than was seen in any of the previous images, with numerous shocks present between the jet and foil. We will start by studying the deflection of the main body of the jet before moving our attention to the various other shocks present.

The axial position of the tip of this curved portion of the jet (at the left of the

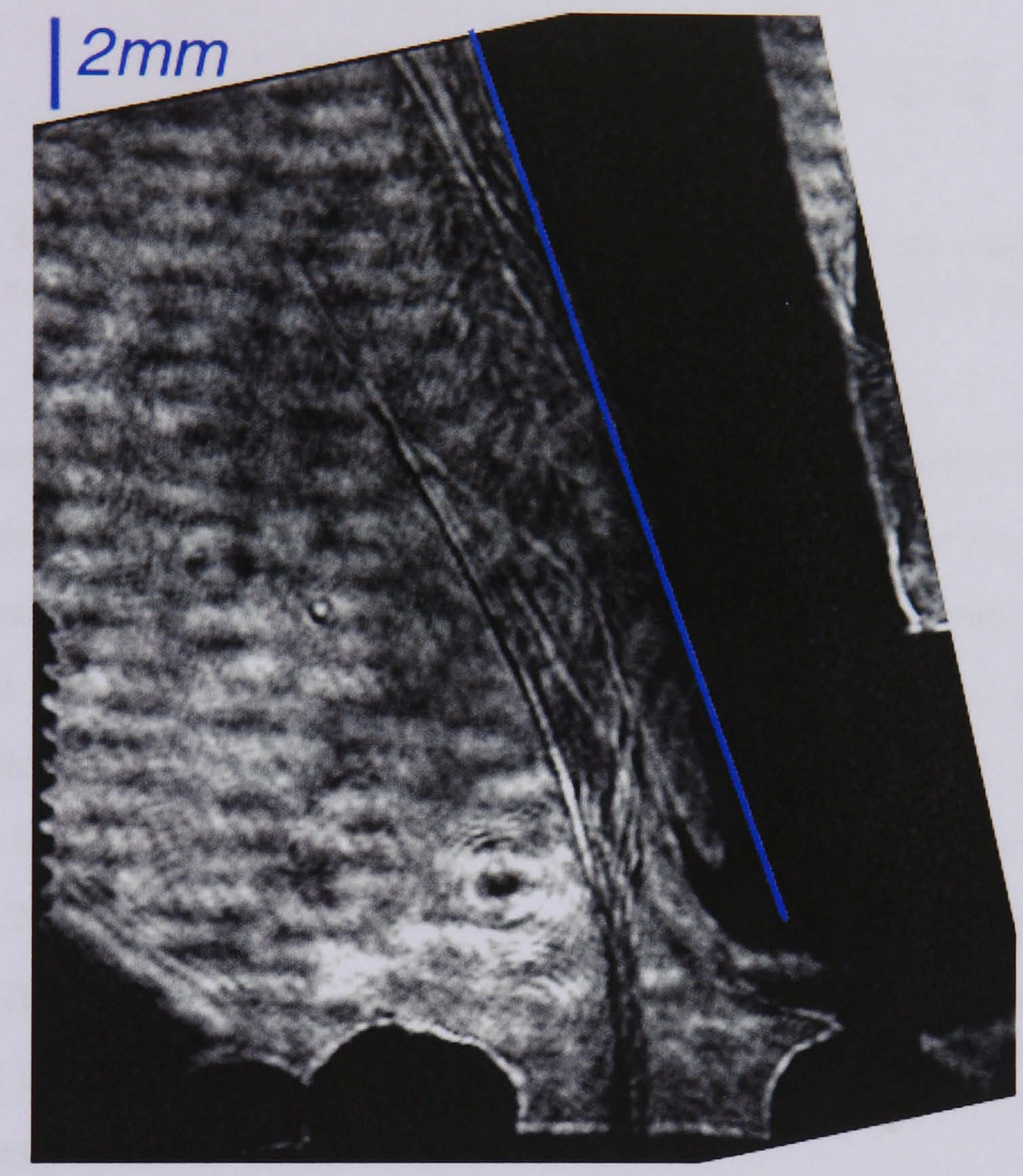


Figure 6.15: Schlieren image of a jet deflected by a longer angled target at $343ns$. The initial foil position is marked in blue. For a more detailed labelling of features on this image see Fig 6.18 later.

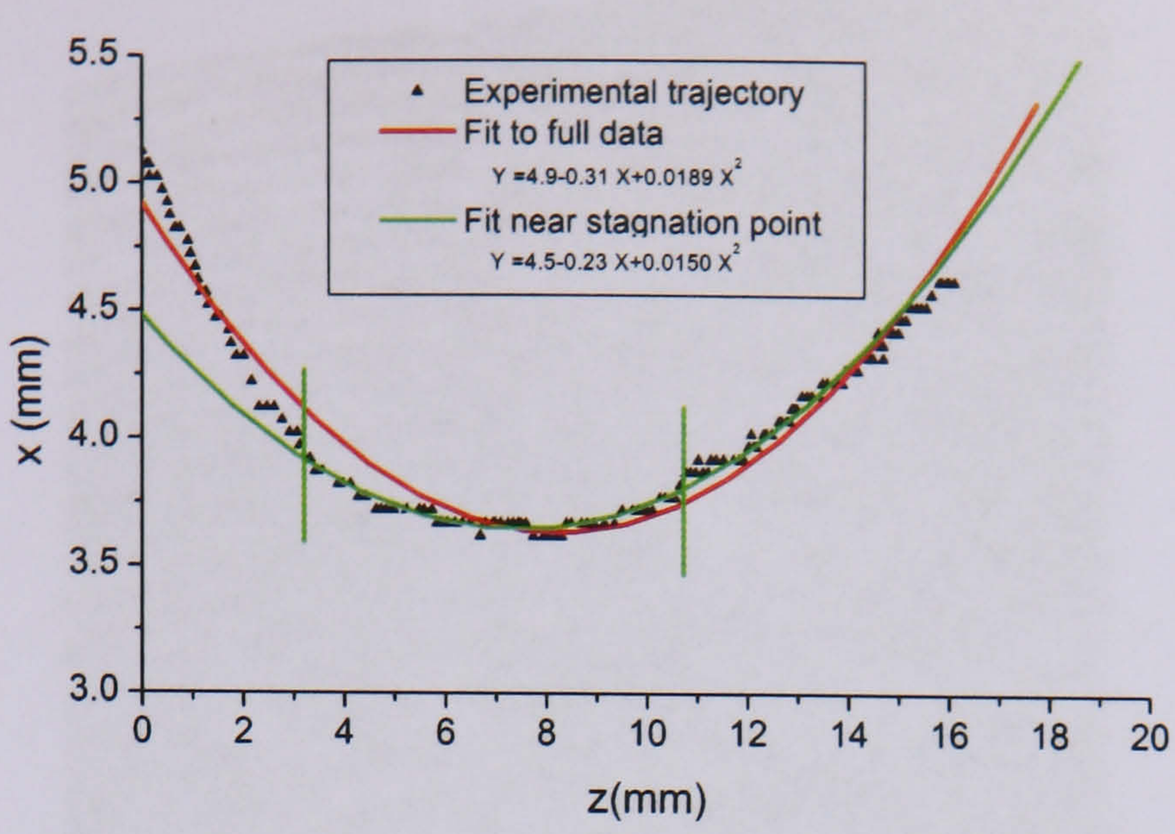


Figure 6.16: Fit to the trajectory in Fig 6.15. The z-axis is the position along the jet, and the x-axis is the distance from the original position of the foil.

interaction) corresponds to the expected axial position of the tip of a jet propagating in vacuum, so our discussion is concerned with the post-collapse jet. The graph in Fig 6.16 shows the measured trajectory of the jet. Shown in red is a quadratic fit to the full length of the jet. This quadratic does not provide a good fit to the trajectory, which is expected as the base of the jet ($z = 0 - 3mm$) is not in the wind. If we choose to limit the fit to the region of the jet near the stagnation point (say $z = 3.1 - 10.7mm$, as shown in green on the graph), then we find a much better fit to the data. It is interesting that, not only is this function matching the data in the region where it was fitted, but it also fits the trajectory further from the wire array (except for very near the tip of the jet).

Near the stagnation point the radius of curvature is determined as $\lambda \sim 33mm$. As the timing of the diagnostics is later than the previous case (now $341ns$) we estimate the jet velocity at the stagnation point to be significantly less than the tip velocity, say $v_j \sim 120km/s$ and the mass flux in the jet should be $\dot{M} \sim 0.086kg/s$. The density of the wind at the stagnation point should be $\rho_a \sim 0.017kg/m^3$.

Now that we know the parameters for this interaction we can compare the model by Canto & Raga to the experiment. Using equation 6.12 we find that the predicted sound speed is $c_s \sim 60km/s$, which corresponds to a Mach number of the jet $\mathcal{M} \sim 2$. This is not in agreement with Fig 6.15, which shows a reasonably well collimated

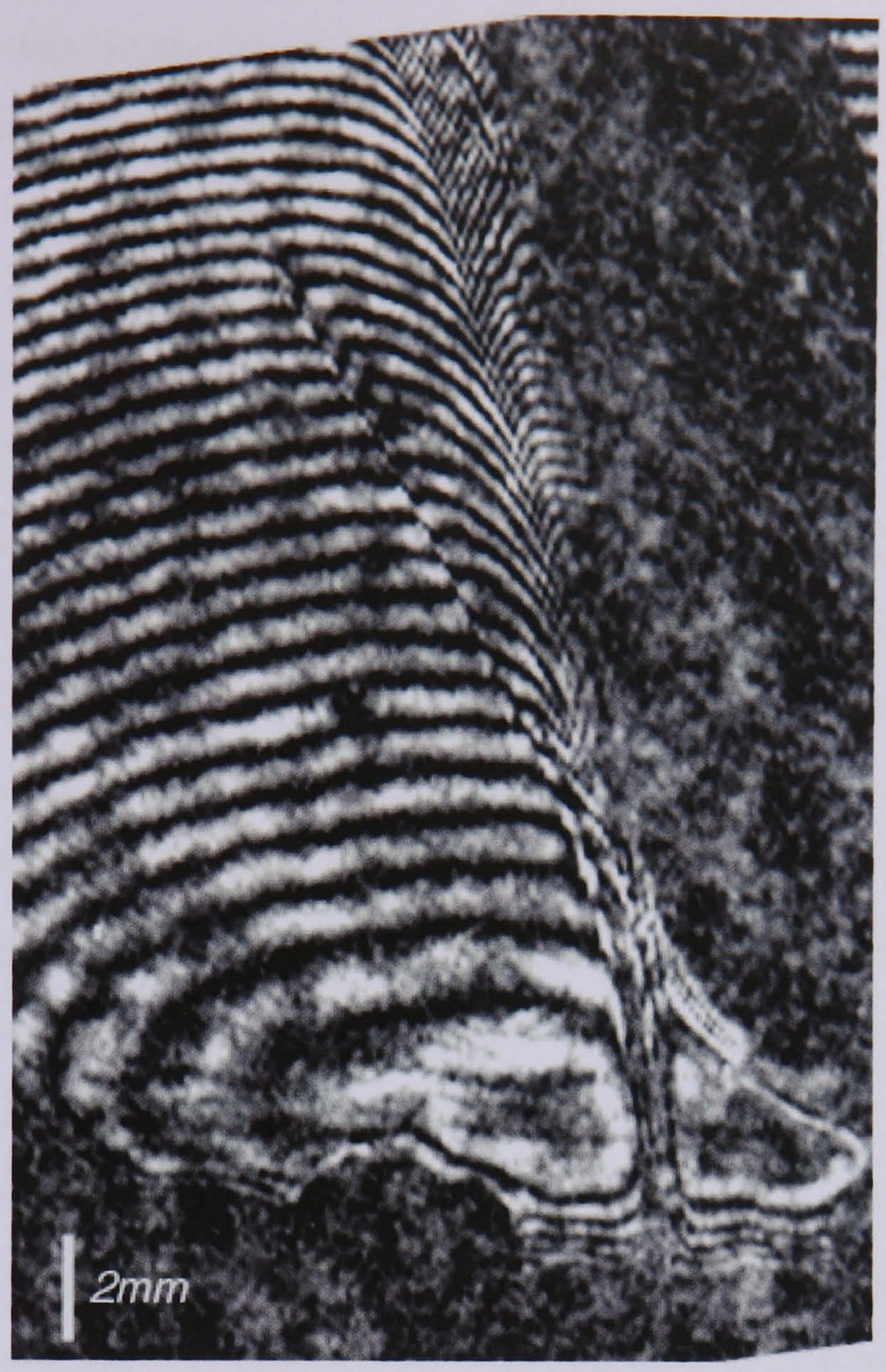


Figure 6.17: Interferometer image of the same experiment in Fig 6.15 at $343ns$.

jet after the deflection. If we look at an interferometer image of this experiment (Fig 6.17) we see that, as for the short interaction case, the jet is actually wider than the well defined edge that is seen on the schlieren image. This broader flow, which extends for $\sim 1mm$ upwind of the sharp edge, is still well collimated with a divergence angle $\phi \sim 3°$. If we look at high magnification schlieren image of the stagnation point (which is shown later in Fig 6.18c), then we find an initial divergence angle of $\phi \sim 6°$ although, as for the earlier short interaction experiments, it is unclear whether this material is then deflected back into the jet or is completely disrupted. The jet density is much higher than the ambient density ($\rho_j > 10\rho_a$) hence the jet should expand at approximately the sound speed. For the Mach number $\mathcal{M} = 2$ found using the model by Canto & Raga, we would expect a divergence angle $\phi \sim 26°$, however we have seen in Fig 6.17 a much smaller divergence ($\phi \sim 3°$).

If we calculate the temperature corresponding to a sound speed $c_s = 60km/s$ we find that the temperature will be many hundreds of eV. If the jet had such a temperature then x-ray framing cameras with CHO filters (therefore $h\nu > 120eV$) would be able to image the emission. No emission is imaged on such cameras, indicating that the temperature is less than $\sim 60eV$, hence $c_s = 60km/s$ is an over-estimate of the sound speed.

We now explore possible explanations why the model by Canto & Raga has not properly described our experiments. Firstly the model is derived for a completely isothermal system, whereas our experiments have a finite radiative cooling length. However we are investigating the deflection near the stagnation point, and it has been shown by Canto & Raga [82] that the solution is valid near the stagnation point even for an adiabatic deflection. Also 3D radiative hydrodynamic simulations by Raga & Lim [83] have found that the radius of curvature calculated by Canto & Raga is a good fit to the simulated trajectory.

Secondly whilst we have estimates of the jet and wind parameters ($\rho_a, \dot{M}, v_a, v_j$) which appear to fit the experimental data, many of these estimates are probably only accurate to within an order of magnitude. Also we note that Canto & Raga assume a constant mass flux in the jet however in our experiments we have an increasing mass flux from the tip of the jet to the top of the conical shock. Similarly, although we have attempted to reduce any axial change in the wind density along the flow, the wind density does still increase with time. If this was affecting the trajectory of the jet, then we would expect that the measured trajectory would depend on the scale of the fit. By decreasing the length of the trajectory fitted in Fig 6.16 we find only a small change in the radius of curvature unless we choose a scale sufficiently small that measurement errors dominate the fit. Thus it appears that the temporal and spatial variations are unlikely to have significantly affected the jet trajectory.

An important difference between our laboratory experiments and the simulations by Raga & Lim is that in our experiments the jet and wind are different materials. The rates of radiative cooling are very different between the high Z jet material (W) and the low Z wind material (C, H & O). Hence the temperature of each material will be different. Also the pressure is dependent on number density - thus the ambient

pressure confining the jet may be greater than if a single material was used.

We conclude that in our experiments we have seen the deflection of a jet without a major effect on the collimation. It is likely that radiative cooling and 3-dimensional effects have enabled the jet to remain collimated. Furthermore we find that the models used to fit such interactions in astrophysics can be used to fit the trajectory, but do not correctly determine the parameters of the flow, although the reason for this is unclear.

We now turn our attention to the many other shocks in the schlieren image. It is possible that such shocks play a role in the improved collimation of the jet compared to the astrophysical models. For clarity this image has been repeated in Fig 6.18, along with another copy with the different shocks that will be discussed drawn and labelled. Also shown in this figure is a high magnification schlieren image of the base of the foil and the start of the jet deflection.

At the base of the target we expect a downward component to the wind. On the schlieren image (Fig 6.18a) two shocks present where the downward travelling wind meets the upwards travelling halo plasma leaving the wire array (labelled Halo shocks). The two shocks are better resolved on the high magnification image (Fig 6.18c). The lower of these two shocks is a shock in the halo and the upper is a shock in the wind.

On the high magnification image (Fig 6.18c) we see that there is an internal shock in the centre of the jet (labelled OS1). As with the earlier experiments with a shorter interaction this is likely to be the oblique internal shock responsible for the initial deflection. We see that this internal shock is not straight, but instead bends each way by a few degrees. It is interesting to note that the most pronounced of these bends coincides with a continuation of the shock in the halo flow. Thus it is likely that this bend in the internal shock is associated with a change in the ambient density. Further experiments would be required to confirm whether this is in fact a real effect from the shock in the halo, or coincidence.

Further along the jet-wind interaction on the low magnification image (near the stagnation point) we see a lot of structure between the foil and the jet. The two most obvious of these shocks are labelled OS2 & WS2. In this image it is unclear what

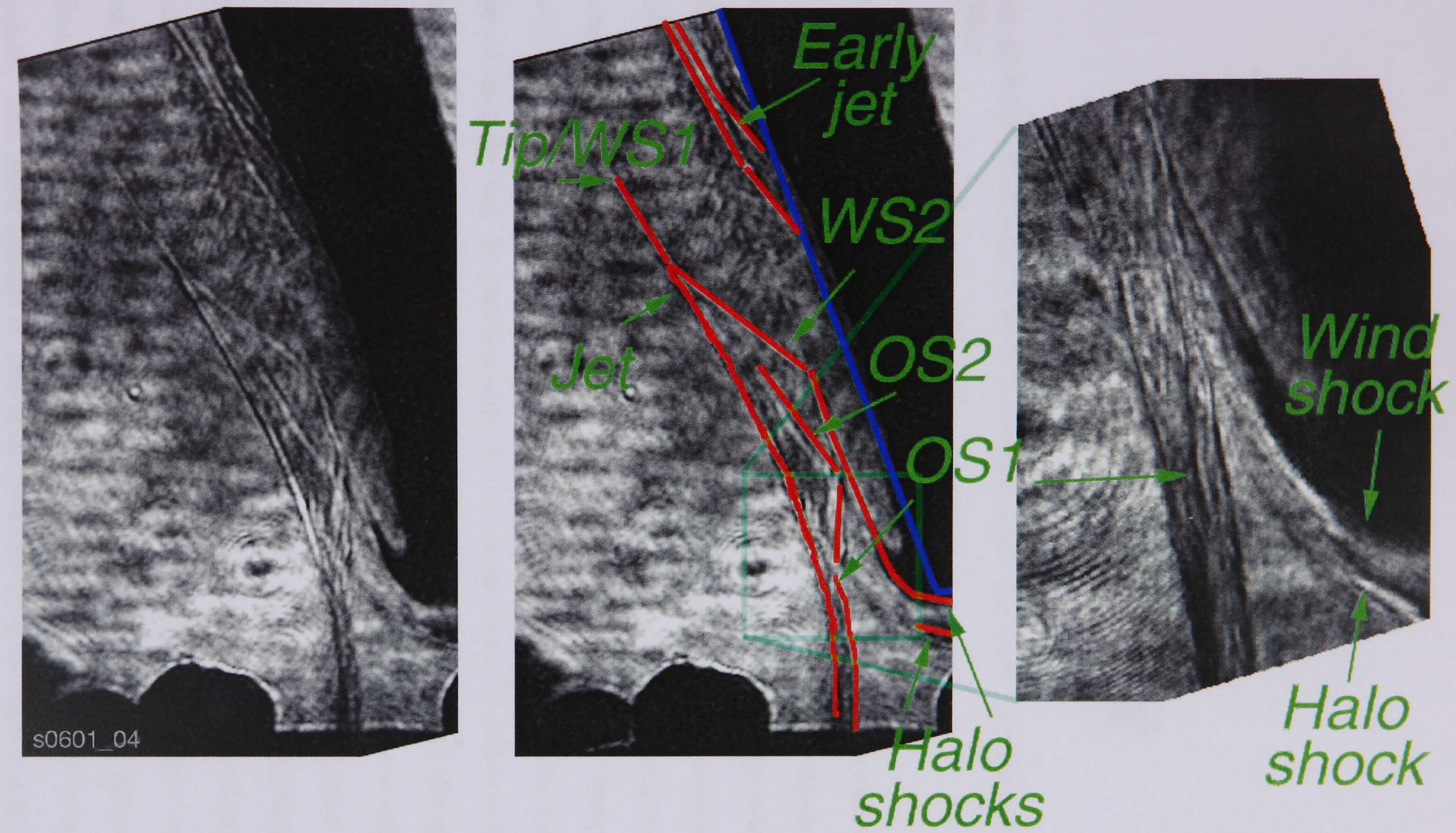


Figure 6.18: Shocks within the jet shown by both high and low magnification schlieren images (both at $343ns$). The labels on the centre image are discussed in the text.

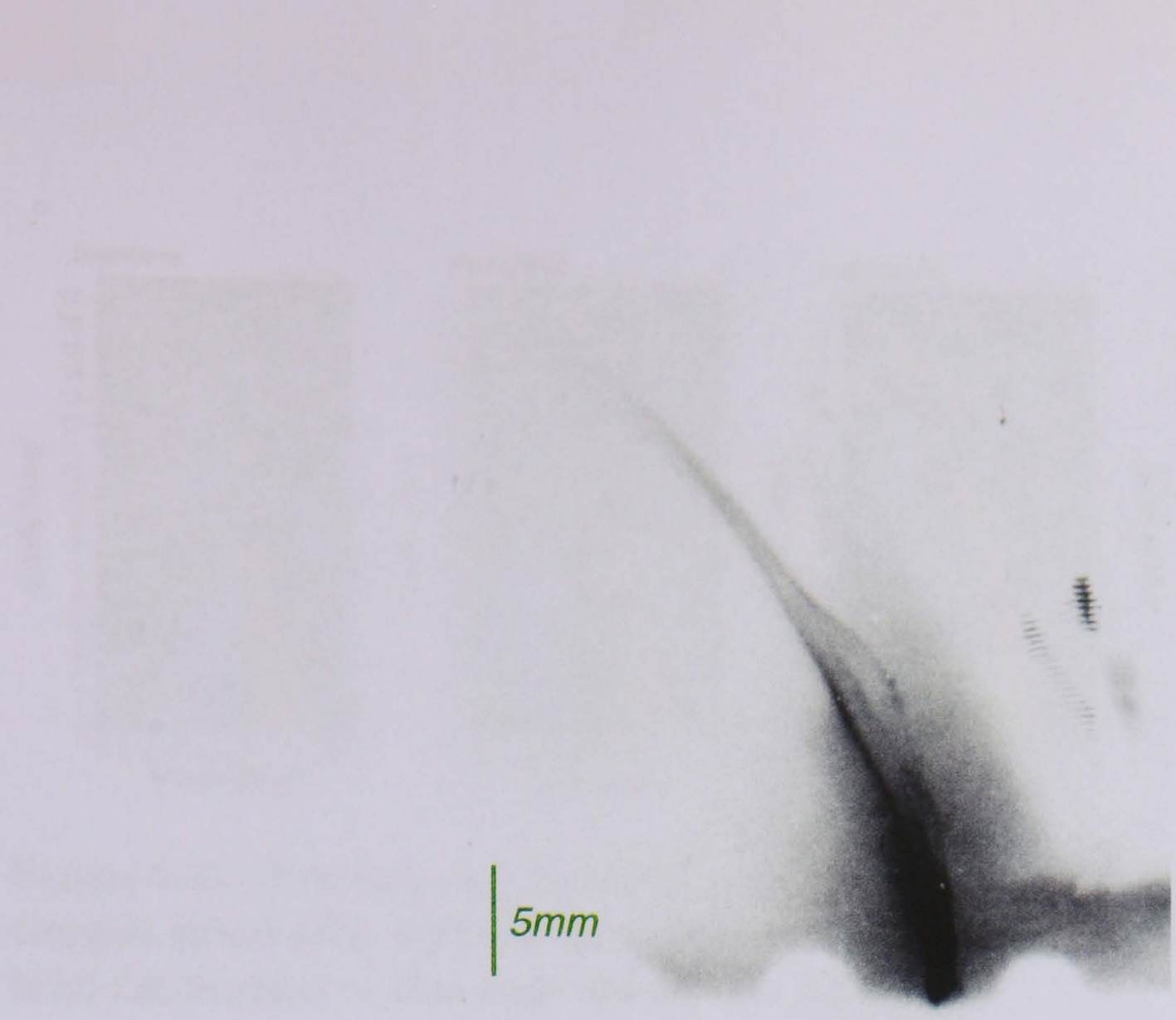


Figure 6.19: XUV ($h\nu > 30eV$) emission from the same experiment as Fig 6.18 at $380ns$

the significance of each of these shocks is, however we can understand this better if we look at XUV emission. Figure 6.19 shows a gated XUV image from the same experiment, however $40ns$ after the schlieren image. This image was taken at 22.5° from the plane containing the laser probe beam and foil, hence some emission from the surface of the foil can be seen in the XUV image. The structure seen in the XUV image is broadly similar to that in the schlieren image, however these shock features have developed slightly. Again we see two shocks between the curved section of the jet and the foil. It appears that the left-most shock is a second internal oblique shock in the jet (OS2), further deflecting the jet. The nature of the right-hand shock (WS2) becomes more clear if we look at simulations of a jet in a side wind.

Figure 6.20 shows a 2D slice taken from a 3D MHD simulation of a jet propagating in a side-wind. For simplicity this simulation has a constant mass flux in the jet, constant jet injection velocity and uniform wind density and velocity. In these simulations we see that as the jet propagates the upwind surface becomes unstable and a second (and in the last frame a third) working surface begins to form. Thus what we see in Figures 6.18 and 6.19 is the formation of this secondary working surface. The development of this structure can be seen experimentally in Fig 6.21, which shows a series of gated XUV images (for a different experiment).

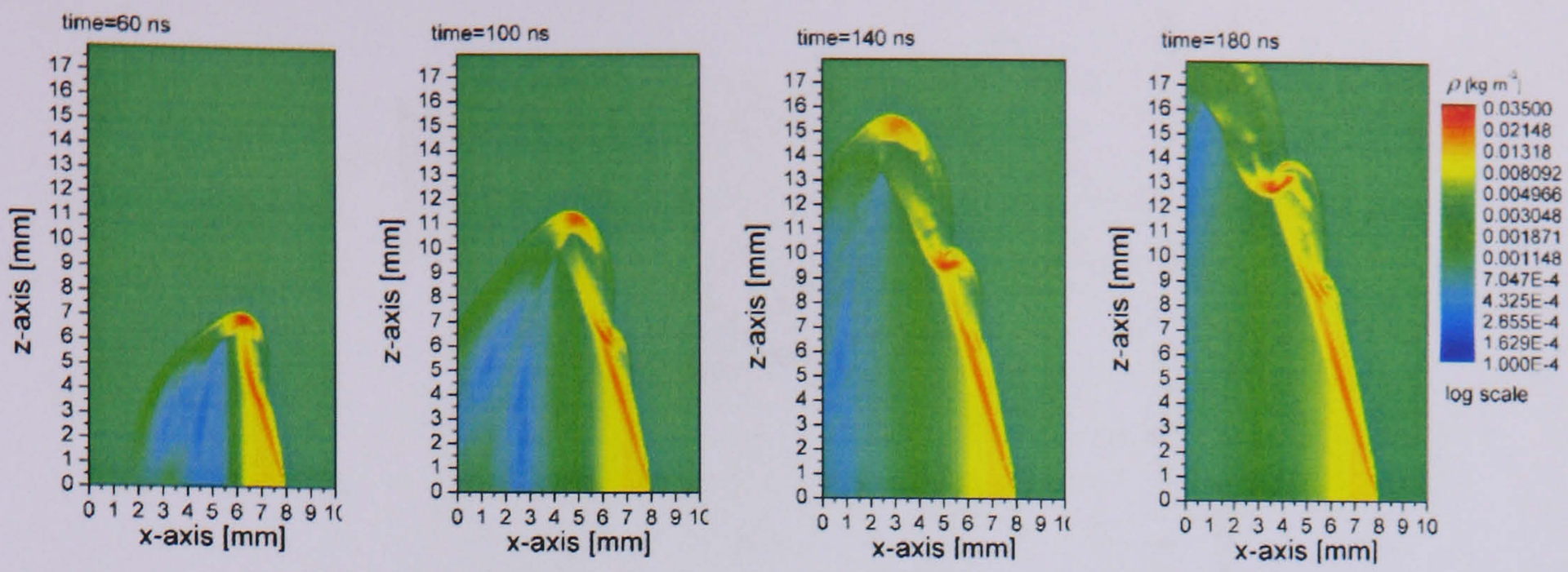


Figure 6.20: Simulations of a jet in propagating in a side-wind. 2D slice from a 3D Gorgon simulation with uniform jet and wind (performed by Dr. A. Ciardi, for a brief description of this code see section 2.6).

If we look above the tip of the jet on the earlier schlieren image (Fig 6.18a) we see that more shocks have formed. The axial position of this material implies that it was ejected before collapse of the conical shock (hence it is labelled early-jet). On this experiment there is no camera looking in detail at this region, however on a subsequent shot with a similar setup we can see this interaction on a high magnification schlieren image (Fig 6.22). This image shows the low density jet through shadowgraphy, and shocks through schlieren effect. We see that there are actually two shocks present. The shock furthest from the foil is an internal shock in the jet, producing yet another region of deflection. The closest shock to the foil is a reverse shock forming in the wind. It is believed that when this jet material passed through the lower area of wind the ambient material was of sufficiently low density that either the mean free path of the jet was too long to be deflected or there was not enough momentum in the wind at that time. Also on this experiment the low magnification schlieren image shows a reverse shock in the wind near the first deflection of the jet.

6.5 Conclusions on jet propagating in a side-wind

Two regimes of jet deflection by a side-wind have been investigated. In the first of these, using a short interaction region, the jet trajectory could be fitted by the

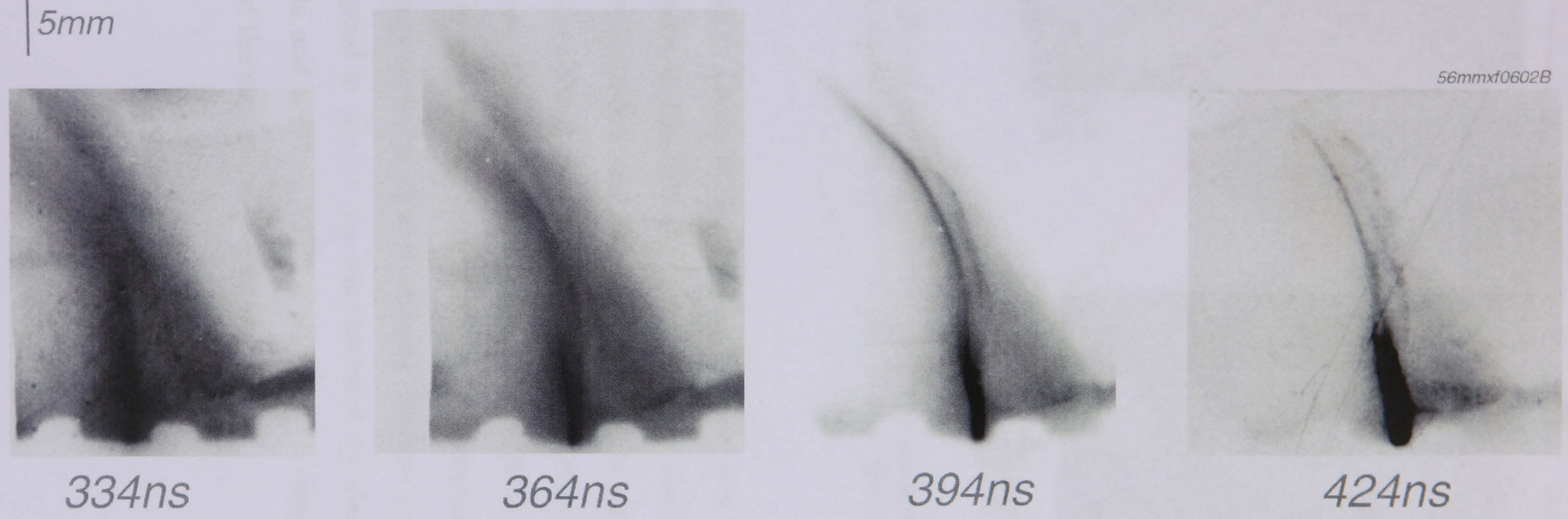


Figure 6.21: Development of the jet-wind interaction with time, shown by XUV emission ($h\nu > 30eV$). In frame 3 shows both an internal shock in the jet and a stand-off shock in the wind. By frame 4 these shocks have begun to go unstable and pull away from the jet.

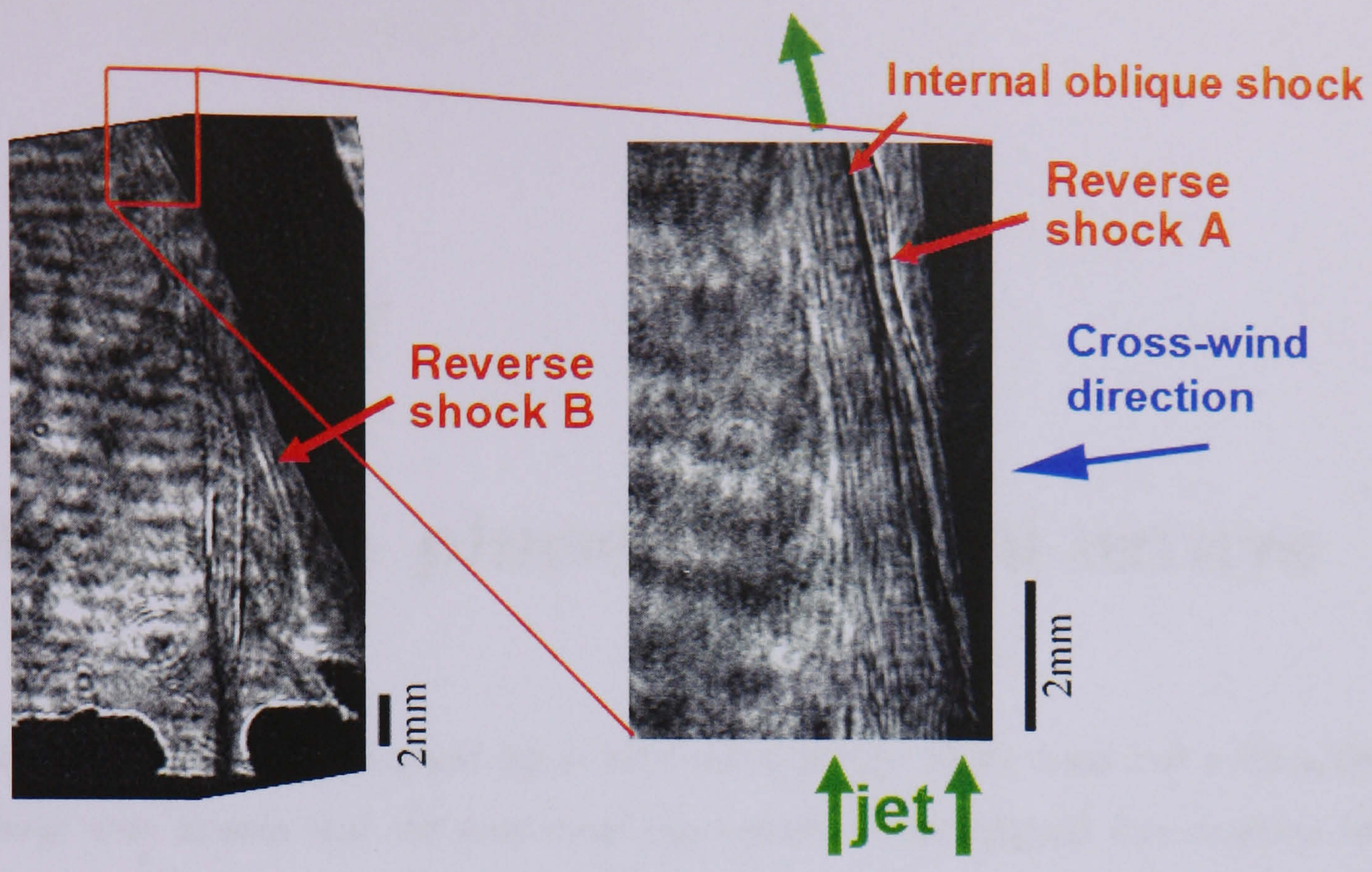


Figure 6.22: High and low magnification schlieren images showing the interaction of the low density, un-collapsed tip of the jet (from a different experiment to all other images)

model described by Canto & Raga [82] in the case of a low ram pressure. Internal structure was seen in the deflecting jets, however the interaction length in these experiments did not allow the internal shock in the jet to fully develop. Using a longer interaction allowed the internal shock to develop, in fact with the formation of more than one discrete internal shock. In addition multiple working surfaces were observed in experiments with this longer interaction length. Attempts to fit the Canto & Raga model to this experiment resulted in a significant over-estimate of the sound speed in the jet (as demonstrated by the small divergence angle in the experiments and no imaging on x-ray framing cameras). The reason for this over-estimate of the sound speed is unclear.

Chapter 7

Implosion phase of conical arrays

The conical arrays discussed up to this point in this thesis have had sufficiently large wire masses that the wire cores can remain at the original wire position for the complete duration of the current pulse ($M > \int \dot{m} dt$). Conical wire arrays with a lower mass per unit length will, when the mass at the original wire positions is sufficiently depleted, implode (similar to the implosion of a cylindrical wire array, as will be described in Section 7.1). The differences between cylindrical and conical arrays (radial component of current, axial variation of azimuthal magnetic field and axial variation in wire spacing) make them a useful tool to further study the physics of wire array z-pinch implosions. Imploding conical wire arrays have previously been proposed as a technique for forming plasma slugs to deliver energy to a hohlraum in an indirect-drive ICF concept [85], and as a method of x-ray pulse shaping for indirect-drive ICF. The interaction of the imploding plasma with the pre-formed axially moving jet may also have connections to the time varying velocity of astrophysical jets.

A limited number of experiments have been performed using conical wire arrays with a lower mass per unit length such that wire mass is exhausted and an implosion can occur. Whilst there is far from a complete data set for these implosions, sufficient data is present to suggest some useful future experiments using imploding conical wire arrays.

7.1 Background on the implosion of cylindrical wire arrays

Before discussing the dynamics of the implosion of conical wire arrays it is useful to first summarise the dynamics of a cylindrical wire array implosion [15, 86, 87, 44].

The early-time wire ablation in a cylindrical wire array have already been discussed in chapter 3. Figure 7.1 shows a streak image and two laser probing images of the implosion of a cylindrical wire array. After the mass in the wires drops below a fraction of the initial wire mass (normally $\sim$ 50%) breaks begin to form in the wires (Fig 7.1b). As these breaks form there is no longer a continuous current path at the original wire positions and the array begins to implode, as is shown on the streak image (Fig 7.1a). This implosion is effectively a current carrying piston which snow-ploughs the mass that was ablated from the wires prior to the implosion. The implosion does not carry all the mass towards the axis, resulting in trailing mass which normally takes the form of fingers of plasma, as can be seen on Fig 7.1b & c. As the piston arrives on the array axis and collides with the precursor column (Fig 7.1b) an x-ray pulse is emitted. The full cause of this x-ray pulse is the subject of much current research, but there are likely to be contributions from the thermalisation of the kinetic energy of the imploding plasma and PdV and ohmic heating of the stagnated column. This x-ray pulse can be seen in Fig 7.2, which shows PCD signals of the implosion phase, along with labels for the times that the implosion starts and when the piston arrives on the array axis. A 'bump' can be seen on the $2.5\mu m$ filtered PCD signal halfway up the pulse. It is thought that this first section of the x-ray pulse is likely to be due to the thermalisation of kinetic energy, and then the final peak is the due to PdV and ohmic heating of the imploded column. The relative timing and intensity of these two pulses changes depending on the symmetry of the array and return current path [15].

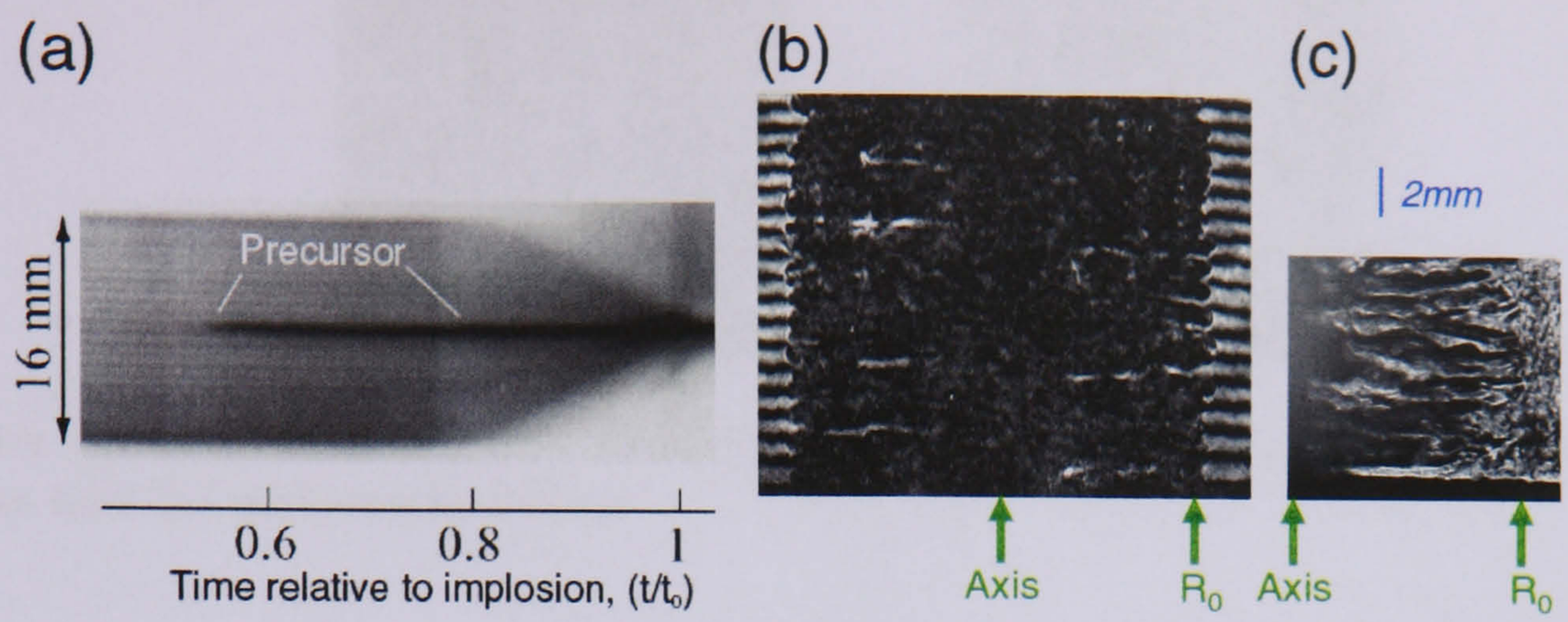


Figure 7.1: Implosion dynamics of a $20\mu m$ Al cylindrical wire array shown on (a) an optical radial streak camera image (radial emission profile vs time), (b) an interferometer image at $231ns$ and (c) a schlieren image at $244ns$.

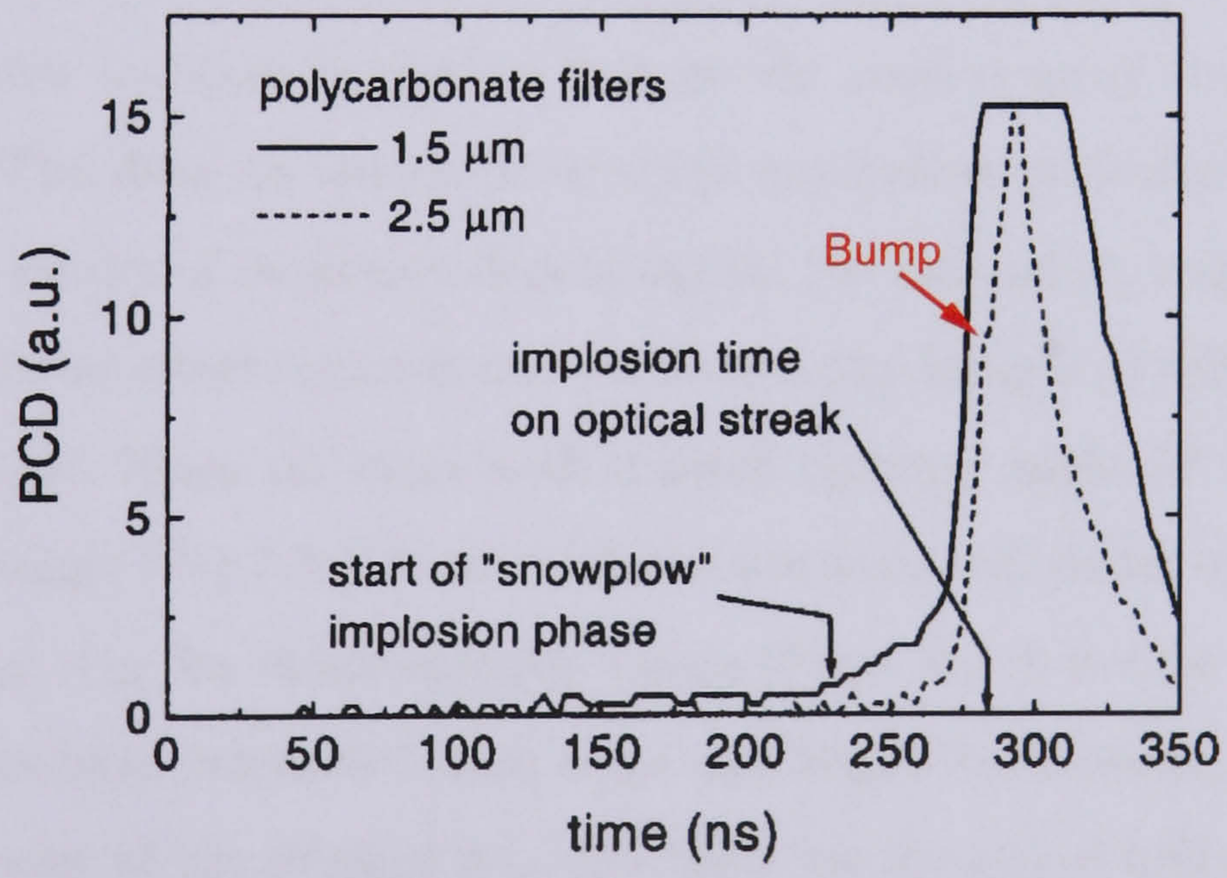


Figure 7.2: X-ray pulse from an imploding cylindrical wire array [87]. The transmission of these filters is shown in Fig 2.8.

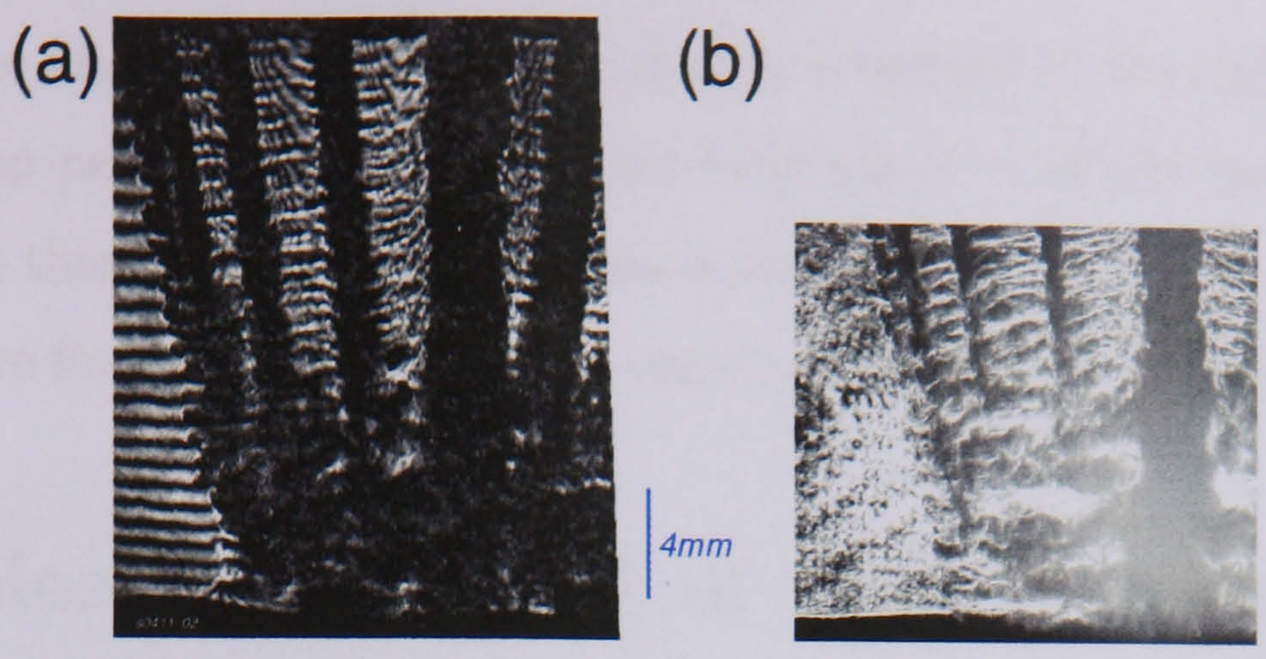


Figure 7.3: Implosion of a $\theta = 16°$ conical array, as shown by (a) interferometry at $253ns$ and (b) schlieren at $265ns$.

7.2 Implosion dynamics of conical wire arrays with small opening angles

As has been discussed in section 3.2, for a conical wire array the mass ablation rate varies along the length of each wire ($\dot{m} \sim \frac{1}{R}$). For imploding conical arrays, as the original mass per unit length is constant along the wire, the time of mass depletion from the wire cores will vary as a function of z. This leads to a delayed implosion of the end of the array with the larger diameter compared to the end with a smaller diameter (cathode imploding first for the conical array arrangement used on MAGPIE). The data on conical wire array implosions indicates that there are potentially two modes of implosion depending on the inclination angle of the wires.

Figure 7.3 shows interferometer and shadowgraphy images at different times for an array of sixteen $20\mu m$ Al wires with a small opening angle ($\theta = 16°$). In the interferometer image (Fig 7.3a) we see that the wires are still intact except for at the base of the array. On the shadowgraphy image (Fig 7.3b) it is clear that the lower part of the wires have exhausted their mass and begun to implode, whilst there is still plasma present at the original wire positions for the upper half of the array. It is assumed that a core is still present within this plasma for the upper half of the array. Comparison of the cathode (lower) end of the array with a cylindrical array with $16mm$ diameter (the same diameter as the cathode of the conical array), also consisting of sixteen $20\mu m$ Al wires (as was shown in Fig 7.1c), indicates that the

behaviour of the lower section of the conical array is similar to the cylindrical array. Between the top part of the wires (that are fully intact) and the lower part (that have imploded) there is a region where breaks are visible in all wires, similar to the broken structure found in cylindrical wire arrays at the start of implosion.

7.3 Implosion dynamics of large opening angle conical wire arrays

Whilst only one large opening angle Al shot has been performed, it appears that the dynamics of this implosion are very different to those for small opening angle experiments. Figure 7.4 shows a laser shadow image of the implosion of the large opening angle array and a series of XUV emission images showing the development of the system. For the large opening angle the variation in magnetic field along the wires is large and appears to dominate over the short wavelength modulation seen in cylindrical arrays. The wires implode in close proximity to the cathode whilst the remainder of the wire has a large mass remaining. This remaining length of the wire is too massive to implode, however a continuous current path is still required. The instability at the base of the precursor column indicates that this is carrying some current. Thus it appears that current has switched to passing up the imploded plasma, along a path of imploding plasma, creating a magnetic bubble, and then out to the wire location and along the remainder of the wire (illustrated in Fig 7.5). This formation of a magnetic bubble (the current path through the imploding plasma) is similar to the process in a radial wire array [22], and may have a similarity to models of astrophysical jet formation [71].

From the XUV images shown in Fig 7.4, the velocity of this bubble can be determined. The bubble is propagating upwards at a velocity of 150km/s. This velocity does not appear to change during the experiment, however more data would be needed to be conclusive. If this bubble is moving at constant velocity then the deceleration from accreting mass will be in balance with the Lorentz force, and it may be possible to determine a density profile within the precursor column or in the pre-fill between the wires and the column.

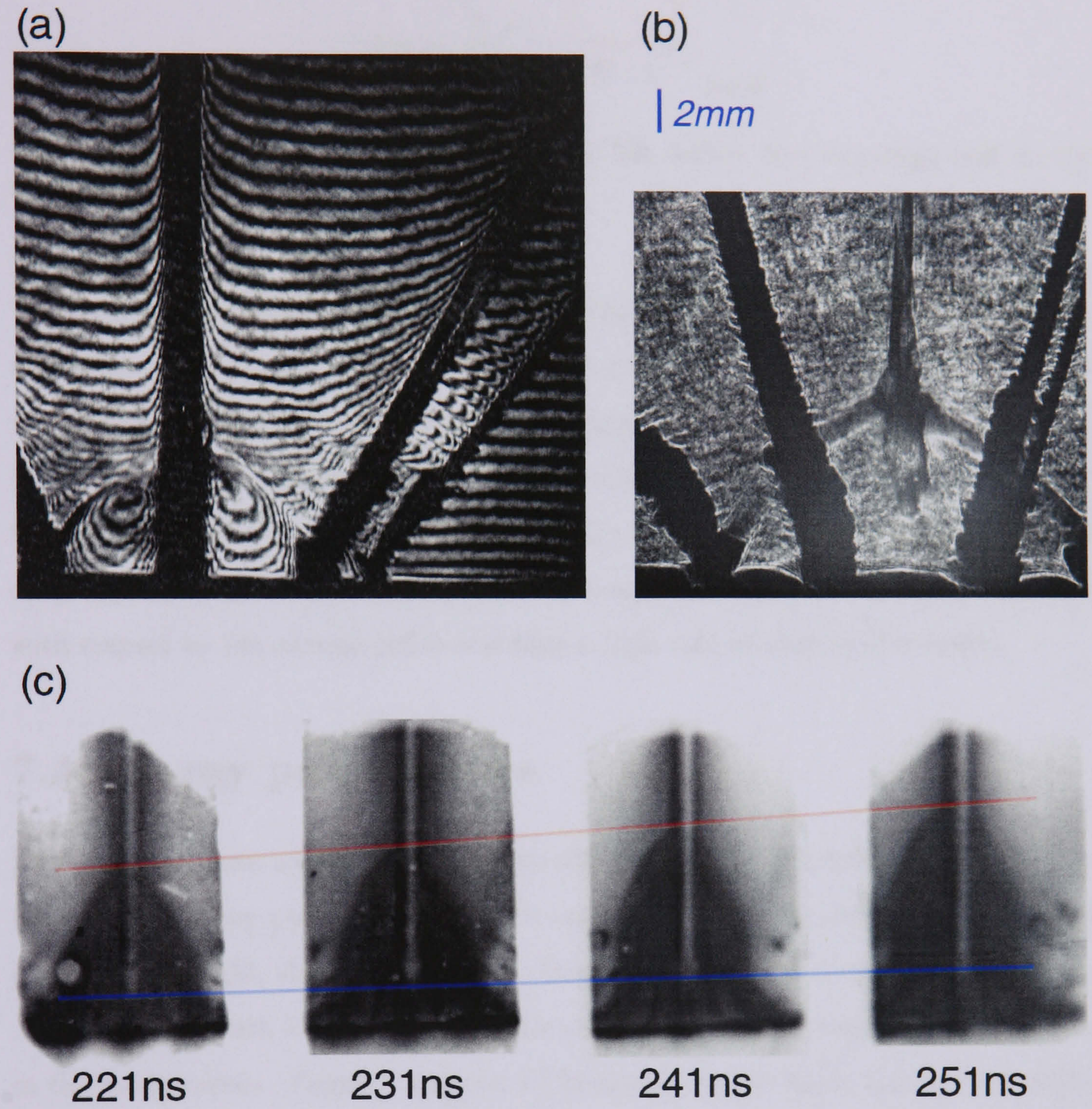


Figure 7.4: Implosion of a $\theta = 38°$ conical array, as shown by (a) interferometry at $180ns$ and (b) schlieren at $192ns$ and soft x-ray emission at 221, 231, 241 and $251ns$. The faint blue line shows the motion of the break-point in the wires moving upwards and the faint red line shows the motion of a bubble upwards.

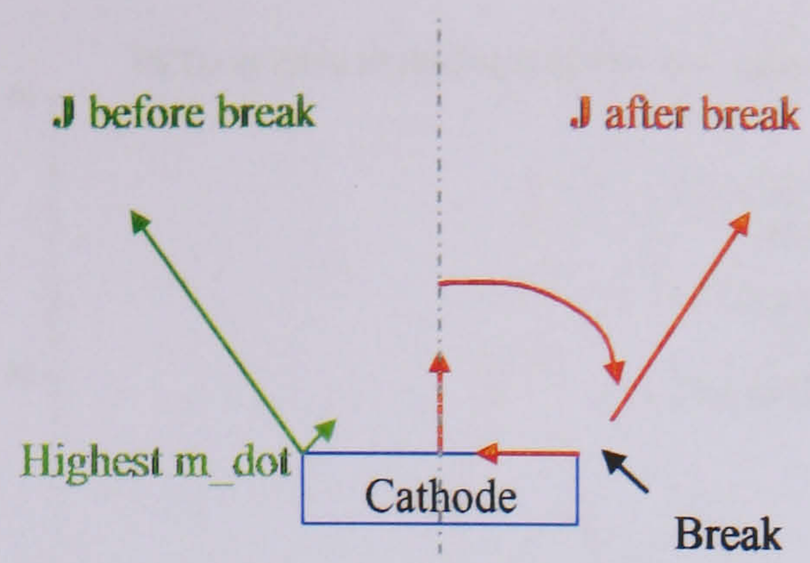


Figure 7.5: Sketch of current paths: on the left before wire breakage and on the right after wire breakage.

There is only a single experiment performed in this wide-angle imploding setup, and other array parameters were also varied compared to the small angle arrangement, hence it is not conclusive that the opening angle is causing the different modes. Other differences in the arrays that produce magnetic bubbles compared to the earlier mode include a large wire spacing (as only 8 wires have been used for the large opening angle case) and a low mass per unit length (which causes an early implosion with respect to the current pulse and thus a high rate of change of current).

7.4 X-ray pulse shapes

Initial experiments indicate that the two different modes of implosion may have an affect on the x-ray pulse shape. For the small opening angle array the x-ray pulse is similar in height, shape and width to that in a cylindrical array.

In contrast, with a large opening angle array there is a more significant difference in the x-ray pulses. Figure 7.6 shows PCD signals for an imploding large opening angle conical array and a cylindrical array. The intensity of radiation emitted by the conical array is much smaller signal than from the cylindrical array. The double peaks of the conical array have a temporal spacing of approximately twice that in the cylindrical case, and each of these peaks has a width much greater (~ 3 times) than those in the cylindrical case. The difference in x-ray pulse between the two configurations may merely be due to the change in expected implosion times of the different ends of the array. This does however demonstrate the potential to use

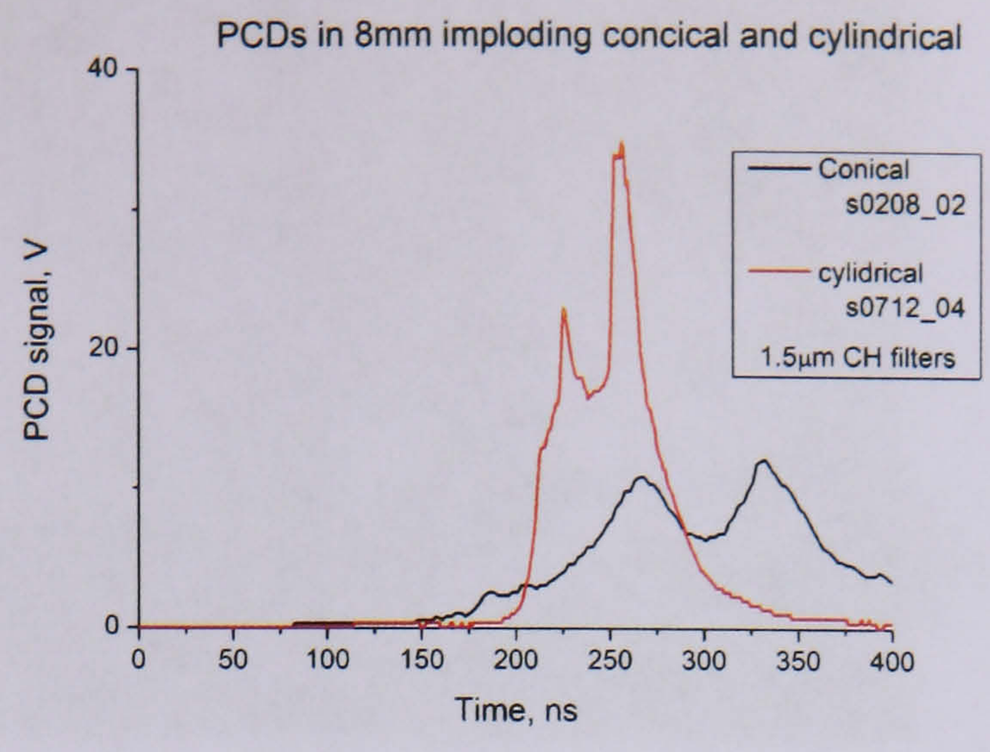


Figure 7.6: X-ray pulse shapes for a large opening angle conical array and a cylindrical wire array.

conical arrays to alter the temporal and spatial characteristics of the x-ray pulses from wire arrays, which may have possible applications in ICF.

7.5 Jets produced by imploding tungsten arrays

A single experiment using imploding tungsten wire arrays has also been performed. In this case a short array was used, allowing diagnosis of the jet as well as the array. Early in time the array will behave in a similar way to non-imploding arrays, with a conical shock which produces a collimated jet. The dynamics of the array from the start of the implosion are unclear in this experiment as the diagnostics were timed too late to help understand this, however the diagnostics do image a jet produced by the array. A shadowgraphy image of the jet is shown in Fig 7.7. The jet appears similar to many of the jets described earlier for non-imploding arrays, however at the base of the jet is a wide disc-like structure $\sim$ 3 times the jet diameter. There are three possible explanations for this. Firstly this feature could be the top of the magnetic bubble (as for large opening angle Al arrays). Secondly, it could be associated with a section of plasma that has been accelerated by pressure gradients brought about by the lagged zipper motion of in a 'cylindrical-like' implosion. Also this material could be jet material that has been driven radially outwards by a shock that has propagated up the precursor and jet, which was started by an implosion

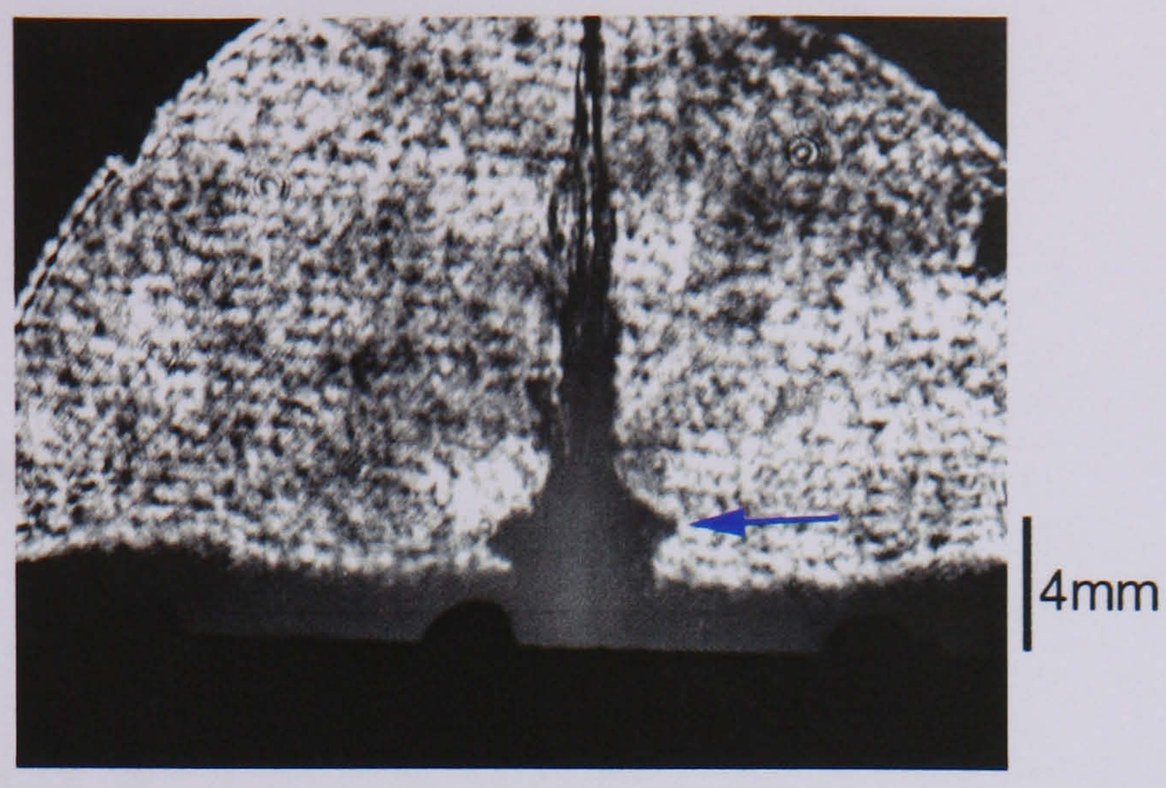


Figure 7.7: Imploding W jet $333ns$ after the start of the current pulse. The blue arrow indicates the disk-like structure possibly produced as a result of the implosion of the array, as discussed in the text.

(of either mode). As this is a single experiment, a further possibility is that this is a one-off feature of this jet that is not linked in any way to the implosion of the array.

7.6 Future imploding conical wire array experiments

It would be interesting to explore whether there are really two modes of implosion for conical wire arrays. If it is found that there are two modes, then it would be useful to investigate the angle (or other parameter) which triggers the switch in modes. This could be particularly interesting for comparisons to simulations, as it provides a comparison between small scale structure and the global dynamics of the array. Experiments are also planned using a narrow band of a spectroscopic tracer element coated onto the wires to explore the axial motion of plasma in an imploding conical wire array.

Chapter 8

Summary

Conical wire arrays provide an interesting and useful testbed for both wire array physics and laboratory astrophysics studies relevant to protostellar jets.

Wire ablation in conical wire arrays exhibits many similarities to cylindrical wire arrays. It has been shown that a rocket model [8] fits the experimental data if a fixed ablation velocity is used. Hence the mass ablation rate depends on radial (and thus also axial) position. Spatial modulations in the mass ablation rate in the wires similar to those in cylindrical wire arrays have been observed. The wavelength of these modulations is similar to cylindrical arrays, and is not affected by the variations in the global magnetic field or inter-wire spacing along the wire. Within a few *mm* of the wire cores the ablated streams exhibit a curved trajectory towards the anode which has not been observed in cylindrical array experiments, however no definitive explanation for this curvature has been found.

When the flows meet on the array axis a conical shock is formed, which thermalises the kinetic energy associated with radial motion, forming an axial flow. Estimates of the timing of the collapse of this column based on the collapse of the precursor column in cylindrical wire arrays agree with experimental data. The axial flow in the conical shock is accelerated at the top of this conical shock producing a jet. Analytic estimates of the density distribution in this flow are in agreement with experimental data.

It has been shown that radiative cooling and angular momentum both significantly affect the collimation of the jet; jet collimation is made worse if a material

with a low rate of radiative cooling is used, or a 'twist' is introduced into the array to impart angular momentum into the jet.

To create a density contrast between the jet and its surroundings similar to that observed for protostellar jets an ambient gas has been introduced around the jet. A working surface has been formed at the head of the early-time jet, and the dependence of the velocity of this working surface on the density contrast between the jet and the gas appears to fit astrophysical models. For stainless-steel jets multiple working surfaces are formed, which propagate at different axial velocities.

We have modelled the effective wind that protostellar jets can be subjected to using a photo-ablated CHO foil near the area of jet propagation. This wind, which is of lower mass density than the jet, causes a deflection of the jet. Although this deflection is substantial (the radius of curvature is of order 60 jet radii) the jet remains well collimated. Various internal oblique shocks have been imaged in the jet during deflection, and the formation of a second working surface is observed. Reverse shocks in the wind are also observed.

In the future, it would be useful to further explore each of the branches of work discussed in this thesis. Additionally, a useful next step would be to begin to combine the different tools developed for controlling the characteristics of jets produced by conical wire arrays. For example it would be interesting to perform experiments where a jet with angular momentum is subjected to a side-wind.

In conclusion, it has been shown (see Table 8.1) that there is a reasonable similarity between the laboratory jets discussed in this thesis and astrophysical protostellar jets far from the source star. Investigations of the effects of radiative cooling, an ambient medium, angular momentum and a side-wind impacting the jet all have astrophysical relevance. To further satisfy the criteria required to perform fully scaled laboratory experiments of protostellar jets, the next step would be to select a specific, well characterised protostellar jet and attempt to identically match the neccessary dimensionless scaling parameters and initial conditions. Such a process would be limited by the incomplete knowledge of the important parameters for the astrophsyical jets, however we have shown that many of the key parameters can be controlled in our experiments. We have shown that the cooling parameter of the jet

can be controlled by varying the wire material in the array. This adjustment of jet temperature would also affect the Mach number of the flow. It has been shown that density contrast between the jet and the ambient medium adjusted by introducing an ambient gas into the system (although further work is needed to ensure that the fully formed jet is interacting with the gas and to fully control this density contrast). To better match other parameters such as the both density and angular momentum distributions, further knowledge of these profiles in the protostellar jets would be required.

Table 8.1: Parameters for protostellar and laboratory jets (based on Table 4.3.1 in Chapter 4). The first group shows some characteristic parameters of the different jets. The second group of parameters are those illustrating the applicability of a fluid description (reproduced from [24]) and the final group shows that there is good agreement in the three dimensionless scaling parameters that characterise radiatively cooled jets (as defined in equations 4.9 - 4.11).

Parameter	YSO	Conical wire array (W on MAGPIE)
General flow variables		
Length (cm)	3×10^{17}	2
Width (cm)	2×10^{16}	0.1
Dynamical time Scale	10^3 years	100ns
Electron temperature (eV)	1	10
Jet tip velocity (km/s)	~ 100	~ 200
Jet density, ρ (g/cm^3)	$\sim 10^{-22}$	10^{-4}
Validity of fluid description		
Localisation parameter $\frac{\lambda_{mfp}}{r_j}$	$\ll 10^{-6}$	$\leq 10^{-4}$
Reynolds Number (Re)	$> 10^8$	$10^5 - 10^8$
Peclet number (Pe)	10^7	$2 - 2 \times 10^3$
Jet scaling		
Mach number, $\mathcal{M}$	> 10	> 20
Density Contrast, η	1-2	~ 1
Cooling Parameter, χ	0.1-10	1

Bibliography

[1] J. Bally, J. Morse, and B. Reipurth. The Birth of Stars: Herbig-Haro Jets, Accretion and Proto-Planetary Disks. *Science with the Hubble Space Telescope - II*, page 491, 1996.

[2] D. Ryutov, R. P. Drake, J. Kane, E. Liang, B. A. Remington, and W. M. Wood-Vasey. Similarity Criteria for the Laboratory Simulation of Supernova Hydrodynamics. *The Astrophysical Journal*, 518:821–832, 1999.

[3] D. D. Ryutov, R. P. Drake, and B. A. Remington. Criteria for Scaled Laboratory Simulations of Astrophysical MHD Phenomena. *The Astrophysical Journal Supplement*, 127:465–468, 2000.

[4] G. A. Kyrala, editor. *Special Issue on High Energy Density Laboratory Astrophysics; (to be published in Astrophys. Space Sci.).* 2005.

[5] K. Shigemori, R. Kodama, D. R. Farley, T. Koase, K. G. Estabrook, B. A. Remington, D. D. Ryutov, Y. Ochi, H. Azechi, J. Stone, and N. Turner. Experiments on radiative collapse in laser-produced plasmas relevant to astrophysical jets. *Physical Review E*, 62:8838–8841, 2000.

[6] D. R. Farley, K. G. Estabrook, S. G. Glendinning, S. H. Glenzer, B. A. Remington, K. Shigemori, J. M. Stone, R. J. Wallace, G. B. Zimmerman, and J. A. Harte. Radiative Jet Experiments of Astrophysical Interest Using Intense Lasers. *Physical Review Letters*, 83:1982–1985, 1999.

[7] D. D. Ryutov, M. S. Derzon, and M. K. Matzen. The physics of fast Z pinches. *Reviews of Modern Physics*, 72:167–223, 2000.

[8] S. V. Lebedev, F. N. Beg, S. N. Bland, J. P. Chittenden, A. E. Dangor, and M. G. Haines. Snowplow-like behavior in the implosion phase of wire array Z pinches. *Physics of Plasmas*, 9:2293, 2002.

[9] S. V. Lebedev, J. P. Chittenden, F. N. Beg, S. N. Bland, A. Ciardi, D. Ampleford, S. Hughes, M. G. Haines, A. Frank, E. G. Blackman, and T. Gardiner. Laboratory Astrophysics and Collimated Stellar Outflows: The Production of Radiatively Cooled Hypersonic Plasma Jets. *The Astrophysical Journal*, 564:113–119, 2002.

[10] P. Hartigan. The visibility of the Mach disk and the bow shock of a stellar jet. *The Astrophysical Journal*, 339:987–999, 1989.

[11] J. Canto and A. C. Raga. The dynamics of a jet in a supersonic side wind. *MNRAS*, 277:1120–1124, 1995.

[12] T. A. Gardiner, A. Frank, E. G. Blackman, S. V. Lebedev, J. P. Chittenden, D. Ampleford, S. N. Bland, A. Ciardi, M. Sherlock, and M. G. Haines. MHD Models and Laboratory Experiments of Jets. *Astrophys. and Space Science*, 287:69–74, 2003.

[13] D. J. Ampleford, S. V. Lebedev, A. Ciardi, S. N. Bland, S. C. Bott, J. P. Chittenden, G. N. Hall, C. A. Jennings, J. Armitage, Blyth. G., S. Christie, and L. Rutland. Formation of Workings Surfaces in Radiatively Cooled Laboratory Jets. *To be published, Astrophys. and Space Science*, 2005.

[14] S. V. Lebedev, D. Ampleford, A. Ciardi, S. N. Bland, J. P. Chittenden, M. G. Haines, A. Frank, E. G. Blackman, and A. Cunningham. Jet Deflection via Crosswinds: Laboratory Astrophysical Studies. *The Astrophysical Journal*, 616:988–997, 2004.

[15] S. V. Lebedev, D. J. Ampleford, S. N. Bland, S. C. Bott, J. P. Chittenden, C. Jennings, M. G. Haines, J. B. A. Palmer, and J. Rapley. Implosion dynamics of wire array Z-pinches: experiments at Imperial College. *Nuclear Fusion*, 44:215, 2004.

[16] S. N. Bland, S. V. Lebedev, D. J. Ampleford, S. C. Bott, and J. P. Chittenden. Plasma formation and dynamics in 'mixed' wire array z-pinches. *In preparation for Physics of Plasmas*, 2005.

[17] S. N. Bland, S. V. Lebedev, J. P. Chittenden, D. J. Ampleford, and G. Tang. Use of linear wire array z-pinches to examine plasma dynamics in high magnetic fields. *Physics of Plasmas*, 11:4911, 2004.

[18] B. Jones, C. Deeney, J. L. McKenney, J. E. Garrity, D. K. Lobley, K. L. Martin, A. E. Griego, J. P. Ramacciotti, S. N. Bland, S. V. Lebedev, S. C. Bott, D. J. Ampleford, J. B. A. Palmer, J. Rapley, and G. Hall. Chemically etched modulation in wire radius for wire array Z-pinch perturbation studies. *Review of Scientific Instruments*, 75:5030, 2004.

[19] B. Jones, C. Deeney, J. L. McKenney, C. J. Garasi, S. N. Bland, S. V. Lebedev, S. C. Bott, D. J. Ampleford, J. B. A. Palmer, J. Rapley, and G. Hall. Study of Three-Dimensional Structure in Wire Array Z-Pinches by Controlled Seeding of Axial Modulations in Wire Radius. *In preparation for Physical Review Letters*, 2005.

[20] S. C. Bott, S. V. Lebedev, F.N. Beg, S. N. Bland, J. P. Chittenden, A. Ciardi, M. G. Haines, D. Ampleford, C. A. Jennings, J. Rapley, J.B.A. Palmer, M. Sherlock, and G. Hall. Dynamics of cylindrically converging precursor plasma flow in wire array z-pinch experiments. *in preparation for Physics of Plasmas*, 2005.

[21] S. V. Lebedev, D. J. Ampleford, S. N. Bland, S. C. Bott, J. P. Chittenden, J. Goyer, C. Jennings, M. G. Haines, J. B. A. Palmer, S. A. Pikuz, T. A. Shelkovenko, and T. Christoudias. Physics of wire array Z-pinch implosions: experiments at Imperial College. *Plasma Physics and Controlled Fusion*, 47:A91–A108, 2005.

[22] S. V. Lebedev, A. Ciardi, D. Ampleford, S. N. Bland, S. C. Bott, J. P. Chittenden, G. Hall, J. Rapley, A. Frank, E. G. Blackman, and T. Lery. Magnetic Tower Outflows from a Radial Wire Array Z-pinch. *in preparation for Monthly Notices of the Royal Astronomical Society*, 2005.

[23] A. Ciardi, S. V. Lebedev, D. Ampleford, J. P. Chittenden, and S. N. Bland. MHD Models and Laboratory Experiments of Jets. *To be published, Astrophys. and Space Science*, 2005.

[24] A. Ciardi. *PhD thesis: Modelling of hypersonic jets in wire array z-pinch experiments*. Imperial College London, 2003.

[25] A. Ciardi, S. V. Lebedev, J. P. Chittenden, and S. N. Bland. Modeling of supersonic jet formation in conical wire array Z-pinches. *Laser Particle Beams*, 20:255–261, 2002.

[26] I. H. Mitchell, J. M. Bayley, J. P. Chittenden, J. F. Worley, A. E. Dangor, M. G. Haines, and P. Choi. A high impedance mega-ampere generator for fiber z-pinch experiments. *Rev. Sci. Instrum.*, 67:1533–1541, 1996.

[27] T. W. Sanford, G. O. Allshouse, B. M. Marder, T. J. Nash, R. C. Mock, R. B. Spielman, J. F. Seamen, J. S. McGurn, D. Jobe, T. L. Gilliland, M. Vargas, K. W. Struve, W. A. Stygar, M. R. Douglas, M. K. Matzen, J. H. Hammer, J. S. de Groot, J. L. Eddleman, D. L. Peterson, D. Mosher, K. G. Whitney, J. W. Thornhill, P. E. Pulsifer, J. P. Apruzese, and Y. Maron. Improved Symmetry Greatly Increases X-Ray Power from Wire-Array Z-Pinches. *Physical Review Letters*, 77:5063–5066, 1996.

[28] M. K. Matzen. Z pinches as intense x-ray sources for high-energy density physics applications. *Physics of Plasmas*, 4:1519–1527, 1997.

[29] C. Deeney, M. R. Douglas, R. B. Spielman, T. J. Nash, D. L. Peterson, P. L'Eplattenier, G. A. Chandler, J. F. Seamen, and K. W. Struve. Enhancement of X-Ray Power from a Z Pinch Using Nested-Wire Arrays. *Physical Review Letters*, 81:4883–4886, 1998.

[30] D. H. McDaniel, M. G. Mazarakis, D. E. Bliss, J. M. Elizondo, H. C. Harjes, H. C. Ives, D. L. Kitterman, J. E. Maenchen, T. D. Pointon, S. E. Rosenthal, D. L. Smith, K. W. Struve, W. A. Stygar, E. A. Weinbrecht, D. L. Johnson,

and J. P. Corley. The ZR Refurbishment Project. *AIP Conf. Proc. 651: Dense Z-Pinches*, pages 23–28, 2002.

[31] R. B. Spielman, R. J. Dukart, D. L. Hanson, B. A. Hammel, W. W. Hsing, M. K. Matzen, and J. L. Porter. Z-pinch experiments on Saturn at 30 TW. *Presented at the 2nd International Conference on High-Density Pinches, Laguna Beach, CA, 26 Apr. 1989*, 1989.

[32] J. Davis, N. A. Gondarenko, and A. L. Velikovich. Fast commutation of high current in double wire array Z-pinch loads. *Applied Physics Letters*, 70:170–172, 1997.

[33] S. N. Bland, S. V. Lebedev, J. P. Chittenden, C. Jennings, and M. G. Haines. Nested wire array Z-pinch experiments operating in the current transfer mode. *Physics of Plasmas*, 10:1100, 2003.

[34] M. Hu and B. Kusse. Mass ablation, charge state and instabilities in linear arrays. *Bull. Am. Phys. Soc.*, 49:PO3:1, 2004.

[35] T. A. Shelkovenko, S. A. Pikuz, D. A. Hammer, Y. S. Dimant, and A. R. Mingaleev. Evolution of the structure of the dense plasma near the cross point in exploding wire X pinches. *Physics of Plasmas*, 6:2840–2846, 1999.

[36] R. Aliaga-Rossel, J. Bayley, A. Mamin, and Y. Nizienko. SBS Pulse Compression Applied to a Commercial Q-Switch Nd-YAG Laser. *AIP Conf. Proc. 409: Dense Z-Pinces: Fourth International Conference*, pages 467–470, 2004.

[37] I. Hutchinson. *Principles of Plasma Diagnostics, Second Edition.* Cambridge University Press, 2002.

[38] M. Burnett and T. R. Judge. *The Automatic Analysis of Interferometric Data - FRAN. Available at http://www.eng.warwick.ac.uk/ espbc/previous/fran.htm.* Department of Engineering, University of Warwick, 1996.

[39] S. N. Bland. *PhD thesis: Plasma dynamics in aluminium wire array z-pinch experiments.* Imperial College London, 2000.

[40] R. B. Spielman, L. E. Ruggles, R. E. Pepping, S. P. Breeze, J. S. McGurn, and K. W. Struve. Fielding and calibration issues for diamond photoconducting detectors. *Review of Scientific Instruments*, 68:782–785, 1997.

[41] G. C. Idzorek and H. Oona. Properties of plasma radiation diagnostics. *Review of Scientific Instruments*, 68:1065–1–68, 1997.

[42] Dr Armin Schulz. MCP efficiency. Personal communication, 2004.

[43] S. V. Lebedev, F. N. Beg, S. N. Bland, J. P. Chittenden, A. E. Dangor, M. G. Haines, M. Zakaullah, S. A. Pikuz, T. A. Shelkovenko, and D. A. Hammer. X-ray backlighting of wire array Z-pinch implosions using X pinch. *Review of Scientific Instruments*, 72:671–673, 2001.

[44] J. P. Chittenden, S. V. Lebedev, C. A. Jennings, S. N. Bland, and A. Ciardi. X-ray generation mechanisms in three-dimensional simulations of wire array Z-pinches. *Plasma Physics and Controlled Fusion*, 46:B457–B476, 2004.

[45] M. Sherlock, J. P. Chittenden, S. V. Lebedev, and M. G. Haines. Ion collisions and the Z-pinch precursor column. *Physics of Plasmas*, 11:1609, 2004.

[46] M. Sherlock. *PhD thesis: Ion collisional effects in z-pinch precursor plasma and laboratory astrophysical jets.* Imperial College London, 2003.

[47] A. Y. Poludnenko, K. K. Dannenberg, R. P. Drake, A. Frank, J. Knauer, D. D. Meyerhofer, M. Furnish, J. R. Asay, and S. Mitran. A Laboratory Investigation of Supersonic Clumpy Flows: Experimental Design and Theoretical Analysis. *The Astrophysical Journal*, 604:213–221, 2004.

[48] D. H. Kalantar and D. A. Hammer. Observation of a stable dense core within an unstable coronal plasma in wire-initiated dense Z-pinch experiments. *Physical Review Letters*, 71:3806–3809, 1993.

[49] F. N. Beg, A. E. Dangor, P. Lee, M. Tatarakis, S. L. Niffikeer, and M. G. Haines. Optical and x-ray observations of carbon and aluminium fibre Z-pinch plasmas. *Plasma Physics and Controlled Fusion*, 39:1–25, 1997.

[50] S. V. Lebedev, D. Ampleford, S. N. Bland, S. C. Bott, J. P. Chittenden, C. J. Jennings, and M. G. Haines. Ablation of wires and implosion phase of wire array z-pinches. *The 4th International Workshop on the Physics of Wire Array Z-pinches, Colorado Springs*, page Available at http://dorland.pp.ph.ic.ac.uk/magpie/publications/workshop2003, 2003.

[51] S. V. Lebedev, I. H. Mitchell, R. Aliaga-Rossel, S. N. Bland, J. P. Chittenden, A. E. Dangor, and M. G. Haines. Azimuthal Structure and Global Instability in the Implosion Phase of Wire Array Z-Pinch Experiments. *Physical Review Letters*, 81:4152–4155, 1998.

[52] S. V. Lebedev, F. N. Beg, S. N. Bland, J. P. Chittenden, A. E. Dangor, M. G. Haines, S. A. Pikuz, and T. A. Shelkovenko. Plasma formation and the implosion phase of wire array z-pinch experiments. *Laser Particle Beams*, 19:355–376, 2001.

[53] M. D. Mitchell, S. V. Lebedev, S. A. Pikuz, T. A. Shelkovenko, K. M. Chandler, D. A. Hammer, and M. Hu. Exploding wire dynamics from a single wire with closely spaced return current. *Bull. Am. Phys. Soc.*, 49:HP1:88, 2004.

[54] S. V. Lebedev, F. N. Beg, S. N. Bland, J. P. Chittenden, A. E. Dangor, M. G. Haines, S. A. Pikuz, and T. A. Shelkovenko. Effect of Core-Corona Plasma Structure on Seeding of Instabilities in Wire Array Z Pinches. *Physical Review Letters*, 85:98–101, 2000.

[55] J. Canto, G. Tenorio-Tagle, and M. Rozyczka. The formation of interstellar jets by the convergence of supersonic conical flows. *Astron. and Astrophys.*, 192:287–294, 1988.

[56] D. E. Post, R. V. Jensen, C. B. Tarter, W. H. Grasberger, and W. A. Lokke. Steady-State Radiative Cooling Rates for Low-Density, High-Temperature Plasmas. *Atomic Data and Nuclear Data Tables*, 20:397, 1977.

[57] B. Reipurth and J. Bally. Herbig-Haro Flows: Probes of Early Stellar Evolution. *An. Rev. Astron. and Astrophys.*, 39:403–455, 2001.

[58] T. Ray. What Role Do Magnetic Fields Play in Jets from Young Stars? *Bull. Am. Phys. Soc.*, 49:CM1:2, 2004.

[59] J. P. Apruzese, J. Davis, K. G. Whitney, J. W. Thornhill, P. C. Kepple, R. W. Clark, C. Deeney, C. A. Coverdale, and T. W. L. Sanford. The physics of radiation transport in dense plasmas. *Physics of Plasmas*, 9:2411–+, May 2002.

[60] D. D. Ryutov, M. S. Derzon, and M. K. Matzen. The physics of fast Z pinches. Sandia Report SAND98:1632, Sandia National Laboratories, Albuquerque, N.M., 1998.

[61] Y. B. Zel'dovich and Y. P. Raizer. *Physics of shock waves and high-temperature hydrodynamic phenomena.* New York: Academic Press, 1967.

[62] L. D. Landau and E. M. Lifshitz. *Fluid mechanics.* Oxford: Pergamon Press, 1987.

[63] S. Atzeni and J. Meyer-ter-Venh. *The Physics of Intertial Fusion.* Oxford University Press, 2004.

[64] J. D. Huba. NRL plasma formulary, revised. Technical Report NRL/PU/6790-00426, Naval Research Laboratory, 2002.

[65] N. Soker and M. Livio. Disks and jets in planetary nebulae. *The Astrophysical Journal*, 421:219–224, 1994.

[66] R. Sahai. Hubble Space Telescope Observations of Young Planetary Nebulae. *Astronomical Society of the Pacific Conference Series*, page 209, 2000.

[67] J. P. Leahy. *Beams and Jets in Astrophysics: Interpretation of large scale extragalactic jets.* Cambridge University Press, 1991.

[68] F. J. Swenson and J. H. Hammer. The Physics of Scaling Radiation and Hydrodynamics. *High Energy Density Physics Summer School, Santa Cruz, California*, 2002.

[69] J. M. Blondin, B. A. Fryxell, and A. Konigl. The structure and evolution of radiatively cooling jets. *The Astrophysical Journal*, 360:370–386, 1990.

[70] B. Reipurth. General Catalogue of Herbig-Haro Objects. *VizieR Online Data Catalog*, 5104, 2000.

[71] D. Lynden-Bell. Magnetic collimation by accretion discs of quasars and stars. *MNRAS*, 279:389–401, 1996.

[72] M. L. Norman, K.-H. A. Winkler, L. Smarr, and M. D. Smith. Structure and dynamics of supersonic jets. *Astron. and Astrophys.*, 113:285–302, 1982.

[73] J. M. Foster, B. H. Wilde, P. A. Rosen, T. S. Perry, M. Fell, M. J. Edwards, B. F. Lasinski, R. E. Turner, and M. L. Gittings. Supersonic jet and shock interactions. *Physics of Plasmas*, 9:2251, 2002.

[74] D. J. Ampleford, S. V. Lebedev, A. Ciardi, J. P. Chittenden, S. N. Bland, S. C. Bott, J. Rapley, M. Sherlock, C. Jennings, A. Frank, and T. Gardiner. Laboratory Modeling of Radiatively Cooled Jets Using Conical Wire Array Z-pinches. *AIP Conf. Proc. 703: Plasmas in the Laboratory and in the Universe: New Insights and New Challenges*, pages 443–446, 2004.

[75] S. C. Hsu and P. M. Bellan. A laboratory plasma experiment for studying magnetic dynamics of accretion discs and jets. *MNRAS*, 334:257–261, 2002.

[76] O.. Kafti, E. Livnat, and E. Keren. Infinite fringe moire deflectometry. *App. Optics*, 21:3884–3886, 1982.

[77] J. Bally and B. Reipurth. Irradiated Herbig-Haro Jets in the Orion Nebula and near NGC 1333. *The Astrophysical Journal*, 546:299–323, 2001.

[78] B. Reipurth, J. Bally, and D. Devine. Giant Herbig-Haro Flows. *The Astrophysical Journal*, 114:2708, 1997.

[79] J. D. Hurka, J. Schmid-Burgk, and P. E. Hardee. Deflection of stellar jets by ambient magnetic fields. *Astron. and Astrophys.*, 343:558–570, 1999.

[80] J. Canto and A. C. Raga. The steady structure of a jet/cloud interaction - I. The case of a plane-parallel stratification. *MNRAS*, 280:559–566, 1996.

[81] D. S. Balsara and M. L. Norman. Three-dimensional hydrodynamic simulations of narrow-angle-tail radio sources. I - The Begelman, Rees, and Blandford model. *The Astrophysical Journal*, 393:631–647, 1992.

[82] J. Canto and A. C. Raga. The dynamics of a jet in a supersonic side wind. *MNRAS*, 277:1120–1124, 1995.

[83] A. J. Lim and A. C. Raga. 3D numerical simulations of a radiative Herbig-Haro jet in a supersonic side wind. *MNRAS*, 298:871–876, 1998.

[84] J. Lindl. Development of the indirect-drive approach to inertial confinement fusion and the target physics basis for ignition and gain. *Physics of Plasmas*, 2:3933–4024, 1995.

[85] J. P. Chittenden, M. Dunne, M. Zepf, S. V. Lebedev, A. Ciardi, and S. N. Bland. Indirect-Drive Inertial Confinement Fusion Using Highly Supersonic, Radiatively Cooled, Plasma Slugs. *Physical Review Letters*, 88(23):235001–+, June 2002.

[86] J. P. Chittenden, S. V. Lebedev, B. V. Oliver, E. P. Yu, and M. E. Cuneo. Equilibrium flow structures and scaling of implosion trajectories in wire array Z pinches. *Physics of Plasmas*, 11:1118, 2004.

[87] S. V. Lebedev, F. N. Beg, S. N. Bland, J. P. Chittenden, A. E. Dangor, M. G. Haines, K. H. Kwek, S. A. Pikuz, and T. A. Shelkovenko. Effect of discrete wires on the implosion dynamics of wire array Z pinches. *Physics of Plasmas*, 8:3734–3747, 2001.

BIBL.
LONDIN.
UNIV.